Université de Lille

Doctoral School **Science de la Matière, du Rayonnement et de l'Environnement (SMRE)**
University Department **Physique des Lasers, Atomes et Molécules (PhLAM) UMR 8523**

Thesis defended by **Loïc Fache**

Defended on **October 9, 2025**

In order to become Doctor from Université de Lille

Academic Field **Physics of diluted medium**

Speciality **Nonlinear physics**

Nonlinear Evolution of Soliton Gases in Optical, Electrical, and Hydrodynamic Systems

Thesis supervised by Stéphane Randoux

Committee members

Referees	Nicolas Pavloff	Professor at Université Paris-Saclay	
	Isabelle Bouchoule	Senior Researcher at Laboratoire Charles Fabry, CNRS	
Examiners	Cristian Focsa	Professor at Université de Lille	Committee President
	Félicien Bonnefoy	Associate Professor at Ecole Centrale de Nantes	
	Gennady El	Professor at Northumbria University	
Supervisor	Stéphane Randoux	Professor at Université de Lille	

Colophon

Doctoral dissertation entitled “Nonlinear Evolution of Soliton Gases in Optical, Electrical, and Hydrodynamic Systems”, written by Loïc Fache, completed on October 19, 2025, typeset with the document preparation system LaTeX and the yathesis class dedicated to theses prepared in France.

Université de Lille

Doctoral School **Science de la Matière, du Rayonnement et de l'Environnement (SMRE)**
University Department **Physique des Lasers, Atomes et Molécules (PhLAM) UMR 8523**

Thesis defended by **Loïc Fache**

Defended on **October 9, 2025**

In order to become Doctor from Université de Lille

Academic Field **Physics of diluted medium**

Speciality **Nonlinear physics**

Nonlinear Evolution of Soliton Gases in Optical, Electrical, and Hydrodynamic Systems

Thesis supervised by Stéphane Randoux

Committee members

Referees	Nicolas Pavloff	Professor at Université Paris-Saclay	
	Isabelle Bouchoule	Senior Researcher at Laboratoire Charles Fabry, CNRS	
Examiners	Cristian Focsa	Professor at Université de Lille	Committee President
	Félicien Bonnefoy	Associate Professor at Ecole Centrale de Nantes	
	Gennady El	Professor at Northumbria University	
Supervisor	Stéphane Randoux	Professor at Université de Lille	

Université de Lille

École doctorale **Science de la Matière, du Rayonnement et de l'Environnement (SMRE)**
Unité de recherche **Physique des Lasers, Atomes et Molécules (PhLAM) UMR 8523**

Thèse présentée par **Loïc Fache**

Soutenue le **9 octobre 2025**

En vue de l'obtention du grade de docteur de l'Université de Lille

Discipline **Physique des milieux dilués**
Spécialité **Physique non-linéaire**

Évolution Non-linéaire de Gaz de Solitons dans des Systèmes Optiques, Electriques et Hydrodynamique

Thèse dirigée par Stéphane Randoux

Composition du jury

Rapporteurs	Nicolas Pavloff	professeur à l'Université Paris-Saclay	
	Isabelle Bouchoule	directrice de recherche au Laboratoire Charles Fabry, CNRS	
Examinateurs	Cristian Focsa	professeur à l'Université de Lille	président du jury
	Félicien Bonnefoy	MCF à l'Ecole Centrale de Nantes	
	Gennady El	professeur au Northumbria University	
Directeur de thèse	Stéphane Randoux	professeur à l'Université de Lille	

This thesis has been prepared at

Physique des Lasers, Atomes et Molécules (PhLAM) UMR 8523

2 Av. Jean Perrin
59650 Villeneuve-d'Ascq Cedex
France

☎ +33 3 20 33 60 37
✉ phlam-contact@univ-lille.fr
Web Site https://phlam.univ-lille.fr/

Acknowledgements

On peut me dire sans rémission
Qu'en groupe, en ligue, en procession
On a l'intelligence bête
Je n'ai qu'une consolation
C'est qu'on peut être seul et con
Et que dans ce cas, on le reste

– Jean Ferrat

À la fin de cette aventure, j'ai une seule certitude : le travail scientifique est avant tout une aventure humaine. Ce manuscrit est le fruit d'un effort collectif, et je me dois ici de remercier toutes celles et tous ceux qui m'ont accompagné et ont contribué à sa réalisation.

Je remercie tout d'abord les membres de mon jury d'avoir accepté d'évaluer mon travail. Je suis honoré qu'Isabelle Bouchoule et Nicolas Pavloff aient accepté de rapporter ce manuscrit. Je remercie également chaleureusement Félicien Bonnefoy, Gennady El et Cristian Focsa d'avoir accepté d'en faire partie. Un grand merci aussi à Cristian Focsa d'en avoir assuré la présidence.

Je tiens ensuite à remercier infiniment Stéphane Randoux, pour son encadrement, ses conseils, nos nombreux échanges, et surtout pour la confiance qu'il m'a accordée, parfois même quand moi-même je ne la trouvais guère. Merci de m'avoir toujours accueilli avec bienveillance dans ton bureau pour tous ces échanges, scientifiques, ou non, même quand je sais ô combien tu étais occupé à d'autres tâches. Je suis enfin fier d'avoir pu travailler aux côtés d'un scientifique que j'admire.

Merci au laboratoire PhLAM, et tout particulièrement à son directeur Cristian Focsa, pour m'y avoir accueilli dans d'excellentes conditions. On m'a souvent répété que le labo était une famille, je peux dire que je l'ai ressenti ! Merci à tous

ses membres, et un clin d'œil à Monsieur le directeur pour Munich.

Je souhaite remercier aussi les membres de l'atelier électronique, notamment Michel Gamot, Cédric Calimet, et tout particulièrement Hervé Damart, qui m'a ouvert les portes de l'atelier pendant de longues semaines (un second chez-moi, diront certains), m'a aidé à de nombreuses reprises, et avec qui j'ai eu tant de discussions enrichissantes. Merci à vous !

Merci également à Christine Yvoz, Walter Kolnierzak et Isabelle Mard-Alard, pour votre patience et votre aide à chaque fois que je suis venu frapper à votre porte. Enfin, un merci chaleureux à Sylvie : tu as été pendant longtemps la première personne que je voyais le matin, et tu avais toujours cette bonne humeur communicative. Merci !

Je remercie les financeurs de ma thèse : l'école doctorale SMRE, ainsi que le CNRS à travers le projet ANR SOGOOD.

Je souhaite maintenant remercier les collègues et collaborateurs qui ont contribué à ce travail, en espérant ne pas en oublier. Merci à François Copie et Pierre Suret, pour leurs nombreuses idées et suggestions. Je n'ai pas eu le temps de toutes les explorer, mais merci beaucoup à vous ! François, merci aussi d'avoir été une oreille attentive auprès de qui j'ai parfois fait ma thérapie, et merci aussi pour tes bons mots.

Merci aussi à Gennady El, Thibault Congy, Thibault Bonnemain, Giacomo Roberti, Guillaume Ducrozet, Félicien Bonnefoy, Filip Novkoski, Guillaume Ricard et Éric Falcon pour votre sympathie et la richesse de nos échanges.

Merci au referee B de m'avoir renommé *M. Frache*, ça me collera probablement à la peau encore un moment, j'imagine...

Elias je te souhaite beaucoup de réussite, tu le mérites vraiment, tu es un travailleur incroyable. Nos échanges ont été essentiels dans mon appréhension de beaucoup de concepts, notamment liés à GHD... j'espère t'avoir apporté autant. Je compte sur toi pour bien t'occuper de ceux qui nous succèdent ! Bonne route camarade !

Adrien, je dois avouer que tu m'as beaucoup impressionné, par ta qualité de raisonnement et surtout ta rapidité ! J'ai hâte de lire ta thèse et de comprendre un peu mieux, enfin peut-être, ces affaires de surfaces de Riemann. Au pire je

me raccrocherai à tes résultats expérimentaux ^^. Merci de m'avoir aidé à mieux comprendre GHD, c'est pas une mince affaire... Mes amitiés à Fred, Karine et Sarah !

Coline,
On ne se connaît pas depuis longtemps, mais ces derniers mois, ça a été un vrai plaisir de partager bien plus que des déjeuners : des discussions, des rires, mes inquiétudes récurrentes sur ma capacité à tenir mon emploi du temps, des respirations dans le quotidien... et, bien sûr, ton légendaire rejet de la noble patate.
Je te souhaite sincèrement le meilleur pour la suite, et je te jure : « nan mais là je suis bien ^^ ».
Et si un jour tu entends à nouveau *T.N.T.*, tu penseras à moi :
'Cause I'm T.N.T., I'm dynamite !
Merci à toi, vraiment.

Jordan,
Tu m'impressionneras toujours, je crois. Tu m'as accueilli dans le salon de thésards avec bienveillance, d'abord en tant que stagiaire, à ta droite, puis en tant que doctorant, à ta gauche. J'ai ainsi eu l'occasion d'observer tous les angles de tes écrans : parfois de la science, souvent... autre chose ^^. J'ai beaucoup apprécié nos échanges, qu'ils soient scientifiques, politiques ou économiques, on partage cette même curiosité insatiable.
Contrairement à ce que disent certains, je ne te qualifierais pas de râleur : tu es simplement un membre de PMI, c'est tout ^^.
Je ne crois pas avoir besoin de te souhaiter bon courage pour la suite... sauf peut-être pour les nuits à venir ! Félicitations à toi et à Tam pour cette belle aventure.

Kayce, que dire ?!
Je t'ai découvert cette année, et quelle découverte !
Merci pour toutes nos discussions (R..f.n, ****!!), pour m'avoir fait découvrir Rachid Taha, la caïpirinha (dans le désordre), pour ta bienveillance naturelle.
Tu es de ces personnes qu'on ne peut qu'aimer (*y'en a pas un sur cent et pourtant...*).
Je ne me fais aucun souci pour la suite.
Prends soin de la bande de loustics quand je ne serai plus là : le clown triste s'en va, à toi de les faire rire !
Le temps d'apprendre à vivre il est déjà trop tard, disait le poète...
Enfin, je vous embrasse Eva et toi, et vous souhaite le meilleur.

Agathe,
Merci d'avoir été toi. Je suis heureux de t'avoir rencontré. Je ne sais pas si c'est ton arrivée, mais ce qui est sûr c'est que celle-ci coïncide avec une affirmation de ma personnalité (dixit Hervé ^^, je ne sais pas si c'est une bonne chose ahah). Je serai toujours une épaule sur laquelle tu pourras t'appuyer. Je te dois bien au moins cela ! Merci d'avoir supporté mes chants intempestifs, et même de les avoir parfois accompagnés. J'espère que celui qui prendra ma place, en face de toi, t'appréciera autant que je t'ai appréciée, c'est-à-dire autant que tu le mérites ! Je sais que tu vas t'en sortir comme une cheffe pour ta thèse : ne laisse personne te faire croire le contraire. Tu nous as déjà tous impressionnés.
You can say it's just the way you are...
Good luck champ
Merci pour tout. Et non, tu ne t'es pas fait un ennemi, bien au contraire !

Martin,
Tu as été le premier doctorant de l'équipe à m'avoir formé, dès mon stage avec Pierre. Tu m'as appris l'essentiel sur les manips d'optique, je ne sais pas si tu dois en être fier... ^^
Merci de m'avoir accueilli dans ton bureau pour les pauses déjeuner, et pour nos discussions, parfois (souvent) loin de la science.
Merci d'être ce catalyseur, ce fédérateur, que tu es naturellement.
Tu es un excellent scientifique, même si tu en doutes parfois, je le rappelle ici.
Merci pour tout, et j'espère qu'on se recroisera très bientôt.

Alexandre... par où commencer ?
Comme c'était dur pour toi de m'accepter ^^. Heureusement que j'ai insisté.
Tu es une personne profondément honnête, bonne, avec tes failles, et c'est ce qui te rend attachant.
Tout a changé pendant ces RNL, deux jours extraordinaires. Pour moi, ce serait un 10/10 sur MAL, je ne sais pas pour toi ? ^^
Tu es devenu bien plus qu'un ami.
Ton départ pour écrire ta thèse m'a laissé un vide, je ne saurais expliquer pourquoi, mais quelque chose manquait, j'avais presque du mal à l'accepter.
Maintenant que j'ai écrit la mienne, je te comprends.
Enfin dans le désordre, merci pour : POE ; Valo (désolé je suis toujours aussi nul) ; les discussions politiques (au fait, tu as tort, mais je t'en veux pas); Dofus (désolé j'ai saturé bien vite...); Les discussions interminables sur discord ; Le fait de nous plaindre collectivement, mais en rigolant bien.
J'ai hâte qu'on se retrouve bientôt mon ami, je te souhaite le meilleur, vraiment !

Quentin.
Je vais essayer de ne pas pleurer en écrivant, et c'est déjà raté.
Mon binôme. Mon frère de thèse.
Depuis le master, on ne s'est jamais vraiment quittés. On a tout partagé : les grandes discussions, les idées brillantes et surtout les moins brillantes, les coups de mou et les moments d'euphorie. Tu connais à peu près tout de moi, mes doutes, mes excès, mes faiblesses, mes rêves et mes coups de gueule.
Je crois qu'on peut dire qu'on a fait cette thèse à deux. Il y a eu peu de jours où l'un de nous n'a pas soutenu l'autre, ou simplement écouté. J'ai toujours pu compter sur toi pour me porter sur tes épaules (dieu sait ce que ça veut dire ^^).
Et puis il y a eu le Carnaval. Dunkerque. Quelle aventure. Une expérience aussi absurde que magnifique qu'on a vécue quasiment à deux, comme un symbole de tout ce qu'on a traversé ensemble.
Ta maison est devenue ma troisième maison. Et chez moi, un matelas, que j'oubliais régulièrement de gonfler, t'attendait.
Tu soutiendras bientôt ta thèse, et je serai là. On se retrouvera très vite. Et on se donne rendez-vous, comme toujours, au carnaval de Dunkerque, c'est une promesse. Garde-moi un peu de rhum arrangé, je veux le goûter vieilli d'un an (mon foie ne te remercie pas). Tu sais ô combien tu as été important pour moi pendant cette thèse. Tu sais aussi ce que je t'ai confié comme mission. Merci infiniment.

Voilà, l'aventure thèse s'achève. Elle fut tout cela à la fois : belle, dure, éprouvante, récompensante, drôle, excitante, triste, joyeuse, stressante, réconfortante, épanouissante, enivrante (dans les deux sens)... Pas étonnant qu'on n'en ressorte pas tout à fait le même.

Enfin, merci à ma famille, et particulièrement à ma « petite Maman ». Tu m'as toujours soutenu, m'as toujours répété la fierté que tu me portais. Ça compte pour beaucoup dans là où j'en suis aujourd'hui. Mon caractère pudique m'empêche de te le dire beaucoup, alors j'en profite que ce soit gravé ici. Je t'aime Maman !

Nonlinear Evolution of Soliton Gases in Optical, Electrical, and Hydrodynamic Systems

Abstract

Solitons are stable, localized nonlinear wave packets that emerge in integrable systems from a balance between nonlinearity and dispersion. When large ensembles of solitons interact in random configurations, they form what is known as a *soliton gas*, a many-body nonlinear wave system whose dynamics call for a statistical treatment. While the theoretical framework for soliton gases has been extensively developed under the assumption of integrability, many physical systems exhibit weak perturbations that break this condition. The impact of such deviations on the spectral and statistical properties of soliton gases remains poorly understood. In this thesis, we experimentally investigate the dynamics of dense soliton gases in three distinct physical platforms: a large deep-water wave tank governed by the focusing nonlinear Schrödinger equation, a nonlinear electrical transmission line modeled by a dissipative KdV equation, and a recirculating optical fiber loop described by a perturbed focusing NLSE. Each system provides a setting to explore the effect of weak integrability breaking, such as damping, diffusion, or optical gain. Our results highlight the limitations of existing kinetic or hydrodynamic theories in weakly non-integrable regimes and point to the need for new frameworks capable of capturing soliton-radiation coupling, spectral reshaping, and non-isospectral evolution.

Keywords: soliton gas, integrable turbulence, integrability breaking, inverse scattering transform

Physique des Lasers, Atomes et Molécules (PhLAM) UMR 8523
2 Av. Jean Perrin – 59650 Villeneuve-d'Ascq Cedex – France

Évolution Non-linéaire de Gaz de Solitons dans des Systèmes Optiques, Electriques et Hydrodynamique

Résumé

Les solitons sont des paquets d'ondes non linéaires stables et localisés qui émergent dans des systèmes intégrables à partir d'un équilibre entre non-linéarité et dispersion. Lorsque de grands ensembles de solitons interagissent dans des configurations aléatoires, ils forment ce que l'on appelle un *gaz de solitons*, un système non linéaire dont la dynamique nécessite un traitement statistique. Bien que le cadre théorique des gaz de solitons ait été largement développé sous l'hypothèse d'intégrabilité, de nombreux systèmes physiques présentent de faibles perturbations qui brisent cette condition. L'impact de telles déviations sur les propriétés spectrales et statistiques des gaz de solitons reste mal compris. Dans cette thèse, nous étudions expérimentalement la dynamique de gaz de solitons denses au sein de trois plateformes physiques distinctes : un grand canal à houle en eau profonde régi par l'équation de Schrödinger non linéaire focalisante, une ligne de transmission électrique non linéaire modélisée par une équation de KdV dissipative, et une boucle de recirculation fibrée décrite par une NLSE focalisante perturbée. Chaque système constitue un cadre permettant d'explorer les effets de faibles brisures d'intégrabilité, telles que les pertes, la diffusion ou du gain optique. Nos résultats mettent en évidence les limites des théories cinétiques ou hydrodynamiques existantes dans les régimes faiblement non intégrables, et soulignent la nécessité de nouveaux cadres capables de décrire le couplage soliton-radiations, les réorganisations spectrales et les évolutions non isospectrales.

Mots clés : gaz de solitons, turbulence integrable, brisure d'integrabilité,transformée de diffusion inverse

Table of contents

General Introduction

Waves are a universal feature of the physical world. We hear thanks to sound waves, we see because of electromagnetic waves (light), and we produce music by bowing the string of a violin, which generates transverse elastic waves. These diverse phenomena share a common underlying mechanism: a localized disturbance propagates through a medium by coupling between neighboring elements, giving rise to a traveling oscillation [1]. At leading order, many such wave phenomena are accurately described by linear wave equations, which capture this fundamental behavior across a wide range of physical systems.

Before the formal development of wave equations, Christiaan Huygens proposed in the 17^{th} century a geometric construction to describe how wavefronts propagate through space [2]. He paved the way for the wave theory. A century later, d'Alembert derived the one-dimensional wave equation for a vibrating string, laying the foundations of the mathematical description of wave propagation [3]. Over time, wave theory became central to both physics and applied mathematics. In the early 19^{th} century, Joseph Fourier discovered that any wave pattern could be represented as a superposition of periodic waves [4]. All wave phenomena could thus be related to the frequencies, amplitudes, wavelengths, and velocities of these elementary wave trains. Fourier analysis thereby provided a powerful framework to decompose complex signals into **independent** modes of vibration, enabling a systematic study of linear wave phenomena across many physical systems. If each of these modes propagates at a different velocity, the wave gradually spreads during propagation, and the system is said to be dispersive.

However, the idealized linear picture begins to break down in many real-world systems where nonlinearities cannot be neglected. As the amplitude of

the wave grows, interactions between spectral modes exist. Thus, the behavior of wave systems departs from the superposition principle. Interactions between wave modes lead to energy transfers across system scales, giving rise to the phenomenon of *wave turbulence* [5–8]. Wave turbulence refers to the dynamics of a large number of weakly nonlinear, interacting waves under external forcing. It has been observed in a wide range of physical systems, including surface waves on fluids [9, 10], ocean waves [11, 12], vibrating elastic plates [13, 14], waves in Bose-Einstein condensates [15, 16], Alfvén waves in the solar wind [17] and optical systems [18, 19].

This has motivated the development of a kinetic theory of wave turbulence, derived under assumptions of weak nonlinearity and random phase statistics and resonant interactions [20, 21]. It predicts the emergence of energy cascades and scale-invariant power-law spectra, which have been experimentally observed in several systems. However, the perturbative nature of this theory limits its applicability when nonlinear interactions become strong.

When the amplitude of the waves increases, nonlinear effects can no longer be treated as small perturbations. In this strongly nonlinear regime, wavefields often develop localized structures that maintain their shape over long distances [22]. Among the most striking of these are *solitons*: nonlinear wave packets that result from a balance between nonlinearity and dispersion. Solitons arise as exact, stable solutions of certain nonlinear partial differential equations and have been observed across a wide variety of physical systems, ranging from water waves [23] and plasmas [24] to optical fibers [25] and condensed matter [26]. Their universal nature make them fundamental building blocks in the dynamics of strongly nonlinear wave systems.

A whole new approach to nonlinear dispersive wave equations emerged in the 1960s with the development of the *inverse scattering transform* (IST) [27, 28]. This method allows for the exact solution of certain nonlinear partial differential equations, such as the Korteweg-de Vries (KdV) or the one-dimensional nonlinear Schrödinger equation (1D-NLSE), by transforming them into linear spectral problems. Just as Fourier analysis decomposes a wavefield into linear modes, IST decomposes it into nonlinear modes, including solitons and radiation [28, 29]. This powerful mathematical tool launched an entire field of research at the

interface of mathematical physics, nonlinear analysis, and integrable systems.

The objective of the present thesis is to explore *soliton gases*, a concept introduced by V.E. Zakharov in 1971 [30]. A soliton gas is defined as a large ensemble of solitons with random amplitudes, velocities, and positions in interaction. The interactions of the solitons within the gas lead to emergent collective behavior, whose complexity calls for a statistical treatment. The theoretical description of such systems has led to the development of a kinetic theory of soliton gases [30–33]. Initially, soliton gases remained a largely theoretical construct within the field of nonlinear physics and statistical mechanics. The topic experienced a significant revival in 2005, when G.A. El and A.M. Kamchatnov generalized Zakharov's kinetic theory to describe *dense* soliton gases [32]. This development provided a more complete framework to describe interacting solitons beyond the dilute regime. More recently, experimental realizations of soliton gases have begun to emerge in various physical platforms, including water waves [34, 35], optical fibers [36], transforming the concept from a purely theoretical model into a subject of active experimental investigation [37].

This theories are built upon integrable condition. However, real physical systems are never exactly integrable: small dissipation, external forcing, or higher-order nonlinear effects can break integrability of the system and raise fundamental questions about the evolution, of the dynamics and statistical properties of the SG in such regimes. In particular, we ask whether concepts from kinetic theory remain valid, and how spectral quantities evolve under weak perturbations.

To investigate these questions, we adopt a combined experimental and numerical approach. We consider three distinct physical platforms admitting 1D soliton propagation: a water tank experiment operating in the deep-water regime (modeled by the focusing 1D-NLSE), a nonlinear electrical transmission line (governed by the KdV equation), and a recirculating fiber-loop setup (modeled by the focusing 1D-NLSE). These complementary systems allow us to probe soliton gases under various integrable and weakly non-integrable conditions.

This manuscript is structured as follows.

Chapter 1 introduces the key mathematical and physical concepts relevant to soliton dynamics. It begins with a historical and conceptual overview of solitons

and the notion of integrability. The two main integrable models discussed throughout the manuscript, the focusing one-dimensional nonlinear Schrödinger equation (fNLSE) and the Korteweg–de Vries (KdV) equation, are presented and compared. The principle of the inverse scattering transform (IST), which underlies nonlinear spectral analysis, is then introduced. The chapter concludes with an introduction to the kinetic theory of soliton gases, along with a brief overview of recent developments in generalized hydrodynamics (GHD).

Chapter 2 presents an experimental investigation of soliton gas interactions. Specifically, it examines the collision between two dense soliton gases composed of solitons with nearly identical amplitudes and equal but opposite velocities. The experimental results, obtained using a 140-meter-long wave tank at École Centrale de Nantes (France), are compared with analytical predictions from the kinetic theory of soliton gases. This study provides one of the first direct tests of the kinetic theory. The results presented in this chapter are based on the publication [38]: *L. Fache, F. Bonnefoy, G. Ducrozet, F. Copie, F. Novkoski, G. Ricard, G. Roberti, E. Falcon, P. Suret, G. El, and S. Randoux, "Interaction of soliton gases in deep-water surface gravity waves", Phys. Rev. E 109, 034207 (2024).*

Chapter 3 focuses on the dynamics of soliton gases in a weakly non-integrable electrical system, namely a nonlinear electrical transmission line subject to small finite linear dissipation. Unlike the integrable Korteweg-de Vries equation, which preserves an infinite number of conserved quantities, this system only conserves the total mass of the wavefield and breaks integrability through linear diffusion. The experiment starts from a dense and fully randomized soliton gas and tracks its evolution in time. Remarkably, nonlinear spectral analysis reveals that the gas undergoes a spontaneous transition into a coherent macroscopic state, identified as a soliton condensate. This condensate is characterized by the spatial delocalization of associated eigenmodes. The formation of this state is driven by nonadiabatic effects: new solitonic components emerge dynamically, and the nonlinear spectrum reorganizes spatially in a way not captured by standard kinetic theories of soliton gases. These results highlight how weak dissipation can trigger profound structural changes in nonlinear wave systems, and provide a clear example of integrability-breaking dynamics leading to new emergent behavior. The results presented in this chapter are based on the

publication [39]: *L. Fache, H. Damart, F. Copie, T. Bonnemain, T. Congy, G. Roberti, P. Suret, G. El, and S. Randoux, "Dissipation-driven emergence of a soliton condensate in a nonlinear electrical transmission line", Phys. Rev. Lett. 134.14, 147201 (2025).*

Chapter 4 investigates the dynamics of optical soliton gases propagating in a recirculating fiber loop, in the presence of weak linear gain or loss. While the system deviates from strict integrability, its evolution remains well approximated by a perturbed version of the one-dimensional focusing nonlinear Schrödinger equation. In this experiment, the full complex optical field, i.e. both amplitude and phase, is measured using a heterodyne detection technique. This enables a direct nonlinear spectral analysis at various propagation distances, allowing us to monitor how the spectral distribution of the soliton gas evolves in the complex spectral plane. The initial state is prepared as a dense soliton condensate, characterized by a Weyl distribution of eigenvalues. As the system propagates under weak amplification or damping, significant and distinct deformations of the nonlinear spectrum are observed. In the presence of gain, a bichromatic soliton gas emerges, whereas weak loss leads to a spectral distribution resembling a semicircle at long propagation distances. These dissipation-induced transformations are not captured by existing kinetic or hydrodynamic theories of soliton gases, and highlight new regimes of integrable turbulence driven by weak perturbations. The results presented in this chapter are based on the manuscript [40]: *L. Fache, F. Copie, P. Suret, and S. Randoux, "Perturbed Nonlinear Evolution of Optical Soliton Gases: Growth and Decay in Integrable Turbulence", Phys. Rev. Lett. 135.15, 157201 (2025).*

Chapter 1

General concepts

Knowledge is to share, mine is for you.

– Adapted from "La Ritournelle" - Sebastien Tellier

In this chapter, we introduce several key concepts, theoretical frameworks, and methodological tools that will be used throughout this thesis. These elements are essential for understanding the physical systems and phenomena discussed in the following chapters.

1.1 A Brief History of Solitons

In 1834, John Scott Russell (1808-1882), a Scottish engineer and shipbuilder who was also among the first to experimentally demonstrate the Doppler effect [41, 42], observed a remarkable phenomenon on the Union Canal near Heriot-Watt University in Edinburgh. While following a boat that had come to a sudden stop, he noticed a solitary elevation of water that continued to travel undisturbed along the canal, maintaining both its shape and speed over a significant distance. This observation stood in stark contrast to the prevailing wave theories of the time, such as those developed by Airy and Stokes [43, 44], who both considered Russell's interpretation to be inconsistent with their theories.

Intrigued by this unexpected behavior, Russell constructed a dedicated wave tank to further investigate what he poetically described as: *"Such, in the month of August 1834, was my first chance interview with that singular and beautiful phenomenon which I have called the Wave of Translation"*. He presented his findings to the British Association for the Advancement of Science in 1844 [45].

Independent confirmations of similar wave phenomena followed. Notably, in 1862, hydraulic engineer Henry Bazin reported related observations on the Burgundy Canal near Dijon and presented his results to the French *Académie des Sciences* [46]. Theoretical understanding progressed significantly in the latter half of the 19^{th} century. In 1872, Joseph Boussinesq developed a theoretical description of long waves in shallow water, laying important preliminary work for the study of nonlinear wave propagation [47]. A few years later, in 1876, Lord Rayleigh provided a formal demonstration of the existence of a *"wave of permanent form"*, highlighting the possibility of a balance between nonlinear and dispersive effects [48].

The mathematical formulation of these ideas culminated in 1895 when Korteweg and de Vries derived the now-famous one-dimensional equation describ-

ing the propagation of long, unidirectional, weakly nonlinear, and weakly dispersive shallow water waves [49]. This equation, known today as the Korteweg-de Vries (KdV) equation, became central in the modern soliton theory.

Russell's early observations remained largely unrecognized for over a century, until the advent of digital computing in the mid-1960s enabled applied scientists to revisit problems in nonlinear wave propagation [50]. The term *soliton* was introduced in 1965 by Zabusky and Kruskal [51], who discovered that solitary wave solutions of the KdV equation interact in a particle-like manner, preserving their shape and speed after collisions. This finding emerged from numerical simulations designed to investigate earlier results obtained by Fermi, Pasta, Ulam, and Tsingou (FPUT) in 1955 [52].

The original FPUT study aimed to explore the process of thermalization in nonlinear systems, with a particular focus on heat conduction in crystalline solids. To this end, they modeled a one-dimensional lattice of point masses connected by nonlinear springs, as schematized in Fig. 1.1.

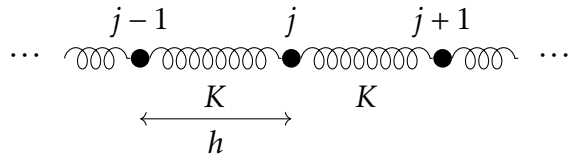

Figure 1.1: Schematic of a chain of mechanical oscillators represented as masses and springs, with spring constant K, and lattice period h, as the one considered by FPUT in their work of 1955.

Their idea was to model the atomic interactions within a crystal by replacing the realistic interatomic potential (such as the Lennard-Jones potential) with a simplified nonlinear force, involving quadratic corrections to Hooke's law.

We present the FPUT approach as outlined in detail in Refs. [50, 53, 54]. In this model, the force acting on the j-th mass shown in Fig. 1.1 is given by:

$$F_j = K(u_{j+1} - u_j) - K(u_j - u_{j-1}) + K\alpha\left[(u_{j+1} - u_j)^2 - (u_j - u_{j-1})^2\right], \tag{1.1}$$

where K is the linear spring constant, α quantifies the strength of the nonlinearity, and $u_j(t)$ denotes the displacement of the j-th mass from its equilibrium

position. In Eq. (1.1), each mass is coupled to its nearest neighbors $j-1$ and $j+1$.

FPUT numerically solved the resulting coupled nonlinear differential equations, arguably the first computational physics simulation, on the MANIAC I computer:

$$m\frac{d^2u_j}{dt^2} = K(u_{j+1} - 2u_j + u_{j-1}) + K\alpha\left[(u_{j+1} - u_j)^2 - (u_j - u_{j-1})^2\right], \tag{1.2}$$

with $j = 1,\ldots,N$, and $N = 64$. This equation simply expresses Newton's second law for the one-dimensional chain of masses connected by nonlinear springs shown in Fig. 1.1. For simplicity, we set $K = m = 1$ in the following discussion.

The displacements $u_j(t)$ can be expressed in terms of the system's normal modes:

$$Q_k(t) = \sqrt{\frac{2}{N}}\sum_{j=0}^{N-1} u_j(t)\sin\left(\frac{kj\pi}{N}\right),$$

where $Q_k(t)$ is the amplitude of the k-th mode. The corresponding energy is:

$$E_k = \frac{1}{2}\left(\left(\frac{dQ_k}{dt}\right)^2 + \omega_k^2 Q_k^2\right) + \alpha\sum_{l,m=0}^{N-1} D_{klm}Q_kQ_lQ_m,$$

where $\omega_k = 2\sin\left(\frac{\pi k}{2N}\right)$ are the normal frequencies of the linear spectrum (i.e. the dispersion relation of the mechanical chain), and the coefficients D_{klm} capture the nonlinear coupling between modes [53].

In the absence of nonlinearity ($\alpha = 0$), the normal modes are independent, and their energies remain constant in time. As a result, no energy transfer between modes occurs, and the system cannot thermalize; energy remains localized in the initially excited mode. The natural hypothesis was that nonlinearity might enable energy transfer across modes, potentially leading to thermalization and energy equipartition.

This was precisely the motivation of the FPUT study: they initiated the system with energy concentrated in a single low-wavenumber mode, expecting it to spread progressively to all others as the system evolved toward equilibrium. Surprisingly, their numerical results contradicted this intuition. Rather than distributing uniformly among the modes, the energy displayed near-periodic

returns to the initial mode as shown in Fig. 1.2. This unexpected behavior is now known as the *FPUT recurrence problem*.

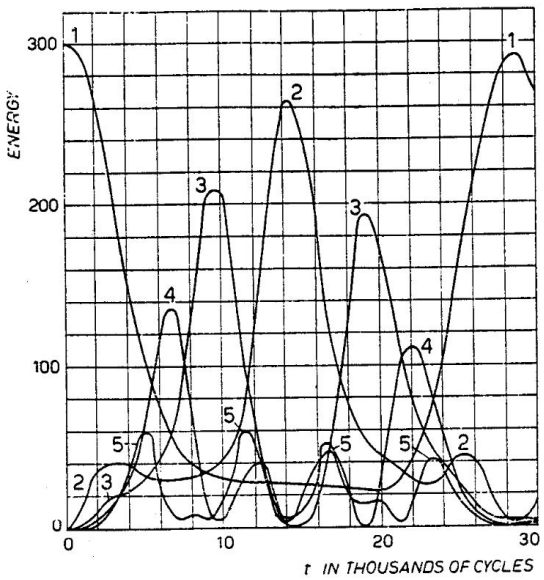

Figure 1.2: FPUT recurrence in the FPUT-α model with $N = 32$ masses and fixed boundary conditions. The plot shows the time evolution of the energy contained in the five lowest normal modes. Initially, only mode $k = 1$ is excited. Although energy is redistributed among the modes over time, it eventually returns almost entirely to the initial mode. Figure extracted from Ref. [52].

Looking at analytical insight into wave propagation in the FPUT chain described by Eq. (1.2), one can consider its continuum limit. Let h denote the uniform spacing between adjacent masses (see Fig. 1.1). In the long-wavelength regime, corresponding to low-wavenumber (small k) modes, $u_j(t)$ can be approximated by a smooth function $u(x,t)$, with $x = jh$. Performing a Taylor expansion of $u_{j\pm1}$ about x, we obtain:

$$u_{j\pm1} = u(x) \pm h\frac{\partial u}{\partial x} + \frac{h^2}{2!}\frac{\partial^2 u}{\partial x^2} \pm \frac{h^3}{3!}\frac{\partial^3 u}{\partial x^3} + \frac{h^4}{4!}\frac{\partial^4 u}{\partial x^4} + \dots$$

Substituting these expansions into Eq. (1.2) and taking the limit $h \to 0$, one obtains:

$$\frac{\partial^2 u}{\partial t^2} = \frac{K}{m}\left(h^2\frac{\partial^2 u}{\partial x^2} + \frac{h^4}{12}\frac{\partial^4 u}{\partial x^4}\right)\left(1 + \alpha\left[2h\frac{\partial u}{\partial x} + \frac{h^3}{3}\frac{\partial^3 u}{\partial x^3}\right]\right). \tag{1.3}$$

In the absence of nonlinearity ($\alpha = 0$), this equation reduces to a dispersive version of the classical wave equation originally studied by d'Alembert [3], describing bidirectional wave propagation in a linear medium. The presence of higher-order derivatives reflects the dispersive nature of the lattice, which arises from the discreteness of the original system. Keeping only the dominant contributions, i.e., the lowest-order terms in h, and using subscript notation for derivatives for simplicity, we obtain:

$$u_{tt} - c^2 u_{xx} = c^2 \left(2\alpha h u_x u_{xx} + \frac{h^2}{12} u_{xxxx} \right), \tag{1.4}$$

where $c^2 = Kh^2/m$ is the characteristic wave speed in the linear regime.

This equation is known as the ill-posed Boussinesq equation. It possesses many of the same integrability properties as the KdV equation, a topic that will be discussed in detail in the next section. Remarkably, it is precisely this integrability that inhibits classical thermalization in the FPUT model.

One might then ask: if the Boussinesq equation is integrable, why not consider it as the definitive continuum model? There are two key reasons why this is not the usual approach [55]. First, the Boussinesq equation lacks the universality of the KdV equation in the description of weakly nonlinear dispersive waves. Second, and more crucially, it suffers from short-wavelength instabilities: for generic initial conditions, the Cauchy problem is ill-posed in forward time [56].

In contrast, the KdV equation emerges as a unidirectional reduction of the Boussinesq equation in the long-wave limit. This reduction eliminates the short-wave instability while preserving both the essential nonlinear and dispersive effects, yielding a well-posed and integrable evolution equation.

Let us now consider small-amplitude waves by introducing a small parameter $\epsilon \ll 1$, and rescaling the displacement as $v = \epsilon u$. We also define the following change of variables,

$$\xi = \epsilon^{1/2}(x - ct), \qquad \tau = \epsilon^{3/2} ct,$$

Expanding the equation of motion and retaining only the leading-order terms

up to $\mathcal{O}(\epsilon^3)$, one obtains:

$$v_{\tau\xi} = -\frac{1}{2}\left(\alpha h (v^2)_{\xi\xi} + \frac{h^2}{12} v_{\xi\xi\xi\xi}\right).$$

Integrating once with respect to ξ (which amounts to selecting unidirectional wave propagation), yields to the KdV equation:

$$v_\tau + \alpha h v v_\xi + \frac{h^2}{24} v_{\xi\xi\xi} = 0. \tag{1.5}$$

It is worth noting that the form of the nonlinear term in the original discrete model determines the continuum limit. If the nonlinearity is quadratic in energy, such as in the so-called β-FPUT chain, the resulting equation is the modified Korteweg-de Vries (mKdV) equation [54], which remains integrable:

$$v_\tau + \kappa v^2 u_\xi + \gamma v_{\xi\xi\xi} = 0, \tag{1.6}$$

where κ and γ are constants that depend on the system parameters (such as h and the nonlinear coefficient β).

While the KdV equation governs soliton dynamics in systems with quadratic nonlinearities (as in the continuum limit of the α-FPUT chain), the mKdV equation arises in the presence of cubic nonlinearities and leads to qualitatively different types of solitary wave solutions.

In their numerical simulations of the KdV equation with periodic boundary conditions, Zabusky and Kruskal observed a recurrence phenomenon very similar to that found in the original FPUT study. As discussed earlier, their work was the first to uncover the existence of *solitons*: starting from the initial condition $u(0) = \cos(\pi\xi)$, the waveform evolved into a train of localized structures that interacted strongly, see Fig. 1.3. Remarkably, after each interaction, these entities retained their shape and speed, except for a position shift, highlighting the elastic nature of soliton collisions and which prevents perfect recurrence.

Recognizing the connection between the KdV equation and the FPUT chain, Zabusky and Kruskal wrote: *"[The KdV] equation can be used to describe the one-dimensional, long-time asymptotic behavior of small but finite-amplitude [...]*

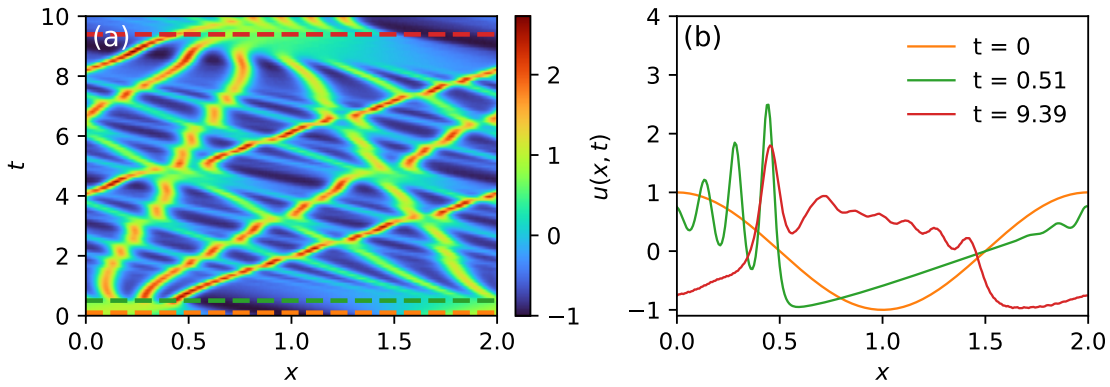

Figure 1.3: Numerical reproduction of the classical Zabusky–Kruskal experiment on the KdV equation [51]. (a) Space-time diagram of the field $u(x,t)$ showing the emergence and interaction of solitons from an initial sinusoidal wave. (b) Field profiles at three different times: initial condition ($t = 0$, orange), intermediate stage ($t = 0.51$, green), and late-time evolution ($t = 9.39$, red).

long waves in anharmonic crystals". They proposed that the recurrences observed in the FPUT system could be interpreted as resulting from soliton interactions: since solitons preserve their identity during collisions, no energy is exchanged between them, preventing thermalization and energy equipartition.

Today, the concept of solitary waves, or solitons, plays a central role in the modeling of complex nonlinear dynamics across a wide range of physical systems [53]. Solitons have been observed in fluid dynamics and nonlinear optics, but also in plasma physics [57], magma flow [58], high-energy physics [59], and condensed matter systems [53].

One of the most promising applications of soliton theory has emerged in the field of optical communications [60]. In 1973, Akira Hasegawa at AT&T Bell Laboratories proposed that solitons could propagate in optical fibers, opening the door to soliton-based data transmission systems [61]. Since then, optical solitons have been studied for dispersion-less signal propagation in fiber-optic transmission [62–70].

However, in practice, modern optical telecommunication systems do not rely on optical solitons. Instead, they predominantly use intensity-modulated signals with optical amplification systems. For a concise overview of fifty years of research on optical solitons and their potential applications, the reader is

referred to Refs. [60, 71].

1.2 Integrability and Inverse Scattering Transform

The existence of soliton solutions in a physical system is a signature of integrability. While the concept of integrability appears in various branches of physics and mathematics, we adopt here the standard definition: a system is said to be integrable if it possesses as many conserved quantities as degrees of freedom [72, 73]. As a consequence, the dynamics of such systems are confined to a restricted region of phase space, which prevents them from exhibiting ergodic behavior by exploring the whole phase space [74].

In this work, we consider the case of *complete integrability*, which applies to systems described by PDEs, with an infinite number of degrees of freedom and a corresponding infinite hierarchy of conserved quantities [75, 76]. Such systems are exactly solvable through powerful analytical techniques, most notably the *Inverse Scattering Transform* (IST), which will be introduced in the following section.

This thesis focuses on one-dimensional systems, which include several prototypical examples of integrable equations of physical relevance, such as the sine-Gordon equation, the NLSE, and the KdV equation.

Why, then, are integrable systems of such interest? As previously discussed, unlike ergodic systems, integrable systems do not relax to thermal equilibrium as described by the standard Gibbs ensemble, (or, in classical wave systems, the Rayleigh-Jeans distribution [77]).

Instead, integrable systems provide an ideal framework for investigating out-of-equilibrium statistical mechanics. In particular, thermalization is often replaced by relaxation to a stationary state described by a *generalized Gibbs ensemble* (GGE) [78], which incorporates all conserved quantities of the integrable system. The GGE thus provides a theoretical framework for studying statistical behavior in integrable models far from equilibrium [37].

1.2.1 Integrable partial differential equations for the description of soliton propagation

This section introduces the main integrable equations that will be central to the analysis developed throughout this thesis, namely the KdV equation and the NLS equation.

1.2.1.1 The Korteweg-de Vries Equation

The KdV equation was first derived in 1895 by Diederik Korteweg and Gustav de Vries as a model for the propagation of long, unidirectional surface waves in shallow water [49]. It takes the form:

$$u_t + 6uu_x + u_{xxx} = 0, \tag{1.7}$$

where $u(x,t)$ represents the deviation of the free surface from its equilibrium level, x is the spatial coordinate along the direction of wave propagation, and t denotes time.

This equation combines a nonlinear term $6uu_x$, responsible for wave steepening, with a dispersive term u_{xxx}, which tends to spread the wave. The competition between nonlinearity and dispersion leads to the formation of solitons, that maintain their shape during propagation and after interactions.

Although originally derived in the context of hydrodynamics, the KdV equation also appears in various other physical settings involving weakly nonlinear, weakly dispersive, and effectively unidirectional wave propagation. Beyond hydrodynamics [79–81], these include plasma physics [82–84], and nonlinear acoustics [85] for example. As an integrable partial differential equation, the KdV equation possesses an infinite hierarchy of conserved quantities. The first three are [29]:

$$M = \int_{-\infty}^{\infty} u \, \mathrm{d}x, \quad P = \int_{-\infty}^{\infty} u^2 \, \mathrm{d}x, \quad E = \int_{-\infty}^{\infty} \left(u^3 - \frac{1}{2} u_x^2 \right) \mathrm{d}x, \tag{1.8}$$

where M, P, and E correspond respectively to the mass, momentum, and energy of the wave field.

To better understand the origin of solitons, it is instructive to examine the role of each term in isolation. Figure 1.4 illustrates the evolution of an initial localized pulse governed by the inviscid Burgers (or Hopf) equation, $u_t + uu_x = 0$, which retains only the nonlinear term of the KdV equation. The solution, computed via the method of characteristics [86], shows wave steepening. This process, sometimes referred to as "wave breaking", is a signature of purely nonlinear dynamics.

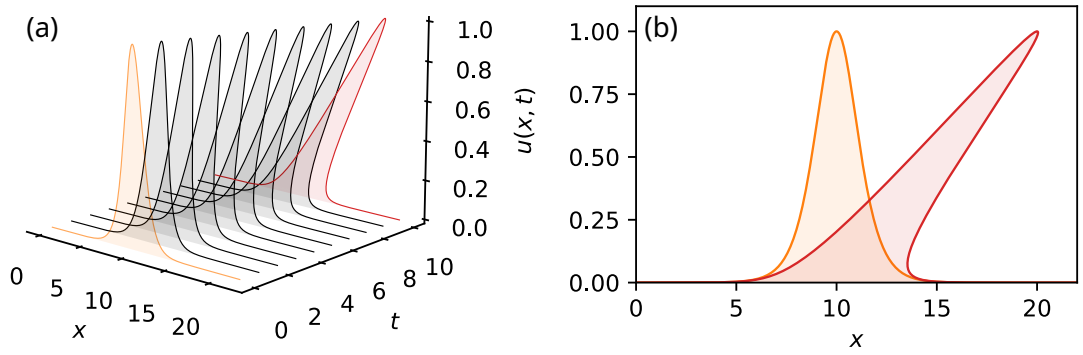

Figure 1.4: (a) Space-time evolution of a KdV soliton governed by the Hopf equation $u_t + uu_x = 0$, obtained via the method of characteristics. (b) Wave profiles at $t = 0$ (orange) and $t = 10$ (red), showing steepening and eventual breaking.

In contrast, Figure 1.5 shows the evolution of the same initial condition under the linear dispersive equation $u_t + u_{xxx} = 0$, which retains only the third-order dispersion. In this case, the wave disperses and develops an asymmetric oscillatory tail. The absence of nonlinear effects results in the complete spreading of the initial pulse.

On the other hand, the single soliton solution of the KdV equation (1.7) reads:

$$u(x,t) = \frac{v}{2}\,\mathrm{sech}^2\left[\frac{\sqrt{v}}{2}(x - vt)\right], \tag{1.9}$$

where $v > 0$ is the soliton velocity. The wave attains its maximum amplitude $u = v/2$ at position $x = vt$.

Figure 1.6 illustrates the evolution of a single soliton, Eq. (1.9), governed by

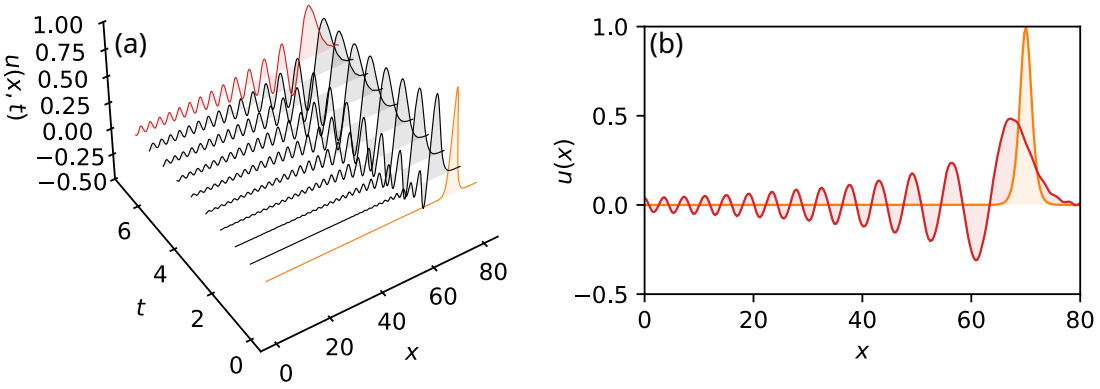

Figure 1.5: (a) Space-time evolution of a KdV soliton under the linear dispersive equation $u_t + u_{xxx} = 0$. (b) Corresponding profiles at $t = 0$ (orange) and $t = 7.5$ (red), showing dispersive spreading and the emergence of an asymmetric Airy tail.

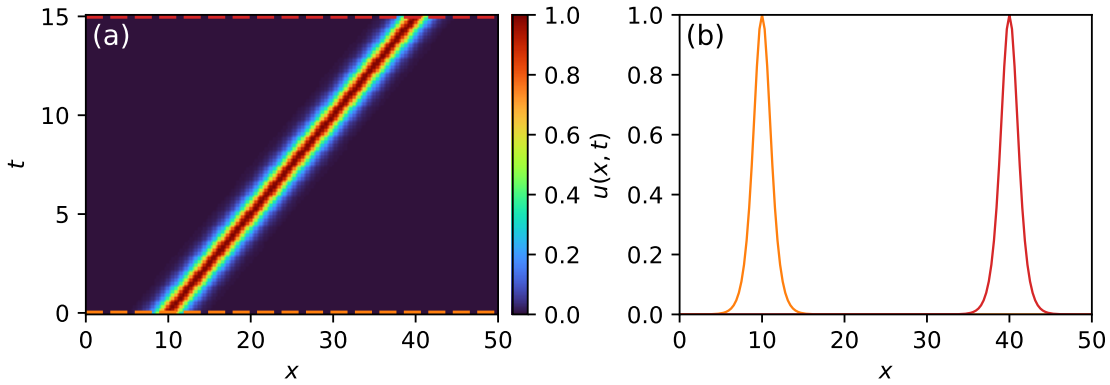

Figure 1.6: Single KdV soliton dynamics. (a) Space-time diagram of the soliton solution (1.9) with $v = 2$, obtained from numerical simulation of Eq. (1.7). (b) Wave profiles at $t = 0$ (orange) and $t = 15$ (red).

the KdV equation (1.7). The soliton maintains its shape and amplitude during propagation (see Fig. 1.6(b)). For an amplitude $v/2 = 1$, the soliton travels a distance $\Delta x = 30$ over a time interval $\Delta t = 15$, consistent with the speed $v = 2$.

A defining property of solitons in integrable systems is their *elastic collision behavior*: after interacting, solitons re-emerge unchanged in shape and velocity, though with a position shift. For two solitons with velocities $v_2 > v_1$, the

interaction-induced shifts in their positions are given by [29]:

$$\Delta x_{1,2} = -\frac{2}{\sqrt{v_1}} \ln \left| \frac{\sqrt{v_1}+\sqrt{v_2}}{\sqrt{v_1}-\sqrt{v_2}} \right|, \quad \Delta x_{2,1} = \frac{2}{\sqrt{v_2}} \ln \left| \frac{\sqrt{v_1}+\sqrt{v_2}}{\sqrt{v_1}-\sqrt{v_2}} \right|. \tag{1.10}$$

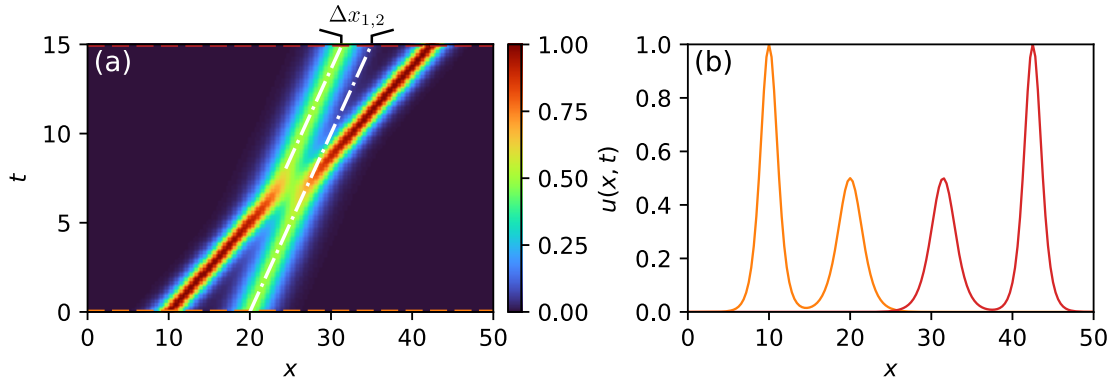

Figure 1.7: Overtaking collision between two KdV solitons. (a) Space-time diagram of two solitons with $v_1 = 1$ and $v_2 = 2$, simulated from Eq. (1.7). (b) Corresponding wave profiles at $t = 0$ (orange) and $t = 15$ (red).

Figure 1.7 displays the overtaking interaction between two KdV solitons with velocities $v_1 = 1$ and $v_2 = 2$. Since the faster soliton (v_2) travels behind the slower one (v_1), it eventually overtakes it. Around $t \sim 7.5$, their interaction causes a temporary deformation: the taller soliton decreases in amplitude, while the smaller one increases, such that both appear nearly equal in height during the collision. After the interaction, both solitons recover their original shapes and velocities. The associated position shift is clearly visible for the slower soliton and is highlighted in Fig. 1.7(a) using dashed-dotted white lines. These shifts are quantitatively described by Eqs. (1.10).

In addition to soliton solutions, the KdV equation also admits periodic traveling wave solutions known as *cnoidal waves*, first derived by Korteweg and de Vries in their original 1895 paper [49]. A normalized cnoidal wave solution takes the form:

$$u(x,t) = z_2 + (z_3 - z_2)\,\mathrm{cn}^2\left(\sqrt{\frac{z_3 - z_1}{2}}(x - vt); m\right), \quad m = \frac{z_3 - z_2}{z_3 - z_1}, \tag{1.11}$$

where $\mathrm{cn}(w;m)$ is the Jacobi elliptic cosine function, and $z_1 < z_2 < z_3$ are real parameters that determine the shape, amplitude, and offset of the wave.

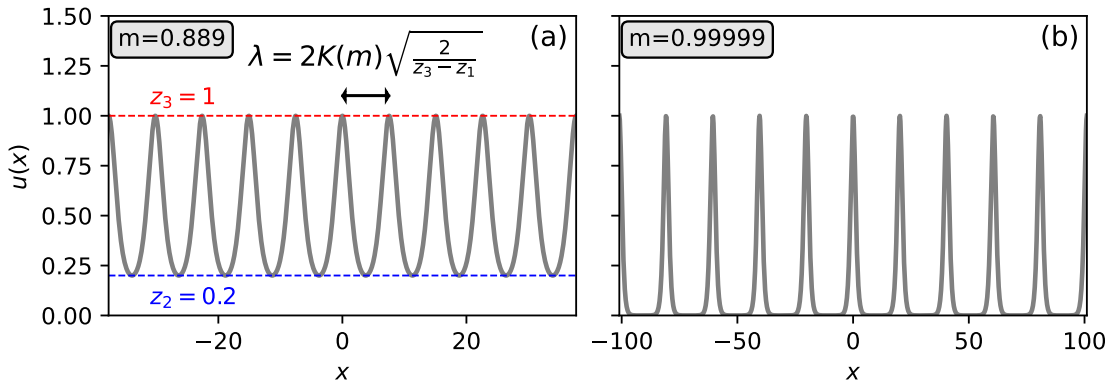

Figure 1.8: Cnoidal wave solutions of the KdV equation. (a) Case with elliptic modulus $m \approx 0.889$, corresponding to parameters $z_1 = 0.1$, $z_2 = 0.2$, and $z_3 = 1$. The wave oscillates between z_2 (blue dashed line) and z_3 (red dashed line), with period $\lambda = 2K(m)\sqrt{2/(z_3 - z_1)}$. (b) In the limit $m \to 1$, with $z_1 = 0$, $z_2 = 10^{-5}$, and $z_3 = 1$, the waveform approaches a train of isolated solitons.

Figure 1.8 illustrates cnoidal wave solutions of the KdV equation. In Fig. 1.8(a), the parameters $z_1 = 0.1$, $z_2 = 0.2$, and $z_3 = 1$ yield a periodic waveform oscillating between z_2 and z_3. The parameter z_2 sets the baseline offset of the wave, while z_3 determines its maximum amplitude. The spatial period λ of the wave depends on all three parameters and is given by

$$\lambda = 2K(m)\sqrt{\frac{2}{z_3 - z_1}},$$

where $K(m)$ is the complete elliptic integral of the first kind.

Fig. 1.8(b) shows a case with $m \approx 1$, corresponding to $z_1 = 0$, $z_2 = 10^{-5}$, and $z_3 = 1$. In this regime, the periodic waveform stretches out, and the cnoidal wave becomes a train of isolated solitons, with $\lambda \to \infty$ as $m \to 1$. In the opposite limit $m \to 0$, the cnoidal wave reduces to a purely sinusoidal wave [87].

1.2.1.2 The Focusing Nonlinear Schrödinger equation

The nonlinear Schrödinger equation (NLSE) is a prototypical integrable equation that arises in a broad range of physical systems, including nonlinear optics, hydrodynamics, and Bose-Einstein condensates. In hydrodynamics, the NLSE models the evolution of unidirectional, small-amplitude gravity waves in deep water, especially in one-dimensional geometries such as 1D water flumes [88–94].

In optics, the focusing NLSE describes the propagation of a quasi-monochromatic wave packet in a single-mode fiber with anomalous dispersion, where higher-frequency components travel faster than lower-frequency ones (*a contrario*, in normal dispersion settings, the group velocity decreases with increasing optical frequency). In this context, the equation governs the evolution of the slowly varying envelope of the electric field [95–101].

The dimensionless focusing NLSE reads:

$$iu_t + u_{xx} + 2|u|^2 u = 0, \tag{1.12}$$

where $u(x,t)$ is the complex envelope of the wave, x is the spatial coordinate, and t denotes time.

As an integrable equation, the NLSE possesses an infinite hierarchy of conserved quantities. The first three are [102]:

$$M = \int_{-\infty}^{\infty} |u|^2 \,\mathrm{d}x, \quad P = \int_{-\infty}^{\infty} u^* u_x \,\mathrm{d}x, \quad E = \int_{-\infty}^{\infty} \left(u^* u_{xx} + |u|^4\right) \mathrm{d}x, \tag{1.13}$$

corresponding respectively to the conservation of mass (or optical power), momentum, and energy.

When considering the normalized focusing NLSE, Eq. (1.12), several particular solutions are of interest. Among them, the fundamental soliton stands out as a stable, localized solution that results from the exact balance between the nonlinear and dispersive terms.

To better understand the nature of this balance, it is instructive to analyze separately the effects of nonlinearity and dispersion as we already did for the KdV equation.

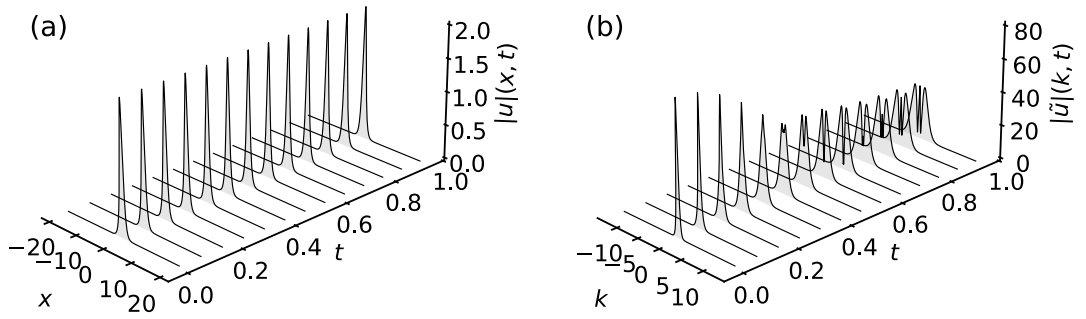

Figure 1.9: (a) Space-time evolution of an initial NLSE soliton under the purely nonlinear equation $u_t + 2|u|^2 u = 0$. (b) Corresponding spectral evolution.

Figure 1.9(a) illustrates the propagation of an initial NLSE soliton when only the nonlinear term is retained, commonly referred to as the Kerr effect in nonlinear optics. In this regime, the wave undergoes a purely local nonlinear phase shift, known as the self-phase modulation (SPM), with a phase given by $\phi_{\mathrm{NL}}(x,t) \propto |u(x,0)|^2 t$. As a result, the temporal envelope remains unchanged, but the spectrum broadens over time due to the generation of new frequency components, as shown in Fig. 1.9(b).

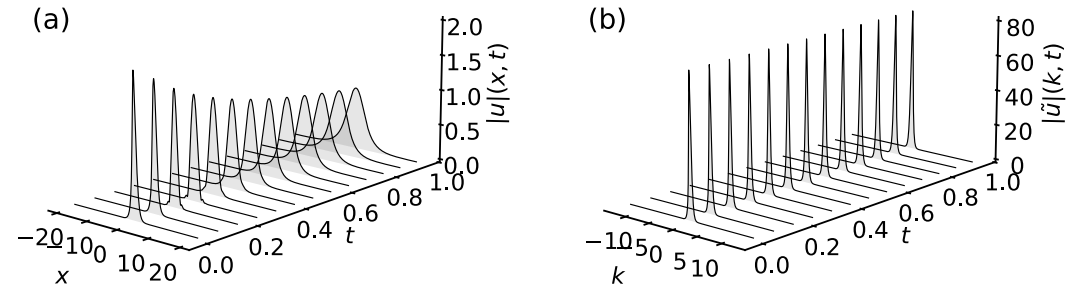

Figure 1.10: (a) Space-time evolution of an initial NLSE soliton under the linear dispersive equation $\partial_t u + \partial_x^2 u = 0$. (b) Corresponding spectral evolution.

Conversely, Figure 1.10(a) shows the evolution under the linear dispersive term alone. This equation implies that only the phases of the spectral components are modified by the dispersion. These changes don't affect the spectrum as shown in Fig. 1.10(b). However they generate a frequency-dependent delay for each spectral component which change the temporal profile of the soliton. In

particular Fig. 1.10(a) shows the soliton broadens with time. The NLSE balances nonlinear and dispersive effects, enabling the formation of stable, localized wave packets known as solitons. The fundamental bright soliton solution is given by [102]:

$$u(x,t) = 2\gamma \,\mathrm{sech}\,[2\gamma(x + 4\alpha t - x_0)] \exp\Big[-2i\alpha x - 4i(\alpha^2 - \gamma^2)t + i\phi_0\Big], \qquad (1.14)$$

where $\gamma > 0$ controls the soliton amplitude and width, α sets the soliton velocity, x_0 is the initial position, and ϕ_0 is the initial phase.

This solution describes a pulse of amplitude 2γ centered at position $x(t) = x_0 - 4\alpha t$, propagating without distortion at velocity -4α. Solitons of this type belong to the class of localized solutions with vanishing boundary conditions at infinity.

However, the NLSE also admits a richer class of exact solutions with non-vanishing boundary conditions. These include so-called *breathers* or *solitons on finite background*, which exhibit localized spatiotemporal structures superimposed on a non-zero continuous wave. Well-known examples include the Peregrine soliton, the Kuznetsov-Ma breather, and the Akhmediev breather, each being a specific case of the general Tajiri-Watanabe breather [102, 103].

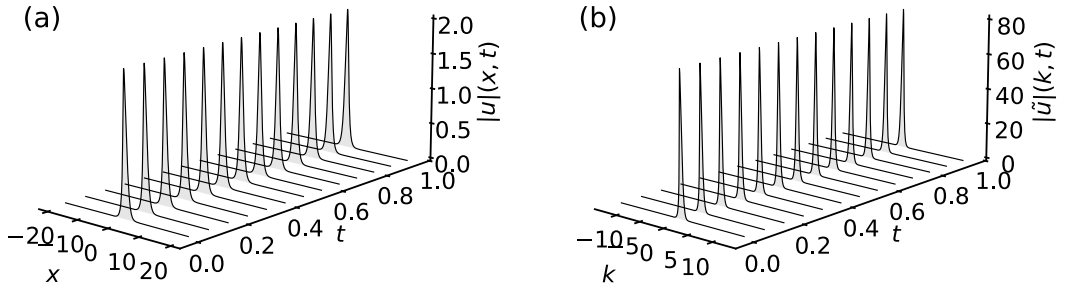

Figure 1.11: (a) Space-time evolution of a NLSE soliton governed by Eq. (1.12), with $\alpha = 0$ and $\gamma = 1$. (b) Corresponding spectral evolution.

Figure 1.11 illustrates the propagation of a bright soliton in a numerical simulation of Eq. (1.12), using parameters $\alpha = 0$ and $\gamma = 1$. As shown in Fig. 1.11(a), the soliton maintains its spatial profile throughout its evolution. Fig. 1.11(b) confirms that its spectral content also remains unchanged.

As in the case of the KdV equation, collisions between solitons in the focusing NLSE are elastic: after interaction, each soliton recovers its original shape and velocity, but undergoes a position shift [25]. For two solitons characterized by complex spectral parameters $\lambda_1 = \alpha_1 + i\gamma_1$ and $\lambda_2 = \alpha_2 + i\gamma_2$, the spatial shift experienced by soliton j due to the interaction with soliton k is given by:

$$\Delta(\lambda_j, \lambda_k) = \frac{\operatorname{sgn}(\operatorname{Re}(\lambda_k - \lambda_j))}{\gamma_j} \ln \left| \frac{\lambda_k - \overline{\lambda}_j}{\lambda_k - \lambda_j} \right|, \quad \text{for } j,k \in \{1,2\}, \quad j \neq k. \tag{1.15}$$

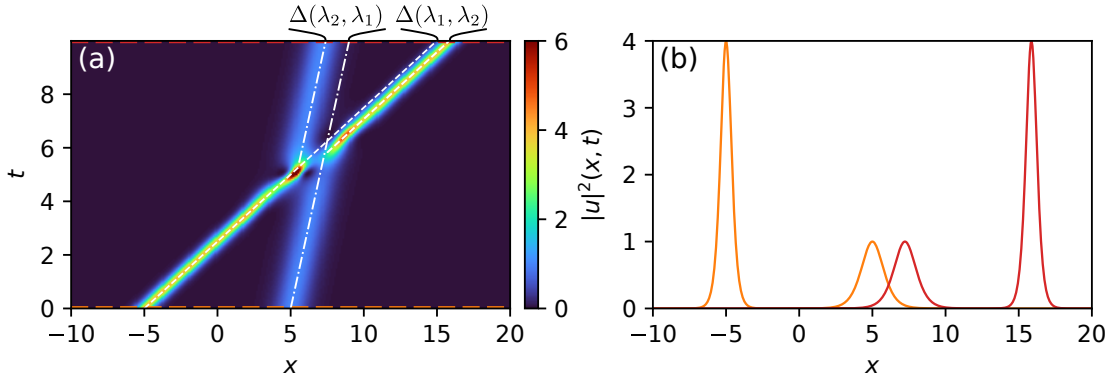

Figure 1.12: Overtaking collision between two NLSE solitons. (a) Space-time diagram of two solitons with $\lambda_1 = 0.5+i$, $\lambda_2 = 0.1+0.5i$, simulated from Eq. (1.12). (b) Corresponding wave profiles at $t = 0$ (orange) and $t \approx 10$ (red).

Figure 1.12(a) displays the space-time dynamics of two interacting NLSE solitons with spectral parameters $\lambda_1 = 0.5 + i$ and $\lambda_2 = 0.1 + 0.5i$. The initial positions were set as $x_{01} = -5$ and $x_{02} = 5$, so that the solitons are well separated at $t = 0$. As shown in Fig. 1.12(b), the taller soliton (with amplitude $2\gamma_1 = 2$ and velocity $-4\alpha_1 = -2$) overtakes the smaller one (velocity $-4\alpha_2 = -0.4$) during the evolution. The white dashed and dash-dotted lines in Fig. 1.12(a) indicate the theoretical position shifts of the solitons due to their interaction, computed from Eq. (1.15).

Another exact solution of the NLSE, and being the simplest, is the plane wave

(or condensate) solution:

$$u(x,t) = u_0 \exp\left(2iu_0^2 t\right), \tag{1.16}$$

where u_0 is a constant complex amplitude. This solution is unstable with respect to long-wavelength perturbations, a phenomenon known as *modulational instability* (MI), or *Benjamin-Feir instability* in hydrodynamics [104].

Modulational instability refers to the exponential growth of small perturbations on top of a plane wave, leading to the formation of localized structures. This mechanism has been experimentally observed in numerous physical systems, including optics [105], electrical transmission lines [106], Bose-Einstein condensates [107], and water waves [12, 104, 108–111].

The early stage of MI, known as the linear stage, can be described by the linear stability analysis of the plane wave background [95, 112]. Considering a weak perturbation of wavenumber k, one finds that it grows exponentially at a rate [113]:

$$g(k) = |k|\sqrt{k_c^2 - k^2}, \tag{1.17}$$

with $k_c = 2u_0$ the cutoff wavenumber. The maximum growth occurs at $k_{\max} = \pm k_c/\sqrt{2}$, and only modes with $|k| < k_c$ are amplified. As the amplitude of the perturbations grows, the dynamics enters a nonlinear regime where coherent structures, such as solitons or breathers, begin to form. This stage is often referred to as the nonlinear or asymptotic stage of MI [114, 115].

Figure 1.13 illustrates a typical scenario of noise-induced modulation instability in the NLSE. Fig. 1.13(a) shows the destabilization of an initially flat condensate due to small random perturbations. As time progresses, the plane wave breaks up into coherent localized structures. Fig. 1.13(b) shows a snapshot of the spatial intensity profile, highlighting the emergence of random modulation. Finally, Fig. 1.13(c) displays the corresponding Fourier spectrum, where two symmetric sidebands grow in accordance with the theoretical gain predicted by Eq. (1.17) shown via the solid green line.

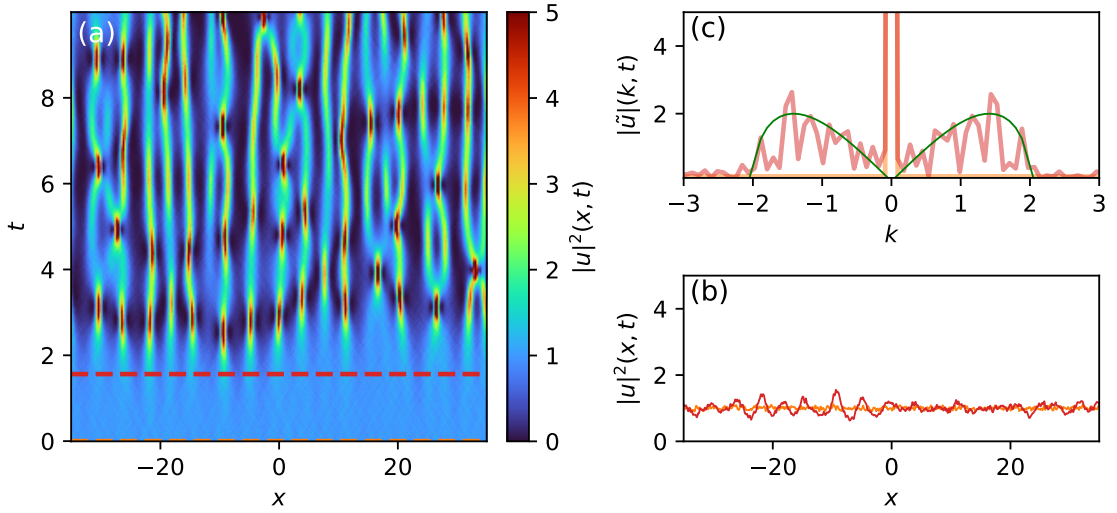

Figure 1.13: Noise-induced modulation instability scenario in the NLSE. (a) Space-time evolution of the wave intensity $|u(x,t)|^2$, starting from a plane wave perturbed by small-amplitude noise. The red dashed line marks $t \approx 1.56$, the time at which the profiles in (b) and (c) are extracted. (b) Spatial intensity profile at $t \approx 1.56$ (red), compared to the initial profile (orange). (c) Corresponding Fourier spectrum $|\tilde{u}(k,t)|$, overlaid with the initial spectrum (orange) and the predicted gain curve from Eq. (1.17) (green).

1.2.2 Inverse Scattering Transform (IST)

The Inverse Scattering Transform (IST) is a powerful analytical technique for solving a broad class of nonlinear partial differential equations that are completely integrable. It was first introduced in 1967 by Gardner, Greene, Kruskal, and Miura [27] to solve the KdV equation. The method was later extended to other integrable systems, notably by Zakharov and Shabat in 1972 [116] for the NLSE. A major conceptual advance came with the introduction of Lax pairs by Peter Lax in 1968 [117], which provided a general framework for identifying and solving integrable equations via the IST [12, 28, 29, 102, 118, 119].

In its standard formulation, the IST recasts the evolution of a nonlinear wavefield[1] as a linear scattering problem. The first step, known as the *direct scattering problem*, consists in associating to the field $u(x,t)$ a linear differential operator, typically a Schrödinger-type operator, whose potential is the field itself. This

[1]We restrict here to fields $u(x,t)$ that vanish at infinity.

yields a spectral problem analogous to wave scattering in quantum mechanics. From the initial condition $u(x,0)$, one computes the *scattering data* $\mathcal{S}(0)$, which generally include a discrete set of eigenvalues λ_j, reflection coefficients, and norming constants.

The key advantage of this approach lies in the fact that the time evolution of the scattering data $\mathcal{S}(t)$ is trivial. Thus, the nonlinear dynamics of the original PDE is effectively mapped to a linear evolution in the spectral domain.

The final step, the *inverse scattering problem*, reconstructs the field $u(x,t)$ at any later time from the evolved scattering data $\mathcal{S}(t)$. While this step is mathematically nontrivial, it can be carried out exactly for integrable systems using methods such as the Gelfand-Levitan-Marchenko equations, Riemann-Hilbert problems, or Darboux transformations [28, 29, 120].

The IST may thus be regarded as a nonlinear analogue of the Fourier transform, where the spectral (Fourier) content of the wavefield is replaced by its scattering data.

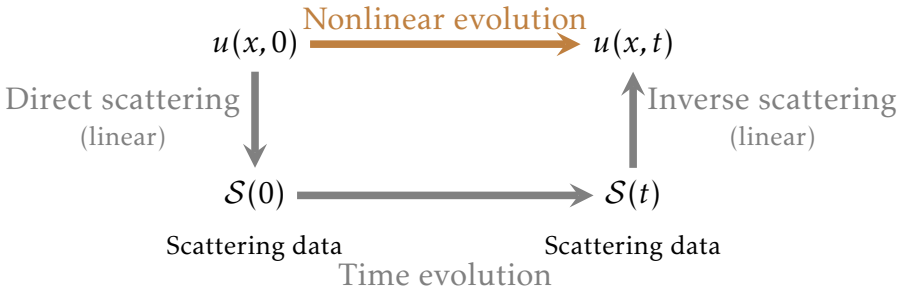

Figure 1.14: Conceptual illustration of the Inverse Scattering Transform (IST). The nonlinear evolution of the field (brown arrow) is replaced by three conceptually simpler, linear steps: direct scattering, time evolution of scattering data, and inverse scattering (gray arrows).

1.2.2.1 Lax Pairs

The IST relies on reformulating the nonlinear evolution of an integrable system as a linear problem in an auxiliary space, where time evolution becomes simple. This reformulation is achieved through the introduction of a *Lax pair*, a concept formalized by Peter Lax in 1968 [117]. The key idea is to associate a nonlinear

partial differential equation with a pair of linear operators, $\hat{L}$ and $\hat{A}$, acting on an auxiliary Hilbert space and depending on the physical field $u(x,t)$.

To motivate this construction, one can draw an analogy with the Heisenberg picture in quantum mechanics, where observables evolve in time while the state vectors remain fixed. In that context, the time evolution of an operator M is governed by the Heisenberg equation $\partial_t M = \frac{i}{\hbar}[H, M]$, involving a commutator with the Hamiltonian H. Similarly, in the Lax representation, the nonlinear evolution equation (for instance KdV or NLS equation),

$$\partial_t u = N(u), \tag{1.18}$$

where $N(u)$ is a nonlinear operator; is encoded in the compatibility condition:

$$\partial_t \hat{L} = [\hat{A}, \hat{L}], \tag{1.19}$$

in which $\hat{L}$ and $\hat{A}$ are linear operators depending on u and its spatial derivatives. Importantly it can be shown that the operateur $\hat{L}$ defines an eigenvalue problem in the form [29, 102, 119]

$$\hat{L}\psi = \lambda\psi, \tag{1.20}$$

where λ is the spectral parameter and ψ the associated eigenfunction. One of the fundamental consequences of the Lax formalism is the preservation of the spectrum of $\hat{L}$ over time, known as *isospectrality* property, if the time evolution of ψ satisfies:

$$\partial_t \psi = \hat{A}\psi. \tag{1.21}$$

This condition guarantees that the eigenvalues λ remain constant in time, which lies at the core of the IST framework.

A classical example is given by the focusing nonlinear Schrödinger equation (NLSE):

$$i\partial_t u + \partial_x^2 u + 2|u|^2 u = 0. \tag{1.22}$$

Zakharov and Shabat [116] showed that this equation admits a Lax representa-

tion with the following operators:

$$\hat{L} = i\begin{pmatrix} \partial_x & -u \\ u^* & -\partial_x \end{pmatrix}, \quad \hat{A} = i\begin{pmatrix} 2\partial_x^2 + |u|^2 & u_x + 2u\partial_x \\ -u_x^* + 2u^*\partial_x & -2\partial_x^2 - |u|^2 \end{pmatrix}. \tag{1.23}$$

This Lax pair satisfies Eq. (1.19) if and only if $u(x,t)$ evolves according to the focusing NLSE, Eq. (1.22).

Another fundamental example is the Korteweg–de Vries (KdV) equation (1.7), which also admits a Lax pair representation with:

$$\hat{L} = -\left(\partial_x^2 + u\right), \quad \hat{A} = -4\partial_x^3 - 6u\partial_x - 3u_x. \tag{1.24}$$

The spatial operator $\hat{L}$ is a Schrödinger operator, where the field $u(x,t)$ plays the role of a potential. In the framework of the IST, finding the soliton content of a given initial condition amounts to solving the spectral problem for the Schrödinger operator with the initial profile $u(x,0)$ as the potential.

1.2.2.2 The direct scattering problem - Scattering datas of the operator $\hat{L}$

In this section, we focus on the first step of the IST method for solving nonlinear partial differential equations: the direct scattering transform. For pedagogical clarity, we only consider here the example of the KdV equation. For a detailed treatment of the NLSE case, we refer the reader to Refs. [28, 50, 102].

Recall that a function $u(x,t)$ is a solution of the KdV equation if and only if there is a pair of linear operators $(\hat{L}, \hat{A})$, known as a Lax pair, satisfying the Lax equation:

$$\partial_t \hat{L} = [\hat{A}, \hat{L}].$$

For the KdV equation, the spatial Lax operator is given by $\hat{L} = -(\partial_x^2 + u)$, and the scattering data are defined from the spectral properties of the operator $\hat{L}$, that is, its eigenvalues and eigenfunctions. The direct scattering step therefore consists of solving the eigenvalue problem:

$$\left(\partial_x^2 + u(x, t=0)\right)\psi(x) = -\lambda\psi(x). \tag{1.25}$$

This is formally identical to the one-dimensional linear Schrödinger equation in quantum mechanics, where the function $u_0(x) = u(x, t = 0)$ acts as a localized potential. In the asymptotic regions where $|x| \to \infty$, the potential $u(x)$ vanishes. In these regions the eigenfunctions $\psi(x)$ behave like:

$$\psi(x) \propto e^{kx}, \quad \text{with } k = \sqrt{-\lambda}.$$

Thus, depending on the sign of the spectral parameter λ, the asymptotic behavior of the eigenfunctions $\psi(x)$ takes two qualitatively different forms:

$$\begin{aligned} &\psi(x) \propto e^{\pm\sqrt{|\lambda|}x}, \quad \text{if } \lambda < 0 \quad \text{(bound states)}, \\ &\psi(x) \propto e^{\pm i\sqrt{\lambda}x}, \quad \text{if } \lambda > 0 \quad \text{(radiative or scattering states)}. \end{aligned} \tag{1.26}$$

These two families define the discrete and continuous spectrum of the operator $\hat{L}$, respectively.

Discrete spectrum. The discrete spectrum consists of a finite number of negative eigenvalues $\lambda_j = -\eta_j^2 < 0$, each associated with a square-integrable eigenfunction $\psi_j(x)$ that decays exponentially as $|x| \to \infty$. These localized states correspond to solitons in the nonlinear evolution. The corresponding eigenfunctions typically exhibit the form at $|x| \to \infty$:

$$\psi_j(x, t) \sim c_j(t)\, e^{-\eta_j |x|},$$

where the complex constant $c_j(t)$ is known as the *norming constant*. Together, the pair (η_j, c_j) encodes the amplitude, velocity and position of the associated soliton [29].

Continuous spectrum. For $\lambda > 0$, the eigenfunctions oscillate at infinity and describe the radiative (dispersive), component of the wavefield. These are analogous to plane waves in quantum mechanics and constitute the continuous spectrum of $\hat{L}$. In this regime, one can define reflection and transmission coefficients that characterize how an incoming wave is scattered by the potential $u(x)$.

A right-going incident wave of the form $e^{i\sqrt{\lambda}x}$ is scattered according to:

$$\psi(x,\lambda) \sim \begin{cases} e^{i\sqrt{\lambda}x} + r(\lambda)\, e^{-i\sqrt{\lambda}x}, & \text{as } x \to -\infty, \\ t(\lambda)\, e^{i\sqrt{\lambda}x}, & \text{as } x \to +\infty, \end{cases}$$

where $r(\lambda)$ and $t(\lambda)$ are the reflection and transmission coefficients, respectively.

In practice, the discrete IST spectrum corresponds to the eigenvalues obtained from the direct scattering transform. Computing this spectrum numerically for a given initial field amounts to solving the eigenvalue problem associated with the corresponding Lax operator. For generic localized potentials, numerical techniques are required.

In the case of the KdV equation, the spectral problem is given by the Schrödinger equation, Eq. (1.25). This is numerically solved using a pseudospectral method, where the second-order spatial derivative is approximated via Fourier-based spectral differentiation [102].

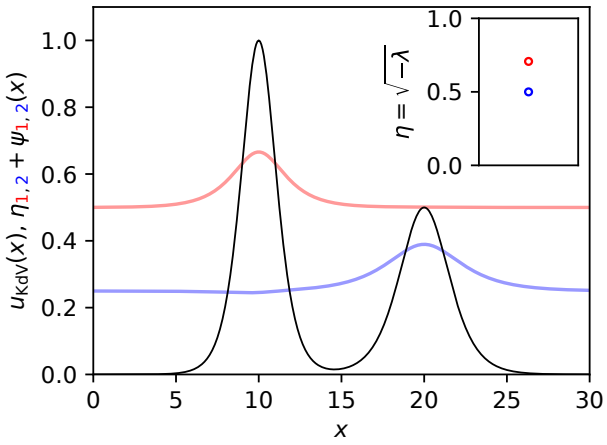

Figure 1.15: Initial field $u_{\mathrm{KdV}}(x)$ composed of two KdV solitons (Eq. (1.9)) of different amplitudes and the associated eigenfunctions $\psi_{1,2}$ obtained by solving Eq. (1.25). Inset: corresponding discrete IST spectrum obtained by solving Eq. (1.25), shown as points on the vertical axis $\eta = \sqrt{-\lambda}$.

Figure 1.15 shows a field composed of two KdV solitons (see also Fig. 1.7) with velocities $v_2 = 1$ and $v_1 = 2$, corresponding to spectral parameters $\eta_2 = \sqrt{v_2}/2 = 0.5$ and $\eta_1 = \sqrt{v_1}/2 \approx 0.7$. The inset displays the associated discrete

eigenvalues on the η-axis. The eigenfunctions $\psi_1(x)$ and $\psi_2(x)$, solutions of the associated Schrödinger problem, are also plotted in red and blue respectively, illustrating their spatial localization around each soliton.

For the NLSE, the direct scattering problem is defined by the Zakharov-Shabat system:

$$\begin{pmatrix} -\partial_x & u \\ u^* & \partial_x \end{pmatrix} \psi = i\lambda\psi, \tag{1.27}$$

which involves a first-order matrix differential operator. To solve this system numerically, we adopt the Fourier collocation method described in Ref. [102]. This method projects the Zakharov-Shabat problem onto a Fourier basis, converting the spectral problem into a finite-dimensional matrix eigenvalue problem that can be solved numerically.

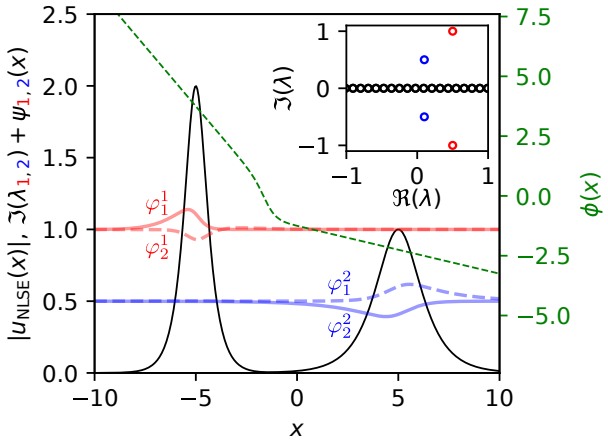

Figure 1.16: Initial field $u_{\mathrm{NLSE}}(x)$ composed of two NLSE solitons (Eq. (1.14)) of different amplitudes and velocities and the associated eigenfunctions $\psi_{1,2}$. The amplitude $|u(x)|$ is shown in black, while the phase $\phi(x)$ is indicated by the green dashed line (right axis). In red lines are indicated the numerical results of calculated eigenfunctions φ_1^1 (solid line) and φ_2^1 (dashed line) when $\lambda = \lambda_1$. In blue lines are indicated the numerical results of calculated eigenfunctions φ_1^2 (solid line) and φ_2^2 (dashed line) when $\lambda = \lambda_2$. Inset: IST spectrum in the complex λ-plane, where discrete eigenvalues (solitons) appear as isolated points in the half-planes, while the continuous spectrum lies along the real axis.

Figure 1.16 presents the field $u(x)$ composed of two NLSE solitons (as in Fig. 1.12). The black curve shows the amplitude $|u(x)|$, while the green dashed

line represents the phase $\phi(x)$. The numerically computed eigenfunctions associated with the Zakharov–Shabat spectral problem are also plotted: $\psi_1 = (\varphi_1^1, \varphi_2^1)$ is shown in red, and $\psi_2 = (\varphi_1^2, \varphi_2^2)$ in blue. The solitons have spectral parameters $\lambda_1 = 0.5 + i$, $\lambda_2 = 0.1 + 0.5i$, and their locations in the complex plane are shown in the inset. Due to the symmetries of the Zakharov-Shabat operator, the IST spectrum is symmetric with respect to the real axis [121]. In the following, we will focus on the upper half of the complex plane ($\mathrm{Im}\,\lambda > 0$), which suffices to characterize the solitons.

1.3 The Concept of Soliton Gas

Solitons are nonlinear coherent structures that preserve their shape after collisions, a behavior reminiscent of elastic particle-like interactions. Motivated by this property, Zakharov introduced in 1971 a statistical description of large ensembles of interacting solitons, now known as the *soliton gas* [30]. In his original formulation, developed in the framework of the integrable KdV equation, solitons with randomly distributed amplitudes and positions interact weakly and remain well separated, a regime referred to as a *rarefied* soliton gas.

Over the past two decades, this theory has been extended to describe *dense* soliton gases, where solitons strongly overlap and undergo continuous nonlinear interactions. In such regimes, individual solitons can no longer be distinctly identified as isolated sech-shaped pulses, but the ensemble as a whole can still be described statistically through kinetic approaches [32, 121, 122].

Despite its early theoretical formulation, the soliton gas concept remained largely a model of interest to mathematical physicists until very recently. The first experimental indications of soliton gas behavior were reported in 2014 by Costa *et al.* [123], who interpreted irregular shallow-water wave packets as KdV soliton gases using nonlinear spectral analysis. This was followed by a more controlled realization by Redor *et al.* [34], who generated a bidirectional soliton gas in a 34-meter wave flume via the fission of a sinusoidal wave.

More recently, a unidirectional soliton gas was both synthesized and fully characterized in the deep-water regime governed by the focusing 1D-NLSE, using a direct implementation of the inverse scattering transform [35]. This

work represents a rare experimental realization that is fully aligned with the original theoretical definition of soliton gases, as it relies entirely on the IST formalism to generate randomized nonlinear spectra and to synthesized the resulting wavefields.

In parallel, soliton gases have emerged as effective models for describing fundamental nonlinear wave phenomena, including spontaneous (noise-induced) modulation instability [122].

In this section, we present the procedure used to synthesize soliton gases both experimentally and numerically.

1.3.1 Nonlinear Spectral Synthesis of Soliton Gases Using the Darboux Method

The IST provides a framework for analyzing and synthesizing exact solutions of integrable equations such as the KdV and 1D-NLSE. In particular, it establishes a correspondence between nonlinear wavefields and the spectral data of a linear operator (Schrödinger for KdV, Zakharov–Shabat for NLSE). In this framework, soliton solutions correspond to discrete eigenvalues of the associated operator, while continuous spectrum components describe dispersive radiation.

Until now, we have illustrated examples involving one or two solitons ($N = 1$ or $N = 2$), associated with a small number of discrete eigenvalues. We now turn to the construction of multi-soliton solutions with a large number $N \gg 1$ of solitons. These solutions are characterized by a purely discrete IST spectrum.

Several analytical and numerical approaches exist to construct such solutions. These include the Gel'fand–Levitan–Marchenko integral equation approach [28], the Crum transformation [124], and the Darboux transformation [125], which is particularly well-suited for numerical synthesis of multi-soliton solutions with prescribed spectral data.

In this section, we outline the mathematical formulation of the Darboux transformation applied to the KdV equation, and describe its practical implementation for the numerical generation of multi-soliton fields with a large number of solitons. Similar approaches can be formulated for the NLSE; we refer the reader to Refs. [35, 122, 126] for detailed applications of the Darboux

method in the focusing NLSE context.

The Darboux transformation provides a recursive scheme to generate higher-order soliton solutions, starting from the trivial (zero) background. In the case of the KdV equation, the fundamental one-soliton solution serves as the seed solution. The method iteratively adds new discrete eigenvalues η_k, each corresponding to a soliton with amplitude $2\eta_k^2$, to build up an n-soliton solution with N large. The algorithm we use follows the method introduced by Liao and Huang [127] and further developed in Refs. [128, 129]. We only provide here the algorithmic recipe to generate the N-soliton solution in a practical way.

We begin by generating a set of N discrete eigenvalues η_k ($k = 1,\dots,N$), sorted in ascending order. Each eigenvalue determines the amplitude of an individual soliton in the final field. Alongside these, we define a corresponding set of initial position parameters x_{0k}, which are sampled randomly according to a prescribed spatial distribution. The choice of distributions for both η_k and x_{0k} depends on the desired properties of the resulting soliton gas.

We then define the auxiliary function

$$\Theta_k(x,t) = \eta_k\left(x - x_{0k} - 4\eta_k^2 t\right), \tag{1.28}$$

computed for all the values of k ($k = 1,...,N$) on a spatial domain $x \in [-L/2, L/2]$ within a numerical box of size L, for a fixed time t.

The recursive Darboux construction proceeds as follows [127]:

- For each $k = 1,\dots,N$, we define the intermediate function $q_1(x,t,\eta_k)$ by:

$$\begin{aligned} q_1(x,t,\eta_k) &= \eta_k \tanh(\Theta_k(x,t)) && \text{if } k \text{ is odd,} \\ q_1(x,t,\eta_k) &= \eta_k \left[\tanh(\Theta_k(x,t))\right]^{-1} && \text{if } k \text{ is even.} \end{aligned} \tag{1.29}$$

- For $k = 2,\dots,N$, we compute recursively:

$$q_k(x,t,\eta_k) = \frac{\eta_k^2 - \eta_{k-1}^2}{q_{k-1}(x,t,\eta_k) - q_{k-1}(x,t,\eta_{k-1})} - q_{k-1}(x,t,\eta_{k-1}). \tag{1.30}$$

- The field $u_k(x,t)$ is then constructed iteratively as:

$$u_k(x,t) = -u_{k-1}(x,t) - 2\eta_k^2 + 2q_k(x,t,\eta_k)^2, \tag{1.31}$$

with the initial condition given by the one-soliton solution:

$$u_1(x,t) = -2\eta_1^2 \operatorname{sech}^2(\Theta_1(x,t)). \tag{1.32}$$

After the final iteration, the N-soliton solution of the KdV equation corresponding to the chosen set of spectral parameters $\{\eta_k\}$ is obtained as

$$u(x,t) = -u_N(x,t).$$

We present in the following two representative realizations of KdV soliton gases synthesized via the Darboux transformation method described above.

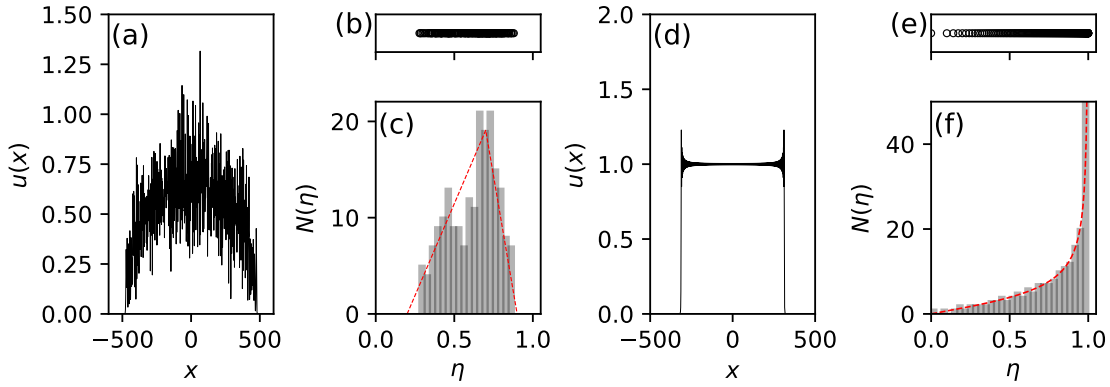

Figure 1.17: Realizations of KdV soliton gases generated using the Darboux transform algorithm. (a) Example of a KdV soliton gas wavefield constructed from 200 discrete eigenvalues distributed according to a triangular distribution shown with red dashed lines in (c). (b) The set of spectral parameters η_k, $k = 1,\ldots,200$, used in (a). (c) Histogram of the discrete eigenvalues corresponding to a single realization; the red dashed line shows the target triangular distribution. Averaging over many realizations would lead to convergence toward the theoretical shape. (d–f) Same as (a–c), but for a Weyl spectral distribution $\eta/\pi\sqrt{1-\eta^2}$.

Figure 1.17 illustrates two examples of KdV soliton gases with peculiar spectral distributions. In Fig. 1.17(a), a wavefield is synthesized using a tri-

angular distribution of eigenvalues $\eta \in [0.2, 0.9]$ centered at $\eta = 0.7$, as shown in Figs. 1.17(b)(c). The corresponding soliton positions x_{0k} are randomly distributed according to a uniform law over the interval $[-500, 500]$. Due to the high density, individual solitons are no longer isolated sech^2-shaped pulses. Instead, the wavefield appears as complex and fluctuating, which is a typical signature of a dense soliton gas where strong spectral overlap and nonlinear interactions dominate. In contrast, Fig. 1.17(d) shows a realization corresponding to a *soliton condensate*, a concept introduced in Refs. [121, 128] to describe the densest possible soliton gas for a given spectral support, where all soliton centers are fixed at $x_{0k} = 0$. This state is achieved by sampling the eigenvalues η_i from the Weyl distribution [128]:

$$\eta_i = \sqrt{1 - \left(1 - \frac{i}{N}\right)^2}, \quad i = 1, \ldots, N, \tag{1.33}$$

with $N = 200$, as shown in Figs. 1.17(e)(f). This expression corresponds to the placement of eigenvalues such that the integral of the Weyl probability density $\Phi(\eta)$ matches uniform increments of i/N [128],

$$\int_0^{\eta_i} \Phi(\mu)\, \mathrm{d}\mu = \frac{i}{N}, \quad i = 1, \ldots, N. \tag{1.34}$$

with $\Phi(\eta) = f(\eta)/\int_0^1 f(\eta)\mathrm{d}\eta$ and $f(\eta) = \eta/\pi\sqrt{1-\eta^2}$. In this case, all solitons are positioned at the same location $x = 0$, leading to their nonlinear superposition into a nearly uniform wavefield of amplitude one. Small oscillations are visible near the boundaries due to the finite number of solitons in the numerical synthesis; their amplitude vanishes as $N \to \infty$ [128]. A detailed discussion on soliton condensates will be provided in Chapter 3.

1.4 Kinetic and Hydrodynamic Theories of Soliton Gases

This section reviews two complementary theoretical frameworks used to describe the large-scale dynamics of soliton gases. In Sec. 1.4.1, we present the spectral kinetic theory of soliton gases, which models the macroscopic evolution of the density of states of the soliton gas based on elementary soliton collisions. In Sec. 1.4.2, we briefly present the Generalized Hydrodynamics (GHD) framework, which builds upon the kinetic description by incorporating elements of thermodynamic characterization.

1.4.1 Spectral Kinetic Theory of Soliton Gases

The goal of the spectral kinetic theory is to provide a macroscopic description of soliton gas (SG) dynamics. This approach was first introduced by Zakharov in his 1971 paper [30], where he proposed a kinetic equation for a rarefied KdV soliton gas, i.e., one in which solitons are sufficiently separated so that their overlap is small. The theory was later extended by Gennady El to account for soliton gases of arbitrary densities [31], including dense SGs where solitons strongly overlap and continuously interact.

Here, we adopt a phenomenological approach to establish the kinetic equation, relying on the cumulative effect of pairwise soliton collisions. This method accounts for the phase (position) shifts generated by elastic two-soliton interactions, and allows for the construction of a kinetic equation valid for unidirectional soliton gases of arbitrary densities. A more rigorous formulation based on the thermodynamic limit of modulated finite-gap solutions is presented in Ref. [130]. While we focus here on the KdV equation, the reader is referred to Refs. [32, 121, 130] for the extension to the nonlinear Schrödinger equation (NLSE).

The KdV soliton gas is described statistically by the density of states (DOS) $f(\eta; x, t)$, defined such that $f(\eta_0; x_0, t_0)\,\mathrm{d}\eta\,\mathrm{d}x$ gives the number of solitons with spectral parameter in $[\eta_0, \eta_0 + \mathrm{d}\eta]$ and spatial position in $[x_0, x_0 + \mathrm{d}x]$ at time $t = t_0$. Here $\eta \in [0, 1]$ denotes the spectral parameter of KdV solitons (related to

amplitude $[2\eta^2]$ and velocity $[4\eta^2]$).

The rarefied regime initially considered by Zakharov can be formally characterised in terms of the spatial density of the soliton gas given by,

$$\beta(x,t) = \int_0^1 f(\eta; x, t)\, \mathrm{d}\eta. \tag{1.35}$$

in the limit $\beta \ll 1$.

The macroscopic dynamics of the soliton gas arises from the elementary pairwise soliton interactions, which are elastic: the spectral parameters η remain unchanged (due to isospectrality), the solitons retain their individual amplitudes and velocities asymptotically. However, each interaction generates a position shift, which can be written in terms of the spectral parameters of each solitons as:

$$\Delta_{ij} = \Delta(\eta_i, \eta_j) = \frac{\sigma_{ij}}{\eta_i} \ln \left| \frac{\eta_i + \eta_j}{\eta_i - \eta_j} \right|, \quad \sigma_{ij} = \mathrm{sgn}(\eta_i - \eta_j). \tag{1.36}$$

The total phase shift experienced by a soliton with spectral parameter η_i after colliding with M other solitons is the sum of the individual shifts resulting from each binary interaction ($\Delta_i = \sum_{j \neq i}^{M} \Delta_{ij}$) [25]. This additivity forms the basis for the derivation of the kinetic equation governing the evolution of the DOS.

In his seminal 1971 work [30], Zakharov considered the cumulative effect of pairwise interactions on a tracer soliton with spectral parameter η propagating within a soliton gas. Over a time interval $\mathrm{d}t$, the total spatial shift experienced by this tracer soliton, due to collisions with solitons of the SG of spectral parameter $\mu \in [0, 1]$, is given by

$$\left(\int_0^1 \Delta(\eta, \mu) \overbrace{[4\eta^2 - 4\mu^2] f(\mu)\, \mathrm{d}\mu}^{\text{Collision rate}} \right) \mathrm{d}t, \tag{1.37}$$

where $\Delta(\eta, \mu)$ denotes the phase shift resulting from a single two-soliton interaction, and $f(\mu)$ is the spectral density of the gas. The term $4\eta^2 - 4\mu^2$ represents the relative velocity between the tracer and solitons of the gas, thus determining the rate of collision.

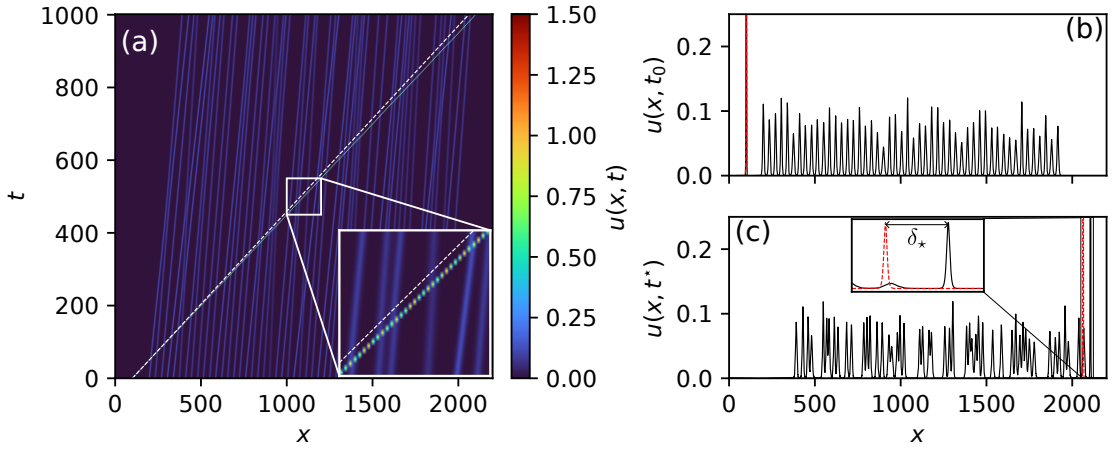

Figure 1.18: Numerical simulation of the interaction between a KdV tracer soliton and a dilute SG. (a) Space-time diagram of the field $u(x,t)$, where a fast soliton with spectral parameter $\eta = 0.7$ travels through a random ensemble of slower solitons drawn from a Gaussian distribution centered at $\eta_0 = 0.2$. The white dashed line shows the expected trajectory of the tracer soliton in the absence of interactions. The inset magnifies the region of collisions, which result in a spatial shift of the soliton path. (b) Initial condition $u(x,t_0)$, consisting of the tracer soliton (red) superimposed on a dilute gas of solitons (black). (c) Snapshot of the field $u(x,t^\star)$ at late time $t^\star \simeq 1000$. The inset zooms in on the tracer soliton, which has emerged from the gas with a visible forward displacement $\delta_\star \sim 42.7$, due to cumulative phase shifts from soliton collisions.

As a consequence, the effective velocity $s(\eta)$ of the tracer soliton inside the gas, accounting for cumulative phase shifts, is modified from its free velocity $4\eta^2$ to (see Fig. 1.18):

$$s(\eta) \approx 4\eta^2 + \frac{1}{\eta}\int_0^1 \ln\left|\frac{\eta+\mu}{\eta-\mu}\right| f(\mu)[4\eta^2 - 4\mu^2]\,\mathrm{d}\mu, \tag{1.38}$$

where we have used the expression of the KdV two-soliton shift

$$\Delta(\eta,\mu) = \frac{1}{\eta}\ln\left|\frac{\eta+\mu}{\eta-\mu}\right|.$$

This integral in Eq. (1.38) term thus represents a mean-field correction to the soliton velocity due to interactions with the rest of the gas. A detailed discussion,

with numerical examples can be found in Ref. [131]. The generalization of Zakharov's kinetic theory to dense soliton gases was developed by Gennady El in Ref. [31], based on the finite-gap spectral theory and the thermodynamic limit of multiphase Whitham modulation equations [132]. In contrast to the dilute case, where soliton interactions are weak, dense soliton gases involve strong and continuous nonlinear interactions that require a more refined description. It was shown that, for a dense KdV soliton gas in a homogeneous (equilibrium) state, the transport velocity $s(\eta)$ of solitons satisfies the following linear integral equation:

$$s(\eta) = 4\eta^2 + \frac{1}{\eta}\int_0^1 \ln\left|\frac{\eta+\mu}{\eta-\mu}\right| f(\mu)\,[s(\eta)-s(\mu)]\,\mathrm{d}\mu, \tag{1.39}$$

which can be interpreted as an equation of state for the soliton gas, linking the transport velocity $s(\eta)$ to the spectral density $f(\eta)$. It is notable (and non-trivial) that this equation of state involves only two-body interactions between solitons. Moreover, in the dilute gas limit, where the total spatial density $\beta \ll 1$, the influence of soliton interactions becomes weak. In this regime, the transport velocity $s(\eta)$ is only slightly perturbed from its non-interacting value $4\eta^2$. Therefore, a consistent approximation is obtained by replacing $s(\eta) \approx 4\eta^2$ and $s(\mu) \approx 4\mu^2$ inside the integral of Eq. (1.39), leading to the simplified expression Eq. (1.38).

In the case of a weakly non-uniform SG, the density of states becomes a function of space and time, $f(\eta) \to f(\eta; x, t)$, and the corresponding transport velocity becomes $s(\eta) \to s(\eta; x, t)$. These quantities evolve on large hydrodynamic scales, much larger than the characteristic width or separation of individual solitons.

The isospectrality property of the integrable KdV dynamics ensures that the spectral parameters η are conserved along the flow. This leads to the continuity equation for the DOS:

$$\partial_t f(\eta; x, t) + \partial_x [s(\eta; x, t) f(\eta; x, t)] = 0, \tag{1.40}$$

Together, Eqs. (1.39) and (1.40) form the basis of the kinetic theory of soliton gases.

A more rigorous derivation for the kinetic theory of soliton gases can be

obtained by considering the thermodynamic limit of the so-called finite-gap solutions of the KdV equation. These solutions, derived from the IST under periodic boundary conditions, are characterized by quasi-periodic nonlinear wavefields whose Lax spectrum consists of a finite number of spectral bands separated by gaps [31, 121, 133].

The thermodynamic soliton gas limit can be understood as a special limiting case of the finite-gap solutions of integrable equations. A finite-gap solution of genus N is associated with a Lax spectrum composed of N finite spectral bands plus a semi-infinite band (which has zero amplitude, ensuring that the corresponding nonlinear wave has no continuous background). The corresponding nonlinear wave is quasiperiodic and described in terms of hyperelliptic functions.

A key observation is that each finite spectral band corresponds to a nonlinear mode: when the width of such a band tends to zero, the corresponding mode becomes a soliton. For instance, the well-known cnoidal wave solution (genus 1) is associated with a two-band spectrum; as the size of the inner finite band shrinks to zero, the wavelength of the cnoidal wave diverges and the solution converges to an isolated soliton, see Sec. 1.2.1.1.

The soliton gas limit corresponds to a situation where the number of spectral bands $N \to \infty$, while their individual widths tend to zero in such a way that each mode becomes soliton-like. To avoid diverging total energy or mass in this limit, the shrinking of the bands must follow an exponential scaling. This ensures that the spectral density of solitons, defined as the number of solitons per unit space and per unit spectral parameter η, remains finite. The resulting object is a gas (due to the limit $N \to \infty$) of solitons (because of the band collapse), and its Lax spectrum becomes dense along a subset of the complex plane. This dense spectrum can then be described statistically by a smooth density of states $f(\eta)$, which characterizes the spectral distribution of the solitons [130].

The technical construction of this limit involves intricate tools from algebro-geometric methods and is beyond the scope of this thesis. The key point, however, is that it provides a mathematically rigorous framework for defining soliton gases as thermodynamic limits of solutions of integrable PDEs.

The kinetic equations of the soliton gas theory involve nonlinear relations

referred to as nonlinear dispersion relations (NDRs), which link the spectral density $f(\eta)$, the spectral flux $v(\eta) = s(\eta)f(\eta)$, and a smooth, positive spectral scaling function $\sigma(\eta)$ which measures how much in interaction is the gas.

Physically, $\sigma(\eta)$ encodes the degree of collectivity in the soliton gas: small values of $\sigma(\eta)$ correspond to strongly interacting, condensate-like states ($\sigma(\eta) \to 0$; see Sec. 3.4.3.6), while large values (e.g., $\sigma(\eta) \to \infty$) represent a non-interacting gas. The coupled integral equations defining the NDRs are [121, 130]:

$$\int_0^1 \ln\left|\frac{\eta+\mu}{\eta-\mu}\right| f(\mu)\,\mathrm{d}\mu + \sigma(\eta)f(\eta) = \eta, \tag{1.41}$$

$$\int_0^1 \ln\left|\frac{\eta+\mu}{\eta-\mu}\right| v(\mu)\,\mathrm{d}\mu + \sigma(\eta)v(\eta) = 4\eta^3, \tag{1.42}$$

These relations, first derived in [31], provide an alternative derivation of the kinetic equation of state (1.39). By eliminating $\sigma(\eta)$ between Eqs. (1.41) and (1.42), one recovers the integral equation linking the soliton effective velocity $s(\eta)$ and the spectral density $f(\eta)$.

From an experimental point of view, these theoretical predictions have recently become testable. In Chapter 1, we present a hydrodynamic experiment involving the collision of two soliton gases. This configuration enables a direct comparison with predictions derived from the kinetic theory of SG [38]. Furthermore, the refraction of soliton by a SG experiment provides one of the first quantitative verifications of the kinetic equations [36].

1.4.2 Generalized HydroDynamics (GHD)

Statistical physics has proven remarkably effective in describing the relaxation of many-body systems toward thermodynamic equilibrium. In this framework, equilibrium states are described by the Gibbs or (grand) canonical ensemble, which depends on a small number of conserved quantities such as energy and particle number. Hydrodynamics complements this picture by providing a macroscopic description of large, spatially inhomogeneous systems, under the assumption of local thermodynamic equilibrium.

However, integrable systems, those possessing an infinite hierarchy of con-

served quantities, exhibit fundamentally different relaxation dynamics. Due to the presence of these additional conservation laws, integrable systems generally do not thermalize in the conventional sense. A paradigmatic illustration of this phenomenon is provided by the famous FPUT experiment. Instead, they relax toward a more elaborate stationary state known as the Generalized Gibbs Ensemble (GGE) [134, 135]. This ensemble extends standard thermodynamics by introducing one Lagrange multiplier β_i for each conserved charge Q_i. In classical statistical mechanics, the concept of temperature arises from a constraint on energy; in the integrable case, the GGE enforces an infinite set of such constraints.

The Generalized Hydrodynamics (GHD) formalism was introduced to describe the large-scale dynamics of locally equilibrated integrable systems governed by a GGE. Initially developed for quantum one-dimensional Bose gases [136–140], GHD accounts for the ballistic transport of conserved quantities and captures the interplay between the full set of conservation laws and macroscopic evolution [134]. While it was first formulated in the context of quantum systems such as the Lieb-Liniger model, GHD has since been successfully applied to classical integrable systems, including soliton gases [56, 141, 142]. One of its key strengths lies in its adaptability to weak integrability-breaking effects, such as external forces or dissipation [143–146].

A paradigmatic example of the classical GHD framework is provided by the work of Bonnemain, Doyon, and El [142], who formulated a hydrodynamic theory for KdV soliton gases. Building on earlier developments in kinetic theory, they derived macroscopic equations governing the evolution of the DOS $f(\eta)$, where η is the spectral parameter associated with the IST. Notably, the hydrodynamic equations obtained within the GHD framework coincide with the kinetic description derived via the thermodynamic limit of finite-gap solutions, establishing a precise correspondence between the Euler-scale GHD equation and the kinetic continuity equation for $f(\eta; x, t)$, as well as between the NDRs and the classical analog of the thermodynamic Bethe ansatz (TBA) [147, 148].

Crucially, GHD goes beyond a purely kinematic description by endowing soliton gases with a full thermodynamic structure. The authors construct an entropy functional (analogous to the Yang-Yang entropy in quantum integrable

systems [148]), a free energy density, and explicit expressions for correlation functions of the nonlinear KdV field $u(x,t)$. These quantities are derived by considering solitons as classical particles undergoing elastic pairwise interactions, neglecting their extended wave nature. They depend on both the spectral distribution $f(\eta)$ and the spectral kernel $\sigma(\eta)$. Interestingly, the soliton condensate corresponds to the configuration that minimizes this entropy functional.

The GHD framework thus offers a comprehensive and flexible description of the non-equilibrium thermodynamics of soliton gases. To date, a comparable classical GHD theory for the NLSE has not yet been developed, although quantum approaches based on the semiclassical limit of the Lieb-Liniger model provide some results [135, 149, 150]. Developing a classical GHD formalism for the NLSE remains an open and important challenge in the field.

While GHD is not used directly in the present thesis, it provides a powerful theoretical avenue to capture physical effects that lie beyond the scope of kinetic theory, such as the impact of weak integrability-breaking mechanisms. In this sense, GHD constitutes a promising direction for future theoretical developments aiming to describe experimentally observed phenomena that cannot be accounted for within strictly integrable models.

Chapter 2

Interaction between monochromatic soliton gases : a testbed for the spectral kinetic theory in hydrodynamic experiments

The truth belongs to those who seek it, not to those who claim to own it.

– Marquis of Condorcet

2.1 Introduction

As discussed in Chapter 1, bright solitons are highly singular wave structures: they are coherent and localized waveforms that maintain their shape during propagation. This stability results from a balance between dispersion, which tends to spread the wave packet, and nonlinearity, which acts to focus it. A particularly remarkable property of solitons is their ability to interact through purely elastic collisions: after interacting, each soliton re-emerges unchanged in shape and velocity, up to a phase and position shift. This elastic collision process, which involves no energy exchange between solitons, has been extensively studied experimentally in a variety of physical systems, see Refs. [25, 26, 151–157].

Because of their particle-like stability and their interaction properties, solitons can be considered as *quasi-particles*. This quasi-particle behavior naturally motivates a statistical description when dealing with large ensembles of solitons with random properties. This yields the concept of *soliton gas* (SG), introduced in Chapter 1. At the heart of this concept lies the notion of *density of states* (DOS), the probability distribution of spectral parameters of solitons. Although theoretically formulated as early as the 1970s, the experimental realization of a soliton gas and the direct measurement of its DOS were only achieved recently [34, 35].

As with classical gases, a kinetic theory for soliton gases has been developed, allowing one to describe their macroscopic behavior using two coupled equations: a continuity equation derived from the isospectrality condition, and an equation of state predicting the velocity of a trial soliton within the gas [32, 121]. An important step toward the experimental validation of this kinetic theory was recently achieved in optical fiber systems, where the *refraction* of a soliton by a dense soliton gas was demonstrated [36]. In that experiment, the velocity change experienced by a tracer soliton passing through an optical SG was found to be in good quantitative agreement with the kinetic theory's predictions. These predictions have also been verified in numerous numerical simulations, see Refs. [128, 131, 158–160].

In this chapter, we report new experiments aimed at further testing the spectral kinetic theory of soliton gases. Rather than considering the interaction

between a single tracer soliton and a soliton gas, as in Ref. [36], we investigate the interaction between two soliton gas *jets* (or *beams*) in hydrodynamics, using deep-water surface gravity waves. By a soliton gas jet, we mean a soliton gas with a narrow distribution of discrete IST eigenvalues, concentrated around a particular point in the complex spectral plane. Such jets are sometimes referred to as *monochromatic* soliton gases, with the DOS modeled by a Dirac delta function [32, 33, 130]. From a mathematical perspective, introducing a DOS as a linear superposition of several Dirac deltas, the so-called *polychromatic ansatz*, leads to a significant simplification of the kinetic equations, allowing for analytical solutions describing SG interactions [130, 160].

The chapter is organized as follows. First we present the theoretical background from kinetic theory of SGs, which is necessary to describe the interaction between SG jets in the framework of the focusing 1D NLSE. We illustrate the theoretical results with numerical simulations of the reduced kinetic equation describing the evolution in space and time of the densities of the two SG components. We also show how the IST method can be used to realize the implementation of two interacting SG jets in direct numerical simulations of the 1D NLSE. The second section presents our experiments. Finally, in the third section we report our experimental results and compare them with the predictions of the kinetic theory as well as with direct numerical simulations of both the integrable NLSE and a non-integrable model incorporating higher-order effects.

2.1.1 Kinetic theory for two monochromatic soliton gases

We investigate nonlinear wave systems governed by the integrable one-dimensional focusing NLSE:

$$i\psi_t + \psi_{xx} + 2|\psi|^2\psi = 0. \tag{2.1}$$

Its fundamental soliton solution, parameterized by $\lambda = \alpha + i\gamma$ with $\alpha \in \mathbb{R}$ and $\gamma \in \mathbb{R}^+$, is given by:

$$\psi(x,t) = 2\gamma\,\mathrm{sech}\,(2\gamma(x + 4\alpha t - x_0))\exp\Big[-2i\alpha x - 4i(\alpha^2 - \gamma^2)t - i\phi_0\Big], \tag{2.2}$$

where x_0 and ϕ_0 denote the initial position and phase, respectively. The real part of the eigenvalue λ determines the soliton velocity -4α in the (x,t) plane, while the imaginary part encodes its amplitude 2γ. We consider a wave field composed of a large number of solitons, each characterized by a spectral parameter $\sim \lambda_j$, forming a soliton gas. In the spectral kinetic theory of SGs associated with the 1D NLSE, the density of states $f(\lambda;x,t)$ describes the distribution of spectral eigenvalues. The quantity $f(\lambda;x,t)\mathrm{d}\alpha\,\mathrm{d}\gamma\,\mathrm{d}x$ gives the number of solitons at time t with spatial coordinates in $[x, x+\mathrm{d}x]$ and spectral parameters λ within the spectral region $[\alpha,\alpha+\mathrm{d}\alpha]\times[\gamma,\gamma+\mathrm{d}\gamma]$. The evolution of the SG is thus determined by the evolution of the DOS $f(\lambda;x,t)$. As discussed in Chapter 1, Zakharov [30] developed a kinetic description for the DOS evolution in the case of a dilute SG in the KdV framework. This approach was later extended by Gennady El [31] in 2003 to describe dense SGs.

Due to the isospectral property inherent to the integrable nature of Eq. (2.1), the space-time evolution of the DOS is governed by a continuity equation [32, 121]:

$$\frac{\partial f}{\partial t} + \frac{\partial (sf)}{\partial x} = 0, \tag{2.3}$$

where $s = s(\lambda;x,t)$ denotes the transport velocity of a tracer soliton in the gas.The corresponding equation of state for the effective velocity s reads [32, 121]:

$$s(\lambda;x,t) = -4\mathfrak{Re}(\lambda) + \frac{1}{\mathfrak{Im}(\lambda)} \iint_{\Lambda^+} \ln\left|\frac{\mu-\lambda^*}{\mu-\lambda}\right| [s(\lambda;x,t) - s(\mu;x,t)]\, f(\mu;x,t)\,\mathrm{d}\xi\,\mathrm{d}\zeta, \tag{2.4}$$

where $\mu = \xi + i\zeta$, and Λ^+ denotes a compact 2D domain or a 1D curve in the upper complex half-plane corresponding to the support of the SG's spectral eigenvalues. This equation expresses the effective velocity of a soliton characterized by the spectral parameter λ, which differs from its bare velocity $-4\mathfrak{Re}(\lambda)$ due to the cumulative position shifts acquired through collisions with all other solitons of parameters μ within the gas. Each elementary shift is given by Eq. (1.15), which describes the spatial displacement resulting from a two-soliton interaction in the NLSE framework. Equations (2.3) and (2.4) constitute the kinetic system for a 1D focusing NLSE soliton gas (see Refs. [32, 121]). These equations are the natural counterparts, for the focusing NLSE, of the kinetic equations (1.40) and (1.39)

introduced in Chapter 1 for the KdV soliton gas. This system admits a significant simplification when the SG is modeled as a finite number of monochromatic components, each represented by a Dirac delta distribution in the spectral density.

Polychromatic soliton gases represent SGs for which the DOS is expressed as a linear combination of Dirac delta functions centered at distinct spectral points λ_j. In the specific case of two monochromatic SGs, the DOS is given by:

$$f(\mu, x, t) = \rho_1(x,t)\delta(\mu - \lambda_1) + \rho_2(x,t)\delta(\mu - \lambda_2), \tag{2.5}$$

where $\lambda_1 = -\alpha + i\gamma$ and $\lambda_2 = \alpha + i\gamma$. With this delta distribution for the DOS, all solitons within a given SG species exhibit nearly identical amplitudes and velocities. As shown in Refs. [32, 121], substituting this ansatz into the kinetic equations leads to a simplified set of coupled equations for the densities ρ_1 and ρ_2, which we present and discuss below.

The interaction between the monochromatic SGs is quantified by the parameter κ, defined as:

$$\kappa = \frac{1}{\gamma}\ln\left|\frac{\lambda_1 - \lambda_2^*}{\lambda_1 - \lambda_2}\right| = \frac{1}{2\gamma}\ln\left|\frac{\lambda_1 - \lambda_2^*}{\lambda_1 - \lambda_2}\right|^2 = \frac{1}{2\gamma}\ln\left(1 + \frac{\gamma^2}{\alpha^2}\right). \tag{2.6}$$

The parameter κ also represents the spatial shift experienced during the collision of two individual solitons with spectral parameters λ_1 and λ_2 (see Ref. [116]).

Substituting the ansatz given by Eq. (2.5) into the state equation (2.4) yields the simplified expressions:

$$\begin{aligned} s_1 = s(\lambda_1) &= 4\alpha + \frac{1}{\gamma}\iint \ln\left|\frac{\mu - \lambda_1^*}{\mu - \lambda_1}\right| [\rho_1\delta(\mu - \lambda_1) + \rho_2\delta(\mu - \lambda_2)]\,(s(\lambda_1) - s(\mu))\,\mathrm{d}\mu, \\ s_2 = s(\lambda_2) &= -4\alpha + \frac{1}{\gamma}\iint \ln\left|\frac{\mu - \lambda_2^*}{\mu - \lambda_2}\right| [\rho_1\delta(\mu - \lambda_1) + \rho_2\delta(\mu - \lambda_2)]\,(s(\lambda_2) - s(\mu))\,\mathrm{d}\mu. \end{aligned} \tag{2.7}$$

The integrals in Eq. (2.7) can be significantly simplified due to the presence of the Dirac delta function, which yields,

$$s_1 = 4\alpha + \kappa\rho_2(s_1 - s_2), \quad s_2 = -4\alpha + \kappa\rho_1(s_2 - s_1), \tag{2.8}$$

and the evolution of the densities, governed by the continuity equation (2.3), becomes:

$$\frac{\partial \rho_1}{\partial t} + \frac{\partial (s_1 \rho_1)}{\partial x} = 0, \quad \frac{\partial \rho_2}{\partial t} + \frac{\partial (s_2 \rho_2)}{\partial x} = 0. \tag{2.9}$$

The soliton velocities can be explicitly expressed in terms of the densities. Rearranging Eqs. (2.8) gives:

$$s_1(1 - \kappa\rho_2) = 4\alpha - \kappa\rho_2 s_2, \quad s_2(1 - \kappa\rho_1) = -4\alpha - \kappa\rho_1 s_1. \tag{2.10}$$

Thus,

$$s_1 = 4\alpha \left(\frac{1 - \kappa(\rho_1 - \rho_2)}{1 - \kappa(\rho_1 + \rho_2)} \right), \quad s_2 = -4\alpha \left(\frac{1 + \kappa(\rho_1 - \rho_2)}{1 - \kappa(\rho_1 + \rho_2)} \right). \tag{2.11}$$

Solving the coupled system of Eqs. (2.9) and (2.11) provides the evolution of the densities ρ_1 and ρ_2 in terms of the velocities s_1 and s_2.

2.1.1.1 Behavior of homogeneous gases

To illustrate the theoretical framework introduced in the previous section, we now consider a simple configuration involving the collision between two homogeneous monochromatic soliton gases with uniform densities ρ_{10} and ρ_{20}, initially separated in space, as illustrated in Fig. 2.1(a). The initial condition used to solve the system of equations (Eqs. (2.9), (2.11)) for this scenario is:

$$\begin{aligned} &\rho_1(x) = \rho_{10}, \quad \rho_2(x) = 0 \quad \text{for} \quad x < 0, \\ &\rho_1(x) = 0, \quad \rho_2(x) = \rho_{20} \quad \text{for} \quad x > 0. \end{aligned} \tag{2.12}$$

This configuration corresponds to a step-like discontinuity in the spatial distribution of the two SG species, as illustrated in Fig. 2.1(a), where the central densities ρ_{1c} and ρ_{2c} are lower than their respective initial values ρ_{10} and ρ_{20}.

The solution of the system, schematically shown in Fig. 2.1(b), consists of three regions separated by two discontinuities [32, 161]. Recalling from Eq. (2.5) that $f = \rho_1 + \rho_2$, with $\rho_j(x,t)$ the local density associated with the component of

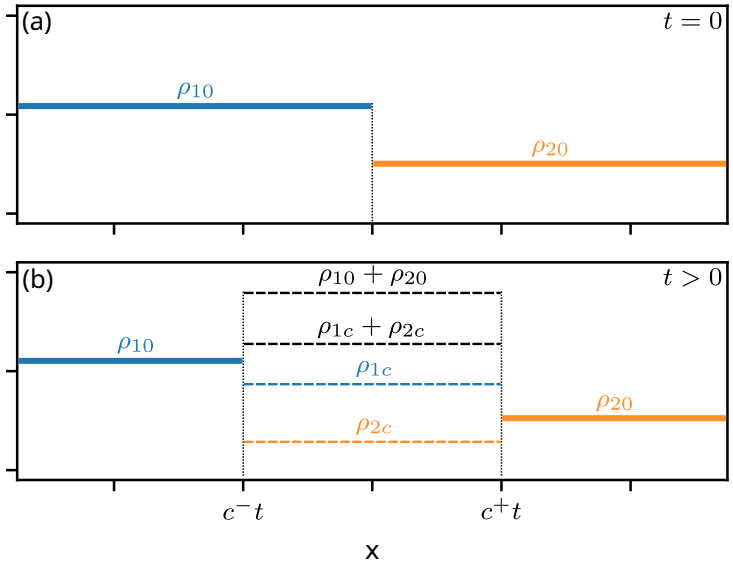

Figure 2.1: Coordinate dependence of the soliton gas densities at the initial time (a), and at a time $t > 0$, during the interaction (b), assuming constant initial velocities and densities.

spectral parameter λ_j, one has:

$$\rho_1(x,t),\ \rho_2(x,t) = \begin{cases} \rho_{10},\ 0, & x < c^- t, \\ \rho_{1c},\ \rho_{2c}, & c^- t \le x < c^+ t, \\ 0,\ \rho_{20}, & x \ge c^+ t, \end{cases} \tag{2.13}$$

The velocities and densities in the interaction region ($c^- t < x < c^+ t$), are given analytically by [32]:

$$c^+ = s_{1c} = \frac{4\alpha\,(1-\kappa(\rho_{1c}-\rho_{2c}))}{1-\kappa(\rho_{1c}+\rho_{2c})}, \quad c^- = s_{2c} = \frac{-4\alpha\,(1+\kappa(\rho_{1c}-\rho_{2c}))}{1-\kappa(\rho_{1c}+\rho_{2c})}, \tag{2.14}$$

and

$$\rho_{1c} = \frac{\rho_{10}(1-\kappa\rho_{20})}{1-\kappa^2\rho_{10}\rho_{20}}, \quad \rho_{2c} = \frac{\rho_{20}(1-\kappa\rho_{10})}{1-\kappa^2\rho_{10}\rho_{20}}. \tag{2.15}$$

These expressions highlight the mutual dilution of the SG components in the interaction region, as shown in Fig. 2.1(b).

Figure 2.2 shows the evolution of the densities and velocities of the SGs in

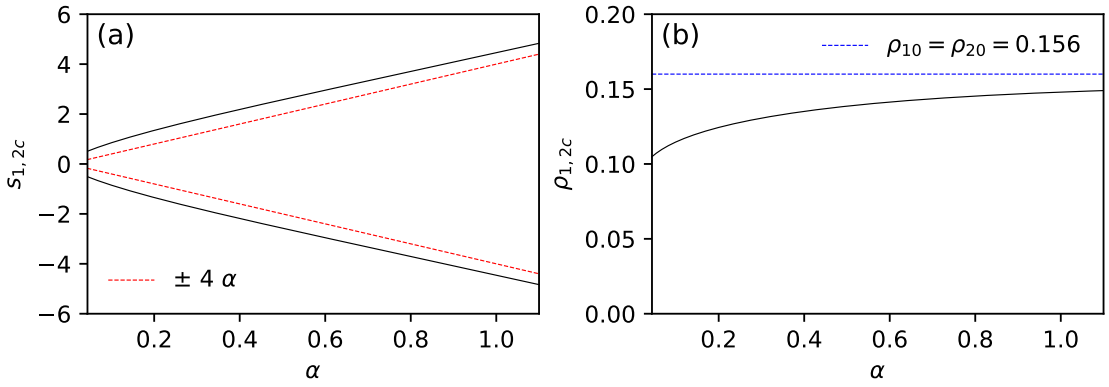

Figure 2.2: (a) Analytical prediction of the velocities s_{1c} and s_{2c} as a function of the spectral parameter $\mathfrak{Re}(\lambda) = \alpha$, as given by Eq. (2.14). The red dashed line shows the free velocities $\pm 4\alpha$ of the two SG species. (b) Analytical prediction for the densities ρ_{1c} and ρ_{2c} from Eq. (2.15). The initial densities are set to 0.156 (blue dashed line), and $\mathfrak{Im}(\lambda) = \gamma = 1$.

the interaction region as a function of the parameter α, which sets the real part of the spectral parameters $\lambda_1 = -\alpha + i\gamma$ and $\lambda_2 = \alpha + i\gamma$. The imaginary part γ is fixed to unity, so that solitons in both SGs have identical amplitudes. In this configuration, the only remaining parameter that influences the interaction strength is the relative velocity between the two gases, determined by α. This can be understood from the expression of the interaction shift κ, Eq. (2.6), which depends on α with γ fixed.

To build physical intuition, consider the simple case of a collision between two solitons with the same amplitude and opposite velocities. When their relative velocity is small, the solitons interact over a longer time, leading to a larger phase shift, i.e., a stronger effective interaction. This is consistent with the fact that for small α, the interaction shift κ becomes larger.

The initial densities are set to $\rho_{10} = \rho_{20} = 0.156$, indicated by the blue dashed line in Fig. 2.2(b). For small α (typically $\alpha < 0.7$), the interaction between the gases is strong, leading to significant changes in density in the interaction region. Conversely, for α approaching 1, the relative velocity is larger, the interaction becomes weaker, and the densities in the interaction region remain close to their initial values. In Fig. 2.2(a), the red dashed line shows the free velocities of the soliton species in the absence of interaction, given by the slopes $\pm 4\alpha$.

One of the objectives of our experimental study is to compare the theoretical predictions shown in Fig. 2.2 with the measurements discussed in Sec. 2.3.

2.1.1.2 Numerical Simulation of the Kinetic Equations

To better illustrate analytical results in Sec. 2.1.1.1, we now integrate the simplified kinetic equations given in Eqs. (2.9),(2.8). The spectral parameters of the SGs are $\lambda_j = \pm 0.5 + i$, with $j = 1, 2$. The initial density distributions are defined as two large boxes of extent $\Delta x = 80$, each with uniform density $\rho_{j0} = 0.4$, as illustrated in Fig. 2.3(a). Figure 2.3 presents numerical simulations of the kinetic equations, illustrating the theoretical results presented in Fig. 2.1. Figures 2.3(d) and (e) show the space-time evolutions of the densities $\rho_{1,2}(x,t)$ of the two SGs. The SGs are initially separated and begin to interact around $t > 5$, crossing each other. As a result of the interaction, the densities of both components decrease from their initial values $\rho_{10} = \rho_{20} = 0.4$ to approximately $\rho_{1c} = \rho_{2c} \sim 0.302$. This can be seen from the colorscale that shifts from yellow to green in Figs. 2.3(d) and (e), and from the blue and orange profiles in Fig. 2.3(c).

The numerical values of the densities computed in the interaction region are in excellent agreement with the theoretical predictions, as shown in Fig. 2.3(c), where the green dotted line represents the densities $\rho_{1c} = \rho_{2c}$ computed using the analytical expressions given by Eq. (2.15). In addition to the density variations induced by the interaction, Figs. 2.3(d) and (e) reveal that the collision also leads to velocity changes in the interaction region for both SG species. These velocity changes observed in the numerical simulations are in excellent agreement with the theoretical predictions. The white dashed lines, which are parallel to the boundaries of the interacting region and correspond to velocities $s_{1c} \sim 3.898$ and $s_{2c} \sim -3.898$, are precisely those predicted by Eq. (2.14).

Finally, Fig. 2.3(f) highlights a key feature of the interaction: although the density of each soliton gas species decreases individually, their combined density $\rho_{1c} + \rho_{2c}$ within the interaction region remains higher than the individual densities observed outside this region. At the same time, the overall effect of the interaction is a net dilution when compared to the initial, non-interacting two-component gas, $(\rho_{1c} + \rho_{2c} < \rho_{10} + \rho_{20})$ as schematically illustrated

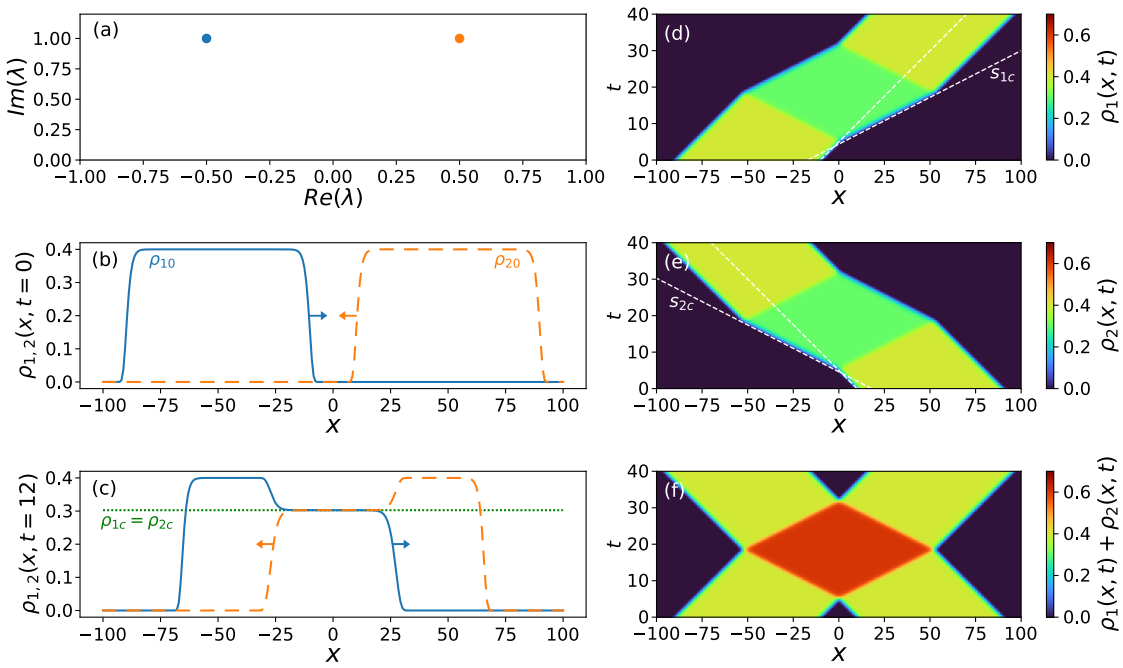

Figure 2.3: Numerical simulation of the kinetic equations, Eqs. (2.9),(2.8), showing the interaction between two SGs. (a) Spectral (IST) parameters of the two interacting SGs, with the DOS being defined by Eq. (2.5) with $\lambda_j = \pm 0.5 + i$, for j=1,2. (b) Initial spatial distribution of the densities $\rho_j(x, t = 0)$. (c) Numerically computed distribution of the densities at t = 12. The green dashed line represents the densities in the interaction region computed using Eq. (2.15) with $\rho_{j0} = 0.4$. (d) Space-time evolution of the density $\rho_1(x, t)$. The interaction region where the density has decreased from $\rho_{10} = 0.4$ to $\rho_{1c} \sim 0.302$ is represented in green. (e) Same as (d) but for the second species $\rho_2(x, t)$. (f) Space-time evolution of the sum of the densities showing that the total density has increased in the interaction region despite the individual densities having decreased.

in Fig. 2.1(b) [32].

We now investigate how these theoretical and numerical results from the kinetic theory of SGs are translated in a numerical simulation of the NLSE.

2.1.1.3 NLSE numerical simulation of the collision of two monochromatic soliton gases

We now examine the interaction of two monochromatic SGs in a numerical simulation of the NLSE. As mentioned in Chapter 1, NLSE has a special class of solutions characterized by a purely discrete spectrum consisting of N complex-

valued eigenvalues λ_n ($n = 1,\ldots,N$) and N associated complex parameters $C_n = |C_n|e^{i\phi_n}$, called norming constants, defined for each λ_n. These discrete eigenvalues determine the amplitudes and velocities of the individual solitons, while the norming constants encode their phases and positions in the physical domain, see Ref. [119].

To generate a multi-soliton wave field, we construct an N-soliton solution (NSS) of Eq. (2.1) using a recursive Darboux transformation scheme implemented in high-precision arithmetic. This approach is required due to the large number of solitons involved, and follows the methodology introduced in Refs. [103, 126]. The constructed NSS consists of two SG species. Each SG is characterized by 50 discrete eigenvalues that are randomly and uniformly distributed within a small square region in the complex plane. These regions are centered around $\lambda_1 = -0.5 + i$ and $\lambda_2 = 0.5 + i$, respectively, as shown in Fig. 2.4(b).

The Darboux transformation construct NSSs by recursively adding discrete eigenvalues to a seed solution of the focusing 1D NLSE. One key property of this method is that the closer the eigenvalues are in the complex plane, the further apart the corresponding solitons appear in physical space. For our SG, the mean distance in physical space between neighboring solitons of each species is therefore determined by the size of the square regions in which the corresponding eigenvalues are distributed, see Fig. 2.4(b).

In addition to the eigenvalue distribution, the mean distance between solitons is also influenced by the norming constants $C_n = |C_n|e^{i\phi_n}$. In the following, we maximize the density of each SG by setting the moduli $|C_n|$ of the norming constants to unity and by distributing their phases ϕ_n uniformly in the interval $[0, 2\pi]$. The SG in Fig. 2.4 cannot be denser than it is, in the sense that any further increase in density would require a different choice of the spectral parameters and of the norming constants. Conversely the SG could be diluted by randomly distributing the moduli of the norming constants over an interval with a nonzero extent.

The synthesized wave field at $t = 0$ consists of two spatially separated SGs with no overlap between the species as shown in Fig. 2.4(a). Each SG contains 50 solitons with nearly identical amplitudes, while remaining individually discernible. The inherent randomness of each gas is evident in physical space due

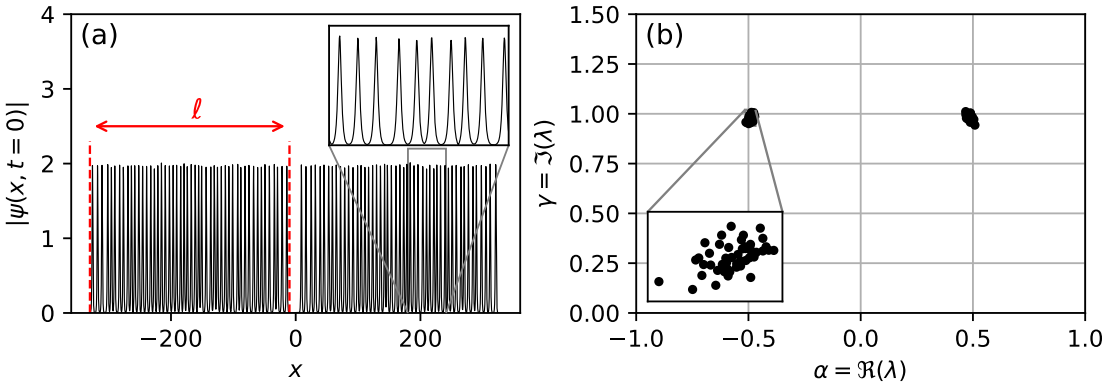

Figure 2.4: (a) Initial condition constructed via the Darboux recursive scheme (see Ref. [122]), consisting of two monochromatic SGs. (b) In the IST complex plane, the spectrum of the two SGs consists of two narrow clusters of points centered around $\lambda = \pm 0.5 + i$. The discrete eigenvalues are specified and the N-soliton solution is computed from these discrete eigenvalues and their associated norming constants.

to the randomly varying distance between adjacent solitons, see the inset in Fig. 2.4(a).

The field depicted in Fig. 2.4(a) serves as the initial condition for the numerical simulation of the NLSE. A standard NLSE solver, based on a pseudospectral method, has been used to compute the time evolution of the wave field, as shown in Fig. 2.5(a). At the initial time, each SG species forms a uniform SG, with density ρ_0 representing the number n of solitons within the interval of length ℓ, $\rho_0 = n/\ell$, as depicted in Fig. 2.4(a). In Figs. 2.5(a) and (c), the initial densities ρ_{10} and ρ_{20} of each of the two non-interacting species are $n/\ell \sim 50/320 \sim 0.156$, which is the maximum possible for the chosen spectral parameters, see Fig. 2.4(b). The field at $t = 50$ presented in Fig. 2.5(b), reveals the interaction dynamics between the two SGs. In the center of the interaction region, at time $t \sim 75$, each of the two species, still containing $n = 50$ solitons, now occupies a broader spatial domain with an extent increased from $\ell \sim 320$ to $\ell' \sim 362$, see the dashed arrows in Fig. 2.5(a). This results in a decrease of the densities, which fall from $\rho_{10} = \rho_{20} \sim 0.156$ to $\rho_{1c} = \rho_{2c} = n/\ell' = 50/362 \sim 0.138$, in good quantitative agreement with the expressions in Eq. (2.15) obtained within the framework of the kinetic theory of SGs.

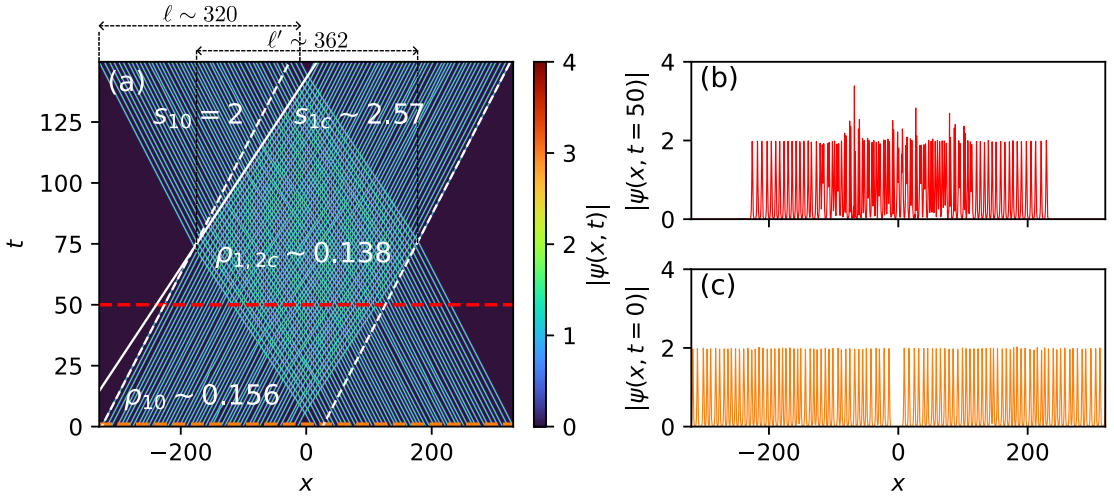

Figure 2.5: NLSE numerical simulation with an initial condition consisting of two monochromatic SGs, each represented as a train of nearly identical solitons. (a) Space-time diagram of the wave field. The white dashed lines indicate the initial velocity $s_{10} = 2$, while the solid white line shows the effective velocity $s_{1c} = 2.57$ in the interaction region. (b) Wave field at $t = 50$, showing non-interacting flanking regions and a central interaction zone. (c) Initial condition of the wave field. The IST spectrum corresponding to these two SGs is shown in Fig. 2.4(b)

In addition to these density changes, Fig. 2.5(a) also reveals that the interaction between the two SG species affects their relative velocities. Fig. 2.5(a) illustrates that the mean velocity of the first species increases from $4\alpha \sim 2$ (indicated by the white dashed lines) to effective value $s_{1c} \sim 2.57$ within the interaction region, as shown by the solid white line. Once again these results are in good quantitative agreement with the results from the kinetic theory given by Eq. (2.14).

To sum up

This section investigates the interaction between two monochromatic soliton gases (SGs) governed by the one-dimensional focusing nonlinear Schrödinger equation (NLSE). Building on the spectral kinetic theory developed in Refs. [32], we consider a theoretical scenario where two initially separated SGs with uniform densities collide. The kinetic equations, which describe the evolution of soliton densities and velocities, admit analytical solutions for this configuration, predicting a mutual dilution of the two SG species and a modification of their effective velocities in the interaction region. To test and illustrate these predictions, we perform direct numerical simulations of the NLSE, using two SGs generated using the Darboux transform as initial condition. These simulations confirm the main theoretical outcomes and provide additional insight into the dynamics of interacting SGs, offering a more intuitive and accessible interpretation of the kinetic theory results.

2.2 Hydrodynamic Experiments

In this section, we address the experimental study of the interaction between two monochromatic soliton gases, relying on hydrodynamic experiments.

2.2.1 Experimental Apparatus Presentation

The experiments were conducted in a large-scale wave basin (140 m long × 5 m wide × 3 m deep) at the Hydrodynamics, Energetics and Atmospheric Environment Laboratory (LHEEA) at *École Centrale de Nantes* (France). The facility consists of a long towing tank typically used for ship resistance tests and hydrodynamic experiments involving a motorized carriage. In the present study, the carriage was not used in order to focus exclusively on unidirectional wave propagation.

Waves were generated by a computer-controlled flap-type wavemaker located at one end of the tank, see Fig. 2.6(b). This system allows the generation of regular and irregular wave trains with carrier wave periods in the range of 0.5 to 5 s. In our experiments, we work with a carrier frequency close to 1 Hz.

At the opposite end of the tank, wave reflections are minimized using a passive absorbing system consisting of a parabolic shaped absorbing beach that is approximately 8 m long, combined with W-shaped floating foam absorbers, see also Ref. [162]. This setup ensures low reflection coefficients, less than 1% in amplitude, for the frequency range used in the experiments[1].

Wave elevation is measured using 20 resistive gauges equally spaced along the tank, every 6 m, as shown in Fig. 2.6(a). Each gauge consists of two vertical metal rods about 1 m long, centered at the mean water level. The voltage difference between the rods, measured via a dedicated acquisition system with amplifiers, is proportional to the local free surface elevation, see Ref. [163]. The calibration coefficient depends on the rod geometry and amplifier channel, and was individually determined for each sensor using a dedicated calibration setup by our collaborators at LHEEA.

[1] More information about the towing tank is available at `https://lheea.ec-nantes.fr/test-facilities/ocean-tanks/towing-tank`

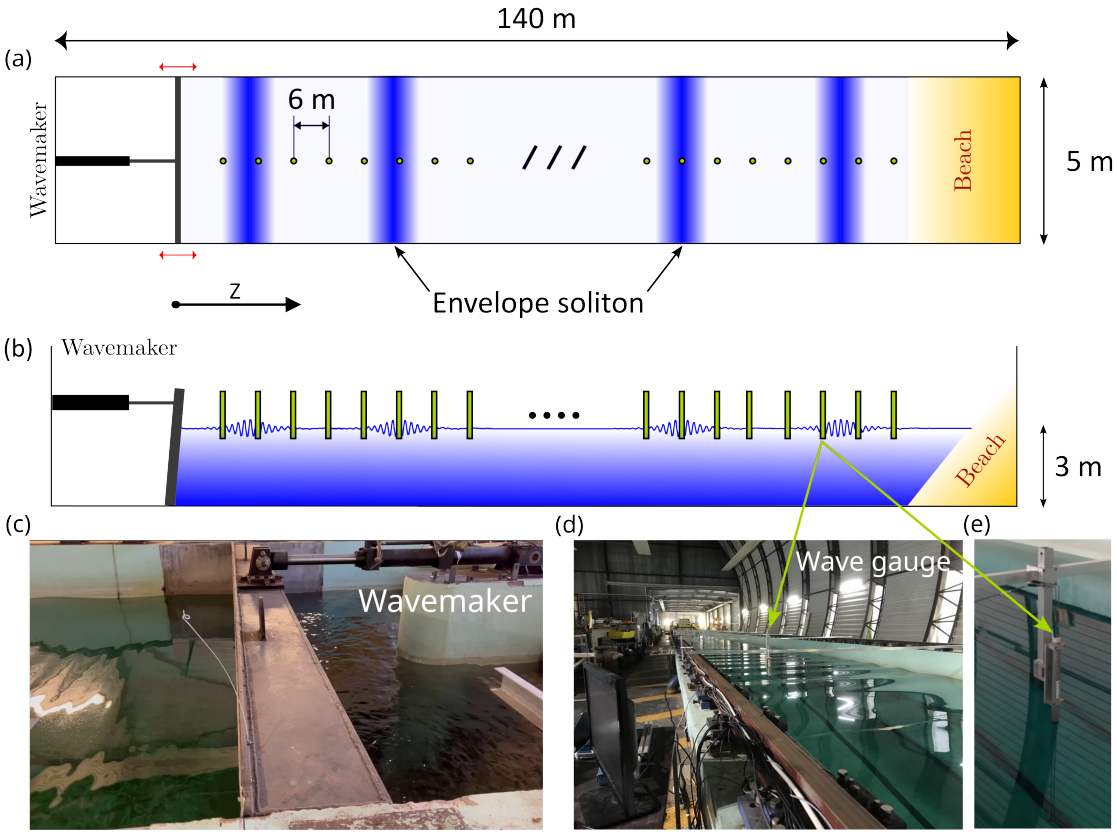

Figure 2.6: (a) Schematic (not to scale) top-view representation of the 1D water tank used in the experiments. (b) (a) Side-view of the water tank. Twenty wave elevation gauges, represented by green rectangles, are placed every 6 meters along the tank, covering a total measurement range of 114 meters. The typical spatial extent of an envelope soliton (represented in blue) is approximately 5 m. The carrier wave has a wavelength of about 1.5 m, corresponding to a frequency of approximately 1 Hz. The typical envelope-soliton amplitude lies between 2 cm and 3 cm. (c) Photograph of the flap-type wavemaker (side view). (d) Photograph of a wave propagating in the water tank, with a close-up of a wave gauge measuring surface elevation shown in (e).

2.2.2 NLSE as a model for the nonlinear propagation of deep water surface gravity waves

In the deep-water and small-amplitude regime, the evolution of a weakly nonlinear, narrow-banded wave packet can be described, under appropriate assumptions, by a nonlinear envelope equation of the focusing type. The one-

dimensional NLSE emerges as an asymptotic model derived from the Euler equations for free-surface flows in the limit of weak nonlinearity, narrow spectral bandwidth, and unidirectional propagation. The fluid is assumed to have constant depth $h \sim 3$ m. We refer the reader to standard derivation of the focusing NLSE in the context of surface gravity waves and detailed treatments in Refs. [12, 50, 88, 164–167].

The free surface elevation $\eta(Z,T)$, measured experimentally, can be approximated by

$$\eta(Z,T) = A(Z,T)e^{i(k_0 Z - \omega_0 T)} + \text{c.c.},$$

where $A(Z,T)$ is a slowly varying envelope function modulating the fast oscillations of the carrier wave. The NLSE governs the evolution of $A(Z,T)$ in time and space under the assumptions of unidirectional propagation, weak nonlinearity, and slowly varying amplitude and phase. These conditions are met in the present experiments, where the carrier wave has frequency $f_0 \approx 1.01$ Hz and wavenumber $k_0 \approx 4.2$ rad/m, corresponding to a deep-water regime with $k_0 h \approx 12.3$.

Under these physical conditions, the envelope $A(Z,T)$ of the deep water surface gravity waves obeys the following dimensional NLSE:

$$\frac{\partial A}{\partial Z} + \frac{1}{C_g}\frac{\partial A}{\partial T} = i\frac{k_0}{\omega_0^2}\frac{\partial^2 A}{\partial T^2} + i\beta k_0^3 |A|^2 A, \tag{2.16}$$

where $C_g = g/(2\omega_0)$ is the group velocity, where $g = 9.81$ m.s^{-2} is the gravity acceleration, and $\beta = 0.91$ is a finite-depth correction to the cubic nonlinearity, accounting for deviations from the ideal deep-water limit (see e.g. [168]). For $k_0 h \gtrsim 10$, β remains close to unity.

In what follows, we examine experimental conditions for which the wave field remains close to the regime of validity of Eq. (2.16), ensuring a suitable framework for testing the kinetic theory of soliton gases.

The connection between the physical envelope $A(Z,T)$ and the dimensionless

variables used in Eq. (2.1) is given by:

$$\begin{cases} \psi = \dfrac{A}{a/2} \\ t = Z\dfrac{\beta k_0^3 a^2}{8} \\ x = \sqrt{\dfrac{\beta k_0^2 \omega_0^2 a^2}{8}}\left(T - \dfrac{Z}{C_g}\right) \end{cases} \tag{2.17}$$

The factor $a/2$ in the definition of ψ arises from the requirement that, in the dimensionless NLSE used here, a soliton with spectral parameter $\gamma = 1$ have an envelope amplitude equal to 2. Since the physical soliton amplitude is a, and the dimensional field is denoted A, we define the normalized field as $\psi = A/(a/2)$ so that the soliton amplitude in normalized units becomes 2.

2.2.3 Propagation of a NLSE Soliton in the Water Tank

We first present a reference experiment illustrating the propagation of an envelope soliton solution of the NLSE, Eq. (2.16), in the water tank.

The analytical expression of an envelope soliton in physical variables is given by [50, 164, 167]:

$$\eta(Z,T) = A_{\text{sol}}\,\text{sech}\left[\frac{A_{\text{sol}}k_0\omega_0}{\sqrt{2}}\left(T - \frac{Z}{C_g}\right)\right]\cos\left[\omega_0 T + k_0\left(1 + \frac{k_0^2 A_{\text{sol}}^2}{4}\right)Z\right], \tag{2.18}$$

where A_{sol} is the amplitude of the envelope, T denotes time, Z the longitudinal spatial coordinate, and $C_g = \omega_0/(2k_0)$ is the group velocity. This solution describes a localized wave packet with a hyperbolic secant envelope modulating a carrier wave at frequency ω_0.

In the experiment presented in Fig. 2.7, a soliton waveform defined by Eq. (2.18) is generated by the flap-type wavemaker at one end of the water tank. Its propagation is recorded along the 114-meter-long measurement section using 20 resistive gauges equally spaced by 6 meters.

Figure 2.7 shows the propagation of a solitary wave packet initially generated according to Eq. (2.18). The carrier wavenumber is $k_0 = 4.10\ \text{m}^{-1}$, corresponding

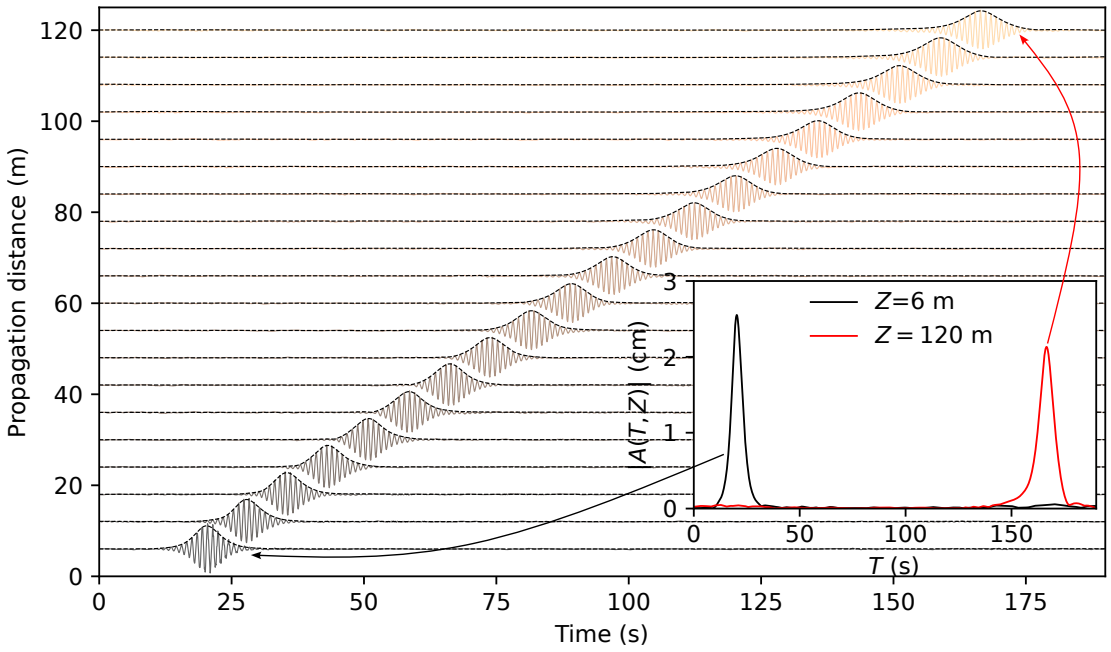

Figure 2.7: Propagation of a solitary wave measured at 20 locations along the tank (colorscale encodes distance from the wavemaker). The waveform is generated with a carrier period $T_0 = 0.99$ s and an initial envelope amplitude $a = A_{\text{sol}} = 2.8$ cm. The dashed black lines indicate the reconstructed envelope obtained using the Hilbert transform, as described in the Appendix. The inset shows the envelope obtained at $Z = 6$ m (black) and at $Z = 120$ m (red).

to a wavelength $\lambda_0 = 2\pi/k_0 \approx 1.53$ m. The associated angular frequency $\omega_0 \approx 2\pi/T_0$ satisfies the deep-water dispersion relation $\omega_0^2 = gk_0$, with $g = 9.81$ m.s^{-2} the gravitational acceleration. The duration of the envelope soliton (full width at half maximum) is

$$\Delta T_0 = \frac{2\sqrt{2}\,\text{arcsech}(1/2)}{A_{\text{sol}}\,k_0\,\omega_0} \approx 5.2 \text{ s}.$$

While the initial wave packet closely matches the soliton solution of the NLSE, its evolution displays slight deviations from ideal soliton behavior. In particular, the envelope broadens and the amplitude decays gradually during propagation, see inset in Fig. 2.7. This indicates that the system does not exhibit integrable dynamics, and higher-order perturbative effects come into play. A more detailed

discussion of these effects is provided in Sec. 2.3.3.

To sum up

We experimentally investigate the propagation of a NLSE envelope soliton in a large-scale wave tank (140 m × 5 m × 3 m) at the LHEEA (Ecole Centrale de Nantes). A single NLSE soliton, is generated using a flap-type wavemaker and its space-time evolution is recorded via an array of 20 wave gauges equally spaced along 114 meters. While the initial waveform matches the expected soliton shape, small deviations from ideal behaviour such as amplitude decay and temporal broadening are observed during propagation. These deviations suggest the presence of perturbative higher-order effects, indicating that the system does not exhibit a purely integrable dynamics.

2.2.4 Interaction of soliton gases in the water tank

We now present the results of the interaction of two monochromatic soliton gases in the water tank, shown in Fig. 2.6. The soliton gas is generated in the same manner as described in the NLSE simulation above, see Sec. 2.1.1.3. Numerical simulations of the NLSE, shown in Fig. 2.5(a), indicate that 140 normalized time units are required for the two monochromatic soliton gases to fully overlap, interact, and separate again. However, this duration does not correspond to physically realistic propagation distances in our experimental setup.

To see this, we recall that the dimensional propagation distance is related to the normalized time via $t = Z\beta k_0^3 a^2/8$. For typical experimental parameters ($a \approx 2.8$ cm, $k_0 \approx 4.2$ m^{-1}, $\beta = 0.91$), a normalized time of $t = 140$ corresponds to a physical distance of approximately 14 km. This is two orders of magnitude longer than the 140-meter wave tank used in our experiments.

In contrast, a propagation over 120 meters corresponds to a normalized time of about $t \approx 1$. Therefore, in the experimental context, the soliton gas dynamics are observed over much shorter timescales than those considered in the idealized numerical simulation.

To account for the limited propagation distance in our experiments (120

meters), we have designed the field such that it is composed of 100 solitons, with one central interaction region (green region in Fig. 2.8(a) denoted II) and two lateral regions where each species of soliton does not interact with the other (orange (resp. red) region in Fig. 2.8(a) denoted I (resp. III)). In other words, we consider the initial condition to be a field already partially in the process of interaction in some given region, as shown in Fig. 2.5(b) and Fig. 2.8(a).

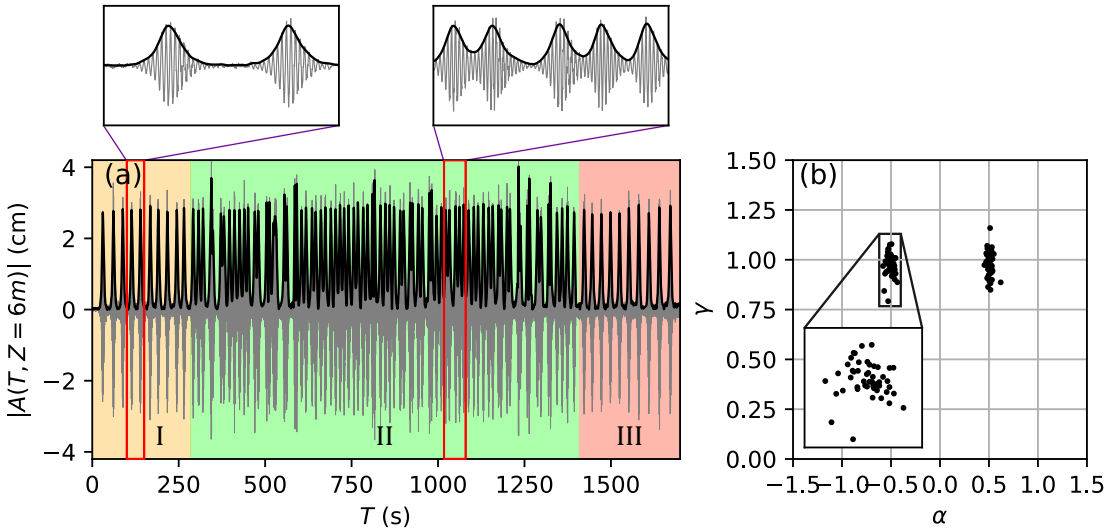

Figure 2.8: (a) SGs measured at the first gauge. The initial condition was prepared as two SGs already in interaction (region II), with non-interacting solitons in the flanking regions (regions I and III). The grey line represents the carrier wave, and the blue line the wave envelope extracted using the Hilbert Transform. (b) Measured IST spectrum calculated from the normalized wavefield.

Figure 2.8 presents the experimental wave field measured at the first gauge. As shown by the grey line in Fig. 2.8(a), the recorded signal consists of a nearly monochromatic carrier wave with frequency $f_0 \approx 1.01$ Hz, slowly modulated in amplitude and phase. The first step in processing the experimental data consists of removing the carrier wave and computing the complex envelope $A(Z, T)$ of the measured wave field, which is achieved using standard Hilbert transform techniques (see Ref. [12] and Appendix 5.1). The resulting envelope, is shown in black line in Fig. 2.8(a).

The discrete IST spectrum computed from the normalized complex envelope at $Z = 6$ m, shown in Fig. 2.8(b), reveals two well-defined clusters of eigenvalues

centered around $\lambda_{1,2} \approx \pm 0.5 + i$. This structure is consistent with the presence of two distinct monochromatic soliton gas species and matches the spectral parameters used in the numerical simulation. Each cluster contains 50 discrete eigenvalues, corresponding to individual solitons within each gas. The clusters appear slightly more spread out in the experimental data, likely due to imperfections in the waveform generation and the fact that the field is measured after 6 meters of propagation. During this initial propagation, small deviations from the ideal NLSE dynamics may already start to appear, slightly perturbing the discrete spectrum.

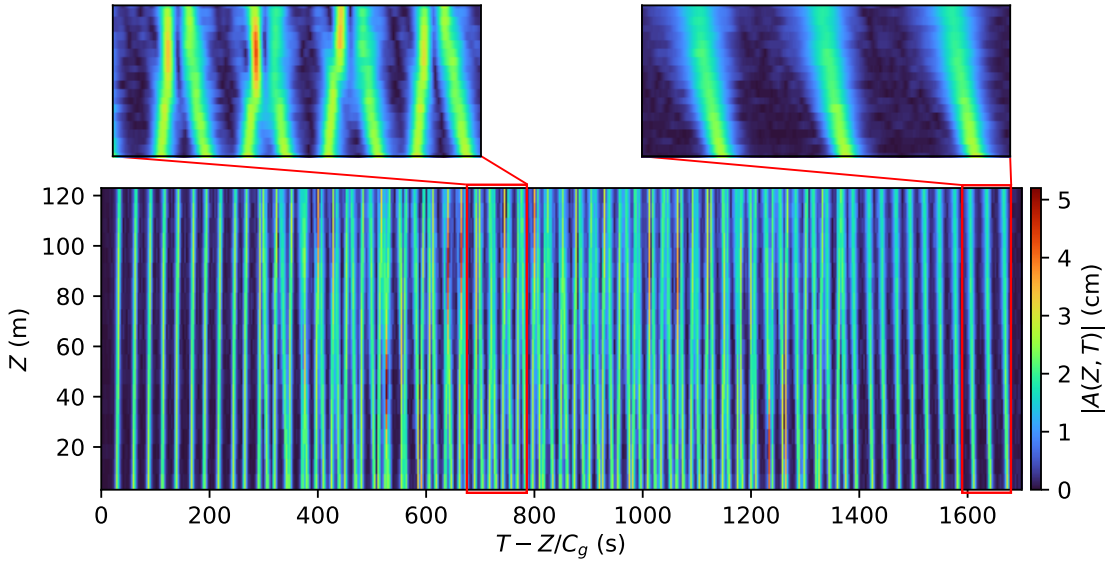

Figure 2.9: Space–time evolution of the two monochromatic SG jets, with the central region corresponding to their interaction. The diagram displays the discrete measurements recorded at each gauge position, without spatial interpolation. In the two outer regions, the two SG species propagate with opposite velocities without interacting.

The space-time diagram in Fig. 2.9 is plotted in a reference frame moving at the mean group velocity C_g of the two monochromatic SG jets. In this reference frame, the two SG jets propagate with opposite velocities of equal magnitude. The wave field consists of a central interacting region (II) and two lateral regions where each species of SGs propagates without interacting with the other (I and III). Despite the relatively short propagation distance achieved in the experiment

(approximately $t \sim 1$), individual interactions occur between pairs of solitons at random propagation distances within the water tank, see the left zoom in Fig. 2.9. These microscopic paired interactions lead to macroscopic changes in density and velocity, which are measurable as we shall see in Sec. 2.3.

To sum up

The propagation of a soliton gas in a water tank is investigated. Due to the limited propagation distance, the initial condition was engineered to contain two monochromatic SGs already partially overlapping, with non-interacting solitons at the edges and an interaction region in the center. The IST spectrum confirms the presence of two distinct soliton species, each corresponding to a cluster of 50 eigenvalues. The space-time diagram reveals two SG jets propagating with opposite velocities in the reference frame moving at the average group velocity of the two soliton species. While the normalized duration time of the interaction between the 2 species is short, random pairwise collisions occur throughout the 140-m long tank. These microscopic interactions collectively give rise to macroscopic changes in the local density and velocity of the SGs as we shall see now in Sec. 2.3.

2.3 Soliton gas interactions: comparison with kinetic theory predictions

In this section, we investigate how the interaction between two soliton gases depends on their relative velocity by varying the real part of their spectral parameters, and assess to what extent the macroscopic predictions of the kinetic theory (e.g., density and velocity changes due to the interaction) can be approached in our experimental setting. Our objective is to explore the feasibility of observing features such as those predicted in Fig. 2.2, by tuning the spectral parameters of the input field.

To this end, we designed a series of nine experiments, each involving the interaction of two SGs with fixed soliton amplitude ($\mathrm{Im}(\lambda) = \gamma = 1$) and varying

real part $\Re\mathfrak{e}(\lambda) = \alpha$, which sets the relative velocity between the two species. The space-time evolution is recorded for each case, and soliton densities and velocities are extracted from the experimental data using methodologies presented in Secs. 2.3.1 and 2.3.2. The case $\alpha = 0.5$ is shown in Fig. 2.9 as a representative example.

In the remainder of this section, we analyze the experimental results in light of the kinetic theory predictions. We focus on two macroscopic observables: the effective velocities and the densities of the two interacting soliton gases. Section 2.3.1 describes the methodology used to extract the velocities of each gas from space-time diagrams, based on the Radon transform. Section 2.3.2 then explains how we estimate the local soliton densities. Finally, in Section 2.3.3, we discuss the influence of higher-order effects and limitations of the NLSE framework in capturing the experimental dynamics.

2.3.1 Measurement of the velocities of the hydrodynamic SGs

Looking at the evolution pattern measured in the experiment, see Fig. 2.9, it may initially seem difficult, if not impossible, to determine the velocities of the SGs both inside and outside the interaction region. However, by following the approach proposed in Ref. [169] for separating right- and left-propagating solitons in a shallow-water bidirectional SG, we found that the Radon transform can be employed to measure the velocities of the solitons in the space-time diagrams recorded in our experiments.

2.3.1.1 Methodology - The Radon Transform

The Radon transform is a mathematical technique that describes an image in terms of integral projections. More precisely, it maps a function to its integrals over radial lines, which are parameterized by an angle θ and a distance r from the origin. These lines correspond to projections of the image along various directions [170]. An illustration of this method is shown in Fig. 2.10(a)(b). The Radon transform is widely used in tomographic applications across various fields, including astronomy [171], medicine [172], and geophysics, particularly in seismology [173].

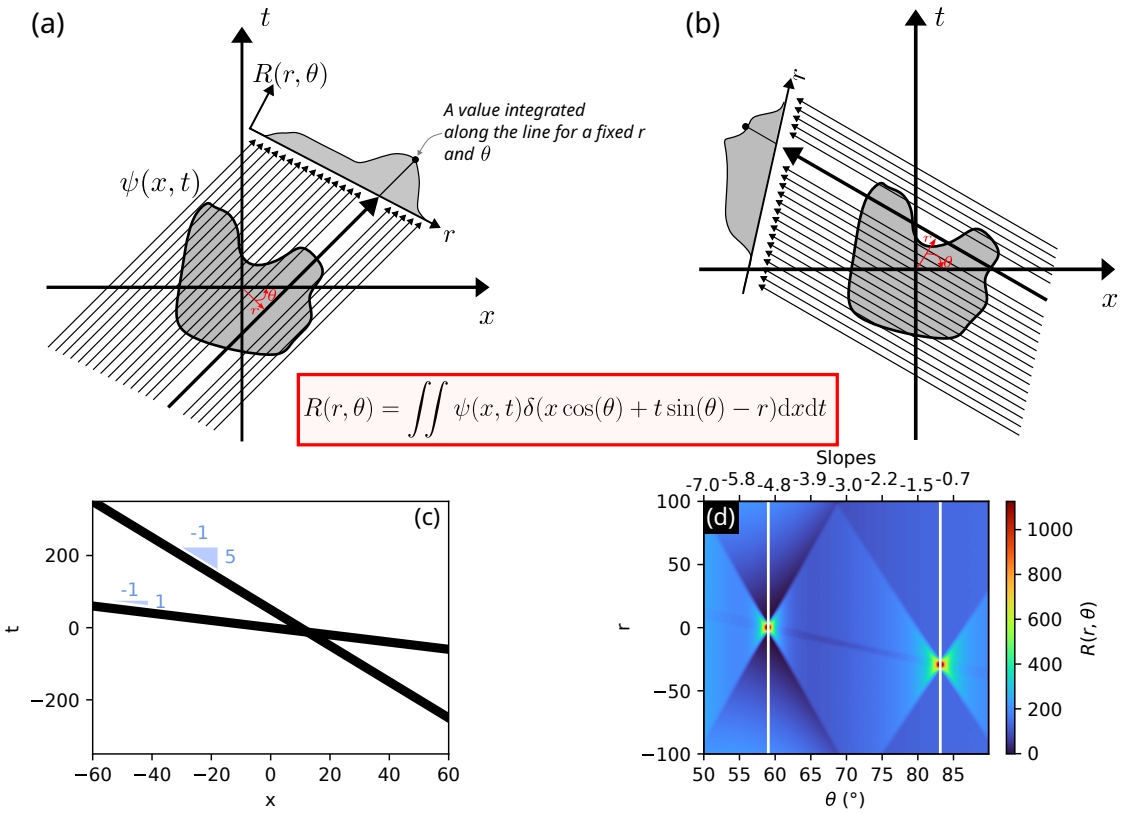

Figure 2.10: (a)-(b) Principle schematic of the radon transform for two different angles. (c) Processing the radon transform of two lines with different slopes. (d) Sinogram got from the Radon Transform, the slopes of the lines are given by the two maximas.

The Radon transform $R(r,\theta)$ of the normalized space-time intensity plots $|\psi(x,t)|$ recorded in the experiment is defined as:

$$R(r,\theta) = \int \sum_n |\psi(x,t_n)|\,\delta\left(x\cos\theta + t_n \sin\theta - r\right) \mathrm{d}x, \tag{2.19}$$

where δ is the Dirac delta function, $r = \sqrt{x^2+t^2}$ is the distance to an origin point located at the center of the (x,t) domain, and θ is an angle. The discrete variable t_n corresponds to the normalized time associated with the positions of the wave gauges Z_n used in the experiment.

A simple example to illustrate this method is to consider an image composed of two straight lines, as shown in Fig. 2.10(c). Since the Radon transform

computes integrals along lines in an image, applying it to a line effectively yields a single value: the sum of the pixel intensities along that line. Because a line is one-dimensional, this integral reduces to a single point in Radon space. Consequently, when the image contains two lines, the Radon transform results in two distinct points, as shown in Fig. 2.10(d). The coordinates of these points correspond to the relative positions of the lines with respect to the center of the image (r), and their orientation or slope (θ), providing information on both position and angle, see Figs. 2.10(c)(d).

2.3.1.2 Application to the experimental space-time diagrams

Measurement of the velocity of an isolated soliton: We first apply the Radon transform to the simple case of an isolated soliton propagating in the wave tank. This soliton belongs to one (region I in Fig. 2.8(a)) of the two non-interacting species in the experiment shown in Fig. 2.9.

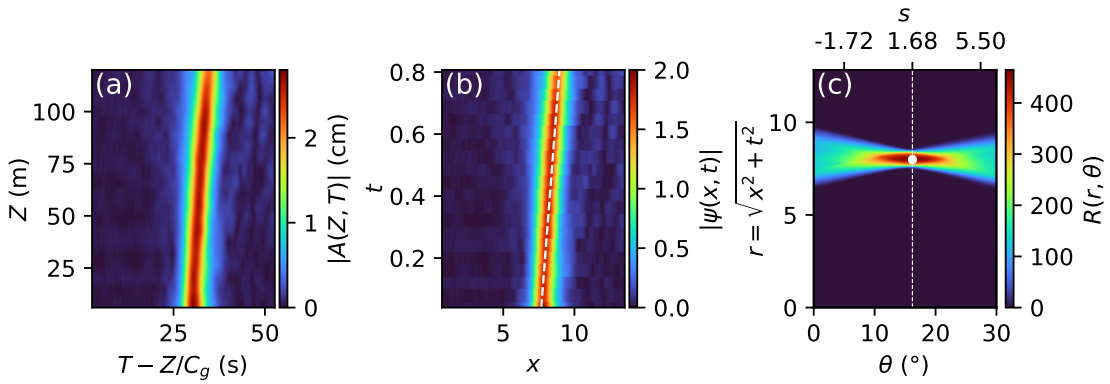

Figure 2.11: Detection of the free velocity of an isolated soliton composing a soliton gas in our experiment. (a) Spatio-temporal diagram $|A(Z,T)|$ reconstructed from wave gauge measurements. (b) Normalized field $|\psi(x,t)|$, obtained using Eq. (2.17). The white dashed line corresponds to the velocity $s = 1.68$. (c) Radon transform of $|\psi(x,t)|$, revealing a dominant velocity s associated with the angle $\theta_{\max}$, highlighted by a white dot and dashed line corresponding to a detected peak in the sinogram. The upper axis shows the velocity coordinate.

Figure 2.11 illustrates the full procedure of detection of velocity using the Radon Transform. Fig. 2.11(a) shows the reconstructed spatio-temporal diagram $|A(Z,T)|$ in physical units, obtained from the wave gauge measurements.

Fig. 2.11(b) shows the corresponding dimensionless field $|\psi(x,t)|$, computed via the change of variables defined in Eq. (2.17). The Radon transform is then applied[2] to this dimensionless field. The resulting Radon sinogram is shown in Fig. 2.11(c), where a distinct peak is detected and highlighted by a white dot and a dashed line.

This peak corresponds to a dominant orientation $\theta_{\max}$, associated with the slope of the soliton trajectory in the (x,t) plane. To convert this angle into a velocity s of the soliton in the (x,t) plane, we use the geometric relation:

$$s = \frac{H\Delta x}{L\Delta t}\tan(\theta), \tag{2.20}$$

where Δx and Δt are the physical extents of the space-time window in space and time, and H and L denote the height and width in pixels of the image used in the Radon transform.

Using this method, we find that the free velocity of the isolated soliton is approximately $s \approx 1.68$, consistent with the direct measure done on the space-time diagram, see the white dashed line in Fig. 2.11(b).

Measurement of the velocity of the solitons in the interaction region: Having validated the method on an isolated soliton, we now apply the Radon transform to the full space-time dynamics of two interacting soliton gases, shown previously in Fig. 2.9 after it has been normalized using the change of variables defined in Eq. (2.17). The resulting sinogram is presented in Fig. 2.12(a).

The Radon transform $R(r,\theta)$ reveals a collection of prominent features : local maxima in the (r,θ) plane, each corresponding to a trajectory in the original space-time diagram. As in the single-soliton case, the angle θ encodes the soliton velocity in the (x,t) plane.

By identifying the local maxima of $R(r,\theta)$, shown as white dots in Fig. 2.12(a), we classify the solitons into distinct velocity groups. This is summarized in Fig. 2.12(b): two outer groups correspond to free (non-interacting) solitons (black points), each comprising eight trajectories with average velocities of ap-

[2]The package we are using to get the Radon Transform is the radon module from the skimage.transform library of python

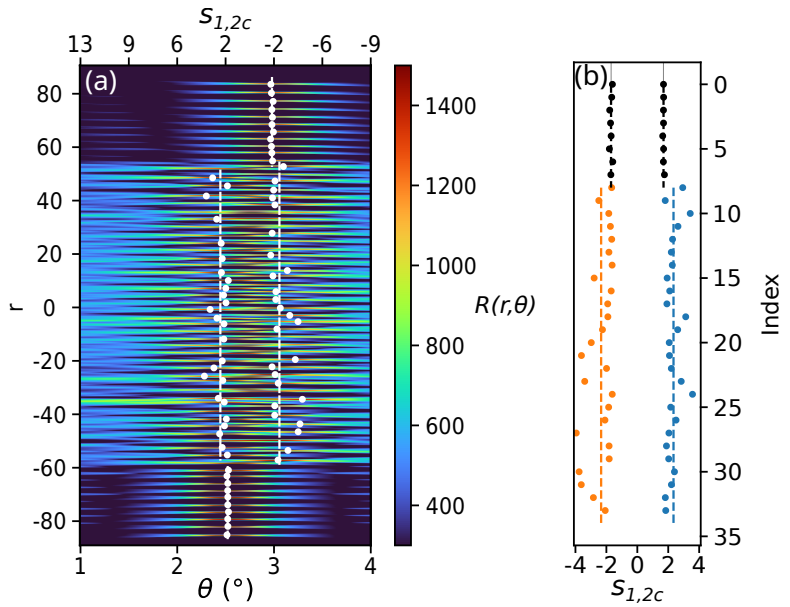

Figure 2.12: (a) Radon transform $R(r,\theta)$ of the experimental space-time diagram of Fig. 2.9 for $\alpha = \pm 0.5$. The white points indicate the positions at which a maximum of the function $R(r,\theta)$ is found. (b) Simplified diagrammatic view of the results obtained in (a) using the Radon transform. Two sets each containing eight free (non-interacting) solitons are found with mean velocities of approximately 1.69 and approximately -1.69 (black points). Two other sets each containing 25 solitons are found in the interaction region with mean velocities of approximately 2.34 (blue points) and approximately -2.34 (orange points)

proximately ±1.69. In the central region, where interaction occurs, two larger groups of about 25 solitons each are detected with mean velocities of approximately ±2.34, see colored points in Fig. 2.12(b).

It should be noted that not all solitons can be reliably detected in this analysis. Due to the limited temporal extent of the interaction region ($L_{NL} = 1/(\beta k_0^3 a^2) \sim$ 20 m , $t \sim 0.8$), some trajectories do not produce well-resolved peaks in the Radon transform. It is important to emphasize that this limitation is primarily a measurement issue, caused by the finite size of the interaction region in the experiment, rather than a consequence of any unexpected physical phenomenon.

Since the Radon transform enables us to extract both the average free velocity of the non-interacting solitons and the effective velocity of solitons within the interaction region, we are able to compare these experimental measurements

with the analytical predictions of the spectral kinetic theory. This comparison is carried out across our nine experiments, in which the real spectral parameter $\alpha = \Re\mathfrak{e}(\lambda)$ was varied from approximately 0.2 to 1.0 in nine steps. The corresponding theoretical velocity relation is given by Eq. (2.14).

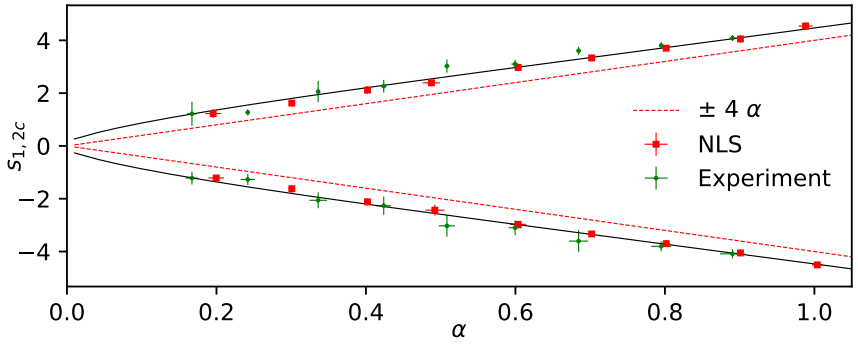

Figure 2.13: Comparison between experimental (green points) and NLSE numerical measurements of soliton velocities (red squares) and analytical predictions from kinetic theory. The red dashed line shows the free velocity $\pm 4\alpha$. The solid black curve corresponds to the theoretical prediction for the effective velocity in the interaction region, given by Eq. (2.14).

Figure 2.13 summarizes the mean soliton velocities extracted from the interaction region (colored points in Fig. 2.12(b)) for each of our nine experiments. In each case, the parameter α, which encodes the free velocity of the SGs, is directly estimated from the measured free velocities using the Radon transform (black points in Fig. 2.12(b)). The experimental results show excellent agreement with the analytical prediction from the spectral kinetic theory, represented by the solid black line corresponding to Eq. (2.14). Error bars indicate the standard deviation of local maxima detected by the Radon transform for each soliton species. The red squares represent velocity measurements extracted from numerical simulations of the NLSE performed with the same initial conditions and normalized propagation time as in the experiments. These results highlight the remarkable agreement between the kinetic theory, the numerical simulations, and the experimental measurements in the specific case of colliding monochromatic soliton gases governed by the NLSE. In this regime, perturbative effects present in the experimental setup remain sufficiently weak to preserve the validity of

the spectral kinetic theory.

However, as will be discussed later (see Chapters 3 and 4), the physical effects that break integrability in certain platforms lead to much more pronounced deviations from the predictions of kinetic theory. These observations highlight the need to better understand the limits of applicability of the integrable soliton gas framework.

To sum up

In this section, we use the Radon transform to extract the velocities of solitons propagating in experimental space-time diagrams. After validating the method on an isolated soliton, we apply it to the full dynamics of two interacting soliton gases. The Radon sinograms reveal distinct velocity classes: free (non-interacting) solitons at the periphery and interacting solitons in the central collision region. For each of the nine experiments, we determine both the free and effective velocities directly from the space-time data. The resulting velocity measurements show excellent agreement with the predictions of spectral kinetic theory and with NLSE simulations. These results demonstrate that, in the regime of weakly non-integrable perturbations explored here, the kinetic theory remains quantitatively valid.

2.3.2 Measurement of the densities of the hydrodynamic SGs

The most accessible macroscopic observables in the experiment are the densities ρ_{1c} and ρ_{2c} of each soliton species within the interaction region. To measure these densities, we first convert the signals recorded in physical units into their dimensionless counterparts using the variable transformations defined in Eq. (2.17). Through this transformation, the retarded time measured in the physical frame becomes a dimensionless spatial variable x, and the measured wave field into a dimensionless field, see Fig. 2.14.

Once in dimensionless form, we analyze the wave field recorded and count the number of solitons n belonging to each species within the interaction region. We also determine the total dimensionless length ℓ over which these solitons are distributed (see Fig. 2.14 where ℓ is delimited via the red dashed lines). The

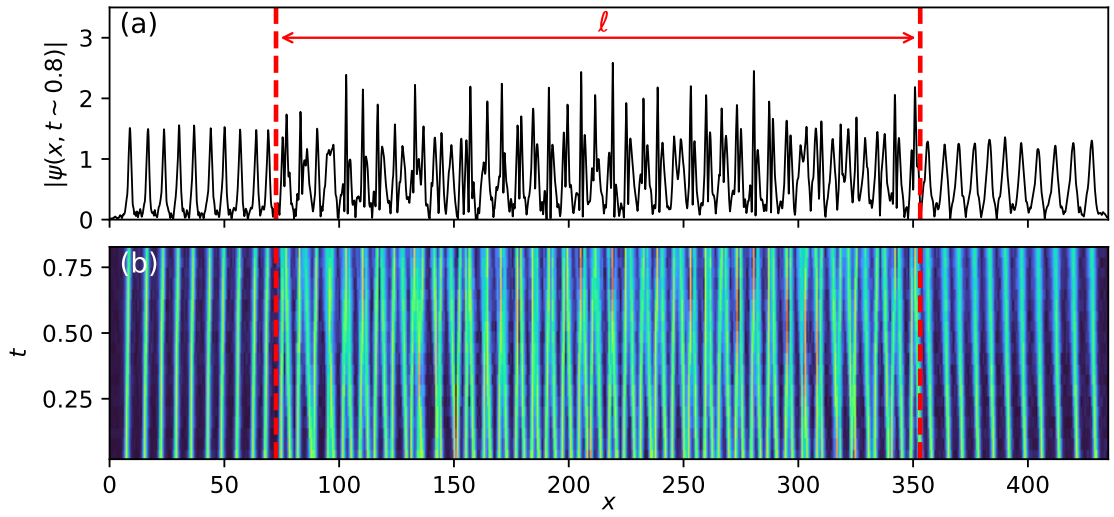

Figure 2.14: Determination of the densities of the SG species. (a) Wave envelope modulus $|\psi(x, t \simeq 0.8)|$ taken at the last gauge located at $Z = 120$ m. The red dashed vertical lines delimit the region of length ℓ over which the density is estimated. (b) Spatio-temporal diagram of the wave field $|\psi(x, t)|$; the soliton gas interaction region corresponds to the same interval ℓ.

corresponding SG densities are then obtained using the relation $\rho_{1,2c} = n/\ell$.

Figure 2.15 shows the experimentally measured densities of each soliton species within the interaction region, represented by the green points. The density decreases from approximately 0.15 to 0.125 as the real part α of the eigenvalue λ_1 (equivalently the relative velocities of the 2 SGs) varies from 1 to 0.2. In the experiments, it was not meaningful to further increase the interaction between the two SGs by reducing α below approximately 0.2. For such small values, the relative velocity between the two soliton species becomes so low that no significant interaction or collision occurs over the finite propagation distance available in the water tank.

The brown dashed line in Fig. 2.15 corresponds to the initial density $\rho_{10} = \rho_{20} = 0.156$, obtained from a single-species SG experiment (not presented here) carried out using the same synthesis method as the two-species SG configuration. The black solid line shows the analytical prediction from the spectral kinetic theory given by Eq. (2.15) (and already illustrated in Fig. 2.2(b)). As α increases, the interaction between the SGs decreases and the measured densities in the

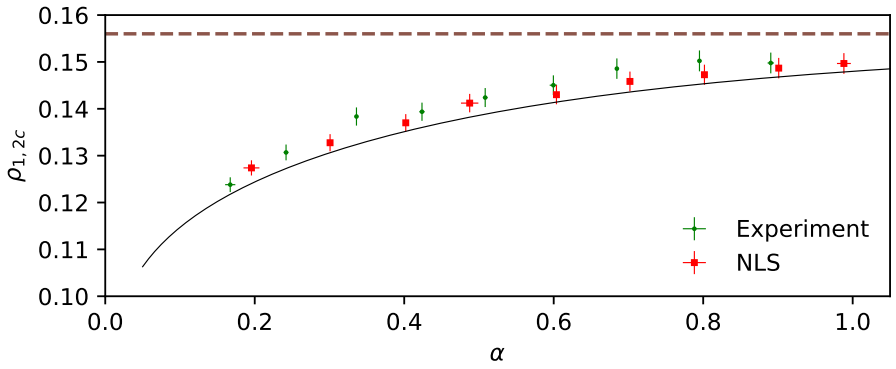

Figure 2.15: Comparison between the soliton densities measured in NLSE numerical simulations and in the experiment, with the analytical predictions from the kinetic theory of soliton gases. The solid black line represents the theoretical prediction from Eq. (2.15) with $\gamma = 1$. The brown dashed line indicates the individual densities of the two gases in the absence of interaction, $\rho_{10} = \rho_{20} = 0.156$. Both experimental and numerical data show that the soliton densities in the interaction region decrease as the parameter α (encoding the free velocity) decreases, that is, as the interaction between the two gases becomes stronger.

interaction region tend toward the initial density $\rho_{1,20}$.

Red squares in Fig. 2.15 represent the results obtained from numerical simulations of the NLSE performed using the same initial conditions and normalized propagation time ($t \sim 1$) as in the experiment.

Error bars are the uncertainties in estimating the spatial extent ℓ of the interaction region, quantified using $\Delta\rho = n\Delta\ell/\ell^2$, with $\Delta\ell$ taken as the typical spacing between two solitons in the non-interacting region ($\Delta\ell \sim 8$).

Figure 2.15 shows a good quantitative agreement between the experimental density measurements, the NLSE simulations, and the predictions of the kinetic theory of soliton gases. This consistency is notable given the presence of higher-order perturbative effects, previously identified in the single-soliton propagation experiment (see Sec. 2.2.3), which are expected to break the exact integrability of the system. In the present case, however, these perturbations remain sufficiently weak so as not to significantly affect the collective soliton dynamics. This suggests that the kinetic theory framework remains quantitatively valid under the near-integrable conditions realized in the water tank.

To sum up

In this section, we measured the densities ρ_{1c} and ρ_{2c} of the two soliton gases in the interaction region by counting the number of solitons per species over a known spatial interval ℓ. The main observation is that the densities decrease as the parameter α is reduced, that is, as the interaction between the two gases becomes stronger. This density drop reflects the mutual dilution of the gases due to nonlinear soliton collisions. In the limit of large α, where the interaction is negligible, the measured densities converge toward the non-interacting value ρ_0. This trend is observed in the experiment, in NLSE simulations, and follows the analytical prediction of the spectral kinetic theory.

2.3.3 Influence of the Higher Order Effects

Building upon the observation of non-ideal soliton propagation in the water tank, we now investigate the impact of higher-order effects (HOE) on the interaction dynamics of soliton gases. In this section, we use numerical simulations of both the integrable focusing 1D NLSE and a modified, non-integrable version of the NLSE to investigate how these effects impact the space-time evolution and the discrete IST spectra of the two interacting SG jets.

As previously mentioned in the discussion of Fig. 2.7, the dynamics of a single soliton showed deviations from ideal NLSE behavior: the soliton did not preserve its shape during propagation through the water tank. This observation reveals the presence of HOEs, and we now examine whether these effects significantly influence the effective velocities and densities measured in the experiment. To characterize the influence of HOEs we first look at the evolution of the spectral distributions of solitons in the SGs. Figure 2.16(a) presents the IST spectra computed at two different propagation distances. It shows that the dynamics is not isospectral, the discrete IST spectrum evolves as the SGs propagate. In particular, we observe a decay in the imaginary parts of the centers of mass of the two clusters of eigenvalues between $Z = 6$ m and $Z = 120$ m. This decay primarily results from weak wave damping due to viscous effects, such as side-wall friction, during propagation. In our setup, the damping coefficient is

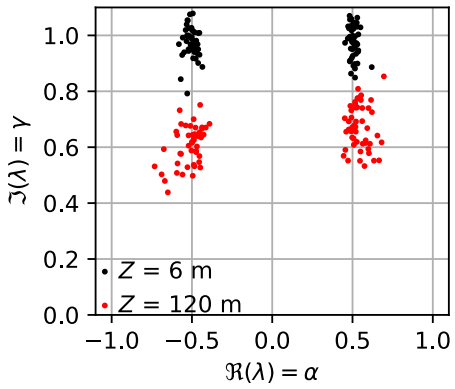

Figure 2.16: Evolution of the IST spectrum measured experimentally. The black points correspond to the IST spectrum at the beginning of the propagation ($Z = 6$ m), and the red points to the spectrum at the end of the tank ($Z = 120$ m).

estimated to be $\sim 6\times10^{-4}$ m^{-1}, corresponding to a characteristic damping length of approximately 1.7 km.

However, this simple damping effect alone may not account for the broadening of the cloud of eigenvalues forming the IST spectrum. Notably, we observe an asymmetry in the imaginary parts of the eigenvalues. This asymmetric distortion arises from the nonlinear evolution of the two SG jets and is a clear indication of HOEs influencing the evolution beyond the standard NLSE description [174–176].

Following previous studies on nonlinear dynamics of 1D water waves [175–179], higher-order effects observed in 1D water wave experiments can be effectively captured by a modified version of the NLSE, known as the Dysthe equation [180, 181]. This model is formulated as a spatial evolution equation:

$$\frac{\partial A}{\partial Z} = i\frac{k_0}{\omega_0^2}\frac{\partial^2 A}{\partial T^2} + i\beta k_0^3|A|^2A - \frac{k_0^3}{\omega_0}\left(6|A|^2\frac{\partial A}{\partial T} + 2A\frac{\partial |A|^2}{\partial T} - 2iA\mathcal{H}\left[\frac{\partial |A|^2}{\partial T}\right]\right) - i\alpha_{\text{eff}}A, \tag{2.21}$$

where $A(Z,T)$ denotes the complex envelope of the wave field, Z is the spatial coordinate, and T is the temporal coordinate, while α_{eff} represents the effective amplitude decay rate of the envelope. The additional terms in parentheses are higher-order corrections that arise at the next order of the perturbative expansion of the Euler equations in wave steepness. They account for nonlinear

self-steepening of the envelope and for mean-flow effects associated with the induced current beneath the free surface, all of which become significant when the carrier wave steepness $\epsilon = k_0 a$ is not negligibly small.

By applying the dimensionless transformation defined in Eq. (2.17), Eq. (2.21) can be recast into a normalized form:

$$\frac{\partial \psi}{\partial t} = i\frac{\partial^2 \psi}{\partial x^2} + 2i|\psi|^2\psi - 2\sqrt{2}\epsilon\left(3|\psi|^2\frac{\partial \psi}{\partial x} + \psi\frac{\partial |\psi|^2}{\partial x} - i\psi\mathcal{H}\left[\frac{\partial |\psi|^2}{\partial x}\right]\right) - i\alpha_{\text{norm}}\psi \quad (2.22)$$

where $\psi(x,t)$ represents the normalized wave envelope, and the small parameter $\epsilon = k_0 a$ denotes the wave steepness. The Hilbert transform $\mathcal{H}$ is defined in the Fourier domain as [182]:

$$\mathcal{F}(\mathcal{H}(f(t))) = -i\,\text{sgn}(\omega)\mathcal{F}(f(t)), \quad (2.23)$$

where $\mathcal{F}$ denotes the Fourier transform and $\text{sgn}(\omega)$ is the sign function of the frequency variable ω.

Figure 2.17 presents a comparison between experimental results and numerical simulations of the focusing 1D NLSE and its higher-order extension Eq. (2.22), for the interaction of two jets of soliton gases, each composed of 50 solitons. The first row (Figs. 2.17(a)(d)(g)) displays the results from the numerical integration of the standard NLSE. As expected for an integrable system, the evolution is isospectral: the discrete IST spectrum remains unchanged during propagation, consisting of two narrow spectral clouds centered at $\lambda_{1,2} = \pm 0.5 + i$ from $Z = 0$ m to $Z = 120$ m.

The third row presents the numerical results obtained by simulating Eq. (2.22), which includes higher-order nonlinear effects and damping. This simulation use the same initial conditions as the NLSE and experimental cases. The corresponding space-time evolution shown in Figs. 2.17(c)(f) closely matches the experimental observations depicted in Figs. 2.17(b)(e)). Notably, in both the experiment and the Dysthe simulations, the solitary waves undergo a visible broadening during propagation, in contrast to the standard NLSE simulation where the soliton profiles remain sharply localized (compare Fig. 2.17(d) with Figs. 2.17(e) and (f)). This broadening is accompanied by the emission of dis-

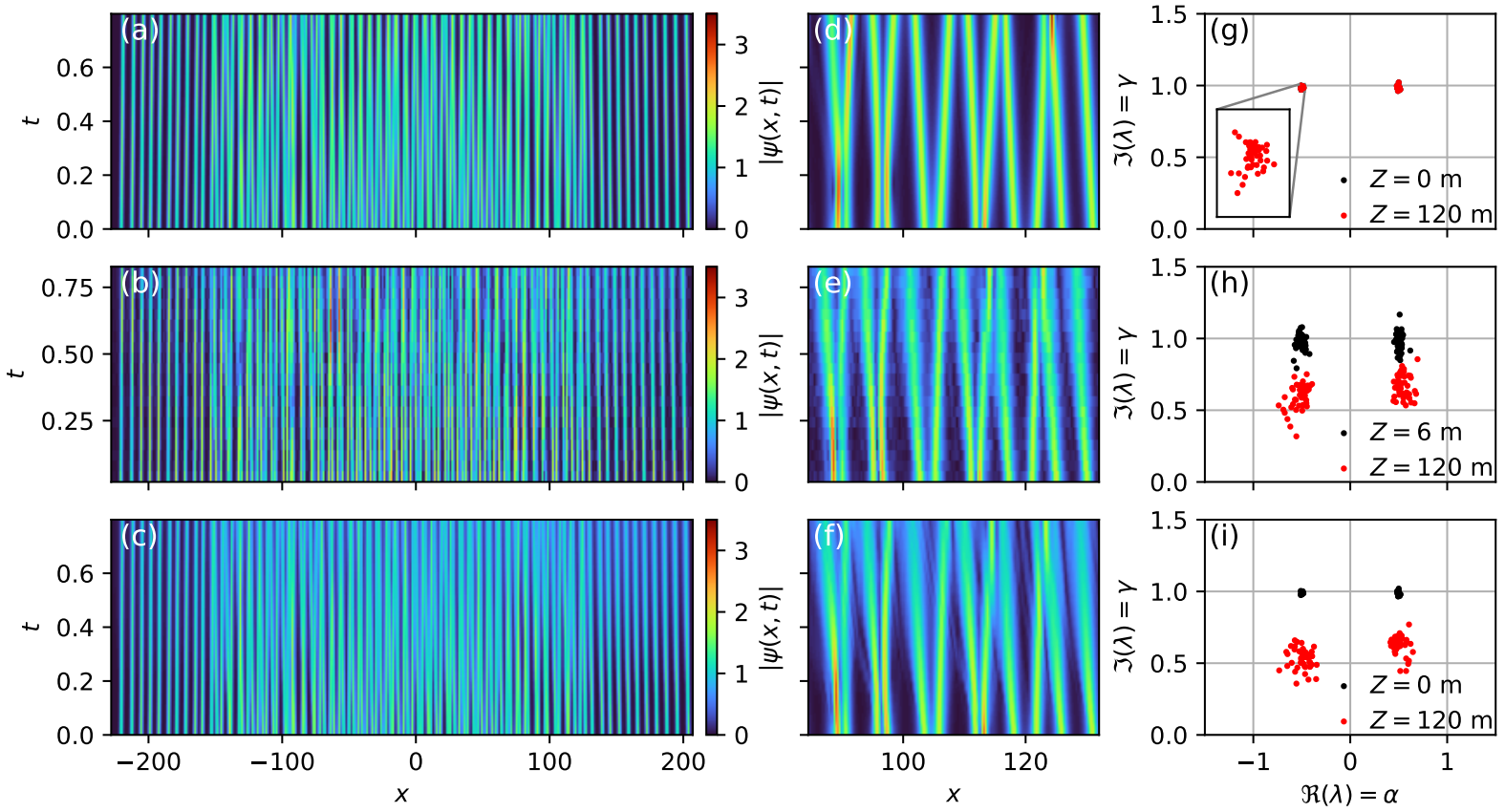

Figure 2.17: Comparison in terms of dynamics for the same initial condition considering either 1D focusing NLSE (Eq. 2.1), experiment results or Dysthe equation (Eq. 2.22). (a) Space-time dynamics of two monochromatic soliton gases obtained in numerical simulation of the NLSE (Eq. 2.1), (b) same but in experiment, (c) same but in numerical simulation of the Dysthe equation (Eq. 2.22). (d)-(f) zoomed region of (a)-(c). (g)-(i) IST spectrum for the whole field at different positions.

persive radiation, which is not captured by the integrable NLSE model. The discrete IST spectra computed at $Z = 6$ m and $Z = 120$ m (Figs. 2.17(g–i)) further confirm that the evolution is no longer isospectral in the presence of higher-order effects. These effects induce a spreading (or diffusion) of the eigenvalues within the complex spectral plane. Nonetheless, the eigenvalues remain grouped into two distinct spectral clouds associated with each soliton species, preserving the global structure of the initial spectrum. The figure 2.18 presents a quantitative

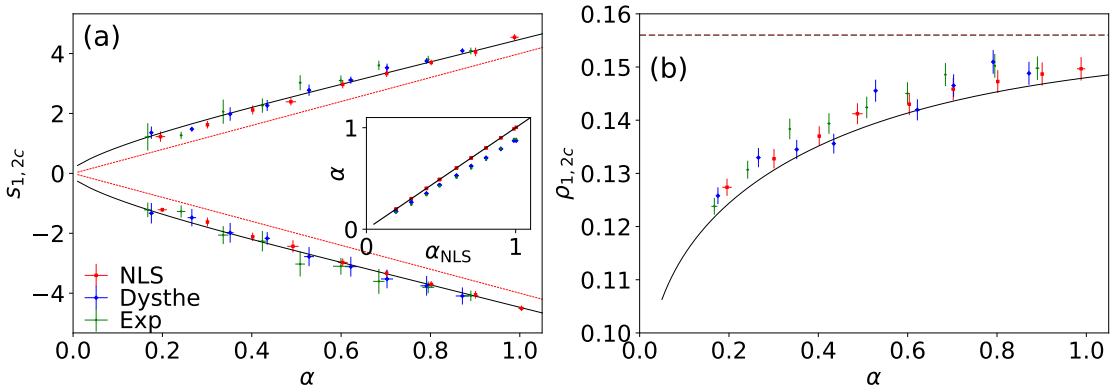

Figure 2.18: Comparison between experiment, NLSE and Dysthe simulations, and spectral kinetic theory. (a) Effective soliton velocities as a function of the parameter α, extracted from the Radon transform of space-time diagrams. The red dashed line shows the free velocity $\pm 4\alpha$. (b) Measured soliton densities in the interaction region as a function of α; the brown dashed line indicates the initial density of each gas without interaction. Experimental results are shown as green circles, NLSE simulations as red squares, and Dysthe simulations as blue diamonds. Analytical predictions from spectral kinetic theory (Eqs. (2.14), (2.15)) are plotted as solid black lines.

comparison of two key observables characterizing soliton gas dynamics: the effective velocity in the interaction region and the soliton gas density. These quantities are measured experimentally (green points), measured from NLSE numerical simulations (red squares) and Dysthe equation numerical simulations (blue diamonds, Eq. (2.22)), and compared with the predictions of the spectral kinetic theory (black lines).

Fig. 2.18(a) shows the effective velocities measured in the interaction region. While the experimental results remain in good agreement with the theoretical predictions from kinetic theory (solid black curve), slight deviations can be

observed particularly in terms of the measured parameter α, see inset. These deviations are accurately reproduced by numerical simulations of the Dysthe equation (blue diamonds), suggesting that they originate from higher-order effects not captured by the integrable NLSE.

Fig. 2.18(b) shows the measured soliton gas densities within the interaction region. As with the velocities, the experimental data are in good overall agreement with the kinetic theory predictions, though small systematic deviations are observed, particularly in terms of the measured parameter α. These deviations are accurately reproduced by the Dysthe simulations, which provide a more accurate description than the NLSE by accounting for higher-order perturbative effects present in the experimental system.

Taken together, these comparisons show that the experimental results, are well captured by the predictions of the spectral kinetic theory. This agreement suggests that, in the present regime, the higher-order perturbative effects, well modeled by the Dysthe equation, remain sufficiently weak to preserve the key features of soliton gas dynamics predicted by the integrable framework. At the same time, the simulations highlight the relevance of including such corrections when aiming for a more accurate description in realistic systems.

To sum up

In this section, we explore how higher-order perturbative effects influence the dynamics of interacting soliton gases in the water tank experiment. Evidence from both the evolution of the IST spectrum and deviations from ideal soliton behavior indicate a breaking of integrability. To investigate this, we compare experimental results with numerical simulations of both the integrable NLSE and a modified non-integrable model, the Dysthe equation, that accounts for weak damping and higher-order nonlinearities. While the NLSE fails to reproduce some of the experimental observations (e.g., spectral broadening, radiative losses), the Dysthe equation accurately captures these key features. Quantitative comparisons of macroscopic observables, such as the effective velocities and densities of soliton gas in the interaction region, reveal that the experimental measurements remain in good agreement with the predictions of the spectral kinetic theory. Small deviations observed are well reproduced by the Dysthe simulations, confirming that they originate from higher-order effects not captured by the NLSE. Overall, these results show that the kinetic theory remains valid under the weakly non-integrable conditions realized in the water tank, and that the Dysthe equation provides a relevant extension for capturing the influence of realistic perturbations.

2.4 Summary of the Chapter

In this chapter, we have investigated the dynamics of interacting soliton gases (SGs) in deep-water surface gravity waves, with a particular focus on the experimental measurement of their macroscopic properties. We have shown how the Radon transform applied to space-time diagrams allows for a determination of the velocities of soliton species, both in the free and interacting regions. The number of solitons was directly counted in the interaction region, which allowed us to determine their respective densities.

These measurements were systematically compared to the predictions of the

spectral kinetic theory of soliton gases, as developed in Ref. [32] and outlined in the first part of this chapter. This theory, provides analytical expressions for the effective velocities and densities of colliding SGs in terms of their spectral parameters.

As the relative velocity between the two soliton gases increases (i.e., for larger values of the spectral parameter α), the interaction between them becomes weaker. In all cases, interactions between the two soliton gases lead to a dilution, with each gas becoming less dense than in the non-interacting regime. However, the extent of this dilution strongly depends on the spectral parameter α: for small α (i.e., strong interactions), the density of each gas is significantly reduced compared to its initial value. In contrast, for larger α, the interaction weakens, and the density remains closer to that of the initial, non-interacting gas. Interactions also affect the effective velocities of the solitons. Due to cumulative phase shifts induced by collisions, solitons tend to acquire larger effective velocities compared to their free velocities. These trends are in excellent quantitative agreement with the theoretical predictions.

Clear signatures of integrability breaking were identified in the experiment: the evolution of the IST spectrum was not isospectral, and solitons exhibited radiative losses and deformation during propagation. These effects are absent from the NLSE description but are accurately captured by simulations of the Dysthe equation, which incorporates higher-order nonlinear corrections and weak damping. Although higher-order effects are present in the experiment and break the integrability of the system, they remain sufficiently weak in the deep-water regime of our setup for the measured soliton velocities and densities to remain in quantitative agreement with the predictions of spectral kinetic theory.

This result highlights a key conclusion of this chapter: in the specific case of colliding monochromatic SGs in the deep-water regime, the spectral kinetic theory remains verified under weak higher-order perturbations. In the following chapters, we will examine situations where weak integrability breaking results on strong effects on soliton gases, in particular on their nonlinear spectral properties such as the density of states. In these cases, even small perturbations lead to substantial deviations from the predictions of integrable kinetic theory.

Chapter 3

Soliton Gas propagation in a nonlinear electrical line

It is through practice that man must prove the truth.

– Karl Marx

3.1 Introduction

As discussed in Chapter 1, the concept of a soliton gas (SG) was introduced by V.E. Zakharov in 1971 [30] within the Korteweg-de Vries (KdV) framework. While the controlled generation and propagation of SGs have been experimentally demonstrated in systems governed by the nonlinear Schrödinger equation (NLSE), such as in hydrodynamics [35, 38] (see Chap. 2), no equivalent realization with full control over the spectral content has yet been achieved for KdV systems. Nevertheless, recent experiments in shallow water have reported the spontaneous formation of soliton gases via soliton fission from large-scale waveforms [34], providing strong evidence of KdV-type SG dynamics, though without direct spectral control over the generated gas.

In this chapter, we investigate the propagation of a SG in a nonlinear electrical transmission line (NLTL). This experimental platform consists of a chain of nonlinear electrical oscillators that can be effectively described at leading order by the KdV equation in the long wave limit. While such systems have been studied since the 1970s, the work presented in this thesis represents the first experimental investigation of the evolution of a KdV SG in an electrical line.

In our experiments, the presence of weak dissipation, inherent to the resistive nature of the circuit components, introduces non-integrable and non-adiabatic effects into the system. Notably, dissipation leads to the generation of new low-amplitude solitons, and significantly affects the long-time dynamics of the soliton gas. To analyze these effects, we conduct a nonlinear spectral analysis using the Inverse Scattering Transform framework. For the first time in a KdV system, we measure the density of states, revealing the emergence of a soliton condensate due to the dissipative nature of the system. Notably, such a transition is strictly forbidden in integrable KdV dynamics, where a soliton condensate cannot spontaneously form from a regular soliton gas [121]. Our experiments thus uncover a nontrivial phenomenon that lies beyond current theoretical predictions and highlights the profound impact of weak perturbations on the nonlinear spectral structure of soliton gases.

The chapter is organized as follows. First we introduce the derivation of the KdV equation as the continuum limit of a NLTL. The second section presents

our baseline experiments in our constructed NLTL, including the propagation of a single KdV soliton and of the study of the wave propagation in the NLTL in linear regime. We also examine soliton collisions and soliton fission in the presence of weak dissipation. The third section focuses on the non-adiabatic evolution of a single soliton, where we discuss both experimental observations and theoretical modeling of the underlying mechanisms. Finally, in the last section, we investigate the propagation of a dense soliton gas, analyzing its spectral properties through IST and presenting the first measurement of the DOS in a KdV system.

3.1.1 The KdV equation for the description of a nonlinear electrical line

The KdV equation provides a first-order description of shallow water wave propagation in 1d hydrodynamic systems (see Chap. 1). Moreover, in the long-wave approximation, it also models the propagation of small-amplitude waves in an anharmonic lattice of masses and springs [50–53]. In the following, we consider an electrical analogue of the mechanical chain presented in Chap. 1, where electrical oscillators replace their mechanical counterparts. This system, known as a nonlinear transmission line (NLTL) is schematically shown in Fig. 3.1.

The electrical NLTL consists of a serial association of N identical cells, each forming an LC circuit (see Fig. 3.1). The inductance L is a linear component with L being constant, while the capacitance C is voltage-dependent, introducing the system's nonlinearity. In analogy with the mechanical chain discussed in Chap. 1, the inductors play the role of masses and the nonlinear capacitors act as nonlinear springs.

The theoretical derivation of the dynamical equations governing voltage evolution along the NLTL, as illustrated in Fig. 3.1, has been extensively detailed in Refs. [50, 183].

For the sake of clarity and completeness, we summarize here the main steps leading to the demonstration that nonlinear wave propagation in the NLTL, under the long-wavelength approximation, is governed by the KdV equation. While Newton's law (as used in Chapter 1) is replaced by Kirchhoff's laws, the

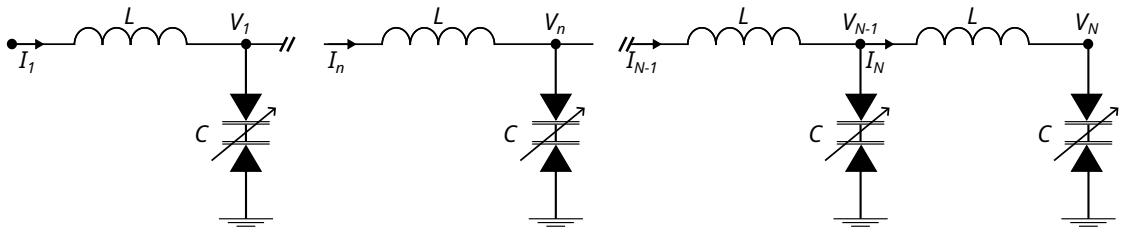

Figure 3.1: Schematic representation of a NLTL of N identical cells, each being composed of an inductor L and a varicap diode with a voltage-dependent capacitance $C(V_n)$. The voltage measured at each capacitance $n = 1,\ldots,N$ is denoted V_n.

derivation of the KdV equation remains analogous. The nodal equations for the voltages and currents in the circuit depicted in Fig. 3.1 are given by:

$$V_{n-1} - V_n = L\frac{\partial I_n}{\partial t} \tag{3.1}$$

$$V_n - V_{n+1} = L\frac{\partial I_{n+1}}{\partial t} \tag{3.2}$$

$$I_n - I_{n+1} = \frac{\partial Q_n}{\partial t} \tag{3.3}$$

where Q_n is the charge stored in the n^{th} capacitor, which satisfies the relation $C_n(V_n) = \partial Q_n/\partial V_n$.

By combining Eqs. (3.1), (3.2), and (3.3), we obtain the dynamical equation showing that the charge of the n^{th} capacitance depends on the voltage at the n^{th} cell but also on the voltage at the neighbors LC cells:

$$L\frac{\partial^2 Q_n}{\partial t^2} = V_{n-1} + V_{n+1} - 2V_n \tag{3.4}$$

For low voltages, the capacitance can be approximated by a linear expansion in voltage:

$$C(V_n) = C_0(1 - 2bV_n), \tag{3.5}$$

which modifies Eq. (3.4) into:

$$LC_0\frac{\partial}{\partial t}\left((1 - 2bV_n)\frac{\partial V_n}{\partial t}\right) = V_{n-1} + V_{n+1} - 2V_n \tag{3.6}$$

When the voltage varies only slightly from one LC cell to the next, i.e., when the wavelength of the signal is large compared to the spacing between adjacent cells, the discrete network can be approximated as a continuous medium. This corresponds to the regime where the typical timescale of signal evolution is much longer than the natural resonance period of each individual oscillator, given by $\sqrt{LC_0}$. In this limit, we follow the same procedure as for the mechanical chain (see Chap. 1), which we briefly recall here for consistency.

In the continuum limit, we replace the discrete voltage variable $V_n(t)$ by a continuous function $V(n,t)$ and perform a Taylor expansion around n:

$$V_{n\pm1} = V \pm \frac{\partial V}{\partial n} + \frac{1}{2!}\frac{\partial^2 V}{\partial n^2} \pm \frac{1}{3!}\frac{\partial^3 V}{\partial n^3} + \frac{1}{4!}\frac{\partial^4 V}{\partial n^4} \pm \dots \tag{3.7}$$

Equation 3.6 transforms into:

$$\underbrace{\frac{\partial^2 V(n,t)}{\partial t^2} - \frac{1}{LC_0}\frac{\partial^2 V(n,t)}{\partial n^2}}_{\text{Linear propagation operator}} = \overbrace{b\frac{\partial^2 [V(n,t)]^2}^{\text{Nonlinear term}}}{\partial t^2} + \underbrace{\frac{1}{12LC_0}\frac{\partial^4 V(n,t)}{\partial n^4}}_{\text{Linear dispersive term}} \tag{3.8}$$

The left-hand side of Eq. (3.8) represents a linear propagation operator, indicating that the wave can propagate freely in both directions (towards increasing or decreasing values of n). The linear dispersive term in the right hand side of Eq. (3.8) represents the leading-order dispersive term in the NLTL.

In soliton systems, there is a balance between dispersion and nonlinearity. To investigate this regime, we follow Ref. [183] and apply the reductive perturbation, introducing a small dimensionless parameter $\epsilon \ll 1$. The following change of variables is considered:

$$\begin{cases} \tilde{V} = \epsilon V, \\ \tilde{n} = \epsilon^{1/2}(n + (\epsilon - 1)v_0 t), \\ T = \epsilon^{3/2} t \end{cases} \tag{3.9}$$

For simplicity, we continue to denote the rescaled variables $\tilde{V}$, $\tilde{n}$, and T by

V, n, and T in the following. This transformation shifts the system of space-time coordinates from the laboratory reference frame (n,t) to a moving frame traveling at the fixed velocity $v_0 = 1/\sqrt{LC_0}$.

Substituting Eq. (3.9) into Eq. (3.8) and keeping only terms of order $O(\epsilon^3)$ yields:

$$2v_0^2\frac{\partial^2 V}{\partial n^2} + 2v_0\frac{\partial^2 V}{\partial n \partial T} + bv_0^2\frac{\partial^2 V^2}{\partial n^2} + \frac{v_0^2}{12}\frac{\partial^4 V}{\partial n^4} = 0 \tag{3.10}$$

By integrating once with respect to n Eq. (3.10), we obtain:

$$\frac{\partial V}{\partial T} + v_0\frac{\partial V}{\partial n} + bv_0 V\frac{\partial V}{\partial n} + \frac{v_0}{24}\frac{\partial^3 V}{\partial n^3} = 0 \tag{3.11}$$

Eq. (3.11) represents one possible form of the KdV equation but it is more convenient for our analysis to further modify it following the approach described in Ref. [184]. Dividing Eq. (3.11) by v_0 gives:

$$\frac{1}{v_0}V_T + V_n + bVV_n + \frac{1}{24}V_{nnn} = 0 \tag{3.12}$$

where the subscripts in Eq. (3.12) now denotes derivation with respect to either n or T.

At leading order, we assume the scaling relation (see Ref. [184]):

$$V_n \sim -\frac{1}{v_0}V_T \Rightarrow V_{nn} = \frac{1}{v_0^2}V_{TT}, \quad V_{nnn} = -\frac{1}{v_0^3}V_{TTT} \tag{3.13}$$

Applying this transformation, the equation governing the space-time evolution of the voltage along the LC oscillator chain reads:

$$\boxed{V_n + \frac{1}{v_0}V_T - \frac{b}{v_0}VV_T - \frac{1}{24v_0^3}V_{TTT} = 0} \tag{3.14}$$

where $V(n,T)$ represents a temporal distribution of voltage measured at a cell n. Finally, a last change of variables connects the KdV equation in the physical variables describing the NLTL to the KdV equation written in its canonical form. Introducing the following normalized space and time variables along with the

field $u(x,t)$ normalized against some arbitrary voltage V_0 :

$$\begin{cases} t = \frac{1}{3}\sqrt{b^3 V_0^3}\, n, \\ x = -2v_0\sqrt{bV_0}\left(T - \frac{n}{v_0}\right), \\ u = \frac{V}{V_0} \end{cases} \tag{3.15}$$

we obtain the canonical KdV equation:

$$u_t + 6uu_x + u_{xxx} = 0 \tag{3.16}$$

3.1.2 State of the art - Solitons in NLTL: A Historical Overview

Research into the properties of nonlinear transmission lines (NLTLs) began in the 1960s, with Rolf Landauer introducing the concept of NLTLs, building upon earlier studies by Cutler [185], Tien [186], and Cullen [187]. Initially, the goal was to achieve parametric amplification of electrical signals [188]. It was later shown that NLTLs are direct analogs of FPUT's nonlinear lattice [52]. The pioneering experiments on solitons in NLTLs were conducted by Hirota and Suzuki in 1973 [152]. Drawing on the analogy with the Toda lattice [189, 190], they demonstrated key features of soliton behavior in electrical NLTLs, such as head-on collisions, overtaking collisions, and soliton fission (the breaking of a broad pulse into a series of solitons, see Fig. 3.2).

Five years later, Nagashima and Amagishi [191] quantitatively verified the theoretical predictions on soliton velocity, width, and interaction in such devices. Hirota and Suzuki, having incorrectly defined the capacitance dependence with voltage, were unable to quantitatively compare experimental results with theory at that time. In the same year, Jäger [192, 193] observed the FPUT recurrence phenomena of a sine wave in an NLTL, drawing an analogy with the KdV equation, a phenomenon already observed in 1970 by Hirota and Suzuki [194]. However, Jäger performed a quantitative validation of theoretical predictions, by measuring the recurrence length, for example.

In 1982, Jäger investigated the influence of dissipation and proposed the KdV-Burgers equation to model wave propagation in an NLTL, stating, "a KdV

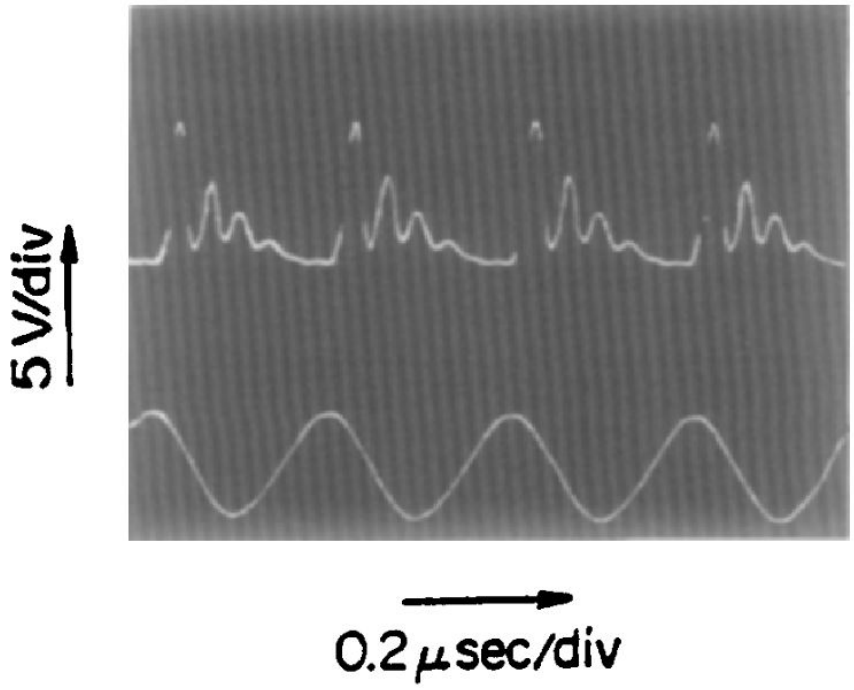

Figure 3.2: Oscillogram traces showing the decomposition of an a.c input of amplitude 4.2 V and frequency 1 MHz into solitons, figure extracted from [152]

system with small frequency-dependent losses is expected" [195]. Concurrently, Watanabe [196] studied soliton formation and propagation in an NLTL, focusing on an LC ladder with constant inductance and treating voltage as a Taylor series expansion around the DC bias voltage. He found that the use of a parallel capacitor deviated from the Toda lattice nonlinearity but confirmed the stable propagation of solitons.

In 1989, Tsuboi [197] examined soliton formation by studying the evolution of a rectangular pulse, observing initial steepening due to nonlinear effects, followed by a decrease and broadening during propagation, with the potential transformation into solitons if a balance between dispersion and nonlinearity was maintained. He also observed a position shift due to soliton collisions, as predicted by Hirota and Suzuki.

In 1995, Ramos [198] explored soliton propagation in NLTLs using perturbation methods, showing that solitons governed by the KdV equation could propagate along a nonlinear, lossless transmission line.

These studies have been extensively compiled in the book *Electrical Solitons* by David Ricketts and Donhee Ham [183], which presents the theory in detail. Additionally, Michel Remoissenet's book [50] provides further insights into the subject of soliton propagation in NLTLs.

3.2 Baseline Experiments in the NLTL: Single Soliton Propagation, Linear Propagation Regime, and Soliton Interactions

Since the 1970s, extensive studies on NLTLs have been conducted, featuring the propagation of a few solitons. Our current objective is to investigate the dynamics of large random ensembles of solitons. As a step towards this goal, we first examine fundamental nonlinear phenomena within our constructed NLTL, including the propagation of a single KdV soliton, the collision of two solitons, and the soliton fission process.

3.2.1 Experimental setup

The experiments presented here were conducted using a NLTL, as shown in Fig. 3.3(b)(c), fabricated by Hervé Damart, an electrical engineer at the PhLAM Lab. The NLTL is composed of a ladder network consisting of 160 lumped inductor-varactor sections, soldered onto a copper plate with dimensions $L \times H = 22 \times 10$ cm. Each inductance (KEMET SBCP-47HY150B) has a value of $L \sim 15$ μH, and each varactor (Varicap: NXP-BB201) exhibits a capacitance $C(V_n)$ that decreases as the voltage V_n applied across it increases (see Fig. 3.5).

The experimental setup for electrical wave generation consists of an Arbitrary Function Generator (AFG, Tektronix AFG31000) with a 100 MHz bandwidth and a 1 GSa/s sampling rate, connected to the NLTL (Fig. 3.3(a)). Voltage measurements across each varactor are performed using a low-capacitance probe (LCP, ~10 pF) and a 200 MHz oscilloscope (OSC, Tektronix TBS2204B) operating at 2 GSa/s. The probe is positioned across the varactor of each LC cell, allowing individual recordings of the local voltage dynamics. These recordings are then

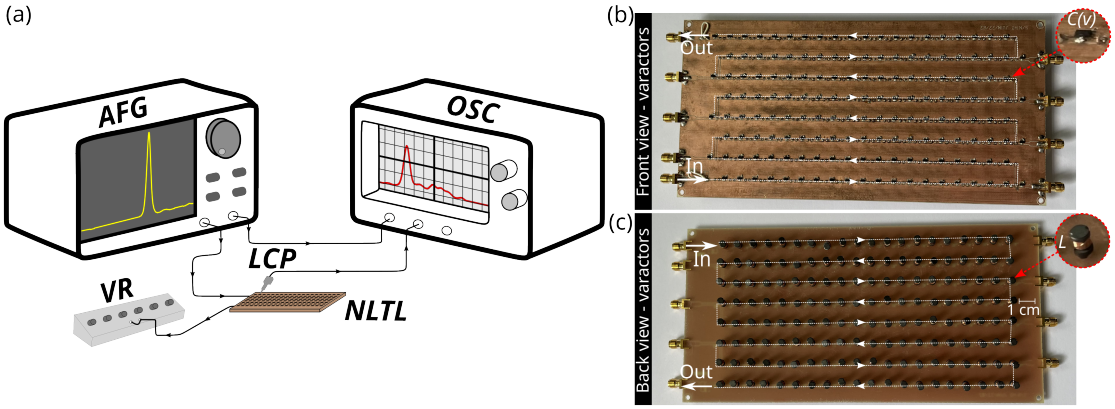

Figure 3.3: (a) Schematic representation of the experimental setup, including the NLTL, an arbitrary function generator (AFG), and a variable resistor (VR) for impedance matching at the output end of the NLTL. Voltage measurements are taken at each LC cell using a low-capacitance probe (LCP) connected to an oscilloscope (OSC). (b-c) Photographs of the two faces of the NLTL. One face (b) contains the varactors, while the other face (c) houses the inductors.

numerically stacked to reconstruct the full space-time diagram of wave propagation along the NLTL. Impedance matching at the NLTL output is achieved by connecting a variable resistor (VR) to the last LC cell to minimize wave reflections.

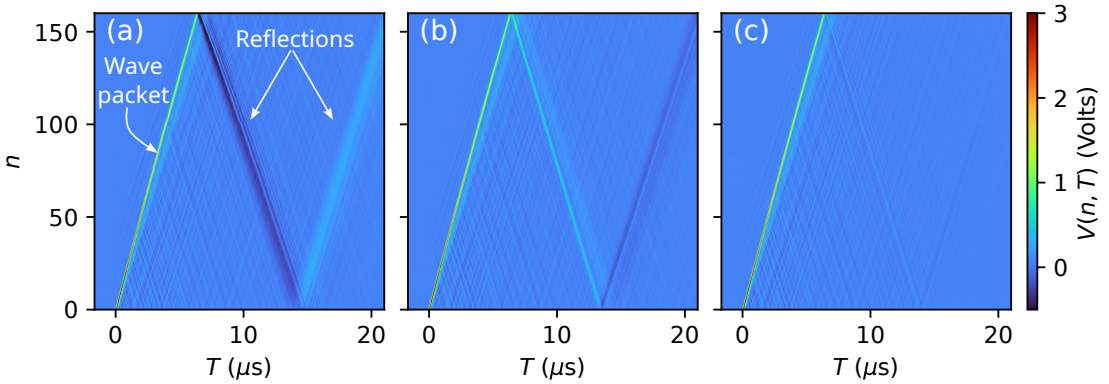

Figure 3.4: Propagation of an electric wave in the NLTL for various values of the load resistor R_0 placed at the last LC cell. (a) $R_0 \sim 0\ \Omega$. (b) $R_0 \sim 1.3\ \text{k}\Omega$. (c) Impedance matching is realized for $R_0 \sim 320\ \Omega$.

Fig. 3.4 shows that if the resistance value R_0 of the VR is not properly adjusted,

reflection phenomena are observed in the NLTL. Notably, when $R_0 \sim 0\ \Omega$, the reflection at the cell n=160 has a negative polarity ($V < 0$, see Fig. 3.4(a)), whereas for large values of R_0 ($R_0 \sim 1.3\ \mathrm{k}\Omega$), the reflection at the last cell ($n = 160$) has a positive polarity ($V > 0$, see Fig. 3.4(b)). The successive reflections resulting from the impedance mismatch cause the polarity to alternate after the first reflection. Optimal reflection minimization is achieved for a resistance value $R_0 = \sqrt{L/C_0} \sim 320\ \Omega$, as shown in Fig. 3.4(c) and discussed in Ref. [183, 199].

The varicap we are using is a low voltage variable capacitance double diode, which takes advantage of the properties of what is called a 'depletion layer', which is an insulating region that forms at the junction of a pn diode when a voltage is applied in the reverse direction [200]. The thickness of the depletion layer changes depending on the amount of reverse voltage applied. As the reverse voltage increases, the thickness of the depletion layer increases, which causes the capacitance to decrease. This is similar to what happens in a usual capacitor when you increase the distance between its two plates, the capacitance drops[1]. However, when the reverse voltage is reduced, the depletion layer becomes thinner and the capacitance increases [201]. Without further entering into the details of semiconductor physics, we present now the electrical characteristics of the varicap, especially how the capacitance evolves according to the applied voltage.

The measurement methods for capacitance $C(V_n)$ as a function of voltage V_n, as well as the determination of resistances R_C and R_L for the varactors and inductors, are detailed in the appendices (see Sec. 5.2). This paragraph focuses on presenting the obtained results. Fig. 3.5 shows the measured capacitance $C(V_n)$ as a function of the voltage V_n. We observe that the capacitance does not decrease strictly linearly over the entire voltage range. However, for positive voltages below approximately 3 V, the capacitance decreases approximately linearly. In this range, the experimental curve (solid black line) can be well approximated by the relation $C(V_n) = C_0(1 - 2bV_n)$, where $C_0 = 140$ pF and $b = 0.154\ \mathrm{V}^{-1}$, represented with the red dashed line. Finally and importantly, the

[1] For a parallel-plate capacitor, if we denote e as the distance between the two plates, S as the surface area of each plate, and $\varepsilon = \varepsilon_0 \times \varepsilon_r$ as the dielectric permittivity of the medium between the plates, then we can establish: $C \approx \frac{\varepsilon S}{e}$

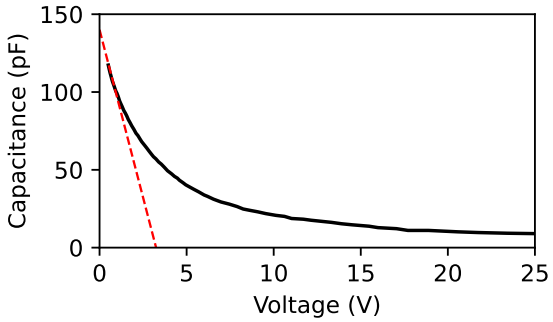

Figure 3.5: Voltage characteristic of the varicap used in the NLTL showing the evolution of the capacitance C as a function of the applied voltage. The characteristic is nearly linear for positive voltages below ~ 3 V. For this range of voltage, it can be approximated by $C(V_n) = C_0(1 - 2bV_n)$ with $C_0 = 140$ pF and $b = 0.154$ V^{-1}. The measurement method used to determine this characteristic is described in detail in Appendix 5.2.

varactors (resp. inductors) have a small but non-negligible resistances $R_C \sim 5$ Ω (resp. $R_L \sim 67$ mΩ). Once again, the interested reader will have more details about the electrical components and the measurement of their properties in Sec. 5.2.

3.2.2 A first experiment : propagation of a KdV soliton

Having established the theoretical foundations and reviewed previous experimental studies on solitons in nonlinear transmission lines, we now turn to our experimental investigation. The previous section (Sec. 3.1.1) demonstrated that, in the long-wavelength limit, wave propagation in the NLTL can be described at leading order by the KdV equation.

In this section, we present a baseline experiment focusing on the propagation of a KdV soliton in the NLTL. At leading order, the soliton's propagation is well-described by the KdV equation in physical variables, Eq. (3.14), as established in prior works [50, 183]. The analytical expression below corresponds to a one-soliton solution of Eq. (3.14), written in terms of physical variables [183]:

$$V(n,T) = A\,\mathrm{sech}^2\left(\sqrt{2bA}\left(n - v_0\left(1 + \frac{bA}{3}\right)T\right)\right), \tag{3.17}$$

where A is the soliton amplitude, T denotes the physical time, and v_0 is given by $v_0 = 1/\sqrt{LC_0}$. The index n corresponds to the LC cell at which the voltage is measured.

A soliton waveform, defined by Eq. (3.17), is generated using the AFG and injected into the NLTL via coaxial. The propagation of the soliton along the NLTL is shown in Fig. 3.6(a) and (b). The measured initial amplitude is approximately $A \sim 95$ mV.

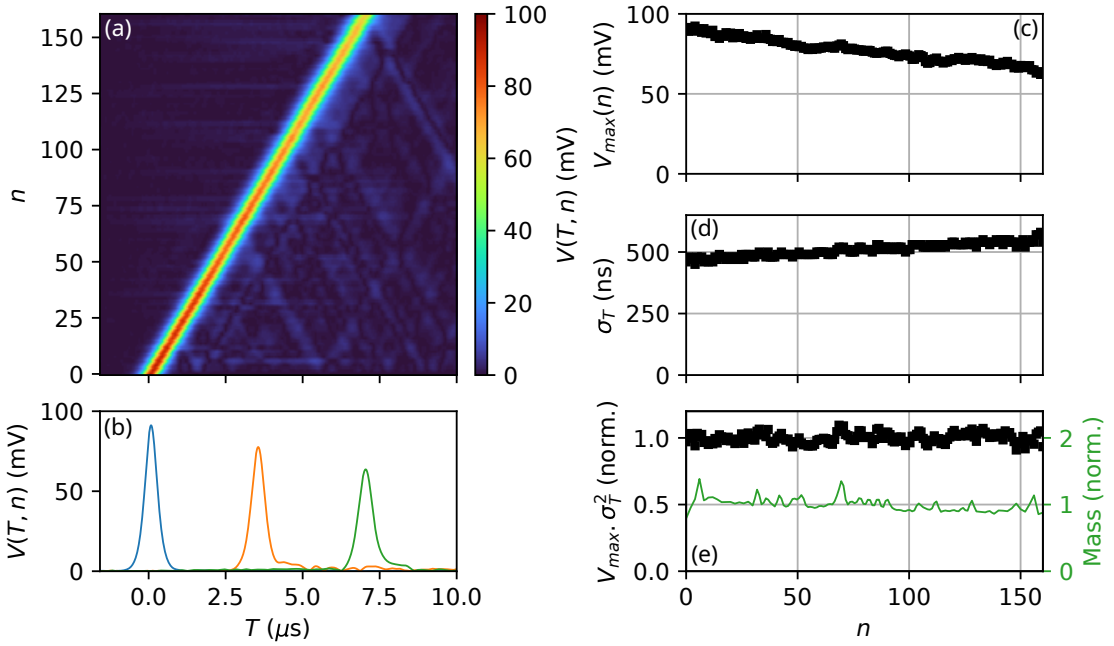

Figure 3.6: Spatio-temporal evolution of one single soliton in our electrical line. (a) Space-time diagram where n denotes the index of the LC cells along the transmission line (with $n = 0,\ldots,160$). (b) Voltage signals measured at different positions along the line: $n = 0$ (blue), $n = 80$ (orange), and $n = 160$ (green) (c) Evolution of the amplitude of the soliton along the line. (d) Evolution of the width of the soliton along the line. (e) Evolution of the product of the amplitude and the width squared of the soliton along the line. In green solid line the mass is also shown.

Figures 3.6(a) and (b) show that we do not observe exactly a soliton as defined by Eq. (3.17). Especially as shown in Figs. 3.6(a)(b), and (c), the peak amplitude of the propagating soliton, denoted $V_{\max}$, decreases slightly as it propagates. However, as illustrated in Fig. 3.6(d), the soliton width σ_T, directly measured

as the full width at half maximum, simultaneously increases, ensuring that the product $V_{\max} \cdot \sigma_T^2$ remains constant, as confirmed in Fig. 3.6(e)[2].

Figure 3.6 shows that the propagation of a soliton in our NLTL is not exactly described by KdV, as the initial soliton is not fully conserved during its evolution. Higher-order effects perturb the KdV dynamics, causing deviations from the ideal soliton behavior described by Eq. (3.17). Those effects will be even more visible considering other experiments at longer propagation time, as here the associated normalized time (defined by Eq. (3.15)) being short, $t \sim 0.1$. Nevertheless, the product $V_{\max} \cdot \sigma_T^2$ is conserved, indicating that while the soliton undergoes changes, it remains a soliton, albeit not the same as the initial one, thus not evolving according to Eq. (3.17). This phenomenon is referred to as an adiabatic evolution of the soliton. Further characterization of the non-integrable features, or dissipation effects, will be discussed later.

Although we are dealing with nonlinear objects, the 2D Fourier spectrum proves to be a useful tool for observing how the energy is distributed throughout the experimental scales [22, 34]. The 2D Fourier spectrum provides a spectrogram of the energy, which can be computed over the entire field by taking the squared modulus of the space-and-time Fourier transform $E(k, \omega)$ of $V(n, T)$, given by:

$$E(k, \omega) = \iint V(n, T) e^{i(\omega T - kn)} \, \mathrm{d}n \, \mathrm{d}T \tag{3.19}$$

The linear dispersion relation associated with Eq. (3.11) is given by:

$$\omega = \pm k v_0 \left(1 - \frac{k^2}{24}\right), \tag{3.20}$$

as obtained by inserting plane-wave solutions $V(n, T) \sim e^{i(kn - \omega T)}$ into the lin-

[2]We can easily verify that the single-soliton solution of the KdV equation, given by

$$u(x) = \frac{c}{2} \operatorname{sech}^2\left(\frac{\sqrt{c}}{2} x\right), \tag{3.18}$$

where c is a constant related to the soliton amplitude, indeed satisfies this conservation law. The product of the soliton amplitude $\frac{c}{2}$ and the squared soliton width $\left(\frac{2}{\sqrt{c}}\right)^2$ is equal to 2, confirming the expected relationship.

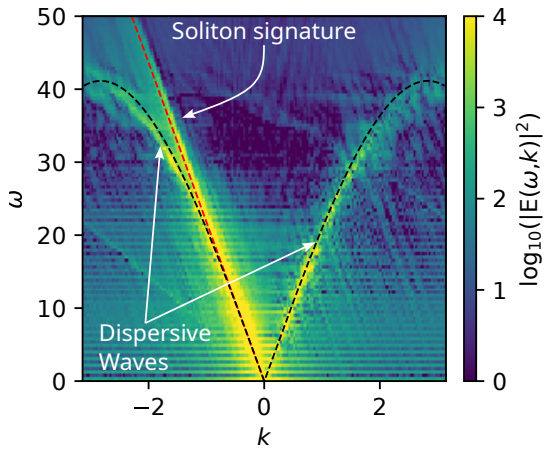

Figure 3.7: 2D Fourier transform (Eq. (3.19)) associated to the space-time diagram Fig. 3.6(a). The black dashed lines correspond to dispersion relation Eq. (3.20), and red dashed line represents the linear long wave phase velocity $-kv_0$.

earized version of the equation (3.11).

Figure 3.7 shows the two-dimensional Fourier spectrum, Eq. (3.19), of the spatio-temporal evolution of the single soliton observed in Fig. 3.6(a). For $\omega > 0$, negative wave numbers $k < 0$ correspond to small-amplitude waves propagating forward along the chain (increasing cell index n), while positive wave numbers $k > 0$ correspond to backward-propagating (reflected) waves. The energy associated with each Fourier mode is encoded in the color scale (in logarithmic scale).

The energy in Fig. 3.7 is predominantly located along a straight line, confirming that all frequency components of the soliton propagate at the same speed $v = |\omega/k| > v_0$, where v_0 is the linear long-wave phase velocity (highlighted in the red dashed line). A small part of the energy is located in the spectral domain around lines given by Eq. (3.20).

The curves corresponding to the linear dispersion relation are shown as black dashed lines in Fig. 3.7. The energy distributed around the dispersion relation arises from the presence of dispersive waves. These waves can originate from various sources, such as imperfections in the initial condition, inhomogeneities between the cells, or dissipative effects. In particular, the linear waves observed

for $k > 0$ likely result from partial reflections at the end of the line or from multiple small reflections caused by structural inhomogeneities (non-identical cells).

To sum up

We experimentally investigate the propagation of a KdV soliton in our constructed NLTL. A single KdV soliton, generated by an AFG, is injected into the NLTL, and its spatio-temporal evolution is recorded. While the soliton's propagation is primarily governed by the KdV equation, deviations from the ideal integrable behavior are observed. Although the soliton's amplitude decreases slightly with propagation distance, its width increases concomitantly, maintaining a near-constant product of amplitude and squared width. This adiabatic evolution indicates that the propagating structure remains a soliton, albeit with evolving parameters. A 2D Fourier analysis reveals that a significant part of the energy is concentrated along a line with a slope corresponding to the soliton velocity. A small part of the energy is located around the linear dispersion relation, corresponding to dispersive radiations.

3.2.3 Study of the linear propagation regime

The simplest experiment consisting in propagating a single soliton in our NLTL reveals to the presence of dissipative effects. In order to characterize the dissipation in the system in a more quantitative way, we propose now to investigate the linear propagtion regime in the NLTL. This regime is obtained for waves of small initial amplitudes, typically $V \ll 50$ mV, for which the varactors behave as linear components ($C(V_n) \sim C_0$). In this section, we illustrate this regime by examining the propagation in the NLTL of a small-amplitude Gaussian pulse.

3.2.3.1 Experiment : Propagation of a Small Amplitude Gaussian Pulse

Figure 3.8 presents the experimental evolution of a single short Gaussian pulse propagating through the NLTL in the linear regime. The initial pulse has a peak amplitude of approximately 17 mV and a duration of approximately 130 ns

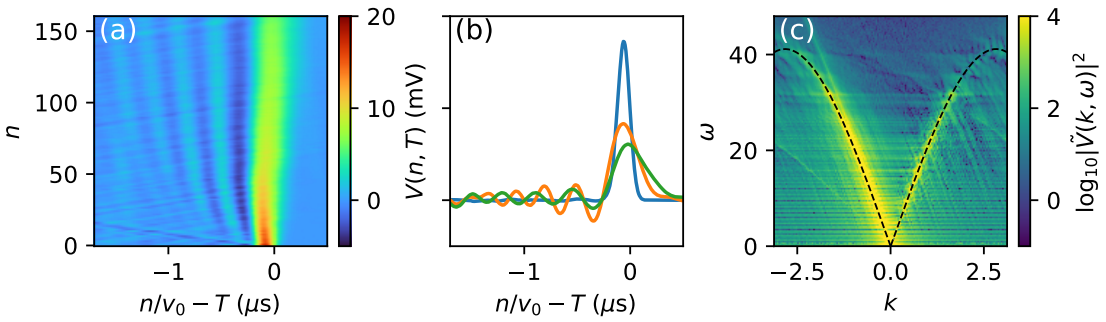

Figure 3.8: (a) Propagation of a Gaussian pulse with a duration of ∼130 ns and an amplitude of ∼17 mV in the NLTL, resulting in an oscillatory linear wave. (b) Waveforms recorded at $n = 0$ (bleu line), $n = 80$ (orange line), and $n = 160$ (green line). (c) Two-dimensional Fourier transform (Eq. (3.19)) of the space-time plot shown in (a). The energy is concentrated around the NLTL's linear dispersion relation (Eq. (3.20)), which is indicated by the black dashed lines.

(see the blue line in Fig. 3.8(b)). Contrary to Fig. 3.6, the space-time evolution recorded in this experiment does not provide evidence of the formation of a soliton in the NLTL. Instead, an asymmetric oscillatory structure with small amplitude develops near one edge of the pulse during propagation, as highlighted by the orange and green lines in Fig. 3.8(b). The 2D Fourier power spectrum of the space-time plot (Fig. 3.8(c)) shows that most of the wave power is concentrated near the linear dispersion relation of the NLTL (Eq. (3.20)), which is overlaid as black dashed lines. These features show that linear propagation of the short gaussian pulse is predominantly driven by third-order dispersive effects, see Refs. [29, 53, 202].

Figure 3.9(a) displays the temporal Fourier spectra of the voltage measured along the NLTL, from cell $n = 0$ to $n = 160$. For each cell, we compute the 1d Fourier transform of the temporal signal $V(T, n)$, defined as

$$\tilde{V}(\omega, n) = \int_{-\infty}^{\infty} V(T, n)\, e^{-i\omega T} \mathrm{d}T,$$

It reveals spectral narrowing that occurs in the linear regime. Figure 3.9(c) illustrates the evolution of the frequency spectrum width, represented by the sigma parameter obtained from Gaussian fits $\exp(-\omega^2/2\sigma^2)$ of the spectra. The ob-

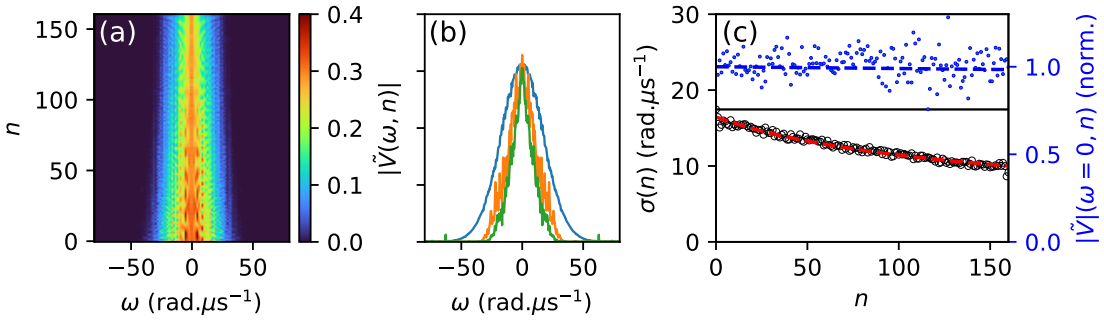

Figure 3.9: (a) Temporal Fourier spectra of the voltage measured along the NLTL, from cell $n = 0$ to $n = 160$. (b) Fourier spectra at three representative positions: $n = 0$ (blue), $n = 80$ (orange), and $n = 160$ (green). (c) Evolution of the spectral width $\sigma(\omega)$ (black circles) along the NLTL. The black solid line shows the expected evolution of $\sigma(\omega)$ in the case of linearized KdV dynamics (pure dispersion). The red dashed line is a fit using Eq. (3.31), with $R_C \sim 6.2\ \Omega$ as the fitting parameter. The blue dashed line represents the exponential decay $\exp(-R_L n/2Lv_0)$, associated with the DC component of the Fourier spectrum (blue points), using the measured value $R_L \sim 67\ \text{m}\Omega$. This contribution remains negligible in the observed dynamics.

served decrease in sigma with propagation distance is associated with a spectral narrowing that is inconsistent with the linearized KdV equation (or third-order dispersion alone), which predicts a constant sigma, as shown by the black solid line. This spectral narrowing cannot be explained by third-order dispersion; it is solely a consequence of dissipation in the NLTL.

3.2.3.2 Modelization of the Dissipative Effects

The observations in Figs. 3.6 and 3.9 indicate the presence of higher-order dissipative effects during soliton propagation. These effects originate from the intrinsic resistive components of the circuit: R_C, the series resistance associated with the varicap diode, and R_L, the resistance of the inductor. To incorporate these dissipative effects into our description, we adopt an extended model of the NLTL presented in Sec. 3.1.1 that includes these resistive elements explicitly (see Fig. 3.10), following the approach of Ref. [183].

For clarity and completeness, we outline the derivation of the equations governing the wave evolution in the NLTL in the presence of dissipation arising from

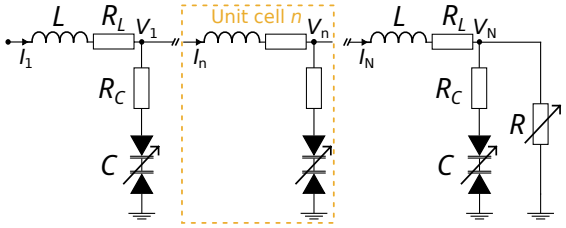

Figure 3.10: Schematic representation of the NLTL, composed of a ladder network with 160 lumped inductor-varactor sections. The varactors (resp. inductors) have a small but non-negligible series resistance of $R_C \sim 5\ \Omega$ (resp. $R_L \sim 67$ mΩ).

the series resistance R_C and R_L. For the NLTL depicted in Fig. 3.10, incorporating the resistors R_C and R_L, Kirchhoff's laws are modified as follows [183]:

$$I_n - I_{n+1} = \frac{\partial Q(V_n)}{\partial t}, \tag{3.21}$$

$$L\frac{\partial I_n}{\partial t} + R_L I_n = \left[V_{n-1} + R_C \frac{\partial Q(V_{n-1})}{\partial t}\right] - \left[V_n + R_C \frac{\partial Q(V_n)}{\partial t}\right], \tag{3.22}$$

$$L\frac{\partial I_{n+1}}{\partial t} + R_L I_{n+1} = \left[V_n + R_C \frac{\partial Q(V_n)}{\partial t}\right] - \left[V_{n+1} + R_C \frac{\partial Q(V_{n+1})}{\partial t}\right]. \tag{3.23}$$

Combining Eqs. (3.21), (3.22), and (3.23), we obtain:

$$L\frac{\partial^2 Q(V_n)}{\partial t^2} + R_L \frac{\partial Q(V_n)}{\partial t} = V_{n-1} + V_{n+1} - 2V_n + R_C \frac{\partial}{\partial t}\left[Q(V_{n+1}) + Q(V_{n-1}) - 2Q(V_n)\right]. \tag{3.24}$$

Following the same procedure as in the case where $R_C = R_L = 0$ (see Sec. 3.1.1), we derive the following equation describing nonlinear wave propagation in the NLTL in physical variables:

$$V_n + \frac{1}{v_0} V_T - \frac{b}{v_0} V V_T - \frac{1}{24 v_0^3} V_{TTT} - \frac{R_C}{2L v_0^3} V_{TT} - \frac{R_L}{2L v_0} V = 0. \tag{3.25}$$

Compared to the lossless case described by Eq. (3.14), Eq. (3.25) includes two additional terms: a dissipative term proportional to V_{TT}, arising from the resistance R_C of the varicap, and a linear damping term proportional to V, associated with the resistance R_L of the inductor.

Finally, introducing the normalized space and time variables, along with the normalized field $u(x,t)$ defined in Eq. (3.15), we obtain the following dissipation-driven KdV equation:

$$u_t + 6uu_x + u_{xxx} = \beta u_{xx} + \delta u, \tag{3.26}$$

where $\beta = 6R_C/(Lv_0\sqrt{bV_0})$ and $\delta = 3R_L/(2Lv_0\sqrt{b^3V_0^3})$, with V_0 being the normalization voltage. The varactor resistance R_C is associated to the diffusion term βu_{xx}, whereas the inductor resistance R_L leads to the damping term δu. Neglecting the damping term ($\delta = 0$) transforms this equation into the KdV-Burgers (KdVB) equation [203], while neglecting the diffusion term ($\beta u_{xx} = 0$) yields the Damped-KdV (DKdV) equation. Numerical simulations of both equations will be conducted to compare with our experimental results.

We observe that the diffusion coefficient β depends on both R_C, which is fixed and measured (see Appendix), and V_0. Consequently, this coefficient is not constant across all experiments. In experiments with a peak voltage of ~ 1.5 V, the diffusion coefficient is $\beta \sim 0.2$, whereas experiments with a peak voltage of ~ 4 V have a diffusion coefficient of $\beta \sim 0.1$.

In the linear regime ($b \sim 0$), Eq. (3.25) becomes fully linear and simplifies to:

$$V_n - \frac{1}{24v_0^3}V_{TTT} - \frac{R_C}{2Lv_0^3}V_{TT} - \frac{R_L}{2Lv_0}V = 0. \tag{3.27}$$

Being linear, Eq. (3.27) can be readily analyzed using a Fourier transform approach. Fourier transforming Eq. (3.27) with respect to T yields:

$$\tilde{V}_n(\omega) = \left(-i\frac{\omega^3}{24v_0^3} - \frac{R_C\omega^2}{2Lv_0^3} - \frac{R_L}{2Lv_0}\right)\tilde{V}. \tag{3.28}$$

The modulus of the solution, $|\tilde{V}(n,\omega)|$, is then given by:

$$|\tilde{V}(n,\omega)| = |\tilde{V}_0(\omega)|\exp\left(-\frac{R_C\omega^2 n}{2Lv_0^3}\right)\exp\left(-\frac{R_L n}{2Lv_0}\right). \tag{3.29}$$

The first exponential term with a ω^2 is associated with diffusion. It acts as

low-pass filter that attenuates Fourier components of high frequencies. On the other hand the second exponential term is associated with damping. It does not have any frequency dependence and is only responsible for the same exponential decay of the weight of all Fourier components (see Fig. 3.9(c) blue dashed line).

As a first approximation, neglecting the damping effect and considering $|\tilde{V}_0(\omega)|$ as the Fourier transform of the initial Gaussian pulse, we have:

$$|\tilde{V}(n,\omega)| = |\tilde{V}_0| \exp\left(-\frac{\omega^2}{2\sigma_0^2}\right) \exp\left(-\frac{R_C \omega^2 n}{2L v_0^3}\right). \tag{3.30}$$

This implies that during propagation, the Gaussian spectrum in the linear regime remains Gaussian, but with a width decreasing as:

$$\sigma(n) = \sqrt{\frac{1}{\frac{1}{\sigma_0^2} + \frac{R_C n}{L v_0^3}}}. \tag{3.31}$$

The red dashed line in Fig. 3.9(c) shows a fit of the experimental data (black points) using the diffusive broadening law given by Eq. (3.31). This fit yields a value $R_C \simeq 6.2\ \Omega$, in very good agreement with the independent value obtained through direct electrical characterization of the varicap, as detailed in Appendix 5.2. This agreement demonstrates that the observed temporal broadening of the Gaussian pulse in the linear regime is well captured by a simple dissipative model, and validates the expression of the diffusion coefficient derived from Eq. (3.27).

The blue dashed line in Fig. 3.9(c) shows the exponential decay of the DC component ($\omega = 0$) of the Fourier spectrum (blue points), following the law $\exp(-R_L n/2L v_0)$, where $R_L \simeq 67\ \text{m}\Omega$ is the value obtained from a direct 4-wire measurement of the inductive resistance. This decay is extremely slow. The consistency of both R_C and R_L with independently measured values further supports the validity of the dissipation-driven KdV model in describing wave propagation in the NLTL.

To sum up

The dissipative nature of the NLTL is investigated by analyzing the linear propagation regime. A small-amplitude Gaussian pulse is injected into the line, and its evolution is observed. Unlike in the nonlinear regime, linear propagation does not lead to soliton formation; instead, an oscillatory wave structure is observed. The 2D Fourier spectrum confirms that the dynamics are dominated by linear dispersion. A progressive narrowing of the frequency spectrum is also observed during propagation, a behavior that cannot be explained by dispersion alone. This spectral narrowing results from dissipative effects, which are modeled by incorporating resistances R_C and R_L into the equivalent circuit of the NLTL. The resulting model leads to a dissipation-driven KdV equation, where dissipation manifests both as damping (from R_L) and diffusion (from R_C). In the linear regime, the model predicts that the spectral envelope remains Gaussian, with a width that decreases with propagation distance. This narrowing allows us to extract, and quantify the strength, of the effective diffusion coefficient in the NLTL.

3.2.4 Collision of solitons and soliton fission in weakly dissipative regime

Having characterized the higher-order linear effects by examining the linear propagation regime, we now turn our attention to the nonlinear regime. This investigation will clarify the nonlinear nature of wave propagation in our NLTL, with the goal of propagating a SG, a highly nonlinear object. In this section, we present experiments investigating the overtaking collision of solitons and the fission of solitons from a square-shaped pulse. Our experimental results are compared with numerical simulations of the dissipation-driven KdV equation (3.26). In order to compare those results with numerical simulations, the results will be normalized using Eqs. (3.15) as illustrated in Fig. 3.11.

Figure 3.11 shows a space-time diagram recorded in the experiment (left column), together with the same diagram converted to dimensionless units (right

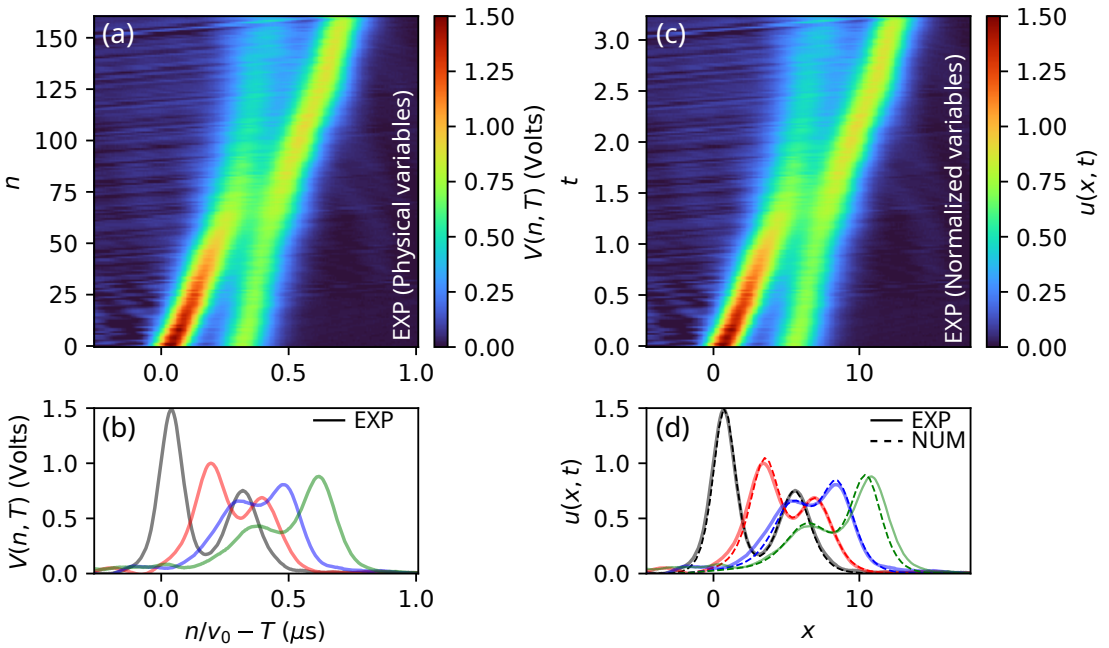

Figure 3.11: Experimental observation of an overtaking collision between two solitons in the NLTL. (a) Space-time plot of the collision (physical units). (b) Waveforms recorded at different cells: $n = 0$ (black), $n = 45$ (red), $n = 78$ (blue), and $n = 123$ (green). (c), (d) Same as (a), (b) but using normalized units. The dashed colored lines correspond to signals obtained from numerical simulations of the dissipation-driven KdV equation (Eq. (3.26)) with $\beta = 0.2$ and $\delta \sim 3\times10^{-3}$.

column) using the transformations defined in Eq. (3.15). In this mapping, the physical time T becomes the dimensionless spatial variable x, and the evolution variable t is related to the cell index n. The experiment shown corresponds to an initial condition consisting of two separated KdV solitons, with spectral parameters $\eta_1 \sim 0.87$ and $\eta_2 \sim 0.61$. Since the soliton velocity scales with η^2, the taller soliton (associated with η_1) propagates faster and eventually overtakes the smaller one (associated with η_2).

During this overtaking collision, we observe the influence of higher-order effects. Most notably, the largest soliton undergoes a significant amplitude decrease after the interaction, which cannot be captured by the integrable KdV equation. To account for these effects, we numerically simulate the dissipation-driven KdV equation, Eq. (3.26), using the same initial condition, with parameters $\beta = 0.2$ and $\delta \sim 3\times10^{-3}$. The results of this simulation are superimposed

on Fig. 3.11(d) as dashed colored lines, and show very good agreement with the experimental data.

Figure 3.11 reveals that the soliton collision is accompanied by a spatial shift: the larger soliton advances compared to its position without interaction, while the smaller soliton recedes. According to the theoretical prediction from Eq. (1.10), the expected shifts are $\Delta(\eta_2, \eta_1) \sim 2.85$ for the small soliton and $\Delta(\eta_1, \eta_2) \sim 2$ for the large one. From the experimental data, direct measurement of the shifts, obtained by fitting the soliton trajectories before and after the interaction, yields $\Delta'(\eta_2, \eta_1) \sim 3.06$ and $\Delta'(\eta_1, \eta_2) \sim 2.5$, respectively. These values are in reasonable agreement with the theoretical ones, despite slight discrepancies. The observed deviations are attributed to dissipation, which alters the amplitudes and velocities of the solitons during propagation. Consequently, the collision is inelastic, indicating energy exchange between the solitons (see Fig. 3.11(d)).

Another important experiment to consider is the soliton fission process, first observed by Zabusky and Kruskal [51] in numerical simulations. This phenomenon has been extensively studied, both experimentally and numerically (see for example, Refs. [151, 152, 194, 204]). In KdV systems, initial profiles of large spatial extent, such as sine waves, Gaussian pulses, or square waves will, after a certain propagation distance, decompose into a rank-ordered train of solitons with increasing amplitudes. Here, we investigate soliton fission using a square-shaped pulse as the initial condition.

Figure 3.12 presents the experimental observation of a square-shaped pulse undergoing fission into a train of four distinct solitons in the NLTL. This figure demonstrates the necessity of including diffusion, rather than just linear damping, in the model to achieve good quantitative agreement between experiment and numerical simulation. As shown in Figs. 3.12(b)-(e), the KdVB equation provides a much better match to the experimental data than the DKdV equation (Figs. 3.12(f)-(i)).

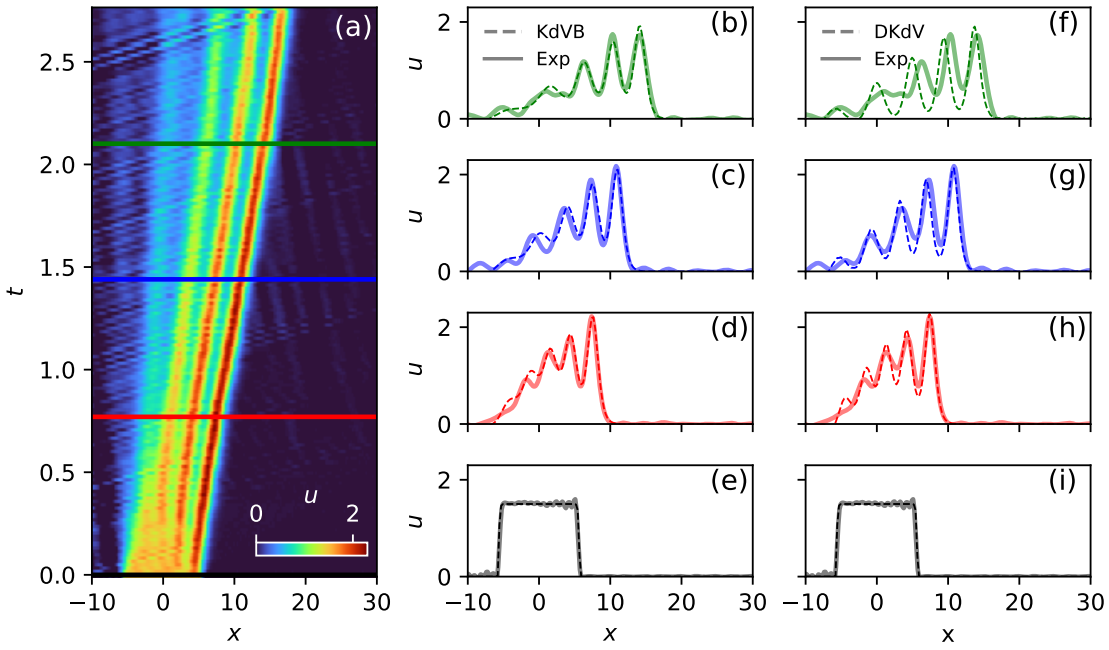

Figure 3.12: Space-time evolution of a small square-shaped pulse propagating in the NLTL. (a) Experimental space-time diagram. (b–e) Normalized voltage waveforms at successive times ($t \sim 0$ in black, $t \sim 0.77$ in red, $t \sim 1.45$ in blue, and $t \sim 2.10$ in green): experimental data (solid lines) are compared with numerical simulations of the KdVB equation with parameters $\beta \sim 0.2$, $\delta \sim 0$ (dashed lines). (f–i) Same experimental data (solid lines), now compared with simulations of the DKdV equation with parameters $\beta \sim 0$, $\delta \sim 0.15$ (dashed lines).

To sum up

The nonlinear propagation regime in the NLTL is explored, focusing on soliton collisions and soliton fission. Experimental results are presented in normalized units, facilitating comparison with numerical simulations of the dissipation-driven KdV equation. An overtaking collision of two KdV solitons demonstrates the inelastic nature of the interaction due to the presence of dissipation, with energy exchange and position shifts observed. Furthermore, the fission of a square pulse into a train of solitons is experimentally observed. It is shown that the KdV-Burgers equation, incorporating a diffusion term, provides significantly better agreement with the experimental data. This highlights the importance of the diffusion term, associated with the varactor resistance, in accurately modeling the nonlinear dynamics of the NLTL.

3.3 Nonadiabatic evolution of a single soliton in the NLTL

3.3.1 Experiment

The previous results enabled us to identify and quantify the weak dissipative effects arising from the intrinsic resistances of the circuit components. In this section, we present an experiment involving the propagation of a high-amplitude soliton ($V_0 \sim 3$ V). The higher voltage allows for a significantly longer normalized evolution time. For comparison, the earlier experiment shown in Fig. 3.6, based on a soliton of 100 mV peak amplitude, corresponded to a short evolution time of $t \sim 0.1$ (as given by Eq. (3.15)). In contrast, the increased amplitude used here results in an effective propagation time of $t \sim 17$ over the same NLTL length (160 cells), thereby revealing non-adiabatic features in the single soliton dynamics.

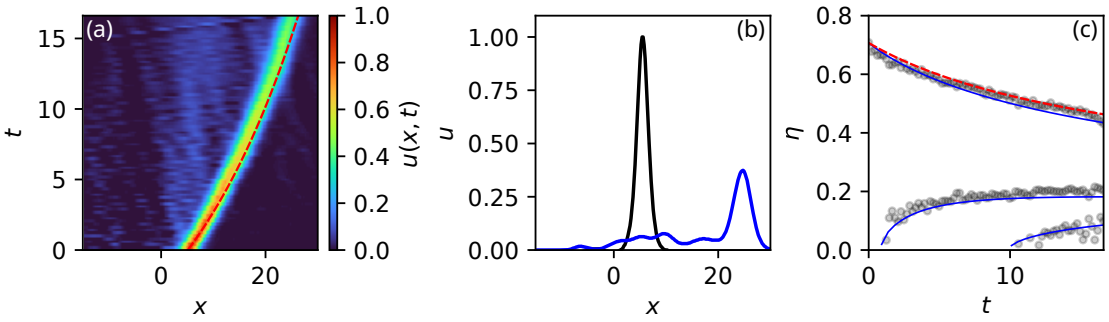

Figure 3.13: Normalized evolution of a single soliton in the NLTL. (a) Space-time evolution of the soliton, showing the formation of a shelf. The red dashed line corresponds to the model prediction (Eq. (3.37)). (b) Normalized waveforms at $t = 0$ (black line) and $t \sim 16.61$ (blue line). (c) Evolution of the discrete eigenvalues. Black points represent computed discrete eigenvalues of the experiment, the blue solid line shows discrete eigenvalues from KdVB numerical simulations using experimental parameters $\eta_0 \sim 0.7$ and $\beta \sim 0.1$, and the red dashed line corresponds to the model prediction, Eq. (3.33).

Figure 3.13 illustrates the normalized evolution of a single soliton propagating along the NLTL. As shown in Fig. 3.13(a) and (b), the soliton's amplitude and velocity, determined from the initial condition, gradually decrease during

propagation. This slow evolution of the solitary wave is accompanied by the formation of a trailing shelf (see Fig. 3.13(b)).

As discussed in Chapter 1, the integrable dynamics of the KdV equation is associated with an isospectral property: the eigenvalues obtained from the spectral problem of the KdV equation (i.e., the linear Schrödinger equation, Eq. (1.25)) for a soliton remain invariant with respect to the evolution variable t. However, the nonlinear spectral analysis of the field $u(x,t)$ measured in Fig. 3.13(a) reveals a gradual decay of the discrete eigenvalue associated with the initial condition, while two new discrete eigenvalues emerge during shelf formation, as shown by the black points in Fig. 3.13(c). This behavior indicates a non-isospectral evolution, characteristic of the non-integrable nature of the experimental dynamics. Furthermore, the creation of these two new discrete eigenvalues exemplifies a non-adiabatic process that cannot be described by perturbative IST theory [205–207]. Numerical simulations of the KdVB equation with the same initial condition show excellent agreement between the experimental results (black points) and the simulations (blue lines) in Fig. 3.13(c).

3.3.2 Modeling the Non-Adiabatic Features

The experiment reveals that the soliton dynamics deviate from the adiabatic regime. Instead of only undergoing a slow decay in amplitude and a corresponding increase in width, as expected for an adiabatic evolution, the soliton generates a shelf behind it, and new eigenvalues (associated with secondary solitons) emerge during propagation.

To gain insight into this non-adiabatic behavior, we turn to a simple toy model previously studied in the literature (e.g., Refs. [208, 209]), based on an analogy with shallow-water waves propagating over a slowly varying bottom topography. Despite its simplicity, this model successfully captures key aspects of the observed dynamics, including the continuous decrease of the soliton amplitude (i.e., of the associated spectral eigenvalue) and the resulting curvature of the soliton trajectory in the space-time diagram.

3.3.2.1 Approximating the space-time trajectory of the soliton

A first approximation is to assume that the soliton evolves adiabatically, meaning that it maintains its soliton-shape throughout the propagation. In this regime, the soliton retains the sech^2 profile given by $2\eta_1^2\mathrm{sech}^2(\eta_1 x)$, while its amplitude (and thus the associated eigenvalue η_1) may vary slowly with time. Under this assumption, one can estimate the evolution of $\eta_1(t)$ by considering the temporal decay of conserved quantities such as the momentum $P = \int u^2 \,\mathrm{d}x$ in the KdVB framework (see Ref. [183]),

$$\frac{\partial P}{\partial t} = \frac{\partial}{\partial t}\int_{-\infty}^{\infty} u^2 \mathrm{d}x = \int_{-\infty}^{\infty} 2\beta u u_{xx} \mathrm{d}x \tag{3.32}$$

We can show by replacing u by the soliton formula in the two sides of Eq. (3.32) (see Ref. [183]) that:

$$\boxed{\eta_1(t) = \eta_1(0)\sqrt{\frac{1}{1+\frac{16}{15}\eta_1^2(0)\beta t}}}. \tag{3.33}$$

This prediction is shown as the red dashed line in Fig. 3.13(c), using $\beta \sim 0.1$ and matches very well the experimental decay. From Eq. (3.33), we can express $\eta_1(0)$ as:

$$\eta_1(0) = \frac{\sqrt{15}\eta_1(t)}{\sqrt{15 - 16\eta_1^2(t)\beta t}}. \tag{3.34}$$

Assuming that the soliton's position at any time t is given by $x(t) = \int 4\eta_1^2(t)\mathrm{d}t$, we can write:

$$x(t) = \int 4\eta_1^2(0)\frac{\mathrm{d}t}{1+\frac{16}{15}\eta_1^2(0)\beta t}. \tag{3.35}$$

The integral in Eq. (3.35) can be easily calculated, yielding :

$$x(t) = \frac{60}{16\beta}\ln\left(1+\frac{16}{15}\eta_1^2(0)\beta t\right). \tag{3.36}$$

Substituting the expression for $\eta_1(0)$ (Eq. (3.34)), we obtain:

$$\boxed{x(t) = \frac{60}{16\beta} \ln\left(1 + \frac{16\eta_1^2(t)\beta t}{15 - 16\eta_1^2(t)\beta t}\right)}. \tag{3.37}$$

This trajectory is shown as the red dashed line in Fig. 3.13(a) and it matches very well the experimental trajectory of the soliton.

3.3.2.2 Finding the discrete eigenvalues associated to the formation of the shelf

Further extending the previous approach, we now present a simple model to describe the creation of discrete eigenvalues observed in Fig. 3.13(c). As discussed in Ref. [210], this phenomenon is linked to the emergence of a trailing shelf behind the soliton. We begin by modeling this shelf using a simple square pulse. As illustrated in Fig. 3.14(a), the numerical solution of the KdV-Burgers equation (black line) for a fundamental soliton initial condition displays a long, nearly flat trailing shelf at $t = 100$. This shelf can be approximated by a square pulse of constant amplitude q_0 and width $L_0(t)$, as shown by the red dashed line. The choice of a square pulse is particularly convenient, as the associated eigenvalue problem is exactly solvable [211]:

$$\cosh(p_n L_0) = \frac{i(\eta_n^2 - p_n^2)}{2\eta_n p_n} \sinh(p_n L_0), \tag{3.38}$$

where q_0 represents the height of the box, determined a posteriori as the mean amplitude of the developed shelf, L_0 is its width, and $p_n = \sqrt{-\eta_n^2 - q_0^2}$. Assuming that the width of the shelf evolves in time as $L_0(t) = \int 4\eta_1^2(t)\mathrm{d}t$, where $4\eta_1^2(t)$ represents the time-varying velocity of the soliton, we can use the computed value of $L_0(t)$ at each time to estimate the created eigenvalues η_n. This is a simplified model, as the actual shelf is not a perfect box but rather a structure with a slowly modulated amplitude (see Fig. 3.14(a)).

As shown in Fig. 3.14(b), the results from the box model (colored points), obtained by numerically solving the transcendental equation (3.38) associated

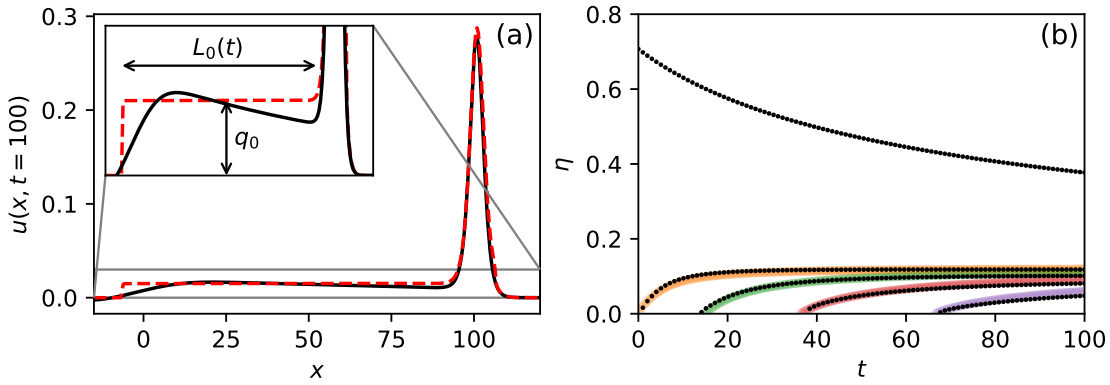

Figure 3.14: Illustration of the shelf model. (a) Comparison of the model solution (red dashed line) at $t = 100$ with the numerical solution of the KdV-Burgers equation (Eq. (3.26), with $\delta = 0$ and $\beta = 0.05$) (black line) for a fundamental soliton initial condition with $\eta_1 = 0.707$. (b) Comparison of the evolution of eigenvalues obtained from the field (black dots) with those predicted by the box model for the shelf, using $q_0 = 0.015$ (colored points).

with the square-shaped pulse, agree well with the discrete eigenvalues extracted from the numerical simulation of the KdVB equation (black points) for a single soliton. Similar models for extended KdV equation have previously been considered by Grimshaw et al., see Ref. [212].

3.3.2.3 Analytical predictions of soliton formation: IST perturbation theory

In their review article from 1989, Kivshar and Malomed (see Ref. [207]), noted that, *'in general the problem of the creation of solitons under the action of a perturbation is not amenable to solution by existing analytical methods. In terms of IST perturbation theory, the reason can be explained as follows. The birth of a new soliton purports the appearance of a new zero of the forward scattering amplitude $a(\lambda)$ at some (generally speaking, complex) value λ_0 of the spectral parameter λ [...] It proves that, in the vicinity of the point λ_0, the effective parameter of a perturbative expansion is not simply ϵ, but rather ϵ/λ, in the case of a perturbed KdV equation [...] Thus at $\lambda \to \lambda_0$ an effective perturbative parameter becomes large, and perturbation theory becomes irrelevant. Due to these difficulties, the generation of new solitons is often studied by means of numerical methods'*.

However, J. Wright (see Ref. [206]), using theoretical IST calculations (for

$\beta \to 0$ in Eq. (3.26)), developed predictions for the short-time evolution of both the initial eigenvalue and the first eigenvalue created in the perturbed KdV evolution (secondary soliton). To the best of our knowledge, this work is unique in providing analytical predictions for the eigenvalue evolutions based on IST theory for KdVB. The basic idea is to track how the discrete spectrum of the Lax operator deforms under a weak diffusive perturbation, and in particular how this perturbation analytically modifies the scattering data $a(\lambda)$ and $b(\lambda)$. He noticed that for small perturbation, new zeros of $a(\lambda)$ could appear, signifying the appearance of a new soliton. Importantly secondary solitons production seems to be crucial to understand conservation laws in perturbed systems. However we noticed that his analytical predictions are not completely correct as they do not match with our numerical simulations. We indeed noticed that he was considering the wrong formula for the evolution of a KdV soliton momentum in presence of diffusion [183] (Eq. (3.32)).

3.3.3 Physical interpretation of the mechanisms behind the non-adiabatic features

While the models based on shelf modeling or perturbed IST provide some insight into the features presented in Fig. 3.13, they do not fully explain the physical mechanisms behind eigenvalue creation, even though they correctly link the creation of the discrete eigenvalues to the emergence of the shelf. We now seek a more physical interpretation of this non-adiabatic phenomenon. The excitation of continuous spectrum radiation has been previously suggested [205, 213] to explain the creation of new eigenvalues in the context of solitary wave propagation in shallow water with slowly varying depth. Here, we present numerical simulations of the KdV-Burgers equation (Eq. (3.39)), detailing the long-time evolution of a solitary wave, to synthesize and illustrate the observed non-adiabatic features. We recall the KdVB equation as,

$$u_t + 6uu_x + u_{xxx} = \beta u_{xx} \tag{3.39}$$

The mass M of the field $u(x,t)$ is defined as,

$$M = \int_{-\infty}^{+\infty} u(x,t)\mathrm{d}x \tag{3.40}$$

The mass M is a conserved quantity both in KdV and in KdVB equations, i.e $\mathrm{d}M/\mathrm{d}t = 0$. The momentum is defined as,

$$P = \int_{-\infty}^{+\infty} u^2(x,t)\mathrm{d}x \tag{3.41}$$

The momentum P is a conserved quantity in KdV equation, i.e $\mathrm{d}P/\mathrm{d}t = 0$, but is not a conserved quantity in KdVB equation. For the KdVB equation, it is easy to show that,

$$\frac{\mathrm{d}P}{\mathrm{d}t} = 2\beta \int_{-\infty}^{+\infty} u u_{xx}\mathrm{d}x = -2\beta \int_{-\infty}^{+\infty} [u_x(x,t)]^2\mathrm{d}x \tag{3.42}$$

which means that the rate at which this quantity decays is determined by the gradient u_x of the field in space. The energy is defined as,

$$E = \int_{-\infty}^{+\infty} \left(u^3(x,t) - \frac{[u_x(x,t)]^2}{2} \right) \mathrm{d}x \tag{3.43}$$

The energy is a conserved quantity in KdV but not in KdVB. In the IST formalism, the mass M and the momentum P have the following expressions,

$$M = \underbrace{4\sum_k \eta_k}_{M_d} + \underbrace{\frac{1}{\pi}\int_{-\infty}^{+\infty} \log\left(1 - \frac{|b(\xi)|^2}{|a(\xi)|^2}\right)\mathrm{d}\xi}_{M_{\mathrm{CS}}} \tag{3.44}$$

$$P = \frac{16}{3}\sum_k \eta_k^3 - \frac{4}{\pi}\int_{-\infty}^{+\infty} \xi^2 \log\left(1 - \frac{|b(\xi)|^2}{|a(\xi)|^2}\right)\mathrm{d}\xi \tag{3.45}$$

where η_k are the discrete eigenvalues that can be computed by solving Eq. (1.25) for the potential $u(x,t)$. $\rho(\xi) = b(\xi)/a(\xi)$ is the reflection coefficient defined in the IST theory (see e.g. Refs. [29, 205, 206, 213]). In Eq. (3.44) (resp. Eq. (3.45)), the discrete summation over the η_k (resp. η_k^3) is related to the discrete part of the spectrum. On the other hand the integral term in Eq. (3.44) (resp. 3.45) rep-

resents the contribution to the mass (resp. to the momentum) of the continuous part of the spectrum that is associated with the radiative modes.

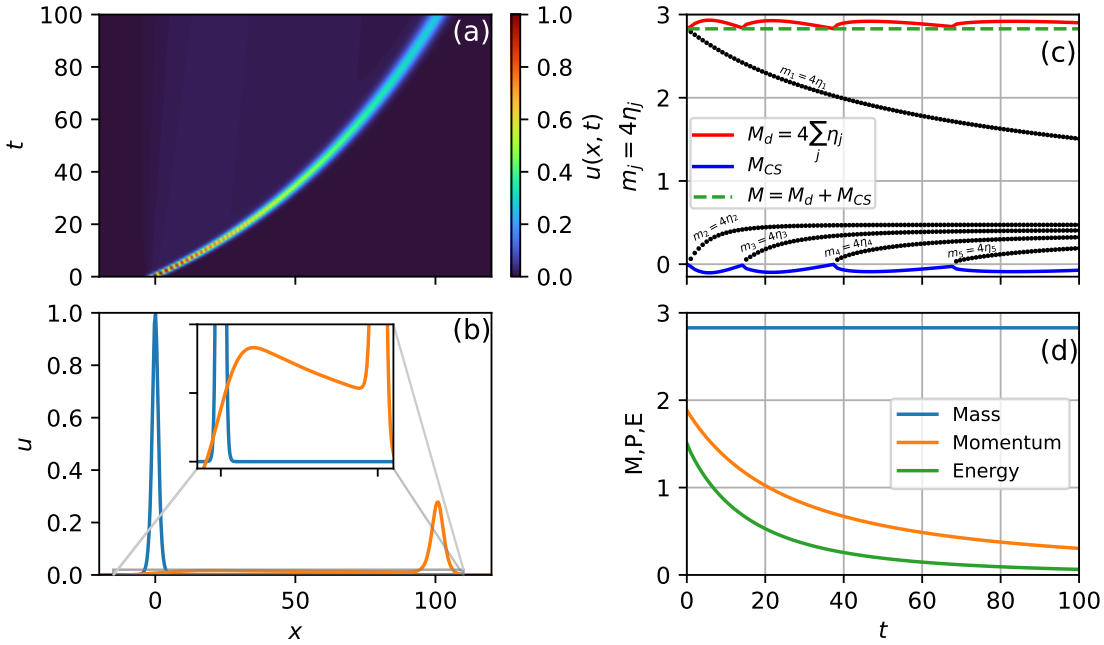

Figure 3.15: (a) Space-time dynamics from a numerical simulation of the KdVB equation (Eq. (3.39), with $\beta = 0.05$) for a fundamental soliton initial condition with $\eta_1 = 0.707$. (b) Waveforms at $t = 0$ and $t = 100$, with an inset showing a zoom of the formed shelf. (c) Time evolution of the discrete masses, defined as $m_j = 4\eta_j$ (black points), and the total discrete mass $M_\mathrm{d} = 4\sum_j \eta_j$ (red solid line). The mass of the continuous spectrum M_CS is shown in blue. The dashed green line represents the total mass, defined as $M = \int u(x,t)\mathrm{d}x$.

The figure 3.15 shows a numerical simulation of the KdVB equation (Eq. (3.39) with $\beta = 0.05$) for an initial condition being under the form of a soliton given by $u(x, t = 0) = 2\eta_1^2 \mathrm{sech}^2(\eta_1 x)$ with $\eta_1 = 0.707$, like in the experiment shown in Fig. 3.13, but for a much longer evolution time ($t = 100$) compared to the experimental case ($t \sim 17$). As already observed previously, the presence of diffusion described by the term on the right-hand side of Eq. (3.39) induces a slow decay in the soliton's amplitude and a gradual decrease in its velocity, as illustrated in Fig. 3.15(a)(b). This evolution is accompanied by the formation of a shelf behind the solitary wave as highlighted by the inset in Fig. 3.15(b). Fig. 3.15(d) shows the conservation of the mass M during the evolution while

the momentum P and the energy E decrease over time.

Fig. 3.15(c) shows that the amplitude η_1 of the discrete eigenvalue linked to the initial condition gradually decays over time, while 4 new discrete eigenvalues are created during the shelf formation. It shows the evolution of the masses $m_i = 4\eta_i$ of each of the 4 discrete eigenmodes, see Eq. (3.44). Of course the discrete masses $m_i(t) = 4\eta_i(t)$ $(i = 1 - 5)$ follow the same time evolution as the discrete eigenvalues $\eta_i(t)$. The interesting point is that the sum of the discrete masses $M_d(t) = \sum_{i=1}^{5} 4\eta_i(t)$ is not constant but slightly fluctuates above the constant value of the total mass $M = \int u(x,t)\mathrm{d}x$, see red solid line in Fig. 3.15(c).

The decay in time of η_1 is associated to a decrease in mass, which must be compensated by an increase to preserve the fact that the total mass $M = \int u(x,t)\mathrm{d}x$ must be conserved [207]. The missing mass is provided by the generation of the new discrete eigenvalue η_2. However the decay of $\eta_1(t)$ and the growing of $\eta_2(t)$ can never be balanced in such an exact way that the mass associated with these two discrete eigenvalues is constant in time : $m_{1,2}(t) = m_1(t) + m_2(t) = 4(\eta_1(t) + \eta_2(t)) \neq$ cte. For the total mass conservation condition $\mathrm{d}M/\mathrm{d}t = 0$ to be fulfilled, there is no choice but for the mass M_{CS} associated with the radiative modes to fluctuate in the same way as M_d but with an opposite sign ($M_{\mathrm{CS}} = \frac{1}{\pi}\int_{-\infty}^{+\infty} \log\left(1 - \frac{|b(\xi)|^2}{|a(\xi)|^2}\right)\mathrm{d}\xi$). This is illustrated in Figure 3.15(c) in blue solid line, which shows that the negative mass fluctuations of the continuous spectrum exactly compensate for the positive fluctuations of the discrete mass M_d, so that the total mass $M = M_d + M_{\mathrm{CS}}$ is constant over time (see Fig. 3.15(c) green dashed line).

Connecting this to our box model, we can interpret this as follows: the soliton loses mass, which is transferred to the continuous spectrum, forming the shelf. When the shelf accumulates sufficient mass (or, equivalently, the soliton loses enough mass), a new eigenvalue is created. As the soliton propagates further, it continues to lose mass, leading to the creation of more eigenvalues. Note that the time between eigenvalue creation events increases with evolution time.

To sum up

The long-term, non-adiabatic evolution of a single soliton in the NLTL is investigated. Experiments reveal that the soliton's amplitude and velocity decrease with propagation distance, accompanied by the formation of a trailing shelf. Nonlinear spectral analysis demonstrates a non-isospectral evolution, with the initial soliton eigenvalue decaying and new eigenvalues emerging, indicative of non-adiabatic dynamics. A simple model, based on the adiabatic evolution of the soliton eigenvalue, provides a good description of the eigenvalue decay and soliton trajectory. Furthermore, a box-shaped pulse model for the shelf allows for estimation of the newly created discrete eigenvalues, showing reasonable agreement with numerical simulations. Numerical simulations of KdVB reveal that the soliton transfer mass to the continuous spectrum, forming the shelf. When the shelf accumulates sufficient mass, new eigenvalues are generated. This process repeats, with subsequent discrete eigenvalue creation events occurring at longer intervals.

3.4 Soliton gas propagation in the NLTL

Here, we present the results of propagating a dense KdV soliton gas, synthesized from 200 uniformely distributed eigenvalues between $\eta = 0.2$ and 0.6, through our NLTL. The soliton gas was generated using the method described in Chapter 1, based on the Darboux recursive scheme operating on the eigenfunctions (see Refs. [122, 127–129, 214]). As previously demonstrated, our electrical line exhibits non-integrable dynamics with linear diffusion being a non-negligible effect. This raises the question of how the dynamics and statistical properties of the SG are affected by these higher-order effects in our NLTL. Specifically, how do the non-adiabatic effects, observed for the single soliton, manifest in a dense SG?

3.4.1 Experimental dynamics of a KdV soliton gas

The position parameters x_{0k} (connected to the so-called norming constants) of the solitons in the Darboux transform are randomly and uniformly distributed over the interval [-25, 25]. The resulting wavefield resembles a random oscillatory field, where individual solitons cannot be distinguished as sech-shaped pulses due to the dense nature of the SG (see Fig. 3.16(a)).

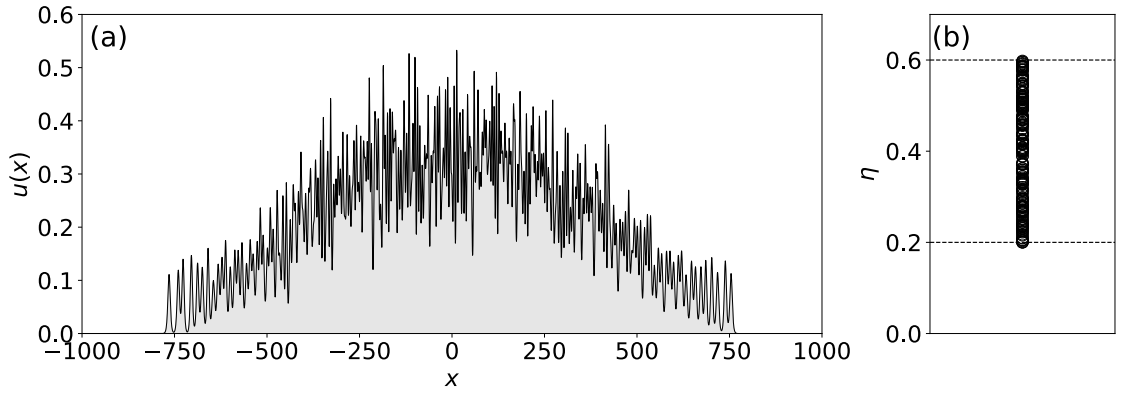

Figure 3.16: (a) Dense SG synthesized using the Darboux transform from an ensemble of 200 eigenvalues randomly and uniformly distributed between 0.2 and 0.6. (b) Associated discrete eigenvalues represented by black circles.

The wavefield shown in Fig. 3.16(a) serves as the initial condition for our NLTL experiments.

Figure 3.17 shows the long-time propagation ($t \sim 420$) of our synthesized soliton gas in the NLTL. This long propagation was obtained by performing six successive "passes" through the 160-cell NLTL, each time reinjecting the output signal as the input for the next pass. Over such long evolution times, the effects of dissipation, primarily due to the finite resistance of the inductors, become significant. As shown in Fig. 3.17(a), we observe a total mass loss of approximately 16% between $t = 0$ and $t \sim 420$. As discussed in previous sections, the small series resistance of the varactors is responsible for diffusion in the NLTL and for the fact that the dynamics is governed by the dissipation-driven KdV equation (Eq. (3.26)). In our experiment with the SG, $V_0 \sim 7.79$ V , which implies that the diffusion coefficient is $\beta \sim 0.1$. We observe that this weak dissipation prevents the dense SG from evolving into a diluted state with

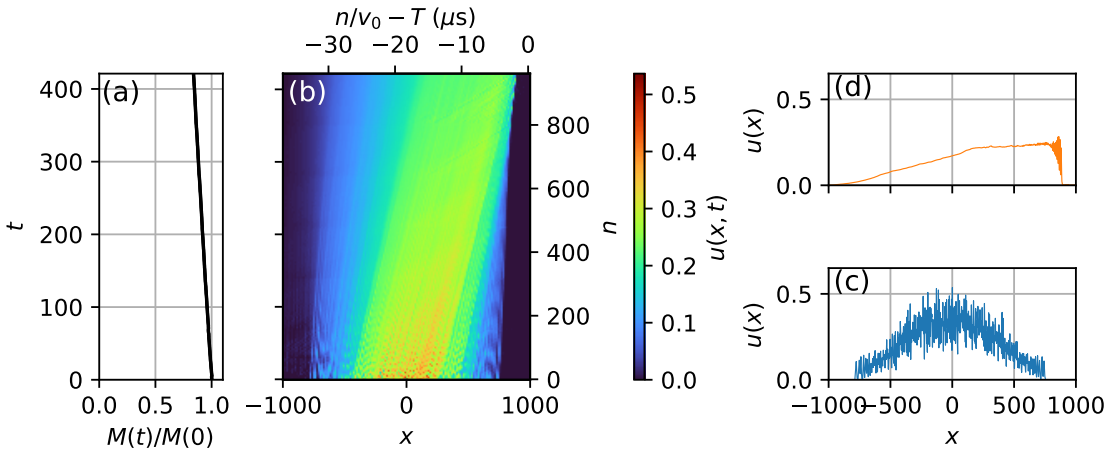

Figure 3.17: (a) Evolution of the SG mass $M(t)$ during propagation along 960 LC cells with small damping $\delta \sim 6.3 \times 10^{-4}$. (b) Space-time plot of the dense SG propagation in the NLTL (normalized and physical units). The secondary (right) vertical axis shows the cell index. The secondary (upper) horizontal axis shows the physical time. (c) Initial condition at $t = 0$, $n = 0$. (d) Normalized field measured at $n = 960$, or equivalently, $t \sim 420$.

separated individual solitons. Instead, a broad, smooth wavefield with a coherent oscillatory structure emerges at long evolution times ($t \sim 420$, Fig. 3.17(d)).

To assess the role of damping in the long-time evolution of the soliton gas, we conducted a new experiment in which the total mass $M(t)$ was kept approximately constant by slightly amplifying the signal before reinjection at each pass through the NLTL. Practically, this compensation is implemented by adjusting the amplitude of the signal measured at the last cell, so that the reinjected waveform has the same mass as the initial one. This procedure effectively cancels the mean effect of linear damping, although it introduces small periodic oscillations in the mass, as seen in Fig. 3.18(a). The resulting compensated propagation is shown in Fig. 3.18(b), and can be directly compared with the uncompensated case in Fig. 3.17.

The resulting wavefield at $t \sim 420$ (Fig. 3.18(d)) is remarkably similar to the uncompensated case (Fig. 3.17(d)), exhibiting the formation of a broad, smooth wavefield. This similarity suggests that damping does not significantly influence the formation of the observed structure. The formation of the broad smooth wavepacket is primarily driven by diffusion

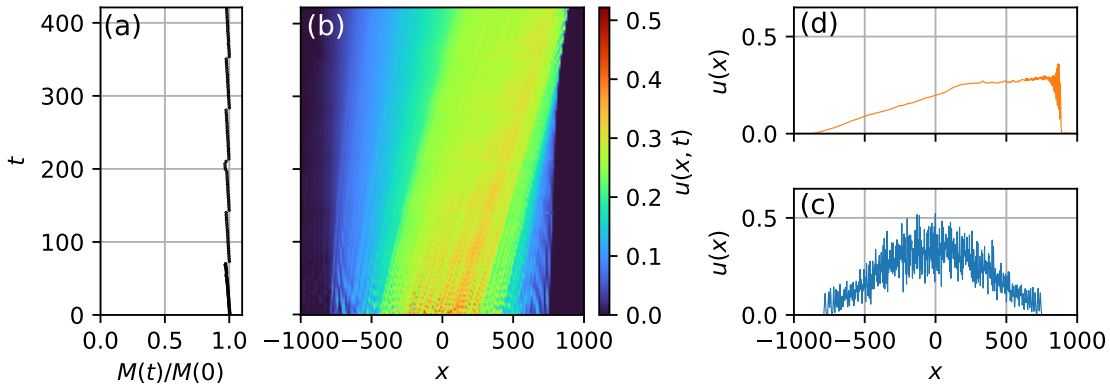

Figure 3.18: (a) Evolution of the SG mass $M(t)$ during propagation along 960 LC cells with periodic loss compensation ($\delta \sim 0$). (b) Space-time plot of the dense SG propagation in the NLTL (normalized units). (c) Initial condition at $t = 0$, $n = 0$. (d) Normalized field measured at $n = 960$, or equivalently, $t \sim 420$.

We observed that the wavefield obtained experimentally exhibits characteristics of a diffusive dispersive shock wave (DDSW), as identified in Refs. [215, 216]. DDSWs can be understood as modifications of dispersive shock waves (DSWs), which arise as solutions to Riemann problems in dispersive hydrodynamics, replacing classical shock waves with expanding oscillatory structures.

The features observed in our experiment with the SG drastically differ from those would be observed if the dynamics were integrable, i.e., without dissipation ($\delta = \beta = 0$). In the integrable case, the dense SG would evolve into a rank-ordered, expanding soliton train, with the solitons being ordered from slowest to fastest (see Refs. [142, 217]), as illustrated in Fig. 3.19(c).

Figure 3.19 presents a numerical simulation of the KdV equation, using the synthesized dense SG as the initial condition (see Fig. 3.19(b)). The space-time diagram in Fig. 3.19(a) demonstrates that the solitons separate at long evolution times (see Fig. 3.19(c)). The inset in Fig. 3.19(a) reveals that the small (i.e., slow) solitons, initially localized on the right of the wavefield, are overtaken by the larger solitons during evolution. Consequently, these small solitons appear to move backwards, exhibiting negative effective velocities. This phenomenon is known as the "backflow" effect (see Ref. [128]). The SG dilutes as the solitons separate due to their differing velocities. At long times, each soliton follows a ballistic trajectory of the form $x_k(t) \sim 4\eta_k^2 t + \tilde{x}_{0k}$, where $\tilde{x}_{0k}$ denotes the effective

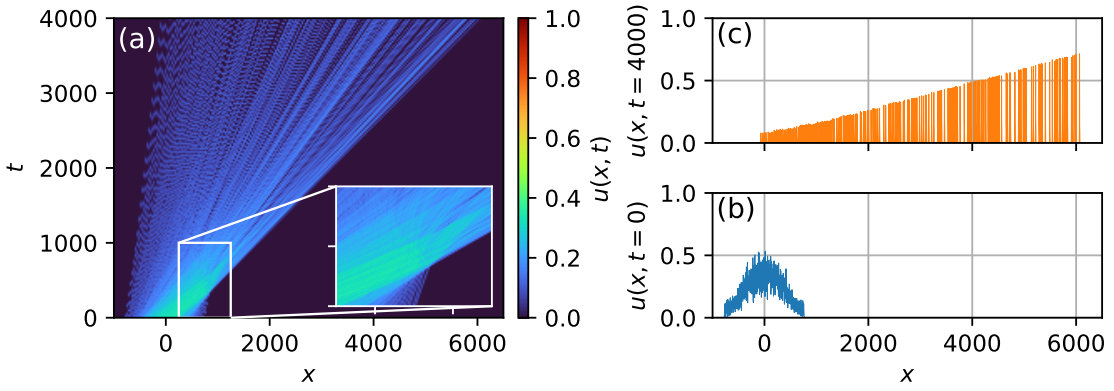

Figure 3.19: KdV dynamics. (a) Space-time plot of the dense SG propagation in a numerical simulation of the KdV equation. (b) Wavefield of the dense SG considered as the initial condition for the numerical simulation. (c) Wavefield at $t = 4000$, showing the separation of solitons within the SG.

initial position, which differs from the initial position used in the soliton gas synthesis.

3.4.2 Nonlinear spectral analysis

Now we use tools of nonlinear spectral analysis to get new insights into the formation of the broad smooth wavefield observed in our experiment. As previously discussed, the (IST) eigenvalue problem associated with the KdV equation is the linear, time-independent Schrödinger equation for an auxiliary function $\psi(x,t)$:

$$\psi_{xx} + (u(x,t) - \lambda)\,\psi = 0, \tag{3.46}$$

where the KdV field $u(x,t)$ acts as a potential, with t being treated as a parameter. For the fundamental soliton solution of the KdV equation, $u_k(x,t) = 2\eta_k^2 \mathrm{sech}^2\left[\eta_k(x - 4\eta_k^2 t - x_{0k})\right]$, Eq. (3.46) admits a single eigenmode, characterized by a real eigenvalue $\lambda_k = -\eta_k^2$ and the associated real eigenfunction $\psi_k(x,t) = \frac{\eta_k}{2}\mathrm{sech}^2(\eta_k(x - 4\eta_k^2 t - x_{0k}))$.

Now, we proceed to the nonlinear spectral analysis of the experimentally measured field $u(x,t)$ (shown in Fig. 3.18(b)) by solving numerically Eq. (3.46). First restricting the analysis to the eigenvalues parametrizing the SG, Fig. 3.20 shows the time evolution of the eigenvalues η_k that are computed numerically.

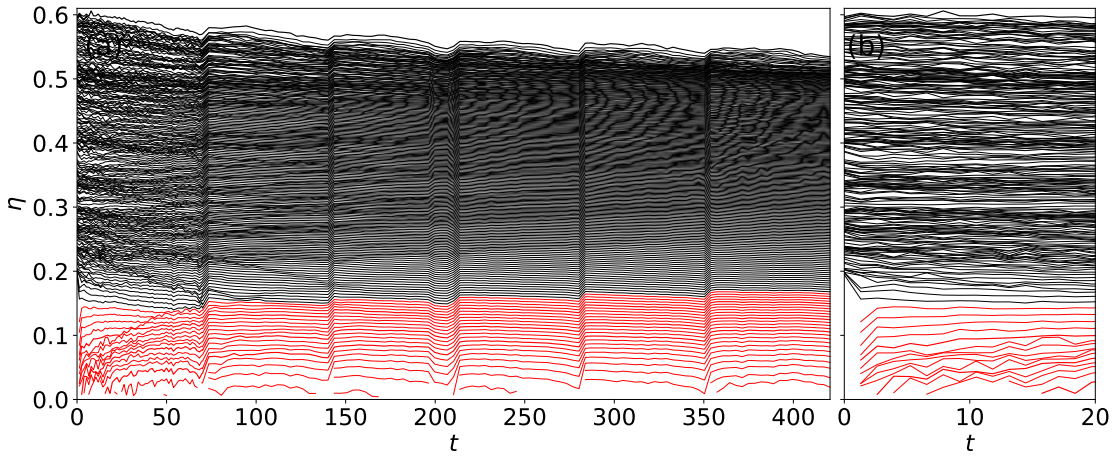

Figure 3.20: (a) Time evolution of the discrete eigenvalues measured during the evolution of the SG. The black flow corresponds to the initial 200 discrete eigenvalues and the red flow corresponds to the newly generated discrete eigenvalues arising from the excitation of the continuous spectrum. (b) Zoom-in between $t = 0$ and $t = 20$.

Figure 3.20 shows that, the measured eigenvalues distribute themselves along two distinct "flows". The first flow (black lines) corresponds to the eigenvalues associated with the initial SG, which slowly decay over time. The second flow (red lines) corresponds to newly formed discrete eigenvalues that progressively emerge during the evolution. The spectrum changes with new small eigenvalues emerging between $\eta = 0$ and 0.2, where there were initially no eigenvalues, as shown in Fig. 3.20(b). The mechanism for eigenvalue creation is the same as that described for the single soliton in the previous section, i.e, the excitation of the continuous spectrum not from only one soliton but this time from a large ensemble of random solitons.

The newly created discrete eigenvalues are associated with the generation of small-amplitude solitons, as a result, the total number of solitons within the SG, N, grows with time, as shown in Fig. 3.21. In our experiment, N increases from $N(t = 0) = 200$ (the number of eigenvalues specified when generating the SG) to $N(t = 420) = 225$. Numerical simulations of the KdVB equation (Eq. (3.39)) with the same initial condition and $\beta = 0.1$ reproduce the same evolution of N, as shown by the orange dashed curve in Fig. 3.21. Note the rapid initial growth of

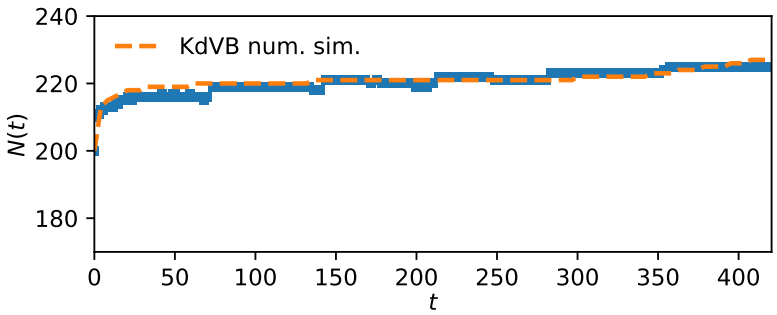

Figure 3.21: Total number $N(t)$ of discrete eigenvalues during evolution. Blue squares represent direct measurements from the experimental fields. The orange dashed line shows the result from a numerical simulation of the KdVB equation (Eq. (3.39) with $\beta = 0.1$).

N between $t = 0$ and $t = 10$, followed by a slower growth rate. This behavior can be understood by analogy with the single-soliton case. As the system evolves, mass is transferred from existing solitons to the continuous spectrum, and from the continuous spectrum to new eigenvalues, leading to the generation of new solitons, see Fig. 3.22(b)(d).

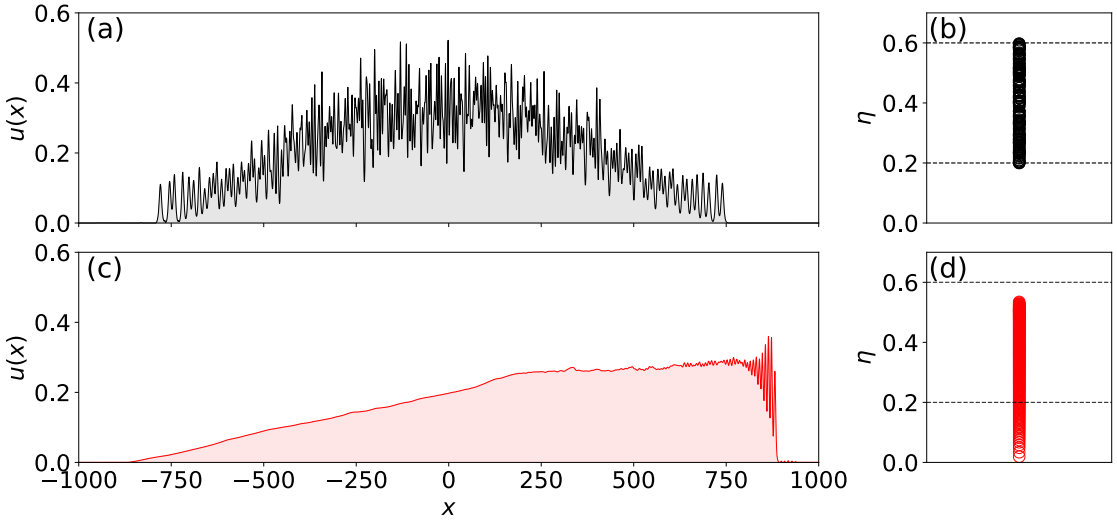

Figure 3.22: (a) Normalized wavefield of the initial condition measured in the NLTL ($n = 0$) under the form of the synthesized SG. (b) Associated eigenvalues represented by black points. (c) Normalized broad smooth wavefield measured at $n = 960$ in the NLTL. (d) Same as (b) but for the wavefield shown in (c).

To sum up

The propagation of a dense KdV SG is investigated in experiments made in the NLTL. The SG, initially composed of 200 solitonic modes parametrized by 200 discrete eigenvalues randomly distributed, is propagated in the NLTL, and its long-time evolution is observed. Due to the presence of diffusion, the SG does not reach a dilute state with solitons becoming discernible and individualized as it would in a KdV dynamics. Instead, a broad, smooth wavefield emerges. This structure is observed both with and without compensation for linear damping, suggesting that diffusion is the primary driver of the observed dynamics. Nonlinear spectral analysis reveals that, simarly to the single-soliton case, new discrete eigenvalues are generated during the evolution and the number of these newly created eigenvalues increases with time, consistent with numerical simulations of the KdV-Burgers equation.

3.4.3 Measurement of the density of states of the dense soliton gas

The nonlinear spectral analysis presented in the previous section revealed a reorganization of the spectrum, notably the creation of new eigenvalues, accompanied by the formation of a broad smooth wavepacket in real space. A natural question that arises is how to connect these two perspectives. In other words, how do the individual solitons within the SG evolve during propagation, and, specifically, how are they distributed spatially within the gas? This question is equivalent to asking: what is the density of states (DOS) of our SG, and how does it evolve? To answer this question we'll need to go further in the nonlinear spectral analysis.

3.4.3.1 Method

The DOS $f(\eta; x, t)$, characterizes the distribution of soliton spectral parameters in space and time. Formally, $f(\eta; x, t)\,\mathrm{d}\eta\,\mathrm{d}x$ gives the number of solitons within

a spatial interval $[x, x + \mathrm{d}x]$ whose discrete eigenvalues lie in $[\eta, \eta + \mathrm{d}\eta]$ at a given time t. In general, f depends on both x and t, making its determination a nontrivial task.

In the special case of a homogeneous soliton gas, the DOS becomes independent of x, and its spatial average reduces to a probability density function over the complex spectral plane. In this context, the DOS has been measured experimentally in the NLSE framework [35], normalized such that it reflects the average number of eigenvalues per unit length (spatial extent of the gas).

In more general, non-homogeneous settings, determining the DOS $f(\eta; x, t)$ requires spatial resolution, which cannot be achieved by computing only the discrete eigenvalues of the full wavefield. A natural idea is to apply a windowing procedure, extracting a finite segment of the wavefield and computing its discrete eigenvalues [158]. However, such truncation introduces boundary artifacts that distort the spectral content. This raises a critical question: does the distribution measured within the truncated region truly represent the unperturbed distribution?

I will present here the method developed by S. Randoux for measuring the DOS of KdV soliton gases, based on the calculation of the eigenfunctions. This approach applies to both homogeneous and inhomogeneous SGs, without truncating the wavefield, thereby avoiding the associated artifacts.

The eigenfunctions of the eigenvalue problem associated with the KdV equation, Eq. (3.46), are spatially dependent, providing additional information about the spatial distribution of the solitons. Specifically, their spatial extent reveals the degree of localization of the solitons in space, which changes with the density of the SG. Extending the nonlinear spectral analysis, we first examine simple cases, such as box-like potential, allowing analytical insight into the structure of the eigenfunctions $\psi_k(x)$ associated with the discrete eigenvalues η_k. These eigenfunctions are obtained by solving the associated linear Schrödinger equation (3.46).

Figure 3.23 shows the computed eigenfunctions and eigenvalues of the Schrödinger problem for a square-shaped (box) potential. Figure 3.23(a) shows the numerical simulation of the KdV equation with the initial condition being under the form of a square-shaped pulse of amplitude 5 and width 5. Fig-

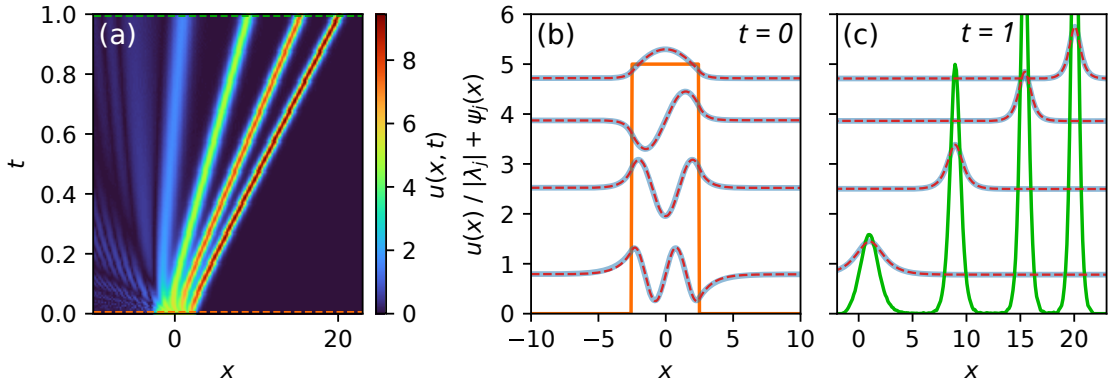

Figure 3.23: (a) Numerical simulation of the KdV equation with a square-shaped pulse as the initial condition. (b) Square-shaped pulse (orange line) and its computed normalized eigenfunctions ψ_j offset by their corresponding eigenvalues $|\lambda_j|$ (blue lines), $j = 1,\ldots,4$. Red dashed lines correspond to analytical eigenfunctions, Eq. (3.48). (c) Same as (b) but at $t = 1$, obtained from a KdV numerical simulation with the wavefield shown in (b) as the initial condition. The wavefield at $t = 1$ is shown in green.

ure 3.23(b) displays the square-shaped pulse as a orange line and the computed eigenfunctions $\psi_j(x)$, offset by their corresponding eigenvalues $|\lambda_j|$, as blue lines, obtained by solving Eq. (3.46). Figure 3.23(c) shows the same square-shaped pulse after its evolution in a KdV numerical simulation at $t = 1$ in green. For both Figs. 3.23(b) and (c), the analytical expressions for the eigenfunctions, also offset by $|\lambda_j| = \eta_j^2$, are shown as red dashed lines (given by Eqs. (3.47) and (3.48)).

For a single-soliton solution of the KdV equation, given by

$$u_k(x,t) = 2\eta_k^2 \operatorname{sech}^2\left[\eta_k(x - 4\eta_k^2 t - x_{0k})\right],$$

Eq. (3.46) admits a single eigenmode, associated with the real eigenvalue $\lambda_k = -\eta_k^2$, and the real eigenfunction [29],

$$\psi_k(x,t) = \frac{\eta_k}{2} \operatorname{sech}^2\left[\eta_k(x - 4\eta_k^2 t - x_{0k})\right]. \tag{3.47}$$

For the square-shaped pulse, the problem is analogous to the well-known finite

well potential in quantum mechanics [218], and the eigenfunctions are given by

$$\psi_j(x) \sim \begin{cases} \cos(k_j x + \phi_j), & \text{if } |x| \leq \frac{L}{2} \\ \cos(k_j L/2 + \phi_j) e^{\kappa(x+L/2)}, & \text{if } x < -\frac{L}{2} \\ \cos(k_j L/2 + \phi_j) e^{-\kappa(x-L/2)}, & \text{if } x > \frac{L}{2} \end{cases} \tag{3.48}$$

where L is the width of the square-shaped pulse, ϕ_j is equal to 0 if j is even and $\pi/2$ if j is odd, $k_j = \sqrt{u_{\max} - |\lambda_j|}$, and $\kappa = \sqrt{u_{\max}}$ and $u_{\max}$ being the amplitude of the pulse. The figures 3.23(b)(c) show the normalized eigenfunctions shifted by the associated eigenvalues, such that,

$$\int |\psi_j(x)|^2 \mathrm{d}x = 1. \tag{3.49}$$

Importantly, Fig. 3.23(b)(c) reveals that when the field represents a bound state (see Fig. 3.23(b)), the eigenfunctions are delocalized within the field. Conversely, when the solitons separate under integrable dynamics (see Fig. 3.23(c)), the eigenfunctions become localized around the soliton position. Delocalized eigenfunctions indicate that the solitons are interacting and are not discernible within the field; they effectively "occupy" the entire field. When the solitons are well-separated and non-interacting, the eigenfunctions become localized.

As previously introduced, the DOS $f(\eta; x, t)$ characterizes the spatial distribution of soliton states with spectral parameter η. It thus provides a phase-space representation of the nonlinear spectral content. Eigenfunctions are therefore essential for computing the DOS. However, the explicit formula for $f(\eta; x, t)$ and its dependence on ψ remain to be determined. To establish this relationship, we must connect results from IST theory and the kinetic theory of SGs.

Kinetic theory of SG tells us that knowledge of the DOS provides the statistical moments of the KdV SG field $u(x, t)$, including its mean value [130, 142]:

$$\langle u(x,t) \rangle = 4 \int_0^1 \eta f(\eta; x, t) \mathrm{d}\eta. \tag{3.50}$$

The IST theory, on the other hand, relates the N-soliton solution of the KdV (of

pure discrete spectrum) directly to the squared eigenfunctions [219]:

$$u(x,t) = 4\sum_{j=1}^{N} \eta_j \psi_j^2(x). \tag{3.51}$$

Combining Eqs. (3.50),(3.51) yields the following formula for the DOS:

$$f(\eta_k; x, t)\mathrm{d}\eta = \sum_{j=k}^{k+\Delta k} \langle \psi_j^2(x,t) \rangle, \tag{3.52}$$

where k and $k+\Delta k$ are integer indices bounding the discrete summation over the squared eigenfunctions associated with eigenvalues between η_k and $\eta_k + \mathrm{d}\eta$. This equation provides a local expression for the DOS of a soliton gas, based on the knowledge of the eigenfunctions that are associated with the discrete IST spectrum. Equation (3.52) provides a local expression for the DOS of a SG, akin to formulas used in other branches of physics. For instance, in surface physics and electron microscopy, the local DOS, $\rho(r,\omega)$ characterizes electronic densities, representing the probality of finding an electron with energy $\hbar\omega$ within an infinitesimal volume dr centered at the point r above a surface. This quantity is similarly directly related to the squared moduli of the electron wave functions at that energy [220, 221].

3.4.3.2 DOS analysis of the initial dense SG wavefield

Now that we have introduced a method for computing the DOS based on the spatial properties of the eigenfunctions, we apply it to analyze the soliton gas dynamics in our NLTL. First, we examine the DOS measurements corresponding to the SG used as the initial condition in our numerical simulations and NLTL experiments.

The analysis presented here focuses on the dense SG synthesized using the Darboux transformation method detailed in Sec. 1.3.1. This SG, shown in Fig. 3.24(a), serves both as the initial condition in our numerical simulations and as the input signal in the NLTL experiments.

Figure 3.24(b) displays the set of discrete eigenvalues and corresponding

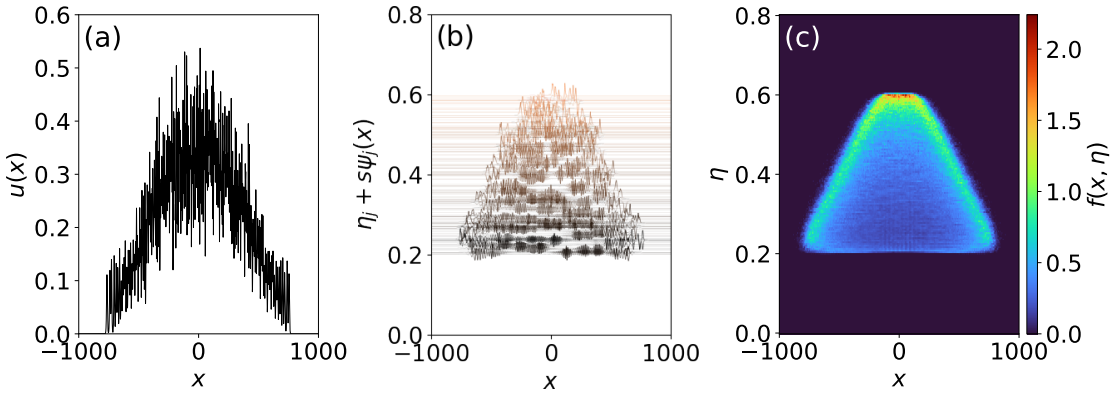

Figure 3.24: Nonlinear spectral analysis. (a) Soliton gas field considered as the initial condition. (b) Spatial distribution of the discrete eigenmodes, represented as $\eta_j + s\psi_j(x)$, where η_j (resp. ψ_j) ($j = 1,...,200$) represent the eigenvalues (resp. eigenfunctions) computed by solving Eq. (3.46). (c) DOS of the SG shown in (a).

eigenfunctions computed from the initial wavefield using Eq. (3.46). To enhance visual clarity, we apply a small vertical scaling factor $0 < s \ll 1$ and plot the eigenfunctions as $\eta_j + s\psi_j(x)$, following the convention introduced in Fig. 3.23. This figure illustrates that the eigenfunctions exhibit irregular spatial modulations and that their degree of localization in space depends strongly on the associated eigenvalue η_j: larger eigenvalues correspond to more localized modes, while smaller eigenvalues yield more delocalized profiles.

To characterize the distribution of these modes in both spectral and spatial dimensions, we compute the local density of states (DOS) $f(x,\eta)$. Since the DOS varies between realizations of the SG, we perform an ensemble average over 950 distinct realizations, all generated using the same method but with independent sets of norming constants and eigenvalues. For each realization, we extract the discrete eigenvalues $\eta_j = \sqrt{-\lambda_j}$ and their associated normalized eigenfunctions $\psi_j(x)$, and we compute the average local DOS $f(\eta;x)$, Eq. (3.52).

Figure 3.24(c) shows the resulting average DOS. It reveals that the smallest eigenvalues are distributed throughout the entire gas, while the largest eigenvalues are highly localized in the center. The DOS exhibits a triangular, symmetric profile that reflects the shape of the initial wavefield envelope: solitons with $\eta \in [0.2, 0.55]$ tend to occupy the edges of the gas, whereas higher-η solitons (e.g., $\eta > 0.55$) concentrate near the center. In other words, nonlinear modes

associated with larger spectral parameters are significantly more localized in space than those with smaller ones.

3.4.3.3 Numerical simulation of the KdV equation: DOS of the SG at long evolution time

We present now the DOS of the wavefield obtained at long evolution time (t = 4000) from a numerical simulation of the KdV equation with the initial condition being under the form of the SG shown in Fig. 3.24(a).

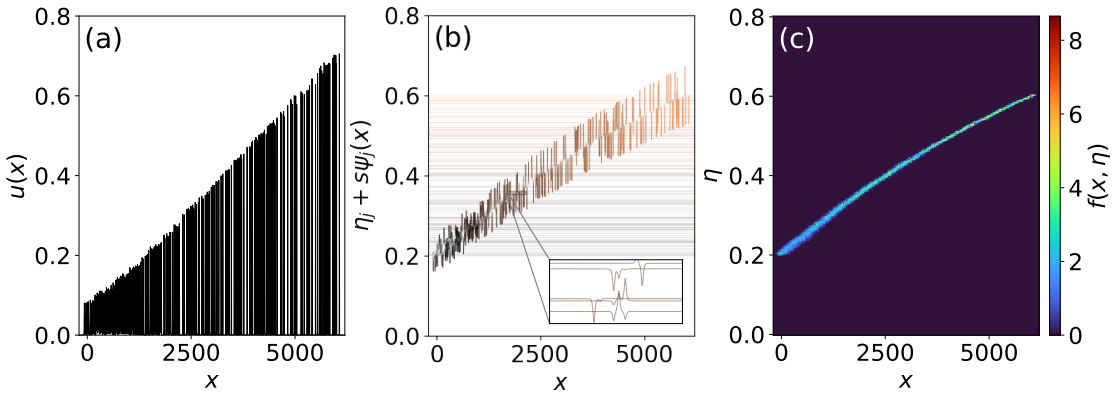

Figure 3.25: Nonlinear spectral analysis. (a) Wavefield obtained from a KdV numerical simulation at t = 4000. (b) Spatial distribution of the discrete eigenmodes, represented as $\eta_j + s\psi_j(x)$, where η_j (resp. ψ_j) (j = 1,...,200) represent the eigenvalues (resp. eigenfunctions) computed by solving Eq. (3.46). (c) DOS of the SG shown in (a).

Figure 3.25 presents the DOS analysis of the wavefield obtained from a long-time numerical simulation of the KdV equation, initialized with the synthesized dense SG presented in Fig. 3.24(a). At long time evolution (t = 4000), the wavefield evolves into a rank-ordered train of well-separated solitons, as shown in Fig. 3.25(a).

Figure 3.25(b) shows the set of discrete eigenvalues and the corresponding eigenfunctions computed from the wavefield shown in Fig. 3.25(a) using Eq. (3.46). Due to the isospectral evolution, the discrete eigenvalue spectrum remains unchanged compared to the situation presented in Fig. 3.24, i.e. the range of the eigenvalues remains bounded between 0.2 and 0.6 like in Fig. 3.24(b).

However, the associated eigenfunctions progressively localize around individual soliton peaks as the system evolves.

Using these eigenfunctions and eigenvalues, we compute the DOS following the same procedure as in the previous section. The resulting DOS is shown in Fig. 3.25(c). The spatial localization of solitons is reflected in the DOS, which becomes concentrated along a characteristic square-root curve. This structure reveals a direct mapping between the spectral parameter η_j and the soliton position x_j, which manifests as a characteristic signature in the DOS associated with the dilution of the soliton gas.

3.4.3.4 DOS analysis of the Experimental dynamics

We now present the DOS extracted from the wavefield measured in the NLTL at time $t = 420$, corresponding to the experiment with the losses compensated. This evolution time is achieved after six successive passes through the 160-cell NLTL, with signal amplification applied after each pass to maintain constant total mass and effectively cancel the mean damping.

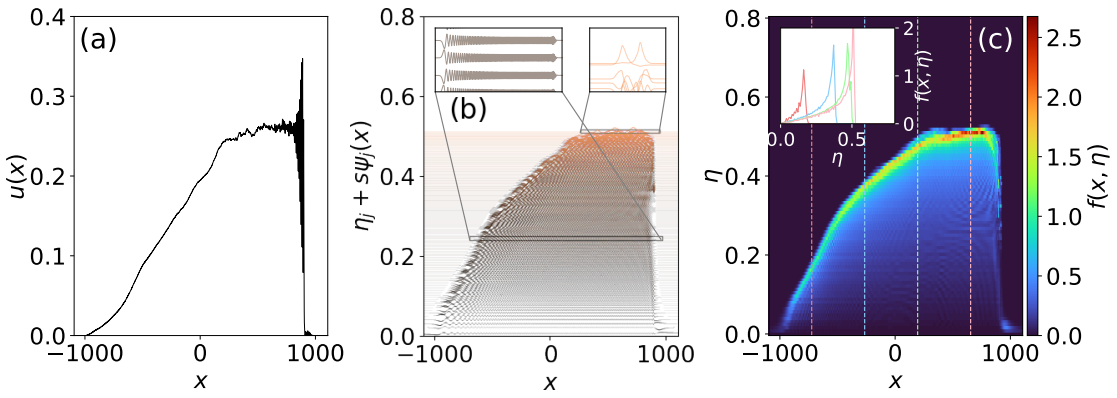

Figure 3.26: Nonlinear spectral analysis. (a) Experimental field measured at $t = 420$. (b) Spatial distribution of the discrete eigenmodes, represented as $\eta_j + s\psi_j(x)$, where η_j (resp. ψ_j) ($j = 1,...,225$) represent the eigenvalues (resp. eigenfunctions) computed by solving Eq. (3.46). (c) DOS of the SG shown in (a). The inset in (c) shows the DOS measured at $x \sim -720, -260, 200, 650$ as highlighted by the dashed colored lines in (c).

Figure 3.26(c) shows the DOS of the SG measured experimentally at $t = 420$. As in previous analyses, the DOS is computed from the discrete eigenvalues and

associated eigenfunctions obtained by solving Eq. (3.46) for the wavefield shown in Fig. 3.26(a). Figure 3.26(b) reveals that the nonlinear evolution under the influence of weak diffusion significantly alters both the eigenvalue distribution and the structure of the associated eigenfunctions.

Most notably, the eigenfunctions no longer exhibit the localized solitonic structure characteristic of a KdV evolution. Instead, they become spatially delocalized and exhibit nearly uniform oscillatory profiles throughout the system, as shown in the inset of Fig. 3.26(b). This delocalization is observed for all modes except those corresponding to the two largest eigenvalues, which retain a degree of spatial localization. Additionally, a dense cluster of new eigenvalues appears in the low-η region, with $\eta \in [0, 0.2]$.

Figure 3.26(c) displays the average DOS computed from 20 experimental realizations of the SG. Its structure differs strinkigly from the square-root profile observed in the integrable KdV case (see Fig. 3.25(c)). The inset highlights that the DOS follows locally (at a given position x) the Weyl distribution [128, 160],

$$f(x,\eta) = \frac{\eta}{\pi\sqrt{\lambda_1^2(x) - \eta^2}}, \qquad \eta \in [0, \lambda_1(x)], \tag{3.53}$$

where $\lambda_1(x)$ is a slowly varying upper bound modulating the local spectral support. This peculiar distribution is characteristic of a soliton condensate of genus zero, a special class of SGs introduced in the spectral kinetic theory [121, 128, 142]. These condensates represent minimal-entropy (or zero-variance) configurations of SGs. A detailed discussion of soliton condensates is provided in Sec. 3.4.3.6.

A key observation is that the behavior observed here drastically differs from the evolution of a dense SG in the integrable KdV system (see Fig. 3.25). In the absence of diffusion, the eigenfunctions become localized in space, each associated with an individual soliton. This localization reflects the deterministic, rank-ordered soliton decomposition characteristic of integrable evolution, and results in a DOS concentrated along the characteristic curve $\eta = \sqrt{(x - x_0)/4t}$.

In contrast, the perturbative diffusion in the NLTL breaks integrability and leads to a radically different behavior: the eigenfunctions become delocalized,

new eigenvalues emerge in the low-η region, and the DOS adopts the continuous Weyl distribution structure. These phenomena mark the spontaneous formation of a soliton condensate from an initially dense SG, a process forbidden in the purely integrable KdV setting [128]. Our results therefore demonstrate that KdVB-type dynamics can naturally drive the emergence of a condensate.

3.4.3.5 DOS analysis of the KdVB dynamics, with a smaller diffusion parameter

We now examine the DOS of a wavefield obtained from a numerical simulation of the KdVB equation with a reduced diffusion coefficient ($\beta = 2 \times 10^{-3}$), significantly smaller than in the experiment. This intermediate case allows us to explore a regime that lies between the ideal integrable KdV dynamics and the experimental scenario characterized by relatively strong diffusion.

By probing this transitional regime, our goal is to determine whether a qualitatively different evolution scenario emerges.

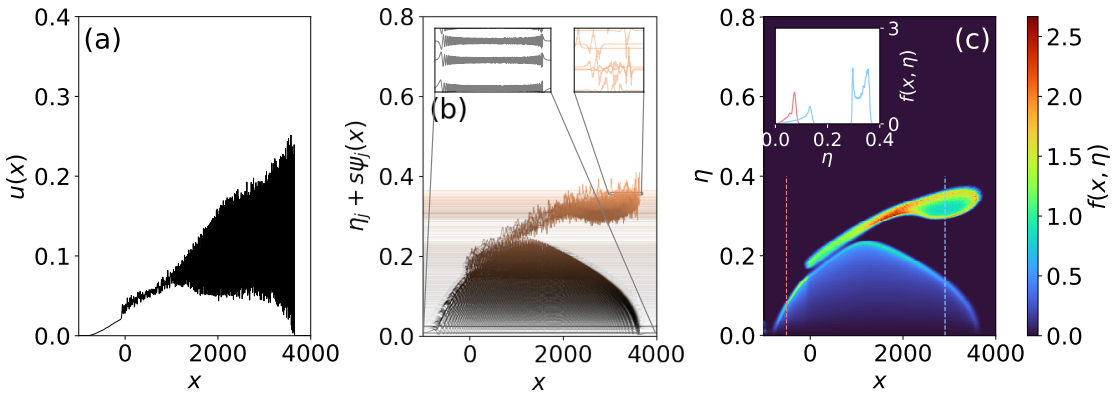

Figure 3.27: Nonlinear spectral analysis. (a) Wavefield obtained from a numerical simulation of KdV-Burgers equation with $\beta = 2 \times 10^{-3}$ at $t = 4000$. (b) Spatial distribution of the discrete eigenmodes, represented as $\eta_j + s\psi_j(x)$, where η_j (resp. ψ_j) represent the eigenvalues (resp. eigenfunctions) computed by solving Eq. (3.46). (c) DOS of the SG shown in (a). The inset in (c) shows the DOS measured at $x \sim -512,2906$ as highlighted by the dashed colored lines in (c).

Figure 3.27(a) shows the wavefield obtained from a numerical simulation of the KdVB equation at long time evolution ($t = 4000$), starting from the same initial SG as in Fig. 3.24(a), and with a reduced diffusion coefficient $\beta = 2 \times 10^{-3}$,

compared to the experimental one. In this scenario, the SG exhibits a slowed-down expansion, with a random soliton train propagating over a non-zero background (see Fig. 3.27(a)).

Figure 3.27(b) shows the eigenfunctions and associated eigenvalues computed from the field at $t = 4000$. One striking feature is that the discrete eigenvalues are now confined to the spectral range $\eta \in [0, 0.4]$, in contrast to the experimental case where eigenvalues were observed up to $\eta \sim 0.55$. This reflects the combined effect of moderate diffusion and long evolution time: although the diffusion strength is lower than in the experiment, the tenfold increase in propagation time significantly alters the nonlinear spectrum, leading to the decrease of higher-η discrete eigenvalues originally present in the initial SG.

The computed eigenfunctions reveal two distinct spectral components: (i) localized modes associated with the eigenvalues of the initial SG, and (ii) delocalized modes, corresponding to a background, appearing below $\eta \sim 0.2$. As a result, the DOS at each spatial position $x > 0$ is supported on two disjoint spectral intervals (see Fig. 3.27(c)). The associated structure can be interpreted as a genus-one soliton condensate, characterized by an oscillatory nonlinear wave supported by a double-band DOS, the genus one condensate coincide with periodic wave solutions (cnoidal waves) of KdV equation [128].

Specifically, the inset of Fig. 3.27(c) shows that the DOS is locally described by the genus-one distribution [128, 160]:

$$f(x,\eta) = \frac{i\eta(\eta^2 - w^2(x))}{\pi\sqrt{(\eta^2 - \lambda_1^2(x))(\eta^2 - \lambda_2^2(x))(\eta^2 - \lambda_3^2(x))}}; \qquad \eta \in [0,\lambda_1] \cup [\lambda_2,\lambda_3], \quad (3.54)$$

where $w^2(x) = \lambda_3^2(x) - (\lambda_3^2(x) - \lambda_1^2(x))\chi(m(x))$, with $\chi(m) = E(m)/K(m)$, and $m(x) = (\lambda_2^2(x) - \lambda_1^2(x))/(\lambda_3^2(x) - \lambda_1^2(x))$. Here, $K(m)$ and $E(m)$ denote the complete elliptic integrals of the first and second kinds, respectively. The band edges $\lambda_1(x), \lambda_2(x), \lambda_3(x)$ are slowly modulated in space, capturing the local structure of the condensate.

Finally, for positions $x < 0$, the DOS retains a single-band structure well described by the Weyl distribution introduced in Eq. (3.53), indicating the coexistence of two qualitatively different soliton condensates within the same

field.

3.4.3.6 On the notion of soliton condensate

The notion of a soliton condensate as the 'densest possible soliton gas' for a given spectral support was introduced in [121] within the context of the focusing NLSE. A detailed theory of soliton condensates for the KdV equation has been developed in [128]. In the spectral kinetic theory, the Nonlinear Dispersion Relations (NDRs) represent the constraints for the DOS $f(\eta)$ and the spectral flux density $v(\eta) = s(\eta)f(\eta)$ given a scaling function $\sigma(\eta)$. In KdV, they take the form [121, 128, 142, 222]:

$$\int_\Gamma \ln\left|\frac{\mu+\eta}{\mu-\eta}\right| f(\mu)\mathrm{d}\mu + f(\eta)\sigma(\eta) = \eta \tag{3.55}$$

$$\int_\Gamma \ln\left|\frac{\mu+\eta}{\mu-\eta}\right| v(\mu)\mathrm{d}\mu + v(\eta)\sigma(\eta) = 4\eta^3 \tag{3.56}$$

where $\sigma(\eta) \geq 0$ is a spectral scaling function characterizing the Lax spectrum of the soliton gas, and Γ is the support of $f(\eta)$ and $v(\eta)$. Spectrally, a soliton condensate is realized by vanishing the spectral scaling function, $\sigma(\eta) \to 0$, in the soliton gas NDRs.

For the simplest case $\Gamma = [0, \lambda_1]$, what we call a genus zero soliton condensate, the NDRs (Eqs. (3.55), (3.56)) are solved for $\sigma = 0$ by:

$$f(\eta) = \frac{\eta}{\pi\sqrt{\lambda_1^2 - \eta^2}}, \quad v(\eta) = \frac{6\eta(2\eta^2 - \lambda_1^2)}{\pi\sqrt{\lambda_1^2 - \eta^2}} \tag{3.57}$$

As shown in Ref. [128], for the general case of a genus N SG[3], where the SG is spectrally supported on Γ given by:

$$\Gamma = [0, \lambda_1] \cup [\lambda_2, \lambda_3] \cup \ldots \cup [\lambda_{2N}, \lambda_{2N+1}] \tag{3.58}$$

[3]The genus being the number of gaps between the bands on which the SG is supported.

the solutions of the NDRs (Eqs. (3.55), (3.56)) are given by:

$$f(\eta) = \frac{iP(\eta)}{2\pi R(\eta)}, \quad v(\eta) = \frac{2iQ(\eta)}{\pi R(\eta)} \tag{3.59}$$

with $R(\eta) = \sqrt{(\eta^2-\lambda_1^2)(\eta^2-\lambda_2^2)...(\eta^2-\lambda_{2N+1}^2)}$, and P and Q are odd monic polynomials of degree $2N+1$ and $2N+3$, respectively [128]. For a genus one soliton condensate, this yields:

$$f(\eta) = \frac{i\eta(\eta^2-w^2)}{\pi R(\eta)}, \quad v(\eta) = \frac{12i\eta(\eta^4-h^2\eta^2-r^2)}{\pi R(\eta)} \tag{3.60}$$

where $R(\eta) = \sqrt{(\eta^2-\lambda_1^2)(\eta^2-\lambda_2^2)(\eta^2-\lambda_3^2)}$, $h^2 = (\lambda_1^2+\lambda_2^2+\lambda_3^2)/2$, $w^2 = \lambda_3^2 - (\lambda_3^2 - \lambda_1^2)\chi(m)$, $\chi(m) = E(m)/K(m)$, and $m = (\lambda_2^2-\lambda_1^2)/(\lambda_3^2-\lambda_1^2)$. $E(m)$ (resp. $K(m)$) is the complete elliptic integral of the second (resp. first) kind, and $r^2 = \Big[\lambda_3^2(\lambda_3^2-\lambda_2^2-\lambda_1^2) - 2\lambda_2^2\lambda_1^2 - (\lambda_3^2+\lambda_1^2+\lambda_2^2)(\lambda_3^2-\lambda_1^2)\chi(m)\Big]/6$. We show that these mathematical expressions fit very well the DOS found in the experiment and numerical simulations of KdVB (Eq. (3.39), with $\beta = 2.10^{-3}$) reported in Figs. 3.26(c) and 3.27(c).

Figure 3.28(a) shows that the DOS of the SG measured at ($x = 755$, $t = 420$) in the experiment is remarkably well fitted by Eq. (3.53) with $\lambda_1 = 0.509$. Fig. 3.28(b) shows that the DOS of the SG measured at ($x = 2900$, $t = 4000$) in the numerical simulations of the KdV-Burgers equation (Eq. (3.39)) with small diffusion ($\beta = 2\times10^{-3}$) is remarkably well fitted by Eq. (3.54) with $\lambda_1 = 0.131$, $\lambda_2 = 0.295$, and $\lambda_3 = 0.359$. It was conjectured and numerically verified in [128] that realizations of the genus one condensate with DOS Eq. (3.60) almost surely coincide with periodic wave solutions (cnoidal waves) of KdV parameterized by λ_1, λ_2, and λ_3. These solutions locally describe diffusive-dispersive shock waves of the KdV-Burgers equation [215].

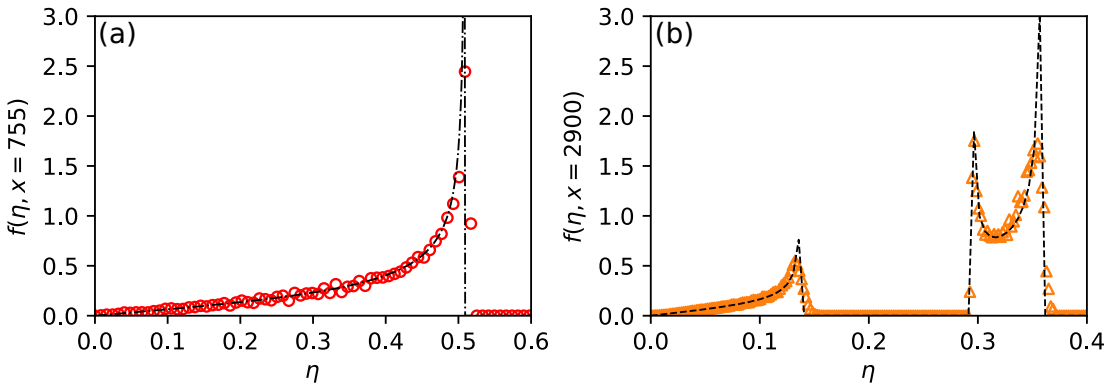

Figure 3.28: (a) The red circles represent the experimental spectral distribution $f(\eta, x = 775)$ shown in the inset of Fig. 3.26(c). The black dotted line fits the red circles with the model Eq. (3.53) with $\lambda_1 = 0.509$. (b) The orange triangles represent the spectral distribution $f(\eta, x = 2900)$ obtained from a numerical simulation of KdV-Burgers with $\beta = 2 \times 10^{-3}$ and $t = 4000$, shown in the inset of Fig. 3.27(c). The black dashed line fits the orange triangles with the model Eq. (3.54) with $\lambda_1 = 0.138$, $\lambda_2 = 0.295$, and $\lambda_3 = 0.359$.

To sum up

This section investigates the local density of states (DOS) $f(x, \eta)$ as a tool to characterize the nonlinear spectral content and spatial distribution of a dense soliton gas. A novel method based on the spatial localization properties of the eigenfunctions of the associated linear Schrödinger problem is used to compute $f(x, \eta)$ without truncating the wavefield. Numerical and experimental results reveal distinct DOS signatures under different dynamical regimes: in the integrable KdV case, solitons separate and eigenfunctions localize around solitonic peaks, reflecting the progressive dilution of the gas; in the NLTL experiment with weak diffusion, new eigenvalues emerge and eigenfunctions become fully delocalized, leading to a DOS that converges locally in space toward a Weyl distribution, characteristic of a genus-zero soliton condensate. An intermediate regime, simulated via the KdV-Burgers equation with reduced diffusion, exhibits a genus-one DOS associated with oscillatory nonlinear wave. These results demonstrate that weak dissipation breaks integrability and drives the emergence of condensate-like states, inaccessible in purely integrable dynamics.

3.5 Summary of the Chapter & Perspectives

In this chapter, we have presented a detailed experimental investigation of soliton gas dynamics in a nonlinear electrical transmission line (NLTL), a physical system described at leading order by the KdV equation in the long-wavelength limit.

Baseline experiments in our NLTL, including single soliton propagation, revealed deviations from integrability. While the soliton maintains its shape, its amplitude decreases and width increases, a phenomenon interpreted as an adiabatic evolution driven by weak dissipation.

To characterize the dissipative mechanisms, we studied the linear propagation regime using small-amplitude Gaussian pulses. Our analysis revealed a frequency-dependent spectral narrowing during propagation, which we attributed to diffusion induced by the intrinsic resistance of the varactors. By incorporating both inductive and capacitive resistive losses into the circuit model, we derived a dissipation-driven KdV equation and demonstrated excellent agreement between theory and experiment. This model distinguishes between two types of dissipation: a diffusive term originating from the varactor resistance R_C, and a damping term arising from the inductor resistance R_L.

We then explored nonlinear interactions, including soliton collisions and the soliton fission of broad pulses. Experiments showed that soliton collisions in the NLTL are inelastic due to dissipation, and the soliton fission process is better described by the KdV-Burgers equation than by the damped KdV equation, highlighting the crucial role of the diffusive term.

In the nonlinear regime, we investigated the long-time propagation of a high-amplitude soliton. We observed a non-adiabatic evolution characterized by the generation of a trailing shelf and the emergence of new discrete eigenvalues in the nonlinear spectrum, demonstrating a breakdown of the isospectral property intrinsic to integrable systems. While perturbative approaches such as momentum decay and shelf models provided useful predictions for the soliton trajectory and eigenvalue dynamics, they proved insufficient to fully capture the physics of soliton creation. Numerical simulations of the KdV-Burgers equation reproduced the experimental observations, and IST spectral diagnostics allowed

us to connect the redistribution of conserved quantities between the discrete and continuous spectral components. The last part of this chapter was devoted to the study of the nonlinear evolution of a dense soliton gas in our NLTL and its nonlinear spectral characterization. Using the IST framework, we performed a direct measurement of the DOS $f(x,\eta)$, which encodes the spatial and spectral distribution of solitons. This measurement revealed a striking behavior: as the soliton gas evolves under the influence of dissipation, new discrete eigenvalues are continuously created and the associated eigenfunctions become delocalized. This evolution is the signature of the emergence of a soliton condensate : the densest possible gas where the nonlinear spectrum fills a compact spectral band, converging toward a Weyl distribution of eigenvalues. Such a condensate cannot emerge in integrable KdV evolution, where the spectrum is preserved and eigenfunctions are localized around solitonic peaks. The formation of this condensate thus constitutes clear evidence of integrability breaking and of the dissipation-driven rearrangement of solitonic eigenmodes within the system, accompanied by the excitation of the continuous spectrum, resulting in the formation of new soliton states.

Future perspectives The NLTL opens several promising avenues for future research. Most notably, our observation of spontaneous soliton condensate formation under weak dissipation raises fundamental questions about nonequilibrium phase transitions in integrable systems. In strictly integrable dynamics, transitions between non-condensed and condensed states are forbidden due to spectral conservation [128]. However, our results demonstrate that weak integrability-breaking perturbations can enable such transitions. This suggests that future experiments could be designed to emulate a Joule expansion: the soliton gas would first evolve under controlled dissipation to form a condensate, followed by a sudden suppression of dissipative effects to investigate its subsequent evolution under (approximately) conservative and integrable dynamics.

On the theoretical side, our findings highlight the need to go beyond existing kinetic theories. While classical soliton gas kinetic theory fails to capture the emergence of a condensate, recent developments in Generalized Hydrodynamics (GHD) offer a promising framework to include weak integrability-breaking

perturbations. However, current hydrodynamic approaches remain limited: in particular, they do not account for the excitation of the continuous spectrum by a statistical ensemble of solitons, a process that appears crucial in our observations. We anticipate that our results will motivate further theoretical developments, especially toward incorporating spectral radiation and soliton creation into the hydrodynamic description of nearly integrable systems.

Chapter 4

Nonlinear evolution of optical soliton gases under the presence of weak perturbative dissipation

Experience without theory is blind, but theory without experience is mere intellectual play.

– Immanuel Kant

4.1 Introduction

As discussed in the previous chapter, the concept of a soliton gas (SG) provides a powerful statistical framework to describe the collective dynamics of nonlinear wave systems governed by integrable equations such as the Korteweg–de Vries (KdV) or the nonlinear Schrödinger equation (NLSE). While SGs are defined in the context of integrable dynamics, realistic physical systems are inevitably subject to perturbations, such as losses, gain, or higher-order effects, that break integrability and modify the evolution of the gas.

In Chapter 3, we examined the influence of weak diffusion on the evolution of a KdV soliton gas in a nonlinear electrical transmission line. We showed that the breaking of integrability could lead to striking and unexpected phenomena such as the emergence of a soliton condensate, characterized by the creation and the redistribution in space of the system's eigenmodes. These results demonstrated how perturbative higher-order effects could give rise to new forms of organization within the gas.

In this chapter, we investigate the evolution of an optical soliton gas in regimes where the integrable dynamics governed by the focusing one-dimensional NLSE is perturbed by small dissipation, i.e. weak linear gain and loss effects. The experiments are conducted in a recirculating fiber loop platform, where the level of damping and amplification (both of which break integrability) can be precisely tuned using Raman amplification. This level of control enables us to probe three distinct regimes: weakly damped, weakly amplified, and nearly conservative evolution.

A key innovation of this work lies in the implementation of a heterodyne interferometry method that allows, the experimental measurement of the discrete (IST) spectral content of the field, and more importantly, its density of states (DOS), a statistical quantity central to the kinetic theory of SGs. This capability enables us to monitor how the DOS of the optical SG is modified with the propagation distance due to effects breaking the integrability of the system's dynamics.

The chapter is organized as follows. We begin by describing the experimental platform, including the generation of the initial condition and the heterodyne

measurement technique. We then investigate the dynamics of the optical SG under weak damping, analyzing both its spatiotemporal evolution and spectral deformation of the DOS. The third section focuses on the gain regime and the formation of a near-bichromatic soliton gas.

4.2 The Recirculating Fiber Loop – Description of the Experimental Setup

This section describes the experimental setup initially developed during Adrien Kraych's PhD and later refined by other PhD's students, including myself, see Refs. [223–225]. We begin with a brief historical overview of the setup's development, followed by a detailed presentation of its components : from the generation of the optical signals to the detection system used to record the spatiotemporal dynamics. The section concludes with the introduction of the mean-field model used to describe light propagation in the system, the 1d NLSE.

4.2.1 Space-time resolved observation of nonlinear wave propagation in optical fibers

In optical fiber experiments, it is generally possible to measure the optical field, or at least its intensity, either at the input or at the output of the fiber. For instance, in the experiment on the Peregrine soliton performed in Ref. [226], measurements are taken before and after propagation through several hundreds of meters of fiber. However, accessing the full spatio-temporal evolution of the field within the propagation medium remains extremely challenging. This contrasts with hydrodynamic or electrical line experiments, where the spatio-temporal evolution is more readily accessible due to the possibility of placing gauges or probes directly within the propagation medium.

A first method developed to partially circumvent this limitation in optical fibers is the so-called *cutback* technique, in which the fiber is progressively shortened to access the signal at different propagation distances [227]. While conceptually simple, this method is destructive, irreversible, and requires metic-

ulous efforts to reproduce identical injection conditions at each cut. Another approach consists in using multiple fibers of different lengths [228–230].

An alternative strategy consists in measuring the field at the output of the fiber (or the propagation medium) and varying the power of the input field. In the nonlinear regime, this effectively modifies the accumulated nonlinear phase shift and can thus be interpreted as probing different effective propagation lengths [95]. Although this method is non-destructive, it only provides an indirect view of the spatial evolution of the wave [63, 231, 232].

A more recent approach involves analyzing weak backscattered Rayleigh Brillouin light, which allows for partial reconstruction of the optical field during propagation, see Refs. [233–238]. This method is also at the operating basis of some distributed fiber sensors (strain of temperature sensors).

In this context, the development of recirculating fiber loops [64, 66, 239–244] in the 1980s provided an effective method for studying long-distance optical propagation. Initially developed to emulate ultra-long distance optical fiber transmission in telecommunications, these systems consist of an optical fiber closed on itself via an optical coupler, typically combined with amplification stages to compensate for losses at each roundtrip. Without such compensation, the signal would rapidly vanish. With each roundtrip, the optical signal experiences an additional effective propagation equal to the full fiber length, enabling a stroboscopic observation of its evolution (see Fig. 4.1).

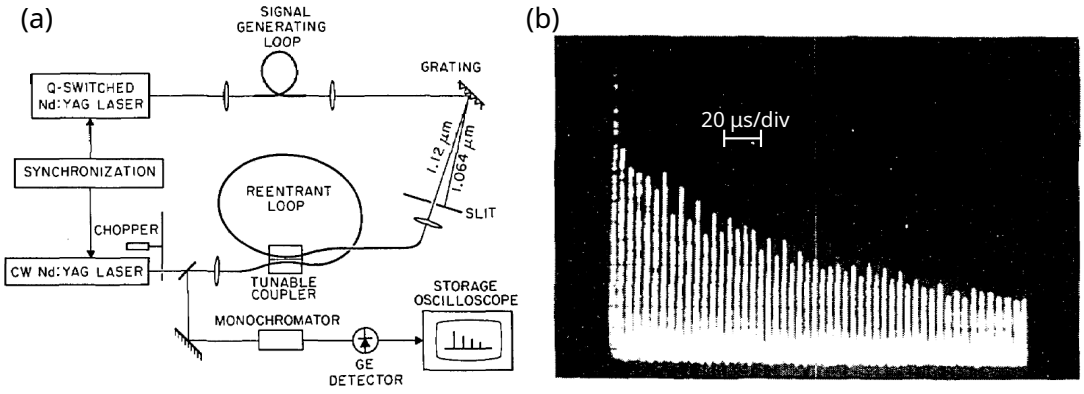

Figure 4.1: Figures extracted from [239]. (a) Experimental setup. (b) Output signal recorded on an oscilloscope showing 50 recirculations.

This technique offers two major advantages. First, in setups where the optical field is extracted at each roundtrip, it enables a stroboscopic view of the propagation, allowing non-destructive, time-resolved access to the spatiotemporal dynamics of the optical field. However, this feature, which is central to our implementation in Lille, is not present in all recirculating loop configurations, for instance, some systems only extract the signal after a fixed number of roundtrips, see Ref. [245]. Second, recirculating loops provide a powerful experimental platform for investigating nonlinear wave dynamics over long effective propagation distances.

Over the past few years, recirculating loops, initially developed for telecommunications, have re-emerged as powerful tools for experimental studies of integrable nonlinear dynamics, see e.g. Refs. [25, 245–249]. This renewed interest has been particularly driven by recent developments within our group, where such platforms have been adapted and optimized to explore soliton gas dynamics and integrable turbulence in optical fibers. In this chapter, we make use of this approach to experimentally investigate the dynamics of soliton gases in near-integrable regimes.

4.2.2 Recirculating Fiber Loop: Architecture, Initial Condition Generation, and Raman Amplification

Figure 4.2 shows a detailed schematic of our experimental setup, highlighting the architecture used to generate and propagate optical soliton gases. This platform was initially developed during the PhD thesis of A. Kraych [223, 246, 247], building on the concept of recirculating fiber loops originally introduced for optical telecommunications.

In the remainder of this section, we present the experimental setup in greater detail, breaking it down into its main functional subsystems. Each subsystem will be described separately and illustrated with dedicated figures. This approach clarifies the role of each element.

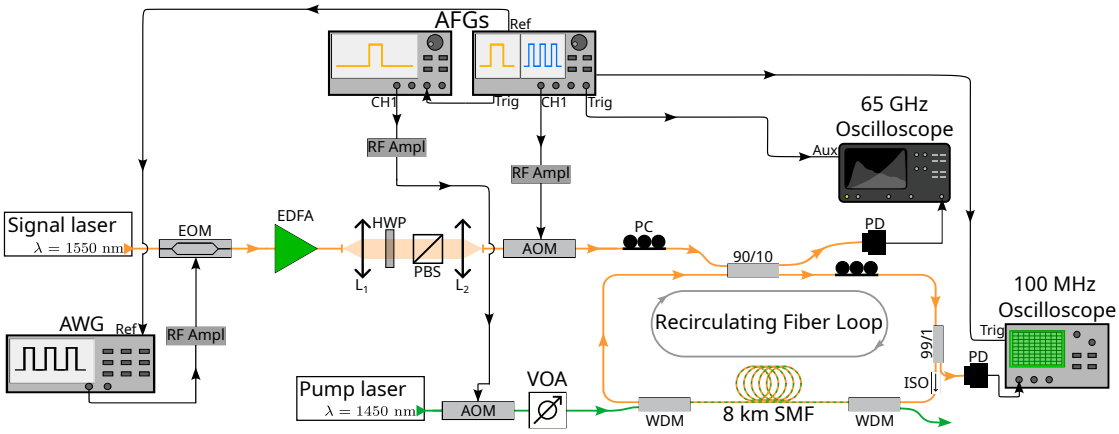

Figure 4.2: Schematic of the experimental setup. AFG: Arbitrary function generator. AWG: Arbitrary waveform generator. EDFA: Erbium-doped fiber amplifier. PBS: Polarizing beam splitter. HWP: Half-wave plate. AOM: Acousto-optic modulator. EOM: Electro-optic modulator. VOA: Variable optical attenuator. PC: Polarization controller.

4.2.2.1 Generation of the Initial Condition

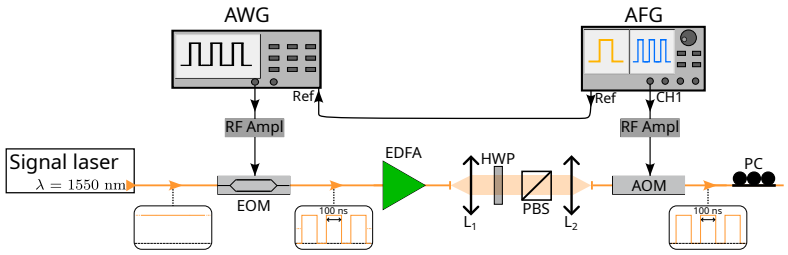

Figure 4.3: Setup used for generating the initial condition. AFG: Arbitrary function generator. AWG: Arbitrary waveform generator. EDFA: Erbium-doped fiber amplifier. PBS: Polarizing beam splitter. HWP: Half-wave plate. AOM: Acousto-optic modulator. EOM: Electro-optic modulator.

Figure 4.3 presents the subsystem dedicated to generating the initial optical field used to form soliton gases. The light source is a single-frequency continuous-wave (CW) laser diode (APEX-AP3350A), operating at a wavelength of $\lambda = 1550$ nm, and delivering an output power of a few milliwatts. The CW laser is modulated using a 20-GHz electro-optic modulator (EOM, iXblue MX-LN-20), driven by an arbitrary waveform generator (AWG, Tektronix AWG70001A) with a 15-GHz bandwidth, to produce flat-top optical pulses with durations

of 100 ns. In practice, a sequence of three such pulses is launched into the loop. Each pulse evolves independently and generates a distinct realization of a soliton gas. This approach increases the number of solitons observed in a single experiment, thereby improving the statistics of quantities such as the density of states.

The pulses are then amplified to the Watt-level using an erbium-doped fiber amplifier (EDFA, Keopsys CEFA-C-BO-HP). Amplified spontaneous emission (ASE) noise originating from the EDFA adds a small but significant level of optical noise to the pulses. This optical noise seeds the nonlinear evolution of the waveform, ultimately driving its transformation into a randomized SG as it propagates within the fiber loop [36, 122, 177, 250–252].

The output power of the EDFA is regulated using a polarization beam splitter (PBS) and a half-wave plate (HWP), which enable precise adjustment of the signal intensity. The optical pulses are then gated using an acousto-optic modulator (AOM, VSF MT110-IR25-Fio). The AOM remains open for approximately 500 ns to allow the injection of the pulse into the fiber loop, then closes for $\sim$ 20 ms, during which the optical signal circulates inside the loop. The gating signals for the AOM are generated by a 250-MHz arbitrary function generator (AFG, Tektronix 31252).

4.2.2.2 Recirculating Fiber Loop and Raman Amplification

Once the initial condition is prepared, it is injected into the recirculating fiber loop. In this section, we describe the architecture of the loop as well as the Raman amplification scheme used to compensate optical losses.

Figure 4.4 shows a simplified representation of the experimental setup, focusing on the propagation stage inside the fiber loop and the associated Raman amplification scheme. The recirculating loop consists of approximately 8 km of single-mode fiber (SMF), arranged in a closed configuration using a 90/10 fiber coupler. The fiber, manufactured by Draka-Prysmian, is characterized by a second-order dispersion coefficient of $\beta_2 = -22$ ps^2.km^{-1} and a Kerr nonlinearity parameter $\gamma \sim 1.3$ W^{-1}.km^{-1} at the working wavelength of 1550 nm.

The 90/10 coupler is configured so that 90% of the intra-loop optical power is

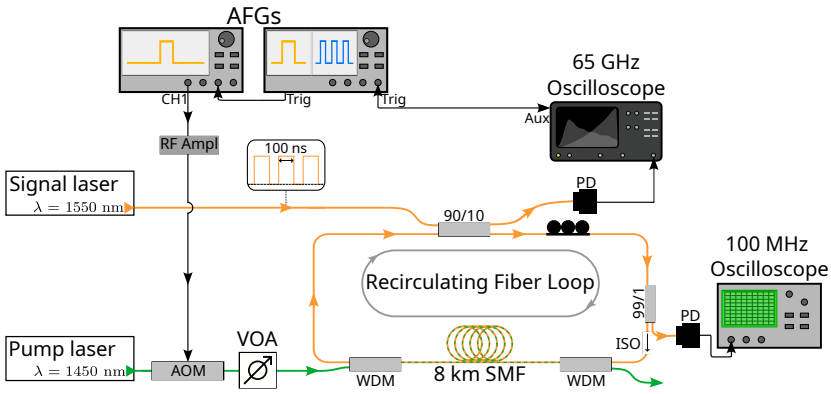

Figure 4.4: Simplified schematic of the fiber loop and Raman amplification system. AFG: Arbitrary function generator. AWG: Arbitrary waveform generator. EDFA: Erbium-doped fiber amplifier. PBS: Polarizing beam splitter. HWP: Half-wave plate. AOM: Acousto-optic modulator. EOM: Electro-optic modulator.

recirculated, while 10% is extracted at each round trip. The extracted signal is detected using a high-speed photodiode (Finisar XPDV2120R) connected to a real-time sampling oscilloscope (Teledyne LeCroy LabMaster 10-65Zi, 160 GSa/s), offering an overall detection bandwidth of 32 GHz [247], see Appendix 5.3. For each round trip, the system records a 500 ns temporal window, triggered by a second output from the AFG. These sequences are later assembled numerically to construct space-time diagrams that provide a single-shot view of the wavefield evolution, as will be discussed in the following section.

The evolution of the mean power within the loop is carefully controlled through Raman amplification via a counter-propagating pump laser at 1450 nm. The pump source is a commercial Raman fiber laser (IPG FiberTech), capable of delivering several watts of optical power at 1450 nm. This pump laser is injected and extracted from the loop using wavelength-division multiplexers (WDMs). In practice, the pump power at 1450 nm is attenuated to about 200 mW using a 90/10 fiber coupler (not shown in Fig. 4.4). Precise tuning of the Raman gain is performed using an additional acousto-optic modulator (AOM) and a variable optical attenuator (VOA), allowing the system to operate in a controlled manner across different regimes : lossy, amplifying, or nearly conservative, while ensuring operation of the fiber loop remains below the lasing thereshold.

Finally, a slow photodetector (Thorlabs DET10C/M), coupled to a 100 MHz

oscilloscope (Agilent 54624A), is used to monitor the slow (millisecond-scale) evolution of the mean power within the fiber loop.

4.2.2.3 Single-shot detection and space-time reconstruction

In this section we provide further details on the detection scheme and the numerical reconstruction of the space-time diagram.

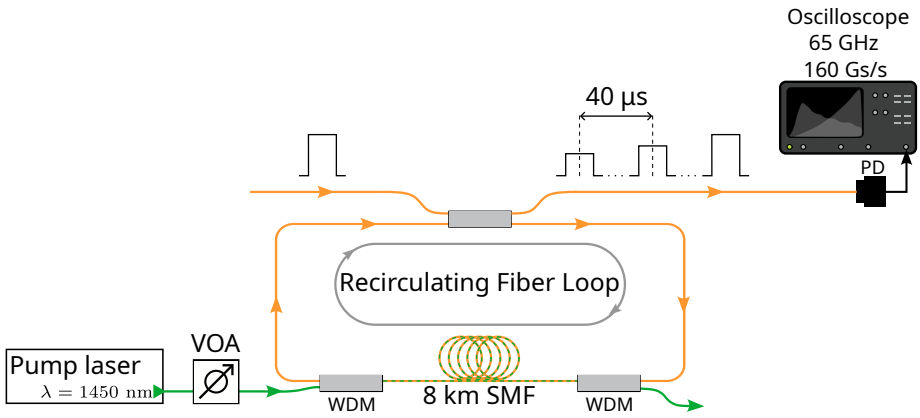

Figure 4.5: Simplified schematic of the detection system. AFG: Arbitrary function generator. AWG: Arbitrary waveform generator. EDFA: Erbium-doped fiber amplifier. PBS: Polarizing beam splitter. HWP: Half-wave plate. AOM: Acousto-optic modulator. EOM: Electro-optic modulator.

At the output of the loop, the optical signal is detected by a high-speed photodiode (Finisar XPDV2120R, 50 GHz bandwidth) and recorded by a real-time sampling oscilloscope (Teledyne LeCroy LabMaster 10-65Zi, 65 GHz bandwidth, 160 GSa/s sampling rate). The temporal separation between two successive arrivals of a signal pulse is approximately 40 μs, as schematically illustrated in Fig. 4.5, corresponding to the round-trip time of light in the 8 km-long fiber loop, where the group velocity is approximately 2×10^8 m/s (see Fig. 4.6(b), orange curve).

However, as described in Section 4.2.2.1, the relevant information is confined to a 500 ns time window : the duration defined by the AOM gating. In standard oscilloscope acquisition mode, this would result in extremely sparse data, with most of the recorded time trace filled with zeros. To avoid this inefficiency, we use the sequence mode of the oscilloscope.

Sequence mode enables the recording of short time segments (here 500 ns) with precise triggering. It significantly reduces dead time between acquisitions and allows time stamping of each segment, which is essential for reconstructing the space-time evolution of the field. The oscilloscope is triggered by a 40 Hz TTL signal provided by the AFG (see Fig. 4.4), synchronized with the AOM signal used to generate the initial condition, thus defining the start of each experimental run.

Individual round trips of the optical pulse inside the loop are captured by triggering the oscilloscope with a 25 kHz square wave signal (black solid line in Fig. 4.6(a)(b)), corresponding to the 40 μs round-trip time. Each segment captures 500 ns of data, centered on the propagating wave packet (see Fig. 4.6(c)). Figure 4.6(b) shows a zoom on the square signal (black) and the actual photodetector output (orange) recorded for each round trip. The green signal in Fig. 4.6(a) corresponds to the AOM gating of the Raman pump laser.

This detection strategy enables efficient and high-resolution tracking of the wavefield over thousands of round trips, providing access to its spatiotemporal evolution in a single experimental shot.

Figure 4.7(a) shows a typical acquisition consisting of 400 sequences of 500 ns each, recorded in sequence mode. This approach reduces the total acquisition time from 16 ms (in continuous mode) to only 200 μs. Figure 4.7(b) presents a zoom on a single 500 ns segment. Within this window, we clearly observe the three 100 ns flat-top pulses.

It is worth noting that the first recorded sequence often exhibits saturation due to the direct detection of the initial pulse, in which 90% of the signal power is directed to the detector during the first pass through the fiber coupler. In contrast, following sequences correspond to pulses that have propagated inside the fiber loop, where only 10% of the power is extracted at each round trip. As such, we define the initial condition of the experiment as the field after one full loop, i.e., after 8 km of propagation.

The time axis in Fig. 4.7(a) represents the concatenation of individually triggered segments and does not correspond to a continuous physical time. However, within each 500 ns sequence, the time scale is real and captures the actual duration of the wavefield during that round trip.

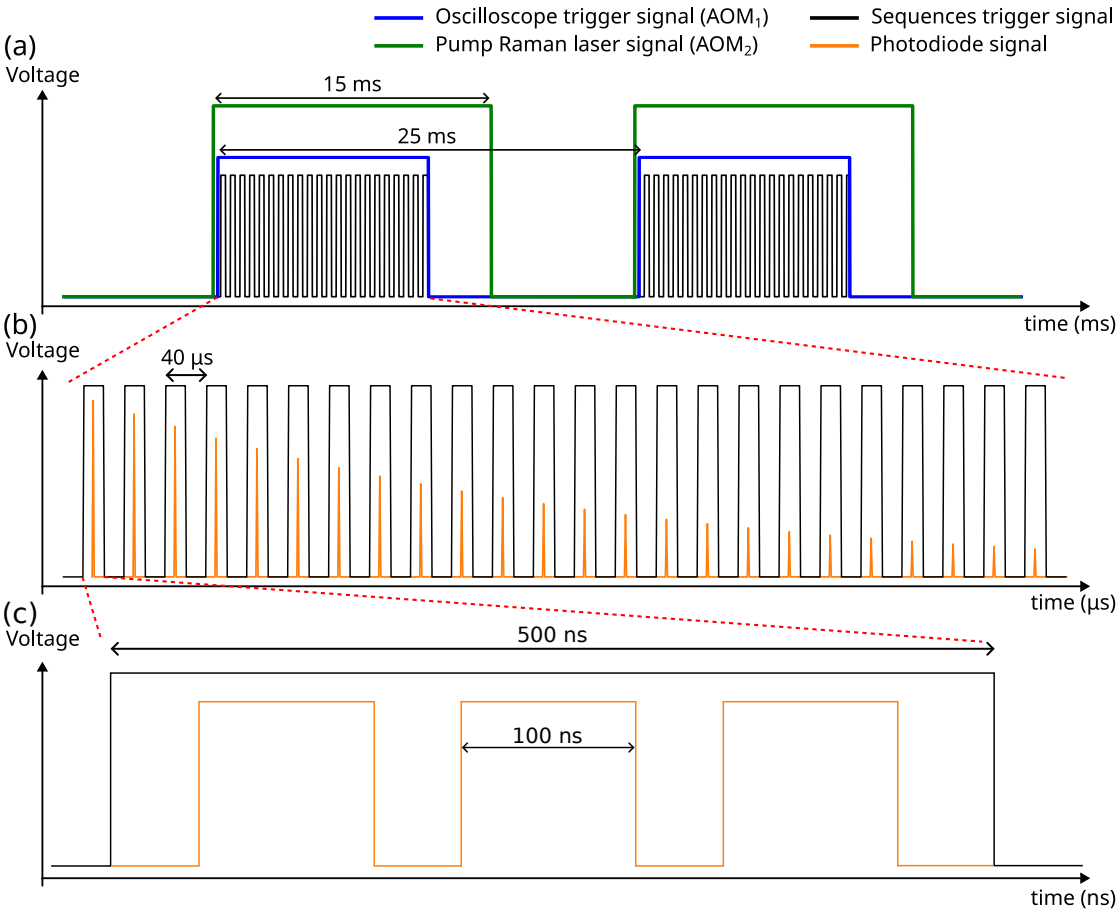

Figure 4.6: Acquisition scheme using the oscilloscope in sequence mode. (a) Overview of the temporal gating signals used in the experiment. The blue curve shows the 40 Hz TTL signal that initiates each experiment cycle. The black trace corresponds to the 25 kHz sequence trigger used to acquire each round trip individually. The green signal drives the acousto-optic modulator (AOM_2) used to control the Raman pump laser at 1450 nm. (b) Zoom on the sequence trigger signal (black) and the corresponding optical signals detected by the photodiode after each round trip (orange). Each detection peak corresponds to the output of the loop at one round trip. (c) Further zoom on a single 500 ns acquisition window, showing three 100 ns flat-top optical pulses detected by the photodiode (orange), corresponding to the three initial pulses launched in the loop.

We now describe the numerical processing used to reconstruct the single-shot space-time diagram from raw data shown in Fig. 4.7.

The two main processing steps are illustrated in Fig. 4.8. First, the raw

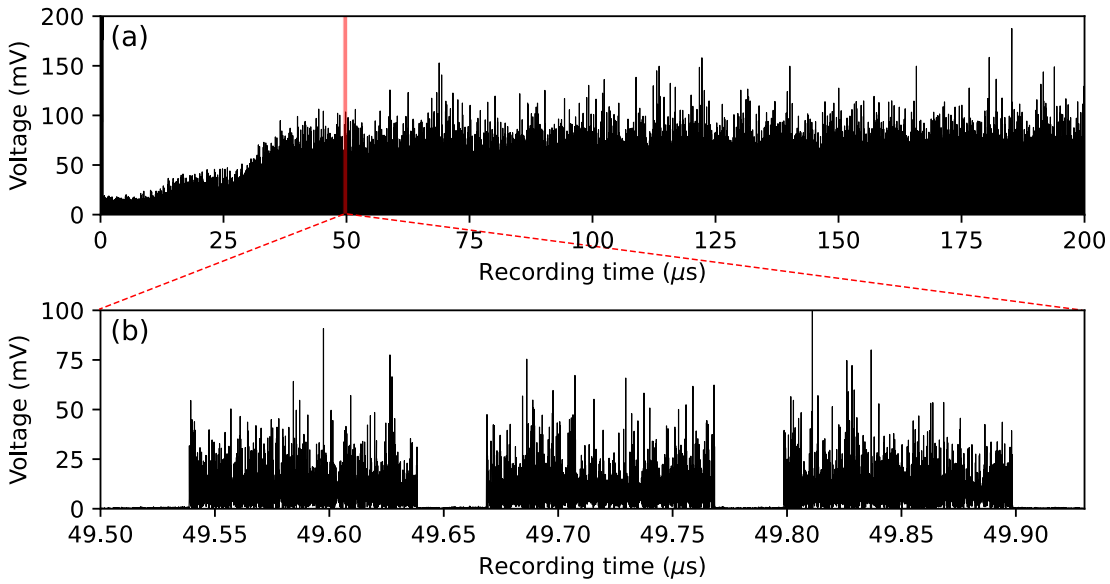

Figure 4.7: Typical oscilloscope trace obtained using sequence mode. The trace contains 400 sequences of 500 ns each, totaling 200 μs of acquisition time. This corresponds to a physical propagation time of 16 ms. (a) Full acquisition. (b) Zoom into a single 500 ns sequence, where the three 100 ns flat-top pulses are clearly visible.

sequences are stacked vertically to form a preliminary space-time diagram, as shown in Fig. 4.8(a). This step includes the correction of slow drifts due to slight mismatches between the actual loop round-trip time and the external trigger signal.

The second step consists in correcting the residual timing jitter between successive sequences. This jitter arises from fluctuations in the oscilloscope's triggering when operating in sequence mode. To compensate for it, we compute the cross-correlation between the signal at round trip i, denoted $s_i(t)$, and the signal from the previous round trip $s_{i-1}(t)$. The cross-correlation function is defined as:

$$C_i(\tau) = \int s_i(t+\tau)\, s_{i-1}(t)\, \mathrm{d}t.$$

The value of τ that maximizes $C_i(\tau)$ corresponds to the time shift that best aligns the two waveforms. Applying this time shift to $s_i(t)$, and repeating the procedure iteratively for each round trip, allows us to construct a jitter-free space-time

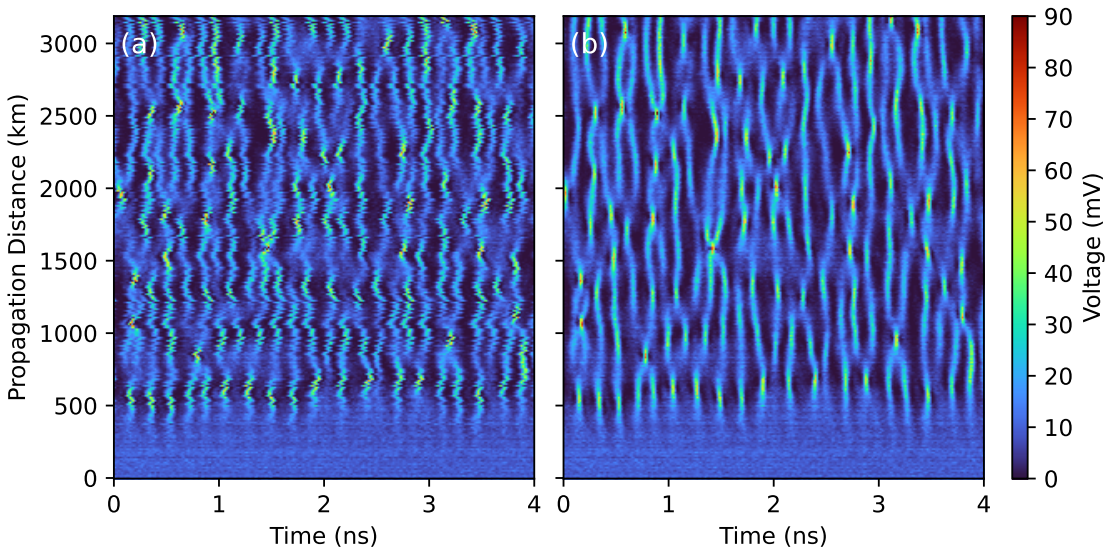

Figure 4.8: Processing steps for constructing the spatiotemporal diagram. (a) Raw oscilloscope sequences stacked to form a propagation diagram. Each horizontal line corresponds to one sequence (500 ns window), and only a 4 ns portion of the recorded 100 ns pulse is shown here. Residual timing jitter between sequences appears as horizontal fluctuations. (b) Same data after temporal realignment using cross-correlation. This procedure corrects the jitter and reveals the true spatiotemporal structure of the optical field during single-shot propagation over 3200 km.

diagram. An example of the result is shown in Fig. 4.8(b).

In some cases, we improve the resolution of the alignment process by increasing the temporal discretization of the signal. Although the oscilloscope samples at 160 GSa/s (i.e., 6.25 ps resolution), finer alignment is achieved using interpolation techniques such as zero-padding.

To sum up

This section detailed the experimental platform used to study optical soliton gases in a recirculating fiber loop. Three 100 ns flat-top optical pulses are generated using a CW laser modulated by a high-speed EOM, then amplified and perturbed by ASE noise from an EDFA. The pulses are injected into an 8 km fiber loop, where propagation is recorded at each round trip via single-shot detection. Optical losses are precisely controlled and compensated using a counter-propagating Raman pump at 1450 nm. A high-speed oscilloscope operated in sequence mode records 500 ns windows synchronized with each round trip. The resulting space-time diagram is reconstructed numerically using cross-correlation to correct for timing jitter. This setup provides access to the spatiotemporal evolution of nonlinear optical wavefields over thousands of kilometers, with high temporal resolution.

4.2.2.4 Intra-Loop Power Calibration and Mean Power Evolution

The final step of the measurement procedure consists in converting the voltage signal recorded from the photodiode into optical power.

Following the method introduced in Ref. [36], we exploit the well-characterized phenomenon of noise-induced modulation instability (MI) in the focusing nonlinear regime [95] for calibration purposes. After sufficient propagation inside the loop, the initially flat-top square pulses perturbed by amplified spontaneous emission (ASE) noise from the EDFA, become unstable, giving rise to a random train of localized structures, see Fig. 4.9(b).

This instability leads to the appearance of two symmetric sidebands in the optical spectrum, shifted by $\pm\Omega_{\max}$ relative to the carrier frequency, see Fig. 4.9(c). The frequency shift $\Omega_{\max}$ depends on the optical power P_0 of the initial continuous wave (or flat-top pulse) through the relation [95]:

$$\Omega_{\max} = \sqrt{\frac{2\gamma P_0}{|\beta_2|}}. \tag{4.1}$$

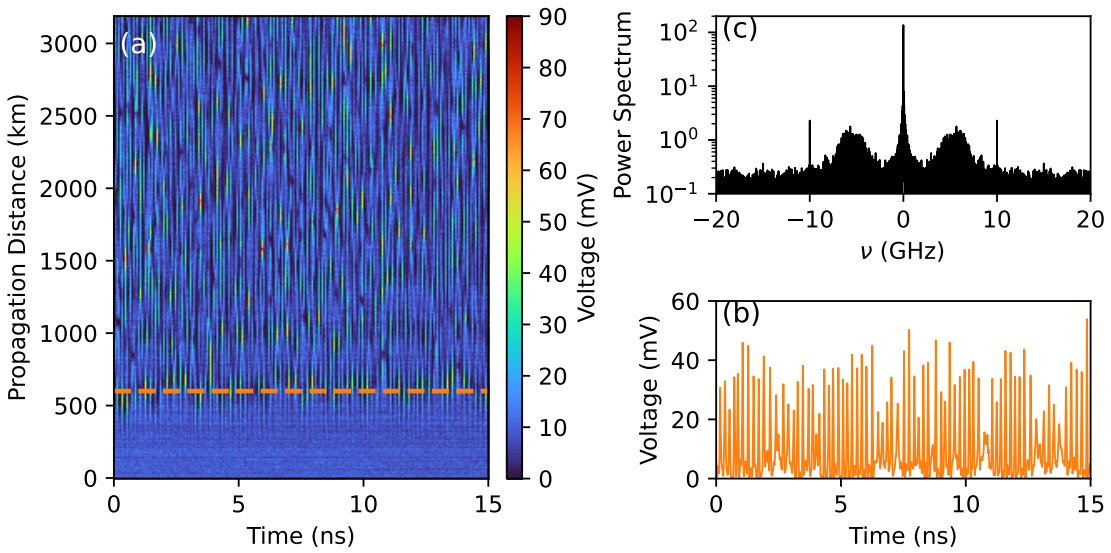

Figure 4.9: Power calibration of the recorded signal. (a) Space-time dynamics of noise-induced modulation istability (MI) of the plane wave optical background (b) Temporal cross-section at $z = 600$ km. The average period of MI is $T_{\mathrm{MI}} \sim 170$ ps, corresponding to an average power of 11.5 mW.

Rather than performing the calibration in the frequency domain, we extract Ω_{max} from time-domain measurements, which offers higher precision. This is done by counting the number of emerging MI peaks over a long temporal window (several tens of nanoseconds), see Fig. 4.9(b). From the measured average MI period $T_{\mathrm{MI}} \sim 170$ ps, we estimate the optical power using:

$$P_0 = \frac{(2\pi/T_{\mathrm{MI}})^2 |\beta_2|}{2\gamma} \sim 11.5 \text{ mW}. \tag{4.2}$$

Note that the measurement of the MI period is not performed at z=8 km, but rather after some propagation, typically at $z \approx 600$ km assuming an exponential evolution of the average power along the loop. A correction factor is then applied to account for this effect. This distance still corresponds to the early exponential stage of the modulational instability, where the spectral sidebands are well defined and the overall spectrum remains narrow. At later stages, once the instability saturates and localized structures form, the spectral pattern evolves and the MI period cannot be clearly identified.

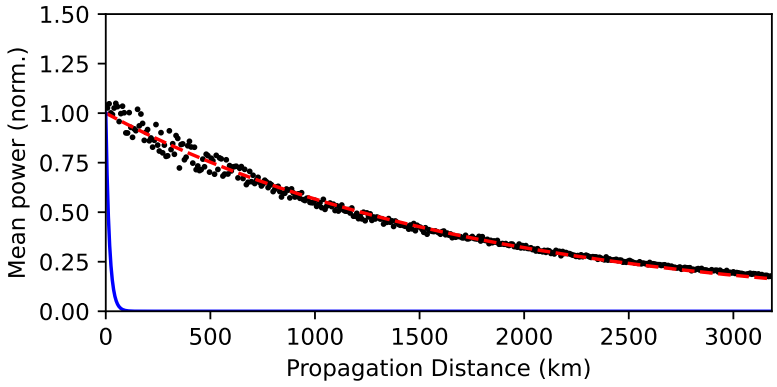

Figure 4.10: Typical evolution of the mean power within the loop. Black points: normalized power measured as a function of propagation distance z. Red dashed line: exponential fit $\exp(-\alpha_{\text{eff}} z)$, with effective loss coefficient $\alpha_{\text{eff}} = 5.68 \times 10^{-4}$ km^{-1}. Blue line: simulated evolution in the absence of amplification.

Optical power in the loop decreases with propagation due to several sources of loss. The main contribution comes from the intrinsic attenuation of standard single-mode fiber, typically 0.2 dB/km, which corresponds to approximately 1.6 dB per round trip. In addition, 10% of the circulating signal is extracted at each round trip for detection, introducing a further 2.06 dB loss per round trip. Altogether, in the absence of amplification, only about 60% of the optical power remains after each round trip.

This situation is illustrated by the blue curve in Fig. 4.10, which shows the expected exponential decay of the mean optical power in a purely passive configuration. In practice, Raman amplification is applied to mitigate these losses, and the effective damping rate can be finely controlled by adjusting the Raman pump power. The configuration shown in Fig. 4.10 corresponds to a typical operating point where the gain partially compensates for the losses, resulting in a residual decay of the mean power. However, by increasing the Raman pump power, it is possible to reduce the effective loss rate α_{eff}, or even to reach regimes of net gain, where the mean optical power grows exponentially along the loop.

This partial loss-compensation regime contrasts with the nearly conservative case discussed earlier (see Fig. 4.9). The black points in Fig. 4.10 show the

measured mean power, which is well fitted by an exponential decay $\exp(-\alpha_{\text{eff}} z)$, with an effective loss coefficient $\alpha_{\text{eff}} = 5.68 \times 10^{-4}$ km^{-1}.

To sum up

In this section, we described the procedure used to calibrate the intra-loop optical power in the recirculating fiber loop. The average power is inferred from time-domain measurements of modulation instability experienced by the flat-top square pulses, whose characteristic period depends on the initial optical power via a known analytical relation. This calibration step is essential to compare experiment and theory.
In the experiment, the effective gain and loss can be accurately controlled by adjusting the Raman pump power. This enables precise control over the intra-loop optical power. In particular it compensates for both fiber attenuation (0.2 dB/km) and the 10% signal extraction occurring at each round trip.

4.2.3 Derivation of the NLS Mean-Field Equation from the Iterative Map

Before turning to the next experimental section devoted to heterodyne detection, we present here a theoretical model describing the average propagation dynamics in the recirculating fiber loop. This model, based on a mean-field approximation of the iterative map, leads to the NLSE that captures the dynamics observed in the experiment.

The propagation of light in a single-mode optical fiber is governed by Maxwell's equations. In a transparent medium with third-order (Kerr) nonlinearity, and under the assumption of single-mode guidance, the transverse profile of the field can be decoupled from its longitudinal evolution. By applying the slowly varying envelope approximation and retaining only second-order dispersion, the dynamics of the optical field envelope along the propagation coordinate z are described by the one-dimensional NLSE [95]:

$$i\frac{\partial A}{\partial z} = \frac{\beta_2}{2}\frac{\partial^2 A}{\partial T^2} - \gamma|A|^2 A - i\frac{\alpha_{\text{eff}}}{2}A \tag{4.3}$$

Here, $A(z,T)$ denotes the slowly varying complex envelope of the electric field in a reference frame moving at the group velocity of the light wave packet. The parameter β_2 is the group velocity dispersion, γ is the nonlinear Kerr coefficient, and α_{eff} accounts for effective distributed losses or gains in the system. In our experiments using standard SMF-28e fiber at 1550 nm, typical parameters are $\beta_2 \sim -22$ ps^2/km and $\gamma \sim 1.3$ W^{-1}km^{-1}.

4.2.3.1 Physical Model and Iterative Propagation

Experiments in the recirculating fiber loop can be modeled by an iterative scheme combining distributed propagation and discrete boundary conditions [253], where the complex envelope $A_n(Z,T)$ evolves over successive round-trips n, each corresponding to a propagation over a fiber segment of length L. During each round-trip, the field propagates according to the nonlinear Schrödinger equation (NLSE) with distributed Raman gain:

$$\frac{\partial A_n}{\partial z} = -i\frac{\beta_2}{2}\frac{\partial^2 A_n}{\partial T^2} + i\gamma|A_n|^2 A_n + \frac{g_r}{2}A_n, \qquad z \in [nL,(n+1)L[. \tag{4.4}$$

At the end of each loop, the field undergoes lumped linear losses due to the output coupler and passive components, these losses are modeled by a simple multiplicative factor:

$$A_{n+1}(0,T) = \rho\, A_n(L,T), \qquad \rho \leq 1. \tag{4.5}$$

n denotes the round-trip index, g_{r} represents the distributed Raman gain, and ρ accounts for local losses, see Fig. 4.11:

$$\rho = \mathrm{e}^{-\frac{(g_{\text{r}}+\alpha_{\text{eff}})}{2}L} \tag{4.6}$$

where α_{eff} account for the imperfect losses compensation.

The key physical length scales in the recirculating loop are estimated as follows, for typical input powers $P_0 \in [2,12]$ mW and pulse durations $T_0 \in [40,80]$ ps used in the experiment:

- Nonlinear length: $L_{\text{nl}} = 1/(\gamma P_0) \sim 60$–$400$ km

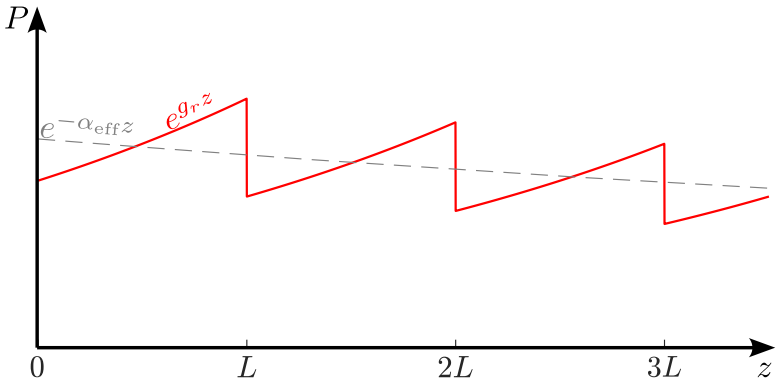

Figure 4.11: Schematic representation of the power evolution inside the loop over successive roundtrips. During each roundtrip, the field experiences distributed Raman gain $\exp(g_r z)$ followed by abrupt loss at $z = nL$, due to the extraction via the coupler. The resulting envelope (dashed gray line) decays exponentially as $\exp(-\alpha_{\text{eff}} z)$. This average trend justifies the use of a mean-field NLSE with an effective loss term. Figure adapted from [253]

- Dispersion length: $L_{\text{d}} = T_0^2/|\beta_2| \sim 70$–$300$ km
- Loss length: $L_{\text{loss}} = 1/|\alpha_{\text{eff}}| \sim 1700$–$10000$ km
- Loop length: $L \sim 8$ km

Since all physical effects occur on scales much longer than the loop perimeter L, a mean-field description is justified, with α_{eff} describing the cumulative loss or gain per round trip.

Note: The effective loss coefficient α_{eff} is adjusted empirically in the experiment and can be either positive or negative, depending on the Raman pump power. This tunability enables controlled exploration of integrability-breaking regimes in soliton gas evolution, as we'll see further.

4.2.3.2 From the Iterative Model to the Mean-Field Equation

Equations (4.4) and (4.5) can be rewritten as a single partial differential equation by replacing the round-trip boundary condition with a Dirac delta-comb term [89, 253]:

$$\left.\frac{\partial A_n}{\partial z}\right|_{z=nL} = \sum_n \ln(\rho)\delta(z - nL)A_n \tag{4.7}$$

Substituting Eq. (4.7) into Eq. (4.4) yields:

$$\frac{\partial A_n}{\partial z} = -i\left(\frac{\beta_2}{2}\frac{\partial^2 A_n}{\partial T^2} - \gamma|A_n|^2 A_n\right) + \frac{g_\mathrm{r}}{2}A_n - \sum_n \left(\frac{g_r + \alpha_\mathrm{eff}}{2}L\right)\delta(z - nL)A_n \tag{4.8}$$

We now derive the mean-field model by integrating Eq. (4.7) over a short interval around $z = nL$ [89, 253]. Let $z_{n\pm} = z_n \pm \epsilon$, with $\epsilon \ll 1$ and integrate across the discontinuity:

$$\int_{z_{n-}}^{z_{n+}} \frac{\partial A_n}{\partial z} dz = \int_{z_{n-}}^{z_{n+}} \left(\sum_n \left(-\frac{g_r + \alpha_\mathrm{eff}}{2}L\right)\delta(z - nL)\right) A_n \, dz \tag{4.9}$$

which yields,

$$A_n(z_{n+}) = A_n(z_{n-})\left[1 - \frac{g_r + \alpha_\mathrm{eff}}{2}L\right] \tag{4.10}$$

Next, we perform a Taylor expansion of A_n over one round trip, assuming small variation of the field A [89, 253]:

$$A_{n+1}(0,T) = \left(A_n(0,T) + \left.\frac{\partial A_n}{\partial z}\right|_{z=0} L\right)\left[1 - \frac{g_r + \alpha_\mathrm{eff}}{2}L\right] \tag{4.11}$$

Assuming that A varies slowly over a round-trip, and identifying $\frac{\partial A}{\partial z} = (A_{n+1} - A_n)/L$ in Eq. (4.4), we finally obtain the continuous mean-field model [253]:

$$\frac{\partial A}{\partial z} = -i\frac{\beta_2}{2}\frac{\partial^2 A}{\partial T^2} + \left[i\gamma|A|^2 - \frac{\alpha_\mathrm{eff}}{2}\right]A \tag{4.12}$$

This NLSE describes the evolution of the envelope over arbitrarily long distances, effectively averaging the discrete loop dynamics into a continuous propagation model. The control of α_eff in the experiment allows access to various damping or amplifying regimes.

4.2.3.3 Normalization of the mean-field equation

For theoretical analysis and numerical simulations, particularly for computing the discrete nonlinear spectrum from IST we introduce a normalized, dimen-

sionless form of the focusing 1D-NLS equation (4.12) using the transformations:

$$\begin{cases} t = \dfrac{\gamma P_0 z}{2}, \\ x = T\sqrt{\dfrac{\gamma P_0}{|\beta_2|}} \end{cases} \quad \begin{cases} \psi = \dfrac{A}{\sqrt{P_0}}, \\ \epsilon = \dfrac{\alpha_{\text{eff}}}{\gamma P_0} \end{cases} \tag{4.13}$$

where P_0 is a reference power found using the calibration method in Sec. 4.2.2.4. This yields the normalized focusing 1D-NLSE:

$$i\psi_t + \psi_{xx} + 2|\psi|^2\psi + i\epsilon\psi = 0 \tag{4.14}$$

4.3 Heterodyne measurement of the amplitude and phase of the optical field

Capturing the evolution of the IST spectrum of soliton gases (SGs) during propagation represents a major challenge in optics, as it requires simultaneous access to both the amplitude and phase of the optical field. During this thesis, we addressed this challenge by implementing a heterodyne detection scheme, in which the signal is mixed with a frequency-detuned reference laser and the resulting beating signal is detected by a fast photodiode.

4.3.1 Amplitude and phase reconstruction via heterodyne detection applied to a controlled phase-modulated optical pulse

Before applying this method to soliton gas experiments, we first validate it in a controlled setting. A proof-of-principle experiment is conducted, in which a continuous-wave (CW) laser is modulated both in intensity and in phase using electro-optic modulators. The goal is to reconstruct the complex envelope of the field (amplitude and phase) from the heterodyne measurement and verify whether the imposed phase modulation can be accurately retrieved by a demodulation procedure we present herein. Figure 4.12 shows the experimental setup used for this validation.

4.3.1.1 Experimental setup for heterodyne detection of a phase-modulated optical pulse

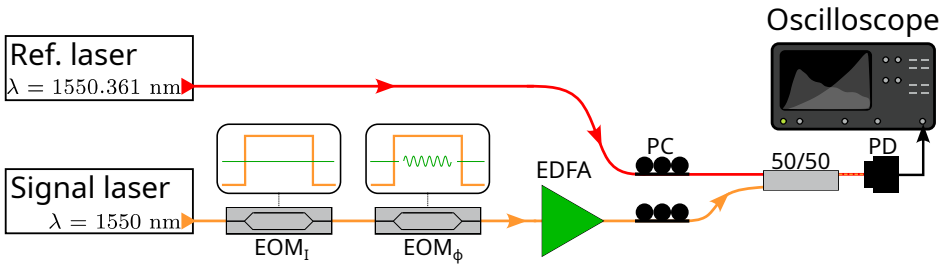

Figure 4.12: Proof-of-principle experiment demonstrating the heterodyne interferometry method for retrieving the amplitude and phase of an optical wavefield. EOM_I: Intensity electro-optic modulator. EOM_Φ: Phase electro-optic modulator. EDFA: Erbium-doped fiber amplifier. PC: Polarization controller.

Figure 4.12 shows the schematic of the experimental setup implemented for the heterodyne measurement of the amplitude and phase of the optical signal. A CW laser at 1550 nm is modulated both in intensity and phase. The phase modulation is performed using a high-speed phase electro-optic modulator (EOM_Φ, iXblue MPZ-LN-10, 16 GHz bandwidth), driven by an arbitrary waveform generator (AWG, Tektronix AWG 70000, 15 GHz bandwidth). Intensity modulation is applied using a second electro-optic modulator (EOM_I), and both modulators are driven by RF amplifiers (iXblue DR-AN-20-MO for EOM_Φ and iXblue DR-DG-20-MO for EOM_I), each with 20 GHz bandwidth. Synchronization of the intensity and phase modulations is ensured using the AWG synchronization module (Tektronix – AWGSYNC01).

As an initial condition, we generate a 50 ns flat-top optical pulse. A phase modulation in the form of a sinusoidal waveform of 1 GHz frequency and 30 ns duration is applied at the center of the pulse, see Fig. 4.13(d). Due to differences in the electrical signal paths, the phase modulation is temporally delayed by 16.1 ns relative to the intensity modulation.

While this test experiment is carried out on a well-controlled phase-modulated waveform, the same signal processing approach is later applied to the output of the recirculating fiber loop during soliton gas experiments. In that case, the detected field corresponds to the complex wavefield emerging after nonlinear

propagation, and the heterodyne reconstruction provides access to both amplitude and phase at each round trip. The present validation therefore serves as a benchmark to verify the accuracy and consistency of the method before deploying it in more complex dynamical regimes.

4.3.1.2 Method of reconstruction of the amplitude and phase of a signal using heterodyne interferometry

At the output of the setup, the optical signal is combined with a narrow-linewidth reference CW laser via a 50/50 fiber coupler, see Fig. 4.12. The reference source (APEX-AP3350A) is a single-frequency diode laser with an output power of a few milliwatts and a linewidth of 300 kHz, as specified in the manufacturer's datasheet. The reference wavelength is offset by 0.361 nm from the signal, corresponding to a frequency detuning of $\Delta f_0 \sim 45$ GHz. The optical signal resulting from the beating between the signal laser and the reference laser is detected by a high-speed photodiode (Finisar XPDV2120R), and its temporal interference pattern encodes both the amplitude and the phase of the signal field.

The voltage $V(T)$ detected by the photodiode can be written as:

$$V(T) = k\left|A_{\text{sig}}(T)e^{i\phi(T)} + A_{\text{Ref}}e^{i(2\pi\Delta f_0 T+\phi_{\text{Ref}})}\right|^2, \tag{4.15}$$

where $A_{\text{sig}}(T)$ and $\phi(T)$ denote the amplitude and phase of the signal field, and A_{Ref}, ϕ_{Ref} are the (constant) amplitude and phase of the reference laser. The constant k depends on the photodiode's characteristics and is determined through the calibration procedure detailed in Sec. 4.2.2.4.

Expanding Eq. (4.15), we obtain:

$$V(T) = k\left(A_{\text{sig}}^2(T) + A_{\text{Ref}}^2 + 2A_{\text{sig}}(T)A_{\text{Ref}}\cos\left[2\pi\Delta f_0 T + \phi_{\text{Ref}} - \phi(T)\right]\right). \tag{4.16}$$

This expression shows that the signal contains a DC component and two sidebands centered at $\pm\Delta f_0$. Given that Δf_0 is sufficiently large to avoid spectral overlap between the sidebands composing the fourier spectrum of the heterodyne signal, we numerically isolate the positive-frequency sideband via post-

processing of the recorded signal.

To extract the information of interest, we apply a 15^{th}-order causal Butterworth bandpass filter centered at Δf_0, with a full-width at half-maximum (FWHM) of 6 GHz, see red line in Fig. 4.13(b). This value is chosen to match the spectral width of the signal in this controlled phase-modulation experiment. In soliton gas experiments presented later, a broader filter (FWHM of 40 GHz) is used to account for the larger spectral content of the signal. In all cases, the filter removes the DC component and the negative-frequency sideband, leaving a complex-valued signal at the output of the filter that reads:

$$V_F(T) = k\, A_{\text{sig}}(T) A_{\text{Ref}}\, e^{i(2\pi\Delta f_0 T + \phi_{\text{Ref}} - \phi(T))}. \tag{4.17}$$

We then multiply $V_F(T)$ by $e^{-2\pi i \Delta f_0 T}$ to shift the signal to baseband:

$$V_{\text{dem}}(T) = k\, A_{\text{sig}}(T) A_{\text{Ref}}\, e^{i(\phi_{\text{Ref}} - \phi(T))}. \tag{4.18}$$

Assuming the reference phase ϕ_{Ref} is constant over the 50 ns pulse duration, it can be absorbed into a global phase offset. The amplitude and phase of the signal can then be retrieved as:

$$A_{\text{sig}}(T) \propto |V_{\text{dem}}(T)|, \tag{4.19}$$

$$\phi(T) = -\text{Arg}\,(V_{\text{dem}}(T)). \tag{4.20}$$

This procedure yields the full complex envelope of the optical field as a function of time.

4.3.1.3 Results of the reconstruction process

Figure 4.13 presents the main steps of the heterodyne field reconstruction applied to the phase-modulated waveform described earlier.

Fig. 4.13(a) shows the time window of the raw heterodyne signal $V(T)$ as recorded by the high-speed oscilloscope. It exhibits fast oscillations, as highlighted by the zoomed-in view in the inset. These rapid oscillations arise from the heterodyne beating between the signal and the local oscillator, occurring at a

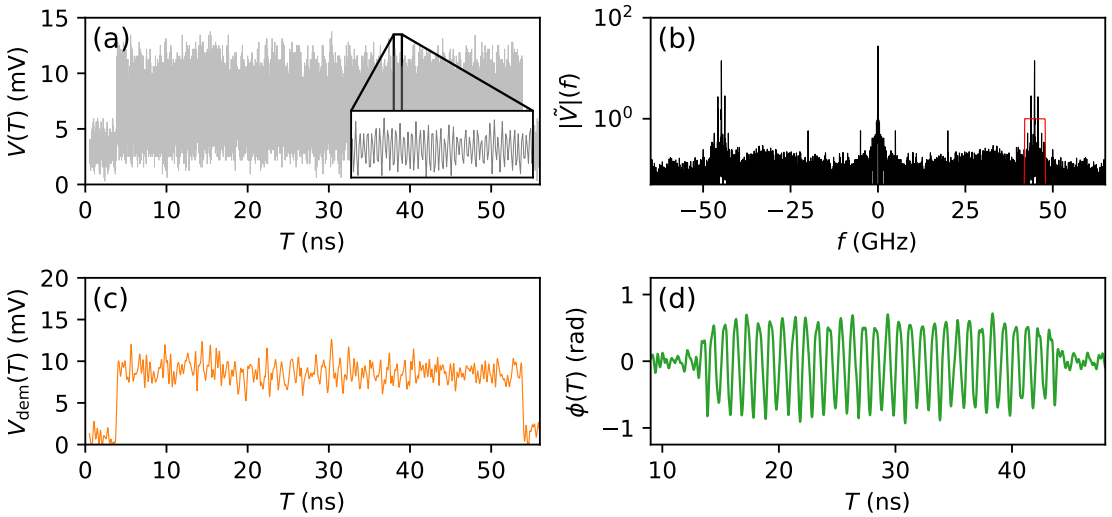

Figure 4.13: Demodulation scheme of the detected optical signal under the form of a pulse modulated in phase. (a) Experimental signal measured by the photodiode and the oscilloscope (b) Fourier power spectrum of the signal plotted in (a). The red line represents the modulus of the transfer function of the passband Butterworth filter used to filter the frequency components centered around 45 GHz, with 6 GHz FWHM. (c) Amplitude of the demodulated signal $A_{\mathrm{sig}}(T)$. (d) phase $\phi(T)$ of the optical signal.

frequency $\Delta f_0 \sim 45$ GHz. The corresponding Fourier power spectrum is shown in Fig. 4.13(b), revealing a well-defined peak centered at 45 GHz, as expected from the mixing of the signal with the detuned reference laser. The red curve represents the transfer function of the 15^{th}-order Butterworth bandpass filter with a 6 GHz FWHM, used to isolate the positive-frequency sideband.

After filtering and numerical demodulation, we reconstruct the complex signal envelope. Fig. 4.13(c) displays the amplitude $A_{\mathrm{sig}}(T) \propto |V_{\mathrm{dem}}(T)|$, which matches the expected 50 ns flat-top pulse shape. Fig. 4.13(d) shows the retrieved phase $\phi(T) = -\mathrm{Arg}(V_{\mathrm{dem}}(T))$, from which the imposed phase modulation can be clearly identified.

To sum up

In this section, we present the heterodyne interferometric method used to reconstruct the full complex envelope of an optical signal, including both amplitude and phase. The technique is demonstrated on a well-controlled waveform consisting of a continuous-wave laser modulated in both intensity and phase using electro-optic modulators. A sinusoidal phase modulation is embedded in a flat-top optical pulse, and the resulting field is mixed with a frequency-detuned reference laser. The interference signal is recorded by a high-speed photodiode and processed using a band-pass filter centered on the beat frequency. After numerical demodulation, the amplitude and phase of the original optical signal are successfully retrieved. This controlled experiment confirms the method's ability to recover phase information accurately, before applying it to more complex signals in soliton gas experiments.

4.3.2 Experimental Measurement System Limitations

In the following, we will compare experimental results, reconstructed using the validated heterodyne technique described in Sec. 4.3, with numerical simulations of the NLSE (Eq. (4.3)). The purpose of this comparison is not to test the heterodyne method itself, whose accuracy and reliability have been established, but rather to investigate how the finite detection bandwidth and additive detection noise affect the reconstruction of the complex optical field in practical conditions. To this end, we first apply the same demodulation and filtering procedure to numerically simulated signals, thereby mimicking the measurement system. This allows us to isolate and quantify the impact of these two limiting factors, and to assess the extent to which they may distort the experimentally reconstructed field.

To evaluate the influence of detection system limitations on the reconstructed signal, we use as a test case a numerically simulated wavefield $A(T) = A_{\text{sig}}(T)e^{i\phi(T)}$ obtained by solving the NLSE (Eq. (4.3)) with parameters closely matching experimental ones. Specifically, the simulated field results from the propagation

of a noisy square-shaped pulse over a distance of 1920 km, with an effective attenuation coefficient $\alpha_{\text{eff}} = 5.8 \times 10^{-4}$ km^{-1} and an initial optical power of 11.5 mW.

To mimic the heterodyne detection procedure, we numerically generate the interference between this simulated complex field and a monochromatic reference wave of constant amplitude and zero phase and detuned of $\Delta f_0 =$ 45 GHz with the signal, consistent with the experimental configuration.

$$I(T) = \left| A_{\text{sig}}(T) e^{i\phi(T)} + A_{\text{Ref}} e^{2i\pi\Delta f_0 T} \right|^2 \tag{4.21}$$

This synthetic heterodyne signal is then post-processed using the same reconstruction pipeline as in the experiment: bandpass filtering around Δf_0, followed by demodulation and extraction of the complex envelope. This approach allows us to selectively introduce experimental imperfections, such as limited detection bandwidth and additive noise, and to quantify their impact on the reconstructed amplitude and phase profiles, independently from the intrinsic performance of the heterodyne technique itself.

4.3.2.1 The finite detection bandwidth

Firstly, we account for the finite detection bandwidth of the experimental measurement setup. As described in Sec. 4.2.2.2, the optical intensity is recorded using a fast photodiode (Finisar XPDV2120R, nominal bandwidth of 50 GHz) connected to a high-speed oscilloscope (LeCroy Labmaster 10-65ZI, 65 GHz bandwidth and 160 GSa/s sampling rate). Together, these devices act as an effective first-order low-pass electrical filter, characterized by the transfer function:

$$H(f) = \frac{1}{1 + i\frac{f}{f_c}}, \tag{4.22}$$

with a cutoff frequency $f_c = 32$ GHz [247]. An experimental measurement of the modulus of this transfer function is presented in Appendix 5.3.

As shown in Fig. 4.14(c) (red dashed line), the frequency response is not flat over the detection bandwidth: the gain decreases significantly beyond 20 GHz,

indicating that spectral components around the carrier frequency $\Delta f_0 = 45$ GHz are already partially attenuated. To model the effect of this limitation, we apply the measured transfer function $H(f)$ to the Fourier spectrum of the heterodyne signal $I(T)$ given by Eq. (4.21).

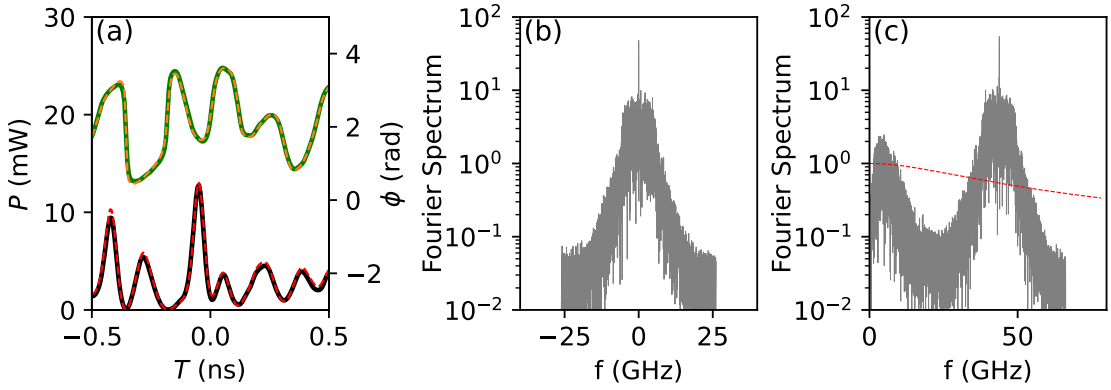

Figure 4.14: (a) Numerical simulation of the NLSE: power (black) and phase (green) of the optical wavefield. The red (resp. orange) dashed line shows the power (resp. phase) reconstructed using the heterodyne scheme described in Sec. 4.3, including finite bandwidth effects. (b) Fourier power spectrum of the simulated wavefield. (c) Fourier power spectrum of the heterodyne signal centered at 45 GHz. The red dashed line represents the magnitude of the 32 GHz low-pass filter used to model the finite detection bandwidth.

Figure 4.14 shows the influence of finite detection bandwidth on the heterodyne reconstruction applied to a simulated NLSE wavefield. The original wavefield (black for power, green for phase) is compared to the reconstructed version (red and orange dashed lines) in Fig. 4.14(a), revealing an excellent agreement. While the heterodyned spectrum shown in Fig. 4.14(c) does experience a frequency-dependent attenuation beyond 32 GHz, consistent with the measured transfer function, the impact on the reconstructed signal remains negligible at this stage. This shows that the detection bandwidth does not significantly alter the reconstructed amplitude or phase of the signal.

However, the finite detection bandwidth introduces a slight spectral tilt around the heterodyne frequency, which in turn causes a distortion of the spectral phase. This effect manifests as an artificial shift in the apparent velocity of the optical pulses, a subtle artifact that will become more apparent in the

IST-based spectral analysis (see Sec. 4.4.3).

4.3.2.2 The detection noise

We now consider the effect of detection noise, which primarily originates from the electrical noise of the photodetector. To model this, we add noise to the Fourier spectrum of the heterodyne signal $I(T)$ defined in Eq. (4.21), with a noise level similar to the experimental detection noise.

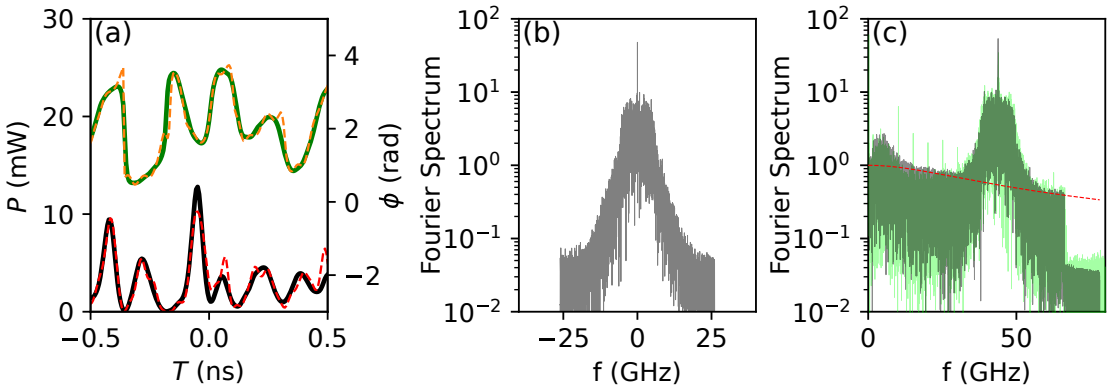

Figure 4.15: (a) The black (resp. green) line represents the power (resp. phase) fluctuations of a wavefield obtained from numerical simulation of NLSE. The red (resp. orange) dashed line represents power (resp. phase) fluctuations that are reconstructed using the heterodyne scheme described in Sec. 4.3 including finite bandwidth effects and detection noise. (b) Fourier power spectrum of the wavefield. (c) Fourier power spectrum of the heterodyne signal perturbated by the added detection noise. The red dashed line represents the modulus of the transfer function of the 32 GHz filter describing finite bandwidth effects. In green is superimposed the associated experimental spectrum.

In Fig. 4.15(c), the power spectrum of the simulated noisy signal is shown in grey (being the spectrum shown in Fig. 4.14(c) with a noise level being the experimental one), while the experimentally measured heterodyne spectrum, corresponding to a similar flat-top pulse measurement, is overlaid in transparent green. This comparison confirms that the noise level introduced in the simulation is consistent with the experimental conditions.

Figure 4.15(c) shows the Fourier spectrum of the heterodyne signal after adding detection noise. For comparison, the ideal bandwidth-limited spectrum

without noise is shown in Fig. 4.14(c). The added noise visibly fills the spectral background and leads to deviations in both the power and phase reconstructions, as illustrated in Fig. 4.15(a). While the heterodyne method still permits the retrieval of meaningful information, the accuracy is noticeably degraded compared to the case without noise.

Compared to the effect of finite detection bandwidth, this degradation is more pronounced and shows the role played by detection noise in limiting the reconstruction accuracy. Just as finite bandwidth induces a subtle artificial velocity in the retrieved waveform, detection noise introduces spectral artifacts that will have consequences when analyzing the IST spectra, as will be discussed in Sec. 4.4.3.

4.4 Evolution of optical soliton gas in the recirculating fiber loop in the presence of small damping

In this section, we investigate the impact of weak effective average power loss on the dynamics of an optical soliton gas initially prepared as a 100 ns flat-top optical pulse with an average power of 11.5 mW. We first analyze the evolution of its dynamical features and then explore the changes in its statistical properties, in particular its density of states (DOS).

4.4.1 Experimental Space-Time Dynamics

Figure 4.16(a) displays the experimentally measured average power $P(z)$ of the circulating wavefield, which decays from its initial value $P_0 \sim 11.5$ mW to approximately 2 mW after a propagation distance of around 3200 km. The red dashed line corresponds to an exponential fit of the decay, yielding an effective loss coefficient $\alpha_{\text{eff}} \sim 5.8 \times 10^{-4}$ km^{-1}, or equivalently about 0.0025 dB/km.

Figure 4.16(b) shows the reconstructed space-time diagram over a narrow 5 ns window. At a qualitative level, the observed dynamics resemble those of noise-driven modulation instability (MI) in systems governed by the focusing 1D-NLSE, as reported in Refs. [98, 112, 247]. Initially, the optical field appears as a noisy plane wave (see Fig. 4.16(d)), and rapidly develops random, highly

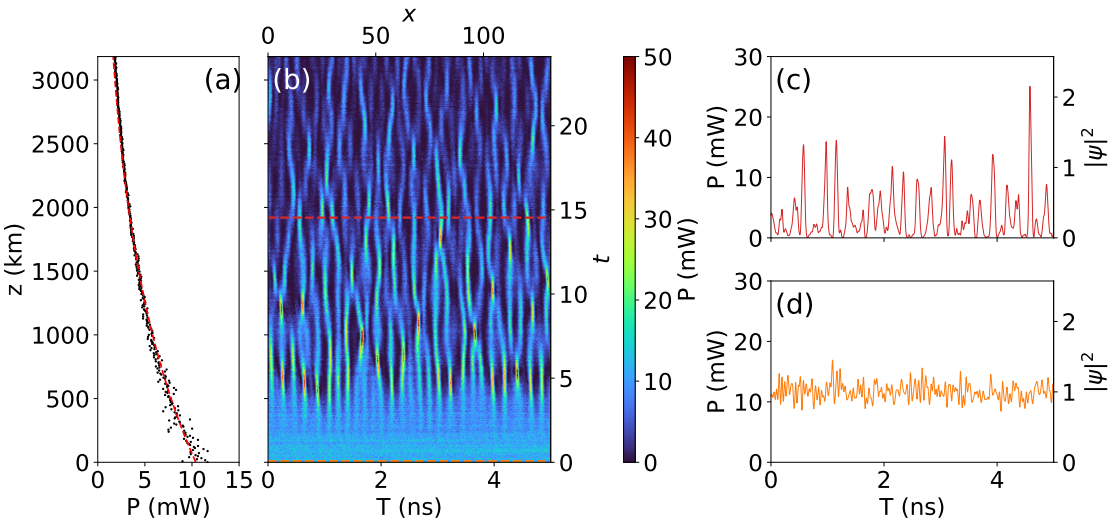

Figure 4.16: Experiment showing the evolution of an optical soliton gas (SG) in a recirculating fiber loop under weak damping. (a) Measured mean optical power as a function of propagation distance z; black points: experimental data; red dashed line: exponential fit with $\alpha_{\text{eff}} \sim 5.8 \times 10^{-4}$ km^{-1}. (b) Experimental space-time diagram showing the evolution of the SG over a 5 ns time window. The top and right axes respectively display the normalized space $x = T\sqrt{\gamma P_0/|\beta_2|}$ and normalized time $t = \gamma P_0 z/2$. (c) and (d) show snapshots of the optical power at $z = 1920$ km and $z = 8$ km, respectively. Right axes indicate the normalized power $|\psi|^2$.

nonlinear breather-like structures characteristic of MI (see Fig. 4.16(c)).

The space-time diagram further suggests that the presence of weak dissipation does not inhibit the onset of MI.

4.4.2 Nonlinear Spectral Analysis and Density of States

We now investigate how the discrete IST spectra of the optical SG is affected by the weak dissipation on the system's dynamics. To perform this analysis, we normalize the experimental complex wavefield obtained from the space-time diagram in Fig. 4.16(b) using the transformation defined in Eq. (4.13).

Within the IST formalism, the discrete spectrum associated with the focusing 1D-NLSE (in the integrable case where $\epsilon = 0$ in Eq. (4.14)) is obtained by solving

the Zakharov–Shabat (ZS) eigenvalue problem [116]:

$$\widehat{\mathcal{L}}\Phi = \lambda\Phi, \qquad \widehat{\mathcal{L}} = \begin{pmatrix} -i\partial_x & -i\psi \\ -i\psi^* & i\partial_x \end{pmatrix}, \tag{4.23}$$

where $\lambda \in \mathbb{C}$ are the discrete eigenvalues associated with the solitonic content of the field $\psi(x,t)$, measured at a given propagation time t (or equivalently at a given propagation distance z in the recirculating fiber loop). The spectrum is computed numerically by solving Eq. (4.23) using the Fourier collocation method described in Ref. [102]. This yields an ensemble of several hundred complex-valued eigenvalues λ_j located in a bounded region of the upper half complex plane. Each eigenvalue is written as $\lambda_j = \xi_j + i\eta_j$, where $\xi_j \in \mathbb{R}$ is the real part and $\eta_j > 0$ the imaginary part. The real part governs the soliton velocity, while the imaginary part determines its amplitude. These spectral parameters will be used to construct the discrete IST spectrum shown in the following figures.

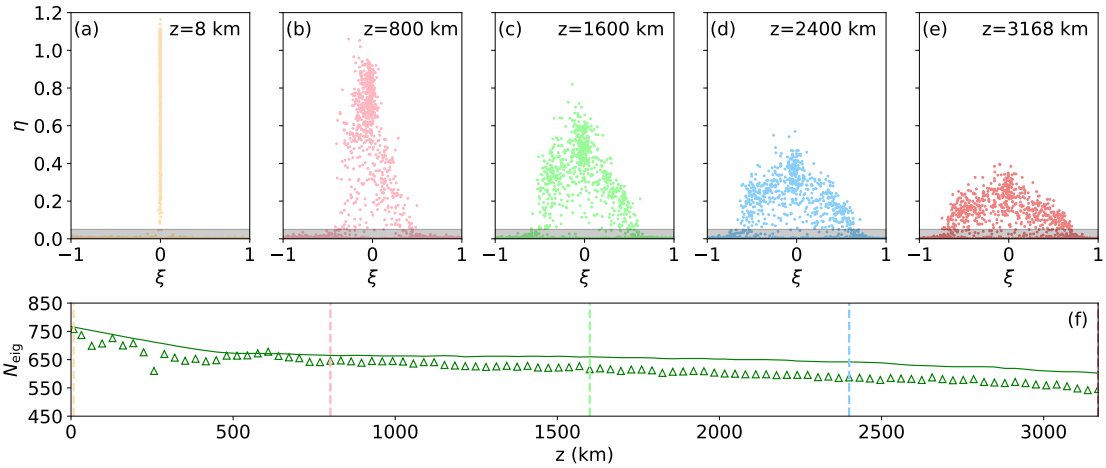

Figure 4.17: Evolution of the IST spectrum of the experimental optical SG. (a) Discrete spectrum computed at $z = 8$ km. (b–e) Same as (a), but at $z = 800$, 1600, 2400, and 3168 km. (f) Evolution of the number of discrete eigenvalues as a function of propagation distance z: green triangles correspond to experimental data, and the green solid line to numerical simulations of Eq. (4.3) using experimental parameters.

Although the dissipation is small ($\epsilon \sim 0.038$ in Eq. (4.14)), the IST analysis re-

mains a valuable tool for characterizing the evolution of the gas. Figures 4.17(a–e) show how the distribution of eigenvalues changes along the propagation. Unlike the integrable case, the dynamics here is non-isospectral: the discrete IST spectrum evolves during propagation.

Two key effects are observed. First, the imaginary parts of the eigenvalues which encode the amplitude of the solitons, gradually decrease. Starting from a maximum imaginary part $\eta_{\max} \simeq 1$ at $z = 8$ km, the imaginary parts shrinks to $\eta_{\max} \sim 0.3$ at $z = 3168$ km. This trend is consistent with the dissipative nature of the system: as the mean power decreases, the individual solitons lose amplitude.

Second, and more surprisingly, the eigenvalues develop non-zero real parts (encoding solitons' velocities) as the system evolves. While the initial spectrum lies almost entirely along the imaginary axis ($\xi_j \sim 0 \, \forall j$), subsequent spectra show a symmetric broadening along the real axis. This spectral deformation suggests the creation of velocity distribution of solitons and reflect emergent collective effects induced by the weak dissipation. During the propagation distance (in particular at $z \sim 1920$ m), the spectrum forms a shape close to a semi-circle, a hallmark of the dissipative rearrangement of soliton states. This spectral transformation will be further observed in the next section through the analysis of the DOS.

While the mechanism responsible for the emergence of soliton velocities remains to be fully understood[1], the fact that the real parts of the eigenvalues broaden symmetrically around zero can be explained by the conservation of momentum [254]. The initial condition is a symmetric pulse, which implies that the field $\psi(x)$ is even and that its initial momentum is zero. The momentum is defined as [102]

$$M = \int_{-\infty}^{+\infty} \left(\frac{\partial \psi}{\partial x} \right) \psi^* \, \mathrm{d}x,$$

and it evolves in the presence of weak dissipation according to $M(t) = M(0) e^{-2\epsilon t}$

[1] Attempts using IST perturbation theory exist for a small number of eigenvalues [254, 255]. Analyses show that, under weak damping, eigenvalues with larger imaginary parts can decay faster than those with smaller ones. This non-uniform evolution could in principle lead to eigenvalue crossings. However, due to the non-degeneracy of the Zakharov–Shabat operator, such crossings are forbidden. As a result, eigenvalues develop non-zero real parts to avoid "collisions", which effectively induces a repulsion mechanism in the complex plane [225].

(see Appendix 5.5). Since $M(0) = 0$, the total momentum remains strictly zero at all times.

Now, in the framework of the IST, the momentum of an N-soliton solution can also be expressed as a weighted sum over the real parts of the discrete eigenvalues $\lambda_j = \xi_j + i\eta_j$ [119]:

$$M = -\frac{1}{2}\sum_{j=1}^{N} \eta_j \xi_j,$$

As a result, the emergence of nonzero real parts $\xi_j \neq 0$ during evolution must occur in a way that preserves the total momentum. This constraint requires that for every eigenvalue acquiring a positive real part, another eigenvalue develops a negative real part of equal magnitude. This explains the observed symmetric spreading of the spectrum along the real axis.

In practice, especially when the initial condition is perturbed by some random noise, this symmetry holds only statistically. Small asymmetries in the real parts ξ_j may appear in a given realization, but the ensemble-averaged momentum remains close to zero.

Figure 4.17(f) shows the evolution of the number of discrete eigenvalues found in the upper complex plane above the threshold $\eta = 0.05$, as indicated by the shaded region in Figs. 4.17(a–e). This threshold is introduced to exclude weak spectral components potentially associated with low amplitude noise in the wavefield. The number of eigenvalues, denoted N_{eig}, decreases from approximately 758 at $z = 8$ km to 546 at $z = 3168$ km, representing a loss of about 27%. In contrast, the average optical power is reduced by nearly a factor of 6 over the same distance (from 11.6 mW to 1.8 mW), see Fig. 4.16(a).

Given the large number of discrete eigenvalues obtained from the nonlinear spectral analysis, we follow the approach introduced in the kinetic theory of soliton gases and compute the so-called density of states (DOS) $f(\lambda; x, t)$ [2] [35]. Since the optical SG is approximately spatially homogeneous, the DOS $f(\lambda)$ can

[2] In this chapter, the spatial variable x corresponds to the fast time T in the frame moving with the group velocity, while the slow evolution variable t is associated with the propagation distance z along the fiber.

be interpreted as the normalized probability density function of the complex-valued eigenvalues λ. It is normalized such that:

$$\int_{-\infty}^{+\infty} d\xi \int_{0}^{+\infty} d\eta\, f(\lambda) = \frac{N}{\Delta x},$$

where N is the number of eigenvalues in the upper half of the complex plane, and $\Delta x \sim 2600$ denotes the spatial extent of the soliton gas, corresponding to a temporal duration of $\Delta T \sim 100$ ns.

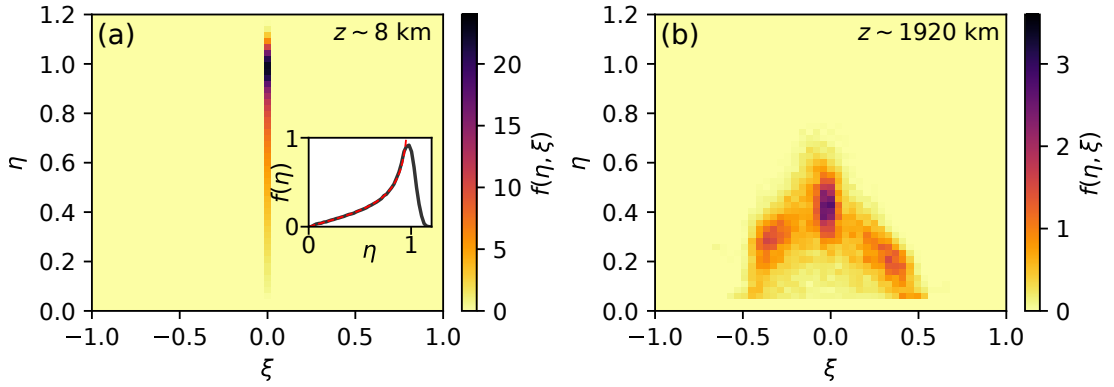

Figure 4.18: Experimental evolution of the density of states (DOS) in the presence of weak damping. (a) DOS corresponding to the initial condition measured at $z = 8$ km. The inset shows the DOS integrated along the ξ-axis, the red dashed line corresponds to the analytical Weyl distribution, Eq. (4.24). (b) DOS measured at $z = 1920$ km.

Figure 4.18 presents the experimentally measured DOS. Rather than relying on a single realization, we average over three identical flat-top pulses that propagate independently within the loop during the same experimental run. In addition, the DOS is computed by averaging over 10 consecutive roundtrips (i.e., ±5 roundtrips around the central propagation distance), corresponding to an 80 km propagation span. This approach increases the size of the statistical ensemble, which includes approximately 23,200 (resp. 18,300) discrete eigenvalues at $z = 0$ km (resp. $z = 1920$ km). This approach assumes minimal evolution of the IST spectra over this short propagation interval.

Fig. 4.18(a) shows the DOS of the initial condition at $z = 8$ km: a flat-top pulse perturbed by weak optical noise. As expected from previous studies [122],

the measured DOS closely follows the Weyl distribution (see the inset), given by,

$$f(\eta) = \frac{\eta}{\pi\sqrt{1-\eta^2}} \tag{4.24}$$

Due to dissipation, the isospectrality condition is broken in our experiment. As a result, the DOS evolves with propagation. Fig. 4.18(b) shows the DOS measured at $z \sim 1920$ km. We observe a striking transformation of the spectral support: while the initial DOS is vertically aligned along the imaginary axis, the damped system exhibits a broadened, nearly semicircular spectral support in the upper complex plane.

It is noteworthy that the concept of circular spectral support for soliton gas DOS was introduced in recent mathematical works [121, 256], although it was not expected to arise either experimentally or in non-integrable settings. Our results provide, to the best of our knowledge, the first experimental evidence of such a structure emerging from dissipative NLS dynamics.

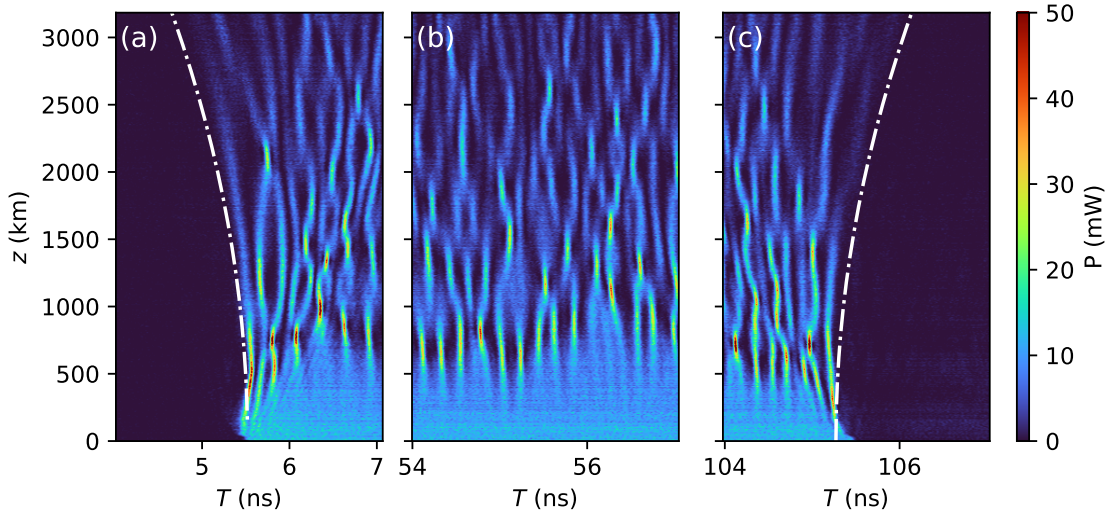

Figure 4.19: Experimental space-time diagrams showing the evolution of three distinct temporal regions of the same optical soliton gas under weak damping. (a) Left edge of the pulse ($T \in [4,7]$ ns), (b) center region ($T \in [54,57]$ ns), and (c) right edge ($T \in [104,107]$ ns). All panels share the same color scale for the optical power. The white dashed lines highlight the spreading of the pulse edges.

To further characterize the spatial evolution of the soliton gas, we examine how different temporal regions of the initial flat-top pulse evolve under

weak damping. Figure 4.19 displays three space-time diagrams extracted from different segments of the 100 ns pulse, each spanning a 3 ns window.

Figure 4.19 shows that the wavefield broadens at both edges of the square pulse (Figs. 4.19(a) and (c)) around $T \sim 5.5$ ns and $T \sim 105$ ns, as highlighted by the dashed white lines. This expansion shows that some solitons acquire non-zero velocities and gradually escape the central region. This dynamical behavior is consistent with the spectral broadening observed in the DOS (Fig. 4.18(b)), where semi-circular spectral contours indicate the emergence of solitons with finite velocities.

4.4.3 NLSE Simulations with a Small Damping Term

To complement the experimental observations, we perform numerical simulations of the NLSE including a small damping term, using the same initial condition as in the experiment: a broad square-shaped pulse with an average power of 11.6 mW. Numerically, the initial condition is under the form of a super-Gaussian pulse, with full width at half maximum $T_0 \approx 100\,\mathrm{ns}$, mean power $P_0 = 11.5\,\mathrm{mW}$, and exponent $p = 200$:

$$A(T, z = 0) = \sqrt{P_0} \exp\left[-\left(\frac{T^2}{2\sigma^2}\right)^p\right], \quad \text{with } \sigma = \frac{T_0}{2\sqrt{2\ln 2}}.$$

This envelope is perturbed by the addition of a small noise generated in the spectral domain from a Gaussian-shaped spectrum with Fourier components having random phases and amplitudes. This results in random intensity fluctuations in the time domain.

Figure 4.20 compares the space-time evolution of the optical SG obtained experimentally (see Fig. 4.20(a)) with the numerical simulation of the damped NLSE, Eq. (4.3) (see Fig. 4.20(b)), using the same initial conditions and parameters. The NLSE simulation qualitatively reproduces the main features observed in the experiment, including the emergence of localized structures from modulation instability and the global decay of the wavefield due to dissipation.

To further analyze the dynamics, we perform a nonlinear spectral analysis on the numerical data like previously in the experiment. From an ensemble of 30

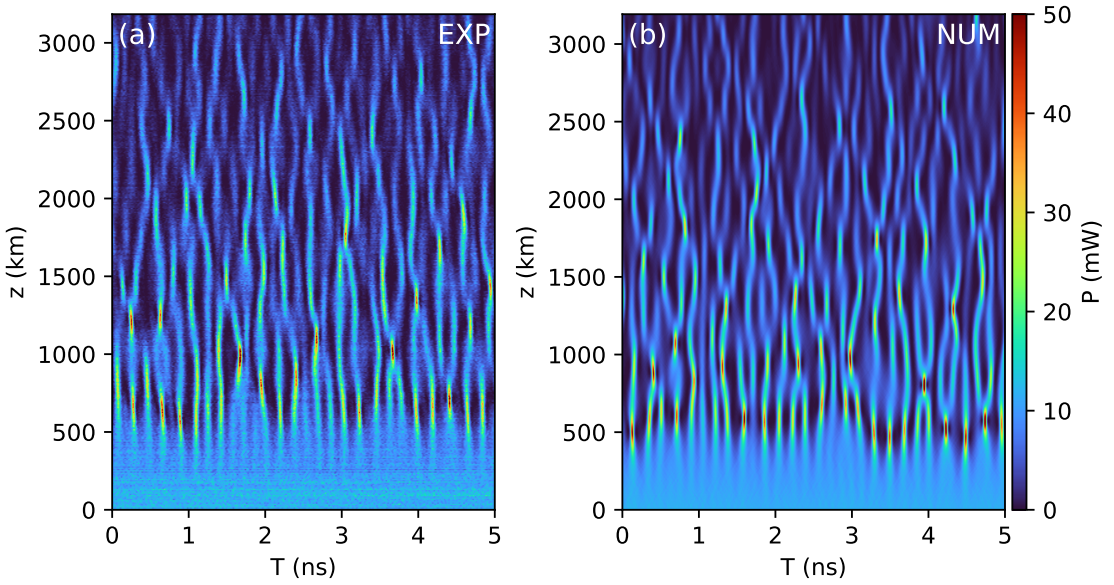

Figure 4.20: (a) Experimental space-time diagram of the optical SG under weak damping. (b) Corresponding numerical simulation of Eq. (4.3) using the experimental parameters: $\gamma = 1.3\ \mathrm{W}^{-1}.\mathrm{km}^{-1}$, $\beta_2 = -22\ \mathrm{ps}^2/\mathrm{km}$, $\alpha_{\mathrm{eff}} = 5.8 \times 10^{-4}\ \mathrm{km}^{-1}$, and $P_0 = 11.5$ mW.

independent simulations, we extract the complex fields at $z = 8$ and $z = 1920$ km and compute the corresponding IST spectra. This allows us to calculate the numerical DOS and directly compare it to the experimentally measured one.

Figure 4.21 presents a detailed comparison between the experimental and numerical DOS. Figs. 4.21(a) and (d) show the experimental DOS at $z = 1920$ km and $z = 8$ km, respectively. As shown in Figs. 4.21(b) and 4.21(e), the dissipation-induced deformation of the DOS support is also reproduced in numerical simulations of Eq. (4.3) using parameters identical to those of the experiment. In particular, the emergence of a semicircular spectral contour, absent in the initial distribution, is clearly observed. This confirms that the NLSE model with weak damping captures the essential features of the nonlinear spectral evolution measured experimentally.

It is worth noting, however, that the DOS obtained from numerical simulations (see Fig. 4.21(b)) displays a perfectly symmetric structure around the imaginary axis, which is not observed in the experiment (see Fig. 4.21(a)). The experimental DOS also appears more diffuse. These discrepancies are attributed

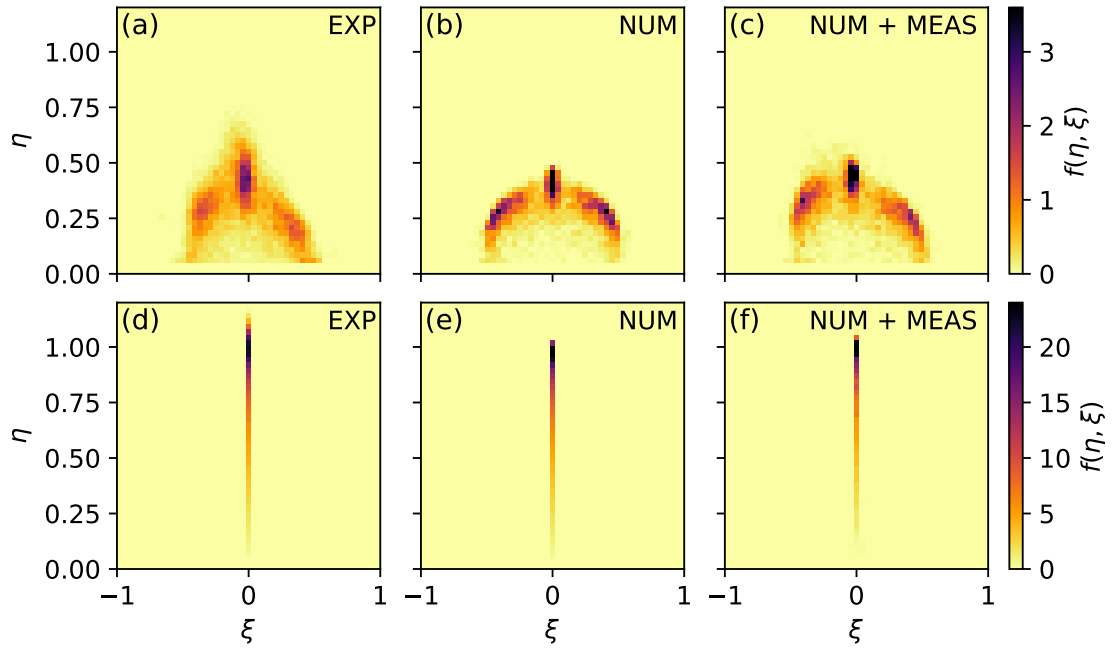

Figure 4.21: (a,d) Experimental DOS of the optical SG at $z = 1920$ km and $z = 8$ km, respectively. (b,e) Same as (a,d), but computed from the NLSE simulations shown in Fig. 4.20(b). (c,f) Same as (b,e), but including detection effects (finite bandwidth and noise) as described in Sec. 4.3.2.

to detection limitations in the heterodyne measurement technique, including finite bandwidth and measurement noise, as demonstrated in Figs. 4.21(c) and (f), and discussed in detail in Sec. 4.3.2.

To sum up

This section investigates the evolution of an optical soliton gas propagating in a recirculating fiber loop in the presence of weak damping. Experimentally a flat-top noisy pulse is generated and develops under the form of a bound state SG, and its dynamics are recorded over thousands of kilometers. Nonlinear spectral analysis reveals two key effects induced by damping: a progressive decay of soliton amplitudes, corresponding to a decay of the imaginary parts of eigenvalues; and the emergence of a symmetric distribution of soliton velocities, associated to the broadening of the real parts of eigenvalues. The associated density of states evolves from a vertical line along the imaginary axis to a broadened, semicircular support. These findings are reproduced in simulations of the NLSE with a small damping term.

4.5 Evolution of optical soliton gas in the recirculating fiber loop in the presence of small gain

Having previously explored the effect of weak damping on the dynamical and statistical properties of an optical soliton gas, we now turn to the complementary case of weak effective average power gain. In this experiment, the SG is prepared as a 100 ns flat-top optical pulse with an initial average power of approximately 2 mW. We first examine its dynamical evolution, followed by an analysis of the corresponding nonlinear spectral properties, particularly the evolution of the density of states.

4.5.1 Experimental space-time dynamics

Figure 4.22(a) shows the measured average power $P(z)$ of the wavefield as it propagates in the fiber loop under the influence of weak gain. The mean power increases from an initial value of approximately 2 mW to around 4 mW after a propagation distance of 6300 km. The effective gain coefficient, extracted from

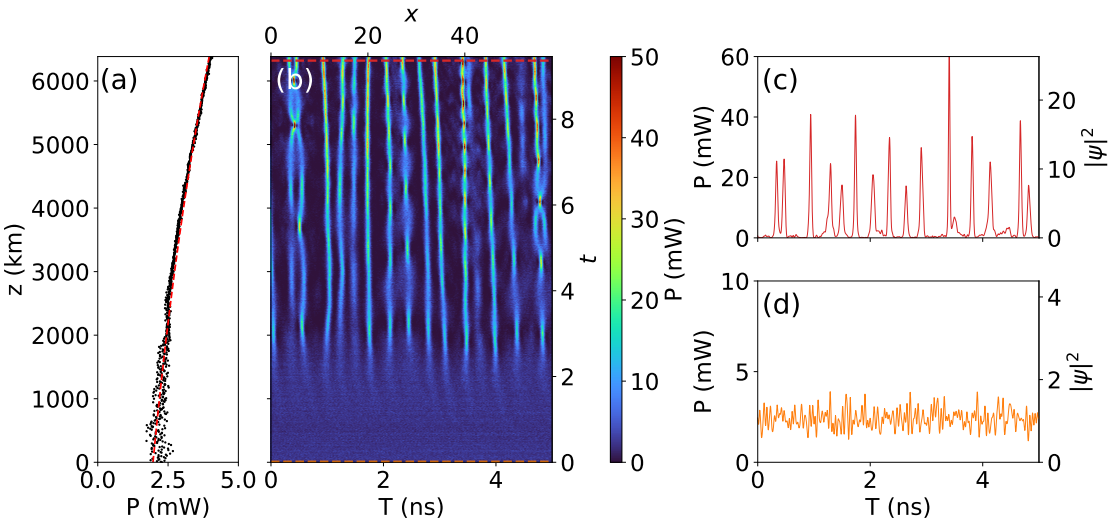

Figure 4.22: Experimental evolution of an optical SG in a recirculating fiber loop under weak gain. (a) Measured mean power as a function of propagation distance z; black points: experimental data; red dashed line: exponential fit with $\alpha_{\text{eff}} \sim -1.1 \times 10^{-4}$ km^{-1}. (b) Space-time diagram showing the evolution of the optical SG over a 5 ns time window. The top and right axes respectively display the normalized space $x = T\sqrt{\gamma P_0/|\beta_2|}$ and normalized time $t = \gamma P_0 z/2$. (c) and (d) show snapshots of the wavefield power at $z = 6320$ km and $z = 8$ km, respectively. Right axes indicate the normalized power $|\psi|^2$.

an exponential fit to the measured intra-loop power, is $\alpha_{\text{eff}} \sim -1.1 \times 10^{-4}$ km^{-1}, or equivalently about -0.00047 dB/km. This weak amplification regime is obtained by slightly increasing the power of the 1450 nm Raman pump laser via the variable optical attenuator (VOA).

Figure 4.22(b) presents the reconstructed space-time diagram of the SG over a narrow 5 ns observation window. The dynamics observed in the presence of gain differ strikingly from the dissipative case discussed in Fig. 4.16(b). While the damping regime typically leads to patterns qualitatively similar to those associated to the noise-induced destabilization of a plane wave through the process of MI, the gain regime induces a qualitatively different behavior: after the initial destabilization of the flat-top pulse, localized coherent structures form and persist over long distances. These structures get separated and individualized, with small relative velocities.

At a qualitative level, this dynamical behavior shares similarities with the

phenomenon of growing integrable turbulence, as reported in numerical studies starting from weak Gaussian noise [257]. To the best of our knowledge, such a regime has never been directly observed in experiments. The observed spatial ordering of localized structures also evokes visual analogies with dissipative soliton crystallization in Kerr resonators [258, 259], although the underlying physics is fundamentally different.

4.5.2 Nonlinear Spectral Analysis and Density of States

We now apply the same nonlinear spectral analysis as in the damping case, by computing the discrete IST spectra of the optical soliton gas from the experimentally reconstructed complex field. This is done by solving the Zakharov–Shabat eigenvalue problem (see Eq. (4.23)) using the Fourier collocation method [102].

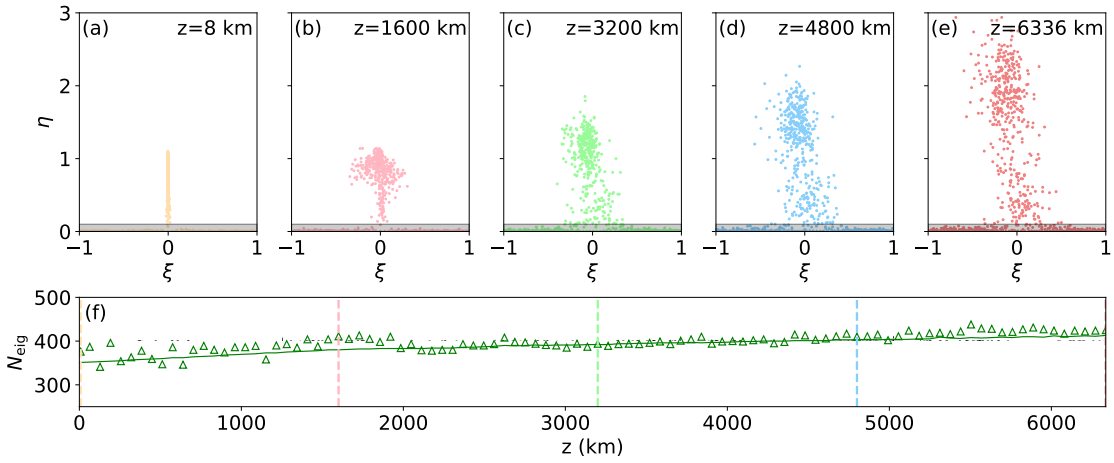

Figure 4.23: Evolution of the experimental IST spectra in the presence of gain. (a) Discrete spectrum computed at $z = 8$ km. (b–e) Same as (a) but at $z = 1600$, 3200, 4800, and 6336 km. (f) Evolution of the number of discrete eigenvalues above $\eta = 0.1$ (gray shaded region in panels a–e); green triangles: experiment; green line: numerical simulations of Eq. (4.3) using experimental parameters.

Figures 4.23(a–e) show the evolution of the IST spectra at increasing propagation distances. As in the damping case, the dynamics is not isospectral: the spectral portrait changes with distance, which highlights the breaking of integrability due to the presence of gain. However, the nature of the spectral evolution is different from the damping regime. In particular, we observe a gradual increase

in the imaginary parts of the eigenvalues. The imaginary part of the largest eigenvalues increases from ~ 1 to ~ 2. This indicates that the solitons in the gas gain amplitude during the evolution, consistent with the amplification.

The real parts of the eigenvalues, which encode the velocities of the solitons, remain concentrated around zero. This spectral signature ($\xi \sim 0$) confirms that most solitons exhibit small relative velocities. This is in stark contrast with the damping case (see Figs. 4.17(a–e)), where dissipation broadened the soliton velocity distribution.

Figure 4.23(f) shows the evolution of the number of discrete eigenvalues with imaginary parts above the threshold $\eta = 0.1$, as indicated by the shaded regions in panels (a–e). The number of eigenvalues increases from approximately $N_{\text{eig}} \sim 376$ to $N_{\text{eig}} \sim 425$, corresponding to a net growth of about 11%. In contrast, the average optical power doubles over the same distance, increasing from 2 mW to 4 mW (see Fig. 4.22(a)).

These observations suggest that, in the presence of weak gain, the total increase in optical power translates only to a limited extent into an increased soliton count; most of the energy is transferred to existing solitons, increasing their amplitudes rather than producing a large number of new ones.

Given the large number of discrete eigenvalues obtained from the nonlinear spectral analysis, we compute the density of states to statistically characterize the soliton gas.

Figure 4.24 presents the experimentally measured DOS at the small ($z \sim 8$ km) and large ($z \sim 6320$ km) propagation distance. The DOS is computed by averaging the IST spectra of three identical flat-top pulses, each propagating independently in the fiber loop during the same experimental run. As in the experiment with damping described in Sec. 4.4.2 , we assume negligible variation in the IST spectra over a short propagation span (80 km), which allows us to increase the statistics for the DOS measurement.

Figure 4.24(a) shows the DOS corresponding to the initial condition at $z =$ 8 km : a flat-top pulse perturbed by weak optical noise (see Fig. 4.22(d)). The DOS is well approximated by the Weyl distribution, Eq.é(4.24), see inset.

Figure 4.24(b) displays the DOS after 6320 km of propagation under weak gain. into two distinct clustered distributions. One of these clusters is centered

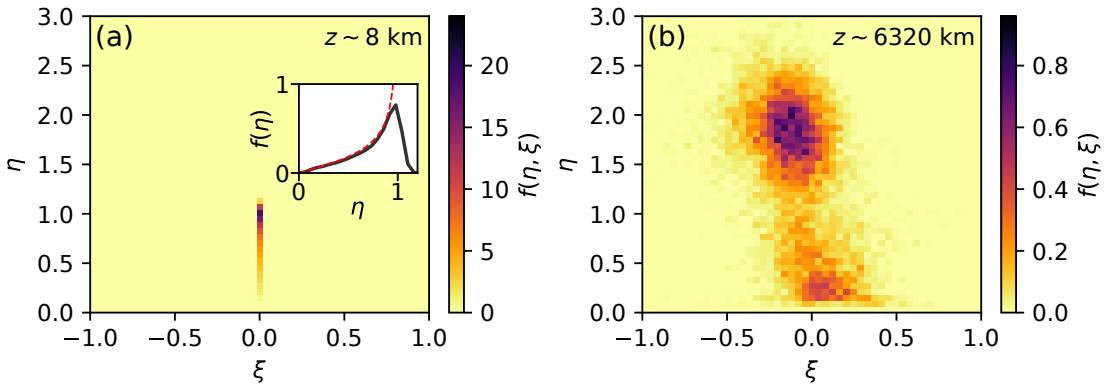

Figure 4.24: Evolution of the experimental DOS in the presence of small gain. (a) DOS of the initial condition at $z = 8$ km. The inset shows the DOS integrated along the ξ-axis, the red dashed line corresponds to the analytical Weyl distribution, Eq. (4.24). (b) DOS of the optical SG measured at $z = 6320$ km in the upper complex plane.

around $\lambda_0 \sim 1.8i$, while the other is centered around $\lambda_1 \sim 0.3i.$, characteristic of a bichromatic SG [32, 38]. The real parts of the eigenvalues remain close to zero, which, as discussed earlier, implies that most solitons propagate with small relative velocities.

4.5.3 NLSE simulation with a small gain term

As in the case of damping, we compare the experimental results obtained under weak gain with numerical simulations of the NLSE that incorporate a small linear amplification term. These simulations are performed by numerically integrating Eq. (4.3) using the experimentally measured parameters.

Figure 4.25 compares the space-time dynamics observed experimentally (see Fig. 4.25(a)) with those obtained from numerical simulations of Eq. (4.3) (see Fig. 4.25(b)). The simulation parameters are the experimental ones, in terms of initial average power, gain coefficient, and pulse shape. The numerical results qualitatively reproduce the key features observed in the experiment, such as the emergence and persistence of localized structures.

To further validate the physical interpretation of the experimental results, we perform a statistical analysis over an ensemble of 30 numerical simulations, each

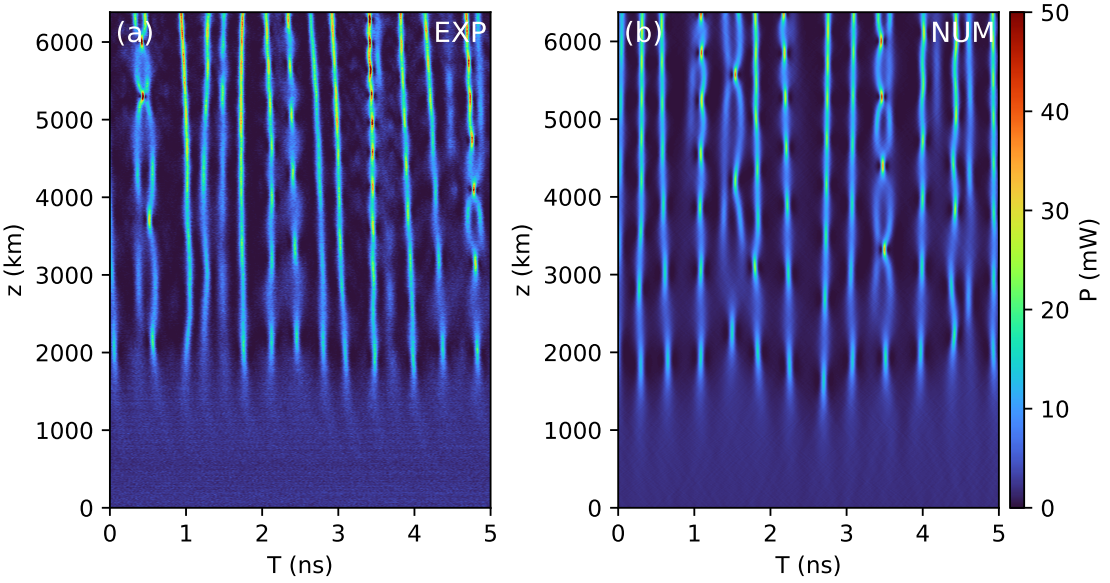

Figure 4.25: (a) Experimental space-time diagram showing the evolution of the optical SG under weak gain. (b) Same as (a), but computed from numerical simulations of Eq. (4.3) with parameters: $\gamma = 1.3\,\mathrm{W}^{-1}.\mathrm{km}^{-1}$, $\beta_2 = -22\,\mathrm{ps}^2.\mathrm{km}^{-1}$, $\alpha_{\mathrm{eff}} = -1.1 \times 10^{-4}\,\mathrm{km}^{-1}$, and $P_0 = 2\,\mathrm{mW}$.

initialized with a different realization of noise. From the complex wavefields at $z = 8$ and $z = 6320$ km, we extract the IST spectra and compute the corresponding DOS.

Figure 4.26 presents a comparison between the experimentally measured DOS (Figs. 4.26(a)(d)) and that obtained from numerical simulations of the NLSE with gain (Figs. 4.26(b)(e)). While the simulations qualitatively reproduce the upward shift and partial clustering of the spectral support, showing the emergence of a nearleay bichromatic SG, noticeable discrepancies remain. A more accurate agreement is obtained when experimental effects such as finite detection bandwidth and noise are taken into account (see Figs. 4.26(c)(f)).

Figs. 4.26(c)(f) show the simulated DOS including the effects of the experimental measurement system : finite detection bandwidth and noise in the heterodyne acquisition scheme. These measurement effects are modeled using the procedure described in Sec. 4.3.2. The resulting DOS is in excellent agreement with the experimental one, demonstrating that the small discrepancies between raw numerical results and measurements can be fully attributed to

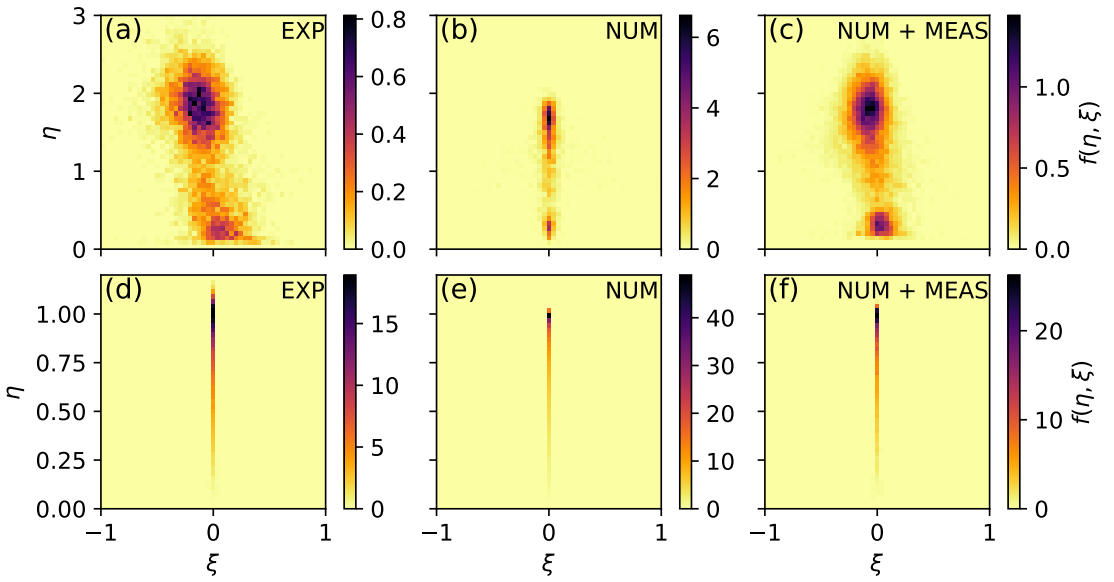

Figure 4.26: Comparison of experimental and numerical DOS. (a,d) DOS measured experimentally at $z = 6320$ km and $z = 8$ km. (b,e) Same as (a,d), but computed from simulations shown in Fig. 4.25(b). (c,f) Same as (b,e), but including finite bandwidth and noise effects in the heterodyne detection process (see Sec. 4.3.2).

detection limitations rather than to physical model inaccuracies.

These results confirm that the amplified NLSE dynamics, combined with the heterodyne detection model, accurately reproduce the main experimental features, including the emergence of two clustered spectral supports around $\lambda_0 \sim 1.8i$ and $\lambda_1 \sim 0.3i$, as well as the absence of significant real parts. This provides direct evidence that weak linear gain can drive a qualitative transformation of the soliton gas: from an initial Weyl distribution to a bichromatic SG.

To sum up

This section investigates the evolution of an optical soliton gas propagating in a recirculating fiber loop in the presence of weak linear gain. The SG is initially prepared as a flat-top noisy pulse of low average power. As the system evolves, localized coherent structures emerge and persist over long distances. These structures gradually separate and individualize, with small relative velocities, qualitatively reminiscent of growing integrable turbulence [257]. Nonlinear spectral analysis reveals that gain leads to a progressive amplification of soliton amplitudes, shown in the increase of the imaginary parts of eigenvalues, while their real parts remain concentrated around zero, indicating weak relative velocities. The corresponding density of states evolves from an initial Weyl distribution to a bichromatic spectral support, characterized by two distinct clusters of eigenvalues. This spectral transformation is fully captured by simulations of the NLSE with small linear gain.

4.6 Spectral mass redistribution under gain and damping

In the kinetic theory of soliton gases, the mass (or equivalently the optical power) can be determined from the nonlinear spectrum by integrating the density of states $f(\xi,\eta)$ over the complex plane [130]:

$$M = \int_{-\infty}^{+\infty} d\xi \int_{0}^{+\infty} d\eta \, 4\eta \, f(\xi,\eta). \tag{4.25}$$

This formulation emphasizes that each soliton contributes to the total mass proportionally to its amplitude, which is encoded in the imaginary part η of its associated eigenvalue. This quantity can be rewritten as,

$$M = 4\int_{0}^{+\infty} \eta \, \tilde{f}(\eta)\, d\eta = \int_{0}^{+\infty} \rho(\eta)\, d\eta, \tag{4.26}$$

where $\tilde{f}(\eta) = \int_{-\infty}^{+\infty} f(\xi,\eta)\,d\xi$ is the DOS integrated along the real axis ξ, and we define $\rho(\eta) = 4\eta\tilde{f}(\eta)$ as the spectral density of mass with respect to η, the coordinate along the imaginary axis. This quantity provides a direct way to visualize how the total solitonic mass is distributed along the imaginary axis.

To quantitatively assess how gain and loss affect the solitonic content of the optical gas, we analyze the evolution of the spectral density of mass

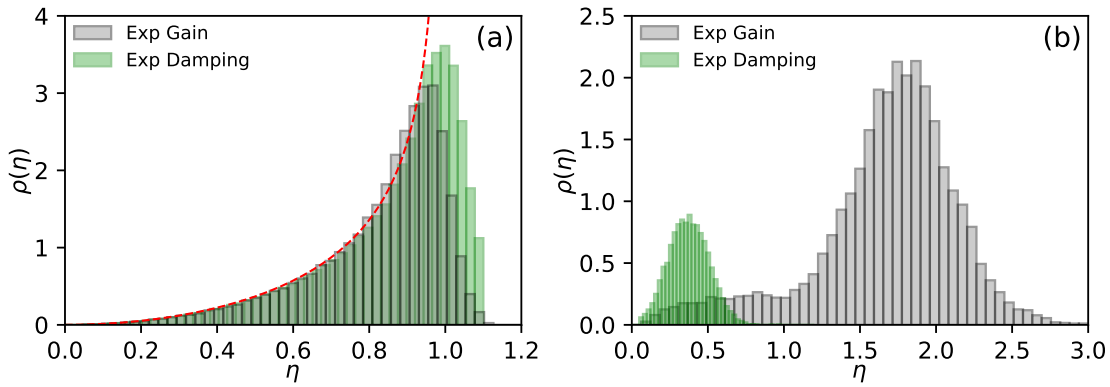

Figure 4.27: Experimental histograms showing the spectral density of mass, $\rho(\eta)$, along the vertical imaginary axis η. (a) The green (resp. grey) histogram represents the initial distribution in the experiment with linear damping (resp. amplification) of the SG. The red dashed line represents the spectral density of mass $\rho_W(\eta) = 4\eta f_W(\eta)$ associated with the Weyl distribution $f_W(\eta) = \eta/(\pi\sqrt{1-\eta^2})$. (b) Same as (a) but at $z \sim 1920$ km (green histogram) and $z \sim 6320$ km (grey histogram).

Figure 4.27(a) shows that the spectral density of mass $\rho(\eta)$ for the initial soliton gas closely follows the analytical Weyl prediction $\rho_W(\eta) = 4\eta f_W(\eta)$ both for the gain (grey histogram) or damping (green histogram) experiment. In contrast, damping transforms $\rho(\eta)$ into a bell-shaped distribution centered around $\eta \simeq 0.4$, indicating a systematic decay of soliton amplitudes (green histogram in Fig. 4.27(b)). Conversely, in the gain regime, the mass distribution becomes asymmetric and shifts toward larger η, with a dominant peak near $\eta \simeq 1.8$ (grey histogram). The contribution from the secondary cluster of eigenvalues centered near $\lambda_1 \simeq 0.3i$, characteristic of the emerging bichromatic soliton gas, accounts for only a few percent of the total mass. This is because the imaginary part of the second cluster is significantly smaller than that of the main peak, and

since the spectral mass density is proportional to 4η, its contribution to the total mass is correspondingly reduced.

4.7 Summary of the Chapter and Perspectives

In this chapter, we investigated the dynamics of optical soliton gases (SGs) in a recirculating fiber loop, focusing on how weak deviations from integrability, namely, linear damping or gain, affect both its spatiotemporal evolution and spectral properties. Using a heterodyne interferometry technique developed during this thesis, we performed in optics, a direct measurement of the discrete IST spectrum of SGs and its associated density of states (DOS) .

Our results show that small non-integrable perturbations reorganize the IST spectrum in a nontrivial way. Damping leads to a broadening of soliton velocities and a redistribution of spectral mass toward lower amplitudes, resulting in a semi-circular spectral distribution. In contrast, gain induces the formation of a two-component, clustered (bichromatic) soliton gas.

These findings demonstrate that the DOS provides a spectral observable to characterize the statistical evolution of SGs under weak integrability-breaking effects. They also highlight the rich dynamical behavior that emerges even under small deviations from integrability, behavior which is currently not captured by any existing theoretical framework.

Future perspectives. The optical fiber loop platform used in this work offers a versatile and high-resolution testbed for exploring the nonlinear dynamics of SGs in both integrable and weakly non-integrable regimes. One promising direction is the controlled engineering of the initial nonlinear spectrum. Starting from a well-characterized Weyl-distributed SG, it becomes possible to imprint specific spectral deformations, for instance by optical shaping of the input field or by introducing programmable gain/loss landscapes, to investigate how different initial DOS configurations evolve under the nonlinear dynamics.

From a theoretical standpoint, the results reported here highlight important limitations of existing kinetic or hydrodynamic approaches. The standard kinetic theory of SGs, developed for purely integrable systems, cannot describe the

observed non-isospectral evolution driven by weak dissipation or amplification. Yet, recent advances in Generalized Hydrodynamics (GHD), particularly those incorporating atom loss in quantum Bose gases [260], provide encouraging signs that a hydrodynamic description of weakly non-integrable SGs (classical system) could be within reach.

Finally, the experimental flexibility of the fiber-loop platform enables the exploration of more advanced protocols. In particular, one could envision time-dependent perturbations, such as switching gain or loss on and off at specific times, or gradually modulating their strength during propagation.

General Conclusion

No problems only solitons.

– François Copie

In this thesis, we have conducted an experimental study of soliton gas dynamics across three distinct physical platforms: surface gravity waves in a large water tank facility, nonlinear electrical transmission line, and recirculating optical fiber loop. Each system provides access to regimes of integrability breaking, enabling a multifaceted exploration of soliton gases beyond the integrable framework.

In the hydrodynamic platform, presented in Chapter 2, we focused on colliding monochromatic soliton gases and performed direct measurements of their densities and effective velocities using the Radon transform of space-time diagrams. Despite weak integrability-breaking effects due to damping and higher-order nonlinear effects, we show that the results remained in excellent agreement with the predictions of spectral kinetic theory.

In the electrical platform presented in Chapter 3, we realized a dense soliton gas governed by KdV-type dynamics. The intrinsic dissipation present in the system, modeled via a dissipation-driven KdV equation, breaks the integrability and modifies the soliton gas dynamics. Using nonlinear spectral analysis based on the inverse scattering transform, we observed the spontaneous formation of a soliton condensate, a state characterized by spatially delocalized eigenfunctions and a compact Weyl distribution for the discrete eigenvalues. Such a transition from a dense soliton gas to a condensate is strictly forbidden in integrable KdV dynamics. Our experiments thus reveal that even weak dissipation can induce a profound nonlinear spectral reorganization, enabling the emergence of soliton condensate. This spectral restructuring, involving both

a rearrangement of solitonic eigenmodes and the excitation of the continuous spectrum, cannot be captured by current kinetic or generalized hydrodynamic theories of soliton gases. Recent theoretical works have started emphasizing the importance of soliton-radiation coupling in weakly non-integrable systems, particularly in deep-water wave models that go beyond the integrable 1D-NLSE framework [261]. However, existing hydrodynamic approaches, including generalized hydrodynamics, do not capture how a statistical ensemble of solitons can collectively excite the continuous spectrum. Our findings highlight this theoretical gap and open new perspectives for the development of models that can describe the interplay between soliton gases and radiative content in weakly non-integrable systems [262].

In the optical platform presented in Chapter 4, we used heterodyne interferometry to directly measure the complex optical wavefield, allowing for the computation of the nonlinear discrete spectrum of soliton gases evolving in a recirculating fiber loop under either linear gain or loss. We showed that even weak integrability-breaking effects can significantly reshape the density of states. In the presence of damping, the spectral support undergoes a deformation toward a semi-circular shape, reflecting a redistribution of spectral mass and a broadening of soliton velocities. Conversely, optical gain leads to the formation of a bichromatic soliton gas, characterized by the clustering of eigenvalues into two distinct spectral components. These observations lie beyond the scope of existing theoretical frameworks, such as the kinetic theory of soliton gases, which do not account for the complex spectral deformations induced by higher-order perturbations. Our experiments demonstrate that such perturbative effects can be deliberately exploited to manipulate the nonlinear spectral (IST) characteristics of soliton gases, offering new experimental pathways to control their macroscopic behavior.

A comparative analysis of the three platforms (see Table 4.1) reveals their complementary strengths. The hydrodynamic setup allows for fast data acquisition with good control of initial conditions, though it suffers from limited propagation distances. The electrical line offers a very low-cost and flexible environment to study long-term evolution though it exhibits strong integrability breaking. Finally, the optical fiber loop combines nonlinear spectral access with

the ability to finely tune dissipation or gain over long propagation distances, making it ideally suited for controlled explorations of non-isospectral dynamics.

Together, these platforms show many physical conditions and degrees of integrability breaking. By leveraging their complementarities, we have been able to investigate a wide range of phenomena, from quasi-integrable soliton collisions to condensate formation and gain-induced spectral clustering that no single system could fully capture on its own. This cross-platform strategy has allowed us to assess the limits of spectral kinetic theory and identify signatures of integrability breaking in both real and spectral space.

Our results motivate the development of an extended kinetic or hydrodynamic framework capable of capturing non-isospectral effects, and even non-adiabatic effects as soliton creation, which appear to be essential ingredients for describing soliton gases in our realistic, weakly non-integrable systems.

Criterion	**Hydrodynamics**	**Electrical**	**Optics**
Initial condition generation	Controllable	Controllable	Limited
Nonlinear propagation time	Short ($t \sim 1$)	Very long ($t \sim 420$)	Long ($t \sim 20$)
Integrability breaking effects	Damping, Higher-order nonlinear effects	Diffusion, Damping	Dissipation (tunable)
Evolution distance	Limited by tank length	Can loop	Can loop
Acquisition time	<5 min.	~20 min.	<10 sec.

Table 4.1: Comparison of the three experimental platforms used in this thesis, evaluated according to practical and physical criteria. Each setup offers complementary advantages in terms of controllability, integrability breaking, and access to observables.

Chapter 5

Appendices

The devil is in the details.

Idiom

5.1 Hilbert Transform

To extract the complex envelope of the free-surface elevation measured in the hydrodynamic experiment, we apply a demodulation technique based on the Hilbert transform, following the formalism used by Osborne [263]. The objective is to isolate the slowly varying complex field $A(Z,T)$ such that the signal can be written as:

$$\eta(Z,T) = \left[A(Z,T)e^{i2\pi f_0 T}\right] + cc., \tag{5.1}$$

where f_0 is the known carrier frequency. This complex field contains the instantaneous amplitude and phase of the wavefield.

The procedure, implemented in Python, consists of the following steps:

1. The signal $\eta(T)$ at each gauge position is Fourier-transformed in time.

2. A spectral window, centered on the carrier frequency f_0, is applied to remove low-frequency background, high-frequency noise, and all negative-frequency components.

3. The resulting band-filtered signal is demodulated by multiplying it by $\exp(-i2\pi f_0 T)$ to remove the carrier.

4. An inverse FFT is performed to recover the complex field $A(Z,T)$.

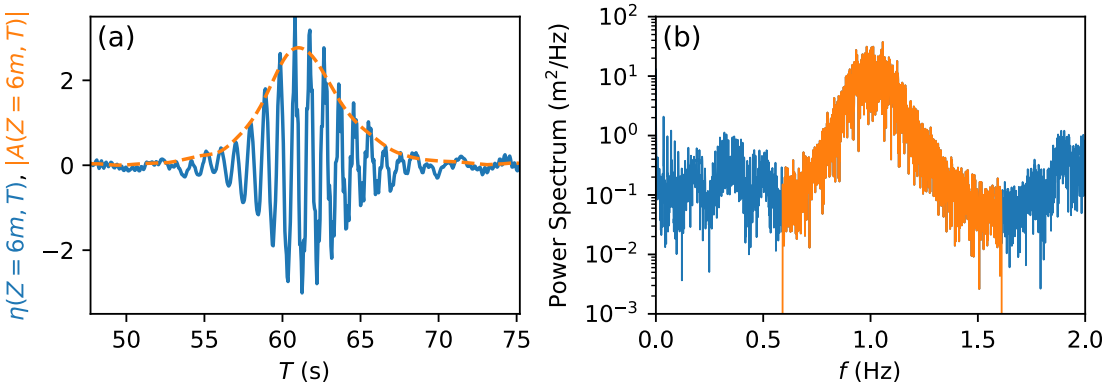

Figure 5.1: (a) Raw temporal signal $\eta(Z = 6\,\mathrm{m}, T)$ measured at a fixed location in the hydrodynamic experiment (blue), and corresponding complex envelope $|A(Z = 6\,\mathrm{m}, T)|$ obtained by Hilbert-transform demodulation (orange). (b) Power spectrum of the original signal (blue) and the band-pass filtered version used in the demodulation procedure (orange). The demodulation is centered on the carrier frequency $f_0 = 1.1\,\mathrm{Hz}$.

Figure 5.1(a) shows the signal $\eta(Z = 6\,\mathrm{m}, T)$, directly measured at a fixed location in the experiment, and its extracted envelope $|A(Z = 6\,\mathrm{m}, T)|$. The demodulation is performed using a Hilbert-transform-based method centered on the known carrier frequency. The envelope captures the slow modulation of the wave packet and removes the fast oscillations of the carrier.

Figure 5.1(b) shows the corresponding power spectral densities. The original signal (blue) exhibits a broadband structure with a clear peak around the carrier frequency f_0. The filtered signal (orange) illustrates the spectral windowing used to isolate the positive-frequency content prior to demodulation.

5.2 Varicap characterisation

5.2.1 Capacitance measure - Bode plot method

The first step in characterizing the varicap diode consists in determining how its capacitance $C(V)$ evolves as a function of the applied voltage. To this end, we implement a simple RC circuit as shown in Fig. 5.2.

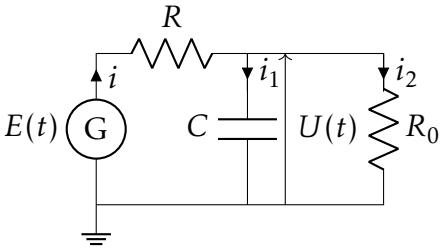

Figure 5.2: Schematic of the RC circuit used to characterize the varicap. G: arbitrary function generator. $R = 461$ kΩ, $R_0 = 1$ MΩ represents the internal resistance of the oscilloscope.

The measurement protocol is as follows. A sinusoidal voltage of small amplitude (a few tens of millivolts) is superimposed on a tunable DC offset. For each offset value, we measure the frequency-dependent voltage gain and reconstruct the Bode diagram of the circuit. By fitting the gain curves with the theoretical transfer function of the RC filter, we extract the corresponding capacitance value $C(V)$ of the varicap.

It is crucial to maintain a small sinusoidal amplitude. Since the varicap's capacitance depends on the instantaneous voltage, using a large-amplitude sinusoid would cause the effective capacitance to vary during the frequency sweep, invalidating the assumption of constant C. The DC offset ensures that the operating point remains well-defined, and that the capacitance is approximately constant during each Bode plot measurement.

The analytical transfer function for the RC circuit reads:

$$\frac{V_{\text{out}}}{V_{\text{in}}} = \frac{1}{j\omega CR + \frac{R+R_0}{R_0}}.$$

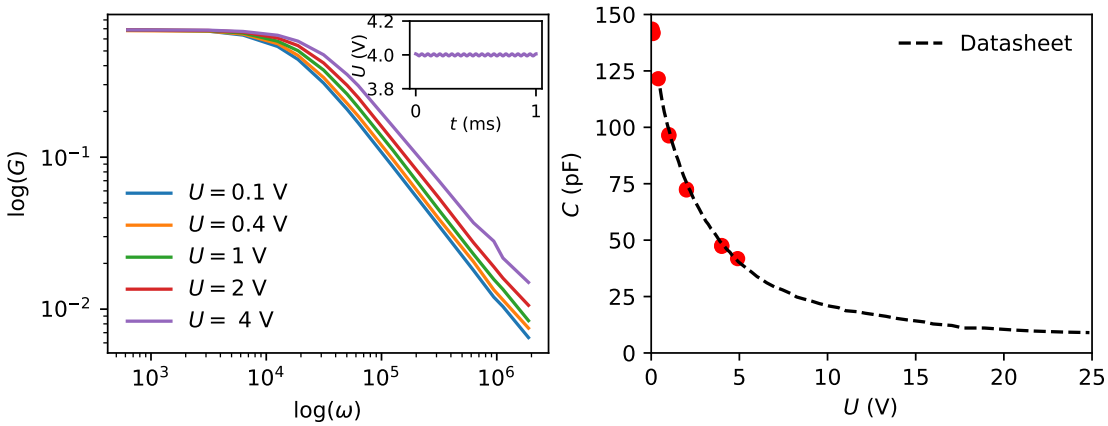

Figure 5.3: Left: Bode plots of the RC circuit with the varicap for several DC offset voltages U. The inset shows an example of the input sinusoid. Right: Extracted capacitance values (red dots) as a function of voltage, obtained by fitting the gain curves. The dashed black line represents the manufacturer's datasheet values.

Figure 5.3 shows that the extracted capacitance values (red dots, right panel) agree well with those provided in the datasheet (black dashed line). A small systematic offset was observed and corrected. This discrepancy was traced to the presence of a coaxial cable (approximately 1 m long) placed after the RC circuit, which introduced a parasitic capacitance of about 60 pF in parallel to the varicap.

5.2.2 Capacitance measure - Charge of the capacitor method

An alternative approach to characterizing the capacitance of the varicap consists in analyzing its charging dynamics in response to a square wave excitation. During the charging phase, the voltage across the varicap spans the full range from 0 V to its maximum value. By recording the temporal evolution of the voltage and deducing the associated current, the capacitance $C(U)$ can be inferred as a function of the voltage.

The circuit used is the same as in Fig. 5.2, and the relevant Kirchhoff's laws

give:

$$i = i_1 + i_2, \qquad i_2 = \frac{U}{R_0}, \qquad i_1 = C\frac{\mathrm{d}U}{\mathrm{d}t}$$

$$E = Ri + U = R\left(\frac{U}{R_0} + C\frac{\mathrm{d}U}{\mathrm{d}t}\right) + U,$$

This yields,

$$\boxed{C(U) = \frac{1}{R}\left(\frac{E - U\left(\frac{R}{R_0} + 1\right)}{\frac{\mathrm{d}U}{\mathrm{d}t}}\right)}.$$

Using a square wave input $E(t)$ of known amplitude (here, 8 V) and period (1.2 ms), and known resistances $R = 461\ \mathrm{k\Omega}$, $R_0 = 1\ \mathrm{M\Omega}$, we measure the voltage $U(t)$ across the varicap. By numerically computing $\mathrm{d}U/\mathrm{d}t$, we reconstruct the time-dependent capacitance, which we then associate with the corresponding voltage values.

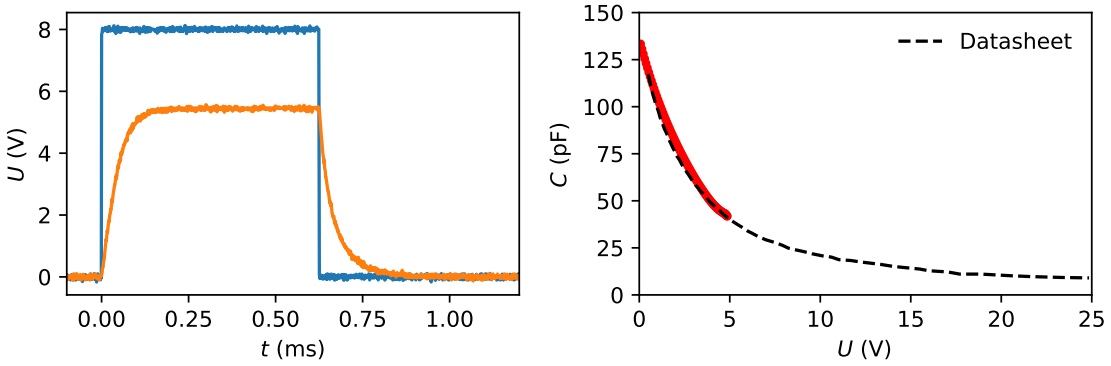

Figure 5.4: Left: Voltage $U(t)$ across the varicap (orange) in response to a square wave excitation $E(t)$ (blue) of period 1.2 ms and amplitude 8 V. Right: Extracted capacitance values (red points) as a function of voltage. The dashed black line shows the manufacturer-provided values.

Figure 5.4 (right panel) shows that the experimentally obtained capacitance-voltage relation (red points) closely matches the datasheet values (black dashed line). A small systematic offset was corrected, attributed to a parasitic capacitance of approximately 60 pF introduced by the coaxial cable connected to the RC circuit.

In the left panel, the difference between the square pulse amplitude (8 V)

and the maximum voltage reached across the capacitor can be explained by the voltage divider formed by R and R_0. Solving the steady-state circuit yields:

$$U(t_\infty) = R_0 E/(R_0 + R) = 5.47V$$

which is consistent with the observed asymptotic voltage.

5.2.3 Measure of the varactor's resistance

The varactor's intrinsic resistance introduces dissipative (diffusive) effects in the system, which can be effectively modeled by a small series resistance R_C. Preliminary numerical simulations suggest that $R_C \approx 5\ \Omega$. The RC circuit used previously to characterize the varactor's capacitance incorporated a high series resistance ($R = 461\ \text{k}\Omega$), rendered the effect of R_C negligible. Therefore, a dedicated setup is required to accurately determine this series resistance.

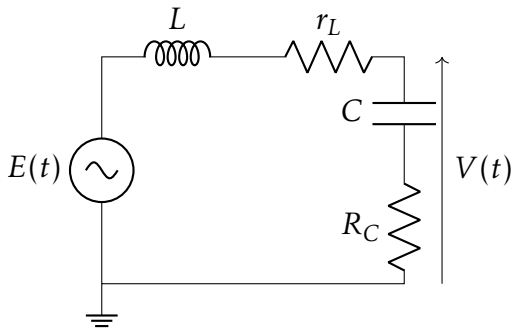

Figure 5.5: Schematic of the LC cell. R_C represents the series resistance of the varicap, and r_L the series resistance of the inductor.

Figure 5.5 shows the modified LC circuit used for this measurement. The setup is operated in the linear regime by applying a low-amplitude sinusoidal voltage (6 mV) and sweeping the frequency from 10 kHz to 100 MHz. In this regime, the LC circuit behaves as a standard RLC resonator, allowing us to extract R_C by fitting the gain curve analytically.

The resistance of the inductor, r_L, is first measured independently using a four-wire method, yielding $r_L = 67\ \text{m}\Omega$. The only remaining unknown is R_C,

which is inferred by fitting the gain profile to the theoretical transfer function:

$$G = |H(\omega)| = \left| \frac{R_C - \frac{j}{C_0 \omega}}{R_C - \frac{j}{C_0 \omega} + r_L + jL\omega} \right|.$$

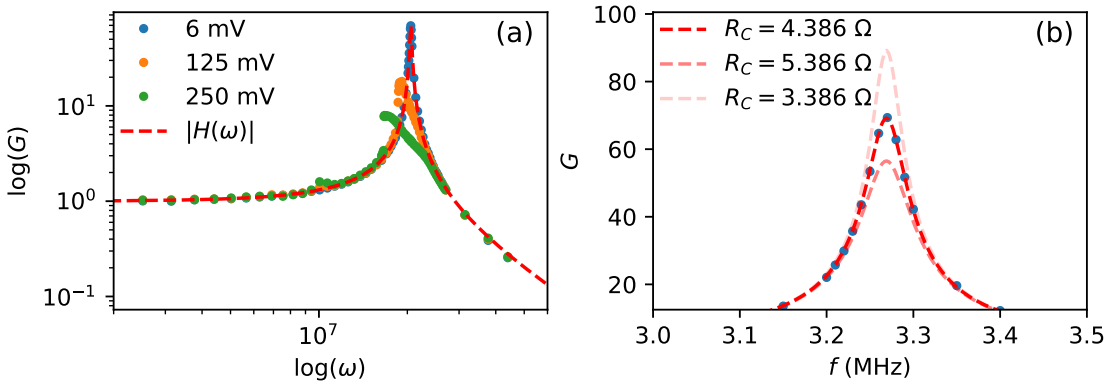

Figure 5.6: (a) Gain curves for various excitation amplitudes. The red dashed line corresponds to the analytical response in the linear regime. (b) Zoomed-in view of the resonance region, with analytical predictions for $R_C = 4.386\ \Omega \pm 1\ \Omega$.

Figure 5.6(b) shows the resonance region, with the best fit obtained for $R_C = 4.386\ \Omega$. This value is consistent with the estimates from numerical simulations but significantly deviates from the manufacturer's specification, which indicates $R_C = 0.25\ \Omega$. Notably, similar discrepancies have been reported in the literature; for example, Ref. [264] reports requiring $R_C = 6.8\ \Omega$ to match experimental data, while the datasheet for the BB809 varactor used in their study specifies a maximum of $0.6\ \Omega$.

In addition to the linear regime, nonlinear effects of the varactor can also be probed using the same circuit at higher input amplitudes. Figure 5.6(a) shows gain curves for excitation amplitudes of 125 mV and 250 mV. The onset of nonlinear resonance is clearly visible, with a distortion and bending of the resonance peak characteristic of the so-called foldover effect. This phenomenon is well-documented in nonlinear dynamics and is a signature of bistability and hysteresis in driven resonant systems.

These observations are in agreement with prior studies [265–267], which show that the LC circuit behaves as a Duffing oscillator in the nonlinear regime,

where the capacitor's charge serves as the dynamic variable. Such systems naturally exhibit nonlinear resonance curves and bistable behavior depending on the amplitude and frequency of the excitation.

5.2.4 Measurement of the nonlinear parameter b from spectral harmonic analysis

When a sinusoidal voltage at frequency f_0 is applied to a nonlinear system such as one with a varicap, the output signal typically contains not only the fundamental frequency f_0, but also higher harmonics, such as $2f_0$, $3f_0$, etc. The presence and amplitude of these harmonics directly reflect the degree of nonlinearity in the system. In this study, we use the second harmonic $2f_0$ as a probe: by measuring how its amplitude scales with that of the fundamental, we can extract the nonlinear coefficient b in the relation $C(V) = C_0(1 - 2bV)$, which plays a key role in the derivation of the KdV equation for the system.

Applying Kirchhoff's laws to a basic LC circuit driven by a source voltage $E(t)$ yields:

$$E(t) - V(t) = L\frac{\mathrm{d}I(t)}{\mathrm{d}t}, \qquad I(t) = \frac{\mathrm{d}Q}{\mathrm{d}t},$$

where Q is the charge stored in the capacitor, and $C(V) = \frac{\mathrm{d}Q}{\mathrm{d}V}$ is its voltage-dependent capacitance. Combining these expressions, we obtain:

$$\frac{\mathrm{d}^2Q}{\mathrm{d}t^2} = \frac{1}{L}\left(E(t) - V(t)\right), \quad \text{and} \quad \frac{\mathrm{d}^2Q}{\mathrm{d}t^2} = \frac{\mathrm{d}}{\mathrm{d}t}\left(C(V)\frac{\mathrm{d}V}{\mathrm{d}t}\right).$$

In the linear case $C(V) = C_0$, this simplifies to the standard equation of a driven harmonic oscillator:

$$\boxed{\frac{\mathrm{d}^2V}{\mathrm{d}t^2} = \frac{1}{LC_0}\left(E(t) - V(t)\right)}.$$

However, in our setup, the varicap exhibits a nonlinear response modeled as $C(V) = C_0(1 - 2bV)$, where b characterizes the strength of the nonlinearity.

Substituting this into the previous expression and applying the chain rule,

$$\frac{\mathrm{d}}{\mathrm{d}t}\left(C(V)\frac{\mathrm{d}V}{\mathrm{d}t}\right) = \frac{\mathrm{d}C(V)}{\mathrm{d}t}\frac{\mathrm{d}V}{\mathrm{d}t} + C(V)\frac{\mathrm{d}^2V}{\mathrm{d}t^2},$$

we obtain the following nonlinear equation:

$$\boxed{\frac{\mathrm{d}^2V}{\mathrm{d}t^2} = \frac{2b}{1-2bV}\left(\frac{\mathrm{d}V}{\mathrm{d}t}\right)^2 + \frac{1}{LC_0(1-2bV)}\left(E(t)-V(t)\right)}.$$

Assuming an harmonic excitation $V(t) = E(t) = V_0 e^{i\omega t}$, we find that the second-order term introduces a nonlinear contribution at 2ω. Specifically, we get:

$$-\left(1-2bV_0e^{i\omega t}\right)\omega^2 V_0 e^{i\omega t} = -2b\omega^2 V_0^2 e^{2i\omega t},$$

which leads to:

$$4bV_0^2 e^{2i\omega t} = V_0 e^{i\omega t}.$$

revealing that the amplitude of the second harmonic scales as V_0^2, with a proportionality constant related to b.

This observation provides a practical method to estimate the nonlinear coefficient b: by measuring the amplitude of the spectral component at $2f_0$ as a function of the amplitude at the fundamental f_0, one can infer the strength of the nonlinearity.

Experimentally, we perform this analysis using an RF spectrum analyzer (Agilent E4407B, 26.5 GHz). A sinusoidal voltage at frequency f_0 is applied to the nonlinear LC cell, and the amplitudes of the components at f_0 and $2f_0$ are recorded while varying the input amplitude.

In Fig. 5.7(a), we observe that the amplitude of the second harmonic increases with the fundamental, as expected. For $\tilde{V}(2f_0) \gtrsim 0.05$, a linear fit (green triangles) yields an estimate $b \sim 0.12$. This value is consistent with the measurement obtained by fitting the capacitance–voltage curve, which gives $b \sim 0.15$ (shown via red dashed line). Figure 5.7(b) confirms this trend at a higher frequency $f_0 = 3$ MHz.

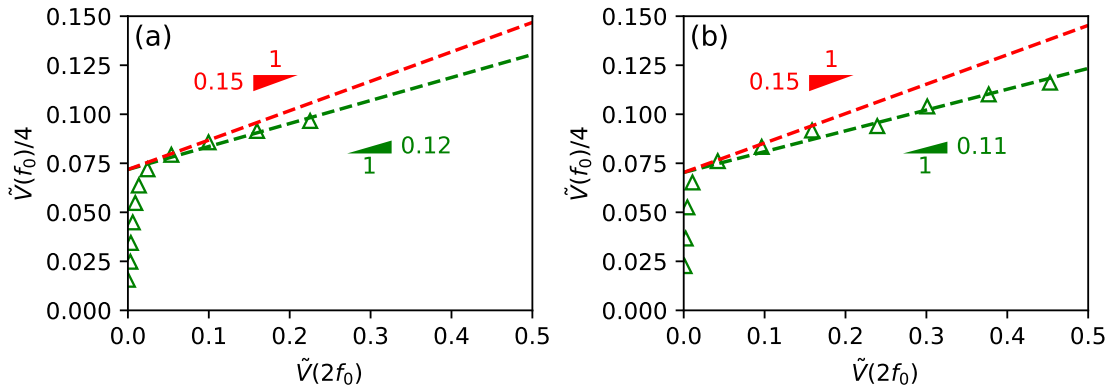

Figure 5.7: Nonlinear coefficient determination. (a) Evolution of the spectral component at $f_0 = 1$ MHz as a function of the amplitude at $2f_0$, measured using an RF spectrum analyzer. (b) Same as (a) for $f_0 = 3$ MHz.

5.3 Measurement of the optical detection system's impulse response and transfer function

To characterize the optical detection system, we begin by measuring the impulse response function (IRF) and, by Fourier transform, its spectral transfer function of the combined photodiode and oscilloscope. This is done by recording the response to a train of 670-fs pulses generated by a PriTel laser spectrally filtered to 8 nm.

Figure 5.8(a) displays a single realization of the detected impulse response, normalized to its maximum and shown as black dots. The red curve corresponds to the averaged impulse response, obtained by interpolating and averaging 10,000 individual realizations. The interpolation improves the signal-to-noise ratio (SNR), reducing the influence of measurement noise at this stage.

Figure 5.8(b) shows the squared magnitude of the spectral transfer function computed from the averaged impulse response (black solid line). For comparison, the green dashed line represents the response of a first-order RC filter with a cutoff frequency of 32 GHz, which follows the transfer function:

$$|H(\nu)|^2 = \left| \frac{1}{1 + j\frac{\nu}{\nu_c}} \right|^2 . \tag{5.2}$$

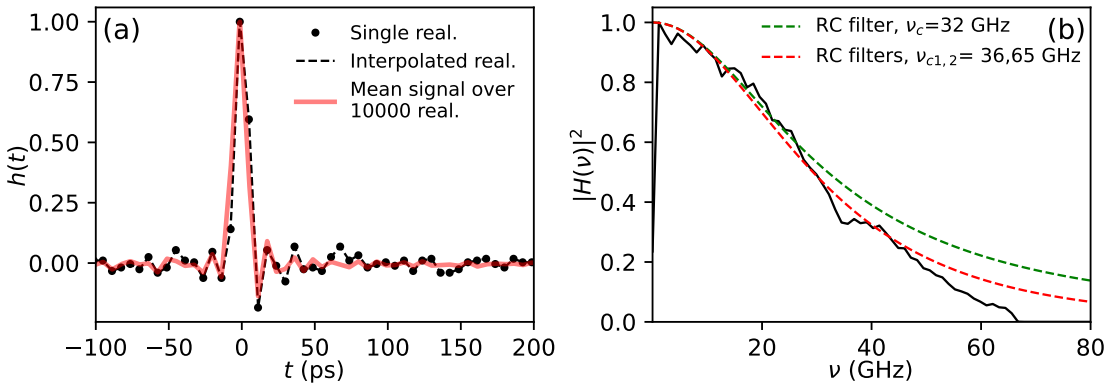

Figure 5.8: (a) Impulse response $h(t)$ of the detection system composed of a 50 GHz photodiode and a 65 GHz oscilloscope. Black dots represent a single measured realization and the dashed line its interpolation. The solid red curve shows the average impulse response computed from 10,000 interpolated realizations. (b) Squared transfer function $|H(\nu)|^2$ obtained from the Fourier transform of $h(t)$. Colored dashed lines correspond to analytical transfer functions of first-order RC filters with different cutoff frequencies ν_c.

The red dashed line corresponds to the theoretical response of two cascaded first-order RC filters with cutoff frequencies of 36 GHz and 65 GHz, respectively. The cutoff at 65 GHz reflects the bandwidth limitation of the oscilloscope, as no signal is detected beyond this frequency.

5.4 Spectral features of a sinusoidally phase-modulated signal

This appendix presents a numerical illustration of the spectral features expected from a sinusoidally phase-modulated optical signal. This simple case provides a useful reference for interpreting the spectral content of modulated signals and highlights how the harmonic structure encodes the modulation amplitude.

We consider the theoretical expression of the intensity detected by the photodiode in a heterodyne configuration as in the experiment presented in Sec. 4.3.1:

$$V(T) = V_0 \cos\left(2\pi\Delta f_0 T + m\sin(2\pi f_m T)\right), \tag{5.3}$$

where V_0 is the amplitude, $\Delta f_0 = 45$ GHz is the heterodyne frequency, $f_m = 1$ GHz is the modulation frequency, and m is the phase modulation amplitude. The signal is sampled over a 30 ns time window to match experimental conditions presented in Sec 4.3.1.

This waveform can be expanded into a sum over Bessel functions of the first kind [268, 269]:

$$V(T) = V_0 \sum_{n=-\infty}^{+\infty} J_n(m) \cos\left[2\pi(\Delta f_0 + n f_m)T\right], \tag{5.4}$$

where $J_n(m)$ denotes the Bessel function of order n. This expansion shows that the power spectrum consists of discrete peaks located at frequencies $\Delta f_0 \pm n f_m$, with amplitudes proportional to $|J_n(m)|$.

In Fig. 5.9(a), corresponding to a modulation amplitude $m = 2.4048$, the Bessel function $J_0(m)$ vanishes, resulting in the suppression of the carrier component at Δf_0. The power is instead distributed among higher-order sidebands. In contrast, for $m = 1$, shown in Fig. 5.9(b), most of the signal energy is concentrated in the central peak and the first sidebands.

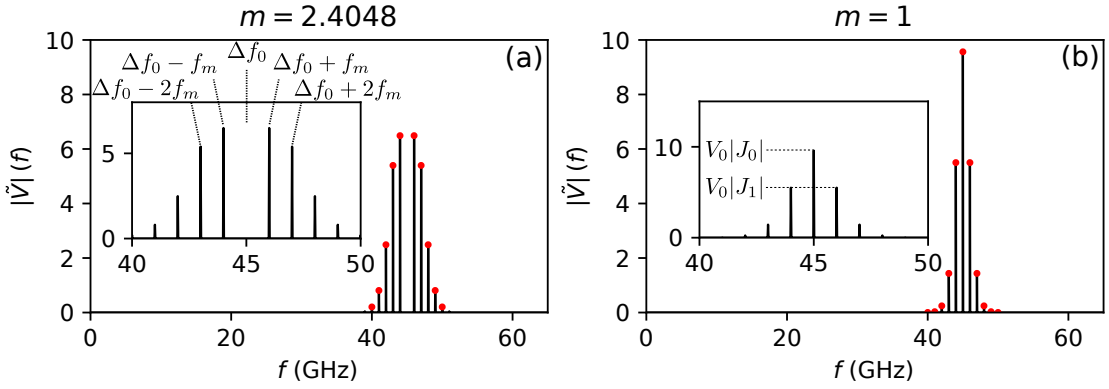

Figure 5.9: Numerical illustration of the power spectrum of a sinusoidally phase-modulated signal $V(T) = V_0 \cos(2\pi\Delta f_0 T + m \sin(2\pi f_m T))$, for two modulation amplitudes: $m = 2.4048$ (a) and $m = 1$ (b). Spectral lines appear at $\Delta f_0 \pm n f_m$, with amplitudes given by $|V_0 J_n(m)|$. Red dots indicate the theoretical Bessel weights. Insets show zoomed-out spectra to highlight the full harmonic structure.

This example highlights how the spectral content of a sinusoidally phase-

modulated signal is entirely determined by the modulation amplitude m. In particular, the relative heights of the spectral peaks provide a direct and quantitative signature of m.

To illustrate this principle in practice, we apply it to an experimentally reconstructed temporal phase profile, obtained via heterodyne detection presented in Sec. 4.3.1. Figure 5.10(a) shows the recovered phase (green line), along with a sinusoidal fit of the form $\phi(T) = m\cos(2\pi f_m T)$, which yields $m \sim 0.637$ rad and $f_m \sim 1$ GHz.

In parallel, the power spectrum of the demodulated signal is shown in Fig. 5.10(b). The spectrum exhibits discrete peaks located at integer multiples of the modulation frequency f_m, with relative amplitudes denoted p_0, p_1, and p_2. These peaks correspond to the spectral components associated with the Bessel terms $J_0(m)$, $J_1(m)$, and $J_2(m)$, respectively, under the assumption that the phase modulation is purely sinusoidal.

Finally, in Fig. 5.10(c), we compare the experimentally measured ratios p_n/p_k, with the theoretical values of $|J_n(m)/J_k(m)|$ as functions of m. The intersection of the experimental ratios with the theoretical curves provides an independent estimate of the modulation amplitude, yielding $m = 0.638 \pm 0.007$ rad, in excellent agreement with the value obtained from the temporal fit.

This comparison confirms that the reconstructed signal exhibits a spectral structure consistent with a sinusoidal phase modulation. Although this does not constitute an independent validation of the reconstruction algorithm itself, it demonstrates that the modulation is preserved through the detection and demodulation process. This simple example thus serves as a useful benchmark for interpreting more complex phase profiles in the experiments.

5.5 Exponential evolution of the momentum under weak dissipation

We consider the damped focusing NLSE:

$$\psi_t = i\left(\psi_{xx} + 2|\psi|^2\psi\right) - \epsilon\psi, \tag{5.5}$$

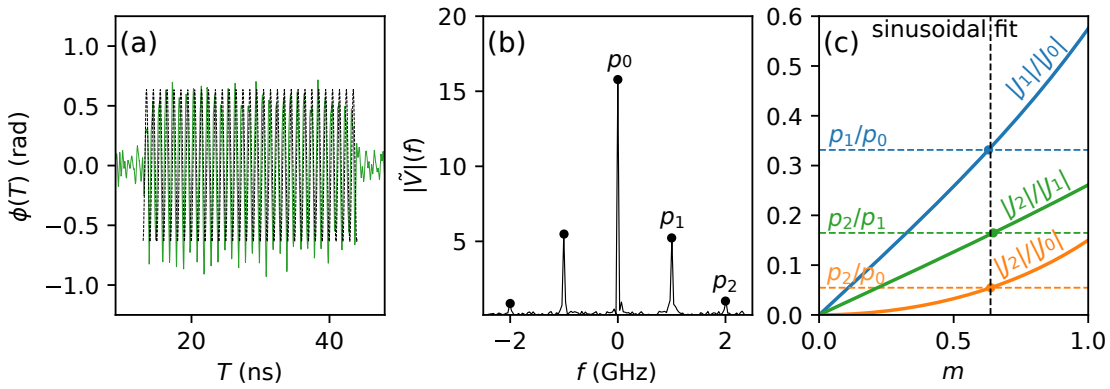

Figure 5.10: Phase modulation analysis of a reconstructed signal. (a) Retrieved phase (green line) and sinusoidal fit of the form $m\cos(2\pi f_m T)$ (black dashed line), with $m \sim 0.637$ rad and $f_m \sim 1$ GHz. (b) Power spectrum of the demodulated signal: harmonic weights $p_0 \sim 15.78$, $p_1 \sim 5.23$, $p_2 \sim 0.86$. (c) Comparison of experimental ratios p_n/p_k (colored dashed lines) with theoretical Bessel ratios $|J_n(m)/J_k(m)|$ (colored curves). The black dashed line indicates the value of m from the sinusoidal fit obtained in (a).

with a real, dissipation coefficient ϵ. We study the evolution of the momentum observable

$$M = \int \psi_x \psi^* \, dx. \tag{5.6}$$

Differentiating with respect to time and using the product rule gives:

$$\frac{dM}{dt} = \int \partial_t \psi_x \cdot \psi^* \, dx + \int \psi_x \cdot \partial_t \psi^* \, dx. \tag{5.7}$$

Substituting Eq. (5.5) and its complex conjugate, we obtain:

$$\frac{dM}{dt} = \int \partial_x \left(i\psi_{xx} + 2i|\psi|^2\psi - \epsilon\psi \right) \cdot \psi^* \, dx - \int \psi_x \cdot \left(i\psi^*_{xx} + 2i|\psi|^2\psi^* + \epsilon\psi^* \right) dx. \tag{5.8}$$

Using integration by parts, the term $i\psi_{xxx}\psi^*$ satisfies::

$$\int i\psi_{xxx} \cdot \psi^* \, dx = -\int i\psi_{xx} \cdot \psi^*_x \, dx = \int i\psi_x \cdot \psi^*_{xx} \, dx, \tag{5.9}$$

which cancels the corresponding part from the second integral. We are left with:

$$\frac{dM}{dt} = \int \Big[2i\,\partial_x(|\psi|^2\psi)\cdot\psi^* - 2i\,|\psi|^2\psi^*\cdot\psi_x - 2\epsilon\psi_x\cdot\psi^* \Big] dx. \tag{5.10}$$

Using integration by parts and the identity $\mathfrak{Re}(\psi\psi_x^*) = \frac{1}{2}\partial_x|\psi|^2$, we find:

$$\int \Big[2i\,\partial_x(|\psi|^2\psi)\cdot\psi^* - 2i\,|\psi|^2\psi^*\cdot\psi_x \Big] dx = -4i\int |\psi|^2\,\mathfrak{Re}(\psi\psi_x)\,dx = -2i\int |\psi|^2\partial_x|\psi|^2\,dx. \tag{5.11}$$

This final integral is a total derivative:

$$\int |\psi|^2\partial_x|\psi|^2\,dx = \frac{1}{2}\int \partial_x\Big(|\psi|^2\Big)^2\,dx = 0, \tag{5.12}$$

assuming that $\psi(x,t)\to 0$ as $|x|\to\infty$. Therefore, the nonlinear and dispersive contributions cancel out, and we are left with the dissipative contribution only:

$$\frac{dM}{dt} = -2\epsilon\int \psi_x\cdot\psi^*\,dx = -2\epsilon M. \tag{5.13}$$

The momentum thus decays exponentially:

$$\boxed{M(t) = M(0)\,e^{-2\epsilon t}}\,. \tag{5.14}$$

Bibliography

[1] William C Elmore and Mark A Heald. *Physics of waves*. Courier Corporation, 2012 (cit. on p. 1).

[2] Christiaan Huygens. *Traité de la lumière: avec un Discours de la cause de la pesanteur*. Gressner & Schramm, 1966 (cit. on p. 1).

[3] Jean le Rond d'Alembert. "Recherches sur la courbe que forme une corde tendue mise en vibration". In: (1747) (cit. on pp. 1, 12).

[4] Jean Baptiste Joseph Fourier. *Théorie de la propagation de la chaleur dans les solides*. 1972 (cit. on p. 1).

[5] VE Zakharov and NN Filonenko. "Energy spectrum for stochastic oscillations of the surface of a liquid". In: *Soviet Physics Doklady*. Vol. 11. 1967, p. 881 (cit. on p. 2).

[6] V. E. Zakharov and N. N. Filonenko. "Weak turbulence of capillary waves". en. In: *Journal of Applied Mechanics and Technical Physics* 8.5 (1971), pp. 37–40 (cit. on p. 2).

[7] Klaus Hasselmann. "On the non-linear energy transfer in a gravity-wave spectrum Part 1. General theory". In: *Journal of Fluid Mechanics* 12.4 (1962), pp. 481–500 (cit. on p. 2).

[8] Klaus Hasselmann. "On the non-linear energy transfer in a gravity wave spectrum Part 2. Conservation theorems; wave-particle analogy; irrevesibility". In: *Journal of Fluid Mechanics* 15.2 (1963), pp. 273–281 (cit. on p. 2).

[9] Eric Falcon, Claude Laroche, and Stéphan Fauve. "Observation of gravity-capillary wave turbulence". In: *Physical review letters* 98.9 (2007), p. 094503 (cit. on p. 2).

[10] Eric Falcon and Nicolas Mordant. "Experiments in surface gravity–capillary wave turbulence". In: *Annual Review of Fluid Mechanics* 54.1 (2022), pp. 1–25 (cit. on p. 2).

[11] Alan C Newell and Benno Rumpf. "Wave turbulence". In: *Annual review of fluid mechanics* 43.1 (2011), pp. 59–78 (cit. on p. 2).

[12] Alfred R Osborne. "Nonlinear ocean wave and the inverse scattering transform". In: *Scattering*. Elsevier, 2002, pp. 637–666 (cit. on pp. 2, 25, 26, 63, 67).

[13] Arezki Boudaoud et al. "Observation of wave turbulence in vibrating plates". In: *Physical review letters* 100.23 (2008), p. 234504 (cit. on p. 2).

[14] Gustavo Düring, Christophe Josserand, and Sergio Rica. "Wave turbulence theory of elastic plates". In: *Physica D: Nonlinear Phenomena* 347 (2017), pp. 42–73 (cit. on p. 2).

[15] Yuri Lvov, Sergey Nazarenko, and Robert West. "Wave turbulence in Bose–Einstein condensates". In: *Physica D: Nonlinear Phenomena* 184.1-4 (2003), pp. 333–351 (cit. on p. 2).

[16] Ying Zhu et al. "Direct and inverse cascades in turbulent Bose-Einstein condensates". In: *Physical Review Letters* 130.13 (2023), p. 133001 (cit. on p. 2).

[17] S Galtier and SV Nazarenko. "Large-scale magnetic field sustainment by forced MHD wave turbulence". In: *Journal of Turbulence* 9 (2008), N40 (cit. on p. 2).

[18] Jason Laurie et al. "One-dimensional optical wave turbulence: experiment and theory". In: *Physics Reports* 514.4 (2012), pp. 121–175 (cit. on p. 2).

[19] Umberto Bortolozzo et al. "Optical wave turbulence and the condensation of light". In: *Journal of the Optical Society of America B* 26.12 (2009), pp. 2280–2284 (cit. on p. 2).

[20] Vladimir E Zakharov, Victor S L'vov, and Gregory Falkovich. *Kolmogorov spectra of turbulence I: Wave turbulence*. Springer Science & Business Media, 2012 (cit. on p. 2).

[21] Sergey Nazarenko. *Wave turbulence*. Vol. 825. Springer, 2011 (cit. on p. 2).

[22] Roumaissa Hassaini and Nicolas Mordant. "Transition from weak wave turbulence to soliton gas". In: *Physical Review Fluids* 2.9 (2017), p. 094803 (cit. on pp. 2, 100).

[23] Mark J Ablowitz and Douglas E Baldwin. "Nonlinear shallow ocean-wave soliton interactions on flat beaches". In: *Physical Review E—Statistical, Nonlinear, and Soft Matter Physics* 86.3 (2012), p. 036305 (cit. on p. 2).

[24] Karl E Lonngren. "Soliton experiments in plasmas". In: *Plasma Physics* 25.9 (1983), p. 943 (cit. on p. 2).

[25] François Copie, Pierre Suret, and Stéphane Randoux. "Space–time observation of the dynamics of soliton collisions in a recirculating optical fiber loop". In: *Optics Communications* 545 (2023), p. 129647 (cit. on pp. 2, 24, 39, 48, 149).

[26] Jason HV Nguyen et al. "Collisions of matter-wave solitons". In: *Nature Physics* 10.12 (2014), pp. 918–922 (cit. on pp. 2, 48).

[27] Clifford S Gardner et al. "Method for solving the Korteweg-deVries equation". In: *Physical review letters* 19.19 (1967), p. 1095 (cit. on pp. 2, 26).

[28] Mark J Ablowitz and Harvey Segur. *Solitons and the inverse scattering transform*. SIAM, 1981 (cit. on pp. 2, 26, 27, 29, 34).

[29] P. G. Drazin and R. S. Johnson. *Solitons: An Introduction*. 2nd ed. Cambridge Texts in Applied Mathematics. Cambridge University Press, 1989 (cit. on pp. 2, 16, 19, 26–28, 30, 103, 118, 130).

[30] VE Zakharov. "Kinetic equation for solitons". In: *Sov. Phys. JETP* 33.3 (1971), pp. 538–540 (cit. on pp. 3, 33, 38, 39, 50, 88).

[31] GA El. "The thermodynamic limit of the Whitham equations". In: *Physics Letters A* 311.4-5 (2003), pp. 374–383 (cit. on pp. 3, 38, 41–43, 50).

[32] GA El and AM Kamchatnov. "Kinetic equation for a dense soliton gas". In: *Physical review letters* 95.20 (2005), p. 204101 (cit. on pp. 3, 33, 38, 48–53, 56, 60, 86, 188).

[33] Gennady A El et al. "Kinetic equation for a soliton gas and its hydrodynamic reductions". In: *Journal of Nonlinear Science* 21 (2011), pp. 151–191 (cit. on pp. 3, 49).

[34] Ivan Redor et al. "Experimental evidence of a hydrodynamic soliton gas". In: *Physical Review Letters* 122.21 (2019), p. 214502 (cit. on pp. 3, 33, 48, 88, 100).

[35] Pierre Suret et al. "Nonlinear Spectral Synthesis of Soliton Gas in Deep-Water Surface Gravity Waves". In: *Physical Review Letters* 125.26 (2020) (cit. on pp. 3, 33, 34, 48, 88, 129, 178).

[36] Pierre Suret et al. "Soliton refraction by an optical soliton gas". In: *Physical Review Research* 5.4 (2023), p. L042002 (cit. on pp. 3, 43, 48, 49, 151, 158).

[37] Pierre Suret et al. "Soliton gas: Theory, numerics, and experiments". In: *Physical Review E* 109.6 (2024), p. 061001 (cit. on pp. 3, 15).

[38] Loic Fache et al. "Interaction of soliton gases in deep-water surface gravity waves". In: *Physical Review E* 109.3 (2024), p. 034207 (cit. on pp. 4, 43, 88, 188).

[39] Loic Fache et al. “Dissipation-driven emergence of a soliton condensate in a nonlinear electrical transmission line”. In: *Physical Review Letters* 134.14 (2025), p. 147201 (cit. on p. 5).

[40] Loic Fache et al. “Perturbed Nonlinear Evolution of Optical Soliton Gases: Growth and Decay in Integrable Turbulence”. In: *Physical Review Letters* 135.15 (2025), p. 157201 (cit. on p. 5).

[41] John Scott Russell. “On certain effects produced on sound by the rapid motion of the observer”. In: *Report of the18th Meeting of the British Association for the Advancement of Science*. 1848, pp. 37–38 (cit. on p. 8).

[42] “Soliton wave receives crowd of admirers”. en. In: *Nature* 376.6539 (1995), pp. 373–373 (cit. on p. 8).

[43] George Biddell Airy. *Tides and waves*. B. Fellowes, 1845 (cit. on p. 8).

[44] George Gabriel Stokes. “On the theory of oscillatory waves”. In: *Trans. Cam. Philos. Soc.* 8 (1847), pp. 441–455 (cit. on p. 8).

[45] JE Allen. “The early history of solitons (solitary waves)”. In: *Physica Scripta* 57.3 (1998), p. 436 (cit. on p. 8).

[46] H Bazin. “Recherches Expérimentales relatives aux remous et à la propagation des ondes”. In: *Deuxième partie des Recherches hydrauliques de Darcy et Bazin* 148 (1865) (cit. on p. 8).

[47] Joseph Boussinesq. “Théorie des ondes et des remous qui se propagent le long d’un canal rectangulaire horizontal, en communiquant au liquide contenu dans ce canal des vitesses sensiblement pareilles de la surface au fond”. In: *Journal de mathématiques pures et appliquées* 17 (1872), pp. 55–108 (cit. on p. 8).

[48] Lord Rayleigh. “On waves”. In: *Phil. Mag.* 1 (1876), pp. 257–259 (cit. on p. 8).

[49] Diederik Johannes Korteweg and Gustav De Vries. “XLI. On the change of form of long waves advancing in a rectangular canal, and on a new type of long stationary waves”. In: *The London, Edinburgh, and Dublin Philosophical Magazine and Journal of Science* 39.240 (1895), pp. 422–443 (cit. on pp. 9, 16, 19).

[50] Michel Remoissenet. *Waves called solitons: concepts and experiments*. Springer Science & Business Media, 2013 (cit. on pp. 9, 29, 63, 64, 89, 95, 98).

[51] Norman J Zabusky and Martin D Kruskal. “Interaction of" solitons" in a collisionless plasma and the recurrence of initial states”. In: *Physical review letters* 15.6 (1965), p. 240 (cit. on pp. 9, 14, 89, 110).

[52] Enrico Fermi et al. *Studies of the nonlinear problems*. Tech. rep. Los Alamos National Laboratory (LANL), Los Alamos, NM (United States), 1955 (cit. on pp. 9, 11, 89, 93).

[53] Thierry Dauxois and Michel Peyrard. *Physics of solitons*. Cambridge University Press, 2006 (cit. on pp. 9, 10, 14, 89, 103).

[54] Roger K Dodd et al. "Solitons and nonlinear wave equations". In: (1982) (cit. on pp. 9, 13).

[55] Thibault Bonnemain. *DS Advanced Lectures Series Part 2 - Introduction to Integrable Field Theories*. Accessed: 2025-01-16. 2023. URL: https://www.youtube.com/watch?v=nlMSMiR_6JY&t=2391s (cit. on p. 12).

[56] Thibault Bonnemain and Benjamin Doyon. "Soliton gas of the integrable Boussinesq equation and its generalised hydrodynamics". In: *arXiv preprint arXiv:2402.08669* (2024) (cit. on pp. 12, 44).

[57] Hans L Pécseli. "Solitons and weakly nonlinear waves in plasmas". In: *IEEE transactions on plasma science* 13.2 (1985), pp. 53–86 (cit. on p. 14).

[58] David R Scott and David J Stevenson. "Magma solitons". In: *Geophysical Research Letters* 11.11 (1984), pp. 1161–1164 (cit. on p. 14).

[59] Danial Saadatmand, Sergey V Dmitriev, and Panayotis G Kevrekidis. "High energy density in multisoliton collisions". In: *Physical Review D* 92.5 (2015), p. 056005 (cit. on p. 14).

[60] Andrea Blanco-Redondo et al. "The bright prospects of optical solitons after 50 years". In: *Nature Photonics* 17.11 (2023), pp. 937–942 (cit. on pp. 14, 15).

[61] Akira Hasegawa and Frederick Tappert. "Transmission of stationary nonlinear optical pulses in dispersive dielectric fibers. I. Anomalous dispersion". In: *Applied Physics Letters* 23.3 (1973), pp. 142–144 (cit. on p. 14).

[62] Akira Hasegawa and Takayuki Nyu. "Eigenvalue communication". In: *Journal of lightwave technology* 11.3 (1993), pp. 395–399 (cit. on p. 14).

[63] Linn F Mollenauer, Roger H Stolen, and James P Gordon. "Experimental observation of picosecond pulse narrowing and solitons in optical fibers". In: *Physical review letters* 45.13 (1980), p. 1095 (cit. on pp. 14, 148).

[64] M Nakazawa et al. "Experimental demonstration of soliton data transmission over unlimited distances with soliton control in time and frequency domains". In: *Optical Fiber Communication Conference*. Optica Publishing Group. 1993, PD7 (cit. on pp. 14, 148).

[65] Masataka Nakazawa, Kazunori Suzuki, and Yasuo Kimura. "3.2-5 Gb/s, 100 km error-free soliton transmission with erbium amplifiers and repeaters". In: *IEEE Photonics Technology Letters* 2.3 (1990), pp. 216–219 (cit. on p. 14).

[66] M Nakazawa et al. "10 Gbit/s soliton data transmission over one million kilometres". In: *Electronics Letters* 27.14 (1991), pp. 1270–1272 (cit. on pp. 14, 148).

[67] NA Olsson et al. "4 Gb/s soliton data transmission over 136 km using erbium doped fiber amplifiers". In: *IEEE Photonics Technology Letters* 2.5 (2002), pp. 358–359 (cit. on p. 14).

[68] Katsumi Iwatsuki, Shigendo Nishi, and Kiyoshi Nakagawa. "3.6 Gb/s all laser-diode optical soliton transmission". In: *IEEE Photonics Technology Letters* 2.5 (2002), pp. 355–357 (cit. on p. 14).

[69] LF Mollenauer et al. "Demonstration, using sliding-frequency guiding filters, of error-free soliton transmission over more than 20 Mm at 10 Gbit/s, single channel, and over more than 13 Mm at 20 Gbit/s in a two-channel WDM". In: *Electronics Letters* 29.10 (1993), pp. 910–911 (cit. on p. 14).

[70] Sergei K Turitsyn et al. "Nonlinear Fourier transform for optical data processing and transmission: advances and perspectives". In: *Optica* 4.3 (2017), pp. 307–322 (cit. on p. 14).

[71] John Michael Dudley et al. "Fifty years of fiber solitons". In: *Optics and photonics news* 34.5 (2023), pp. 26–33 (cit. on p. 15).

[72] Joseph Liouville. "Note sur l'intégration des équations différentielles de la Dynamique, présentée au Bureau des Longitudes le 29 juin 1853". In: *Journal de Mathématiques pures et appliquées* 20 (1855), pp. 137–138 (cit. on p. 15).

[73] Vladimir Igorevich Arnol'd. *Mathematical methods of classical mechanics*. Vol. 60. Springer Science & Business Media, 2013 (cit. on p. 15).

[74] Léa Dubois. "Dynamique hors d'équilibre d'un gaz de Bosons unidimensionnel étudiée via la mesure spatialement résolue de la distribution des quasiparticules". PhD thesis. Université Paris-Saclay, 2024 (cit. on p. 15).

[75] Nigel J Hitchin, Graeme B Segal, and Richard Samuel Ward. *Integrable systems: Twistors, loop groups, and Riemann surfaces*. Vol. 4. OUP Oxford, 2013 (cit. on p. 15).

[76] Giacomo Roberti. "Analysis and control of rogue waves in fibre lasers and in hydrodynamics: integrable turbulence framework". PhD thesis. University of Northumbria at Newcastle (UK), 2022 (cit. on p. 15).

[77] Andrea Pezzi. "The Rayleigh-Jeans Distribution for the FPUT chain". In: *Catenadiatomica* (2025) (cit. on p. 15).

[78] Marcos Rigol et al. "Relaxation in a completely integrable many-body quantum system: an ab initio study of the dynamics of the highly excited states of 1D lattice hard-core bosons". In: *Physical review letters* 98.5 (2007), p. 050405 (cit. on p. 15).

[79] Joseph L Hammack and Harvey Segur. "The Korteweg-de Vries equation and water waves. Part 3. Oscillatory waves". In: *Journal of Fluid Mechanics* 84.2 (1978), pp. 337–358 (cit. on p. 16).

[80] Ivan Redor. "Étude expérimentale de la turbulence intégrable en eau peu profonde". PhD thesis. Université Grenoble Alpes, 2019 (cit. on p. 16).

[81] Thibault Leduque. "Étude expérimentale et numérique d'ondes non-linéaires multidirectionelles en eau peu profonde : application aux gaz de solitons". PhD thesis. Université Grenoble Alpes, 2024 (cit. on p. 16).

[82] Clifford S Gardner and George Kiyoshi Morikawa. "The effect of temperature on the width of a small-amplitude, solitary wave in a collision-free plasma". In: *Communications on Pure and Applied Mathematics* 18.1-2 (1965), pp. 35–49 (cit. on p. 16).

[83] Haruichi Washimi and Tosiya Taniuti. "Propagation of ion-acoustic solitary waves of small amplitude". In: *Physical Review Letters* 17.19 (1966), p. 996 (cit. on p. 16).

[84] Yoshiharu Nakamura. "Experiments on ion-acoustic solitons in plasmas invited review article". In: *IEEE Transactions on Plasma Science* 10.3 (1982), pp. 180–195 (cit. on p. 16).

[85] V Achilleos et al. "Acoustic solitons in waveguides with Helmholtz resonators: Transmission line approach". In: *Physical Review E* 91.2 (2015), p. 023204 (cit. on p. 16).

[86] Scott A Sarra. "The method of characteristics with applications to conservation laws". In: *Journal of Online mathematics and its Applications* 3 (2003), pp. 1–16 (cit. on p. 17).

[87] Nate Bottman and Bernard Deconinck. "KdV cnoidal waves are spectrally stable". In: *Discrete and Continuous Dynamical Systems-Series A (DCDS-A)* 25.4 (2009), p. 1163 (cit. on p. 20).

[88] Nikolay K Vitanov, Amin Chabchoub, and Norbert Hoffmann. "Deep-water waves: on the nonlinear schrodinger equation and its solutions". In: *Journal of Theoretical and Applied Mechanics* 43.2 (2013), pp. 43–54 (cit. on pp. 21, 63).

[89] Mark J Ablowitz. *Nonlinear dispersive waves: asymptotic analysis and solitons*. Vol. 47. Cambridge University Press, 2011 (cit. on pp. 21, 163, 164).

[90] Amin Chabchoub. "Tracking breather dynamics in irregular sea state conditions". In: *Physical review letters* 117.14 (2016), p. 144103 (cit. on p. 21).

[91] Stéphane Randoux et al. "Nonlinear spectral analysis of Peregrine solitons observed in optics and in hydrodynamic experiments". In: *Physical Review E* 98.2 (2018), p. 022219 (cit. on p. 21).

[92] Gang Xu et al. "Observation of modulation instability and rogue breathers on stationary periodic waves". In: *Physical Review Research* 2.3 (2020), p. 033528 (cit. on p. 21).

[93] Amin Chabchoub et al. "Phase-suppressed hydrodynamics of solitons on constant-background plane wave". In: *Physical review fluids* 5.11 (2020), p. 114801 (cit. on p. 21).

[94] Yuchen He, Pierre Suret, and Amin Chabchoub. "Phase evolution of the time-and space-like Peregrine Breather in a laboratory". In: *Fluids* 6.9 (2021), p. 308 (cit. on p. 21).

[95] Govind P Agrawal. "Nonlinear fiber optics". In: *Nonlinear Science at the Dawn of the 21st Century*. Springer, 2000, pp. 195–211 (cit. on pp. 21, 25, 148, 158, 161).

[96] Pierre Walczak, Stéphane Randoux, and Pierre Suret. "Optical rogue waves in integrable turbulence". In: *Physical review letters* 114.14 (2015), p. 143903 (cit. on p. 21).

[97] Pierre Suret et al. "Single-shot observation of optical rogue waves in integrable turbulence using time microscopy". In: *Nature communications* 7.1 (2016), p. 13136 (cit. on p. 21).

[98] Mikko Närhi et al. "Real-time measurements of spontaneous breathers and rogue wave events in optical fibre modulation instability". In: *Nature communications* 7.1 (2016), p. 13675 (cit. on pp. 21, 174).

[99] Alexey Tikan et al. "Single-shot measurement of phase and amplitude by using a heterodyne time-lens system and ultrafast digital time-holography". In: *Nature Photonics* 12.4 (2018), pp. 228–234 (cit. on p. 21).

[100] Nail Akhmediev, VM Eleonskii, and NE Kulagin. "Generation of periodic trains of picosecond pulses in an optical fiber: exact solutions". In: *Sov. Phys. JETP* 62.5 (1985), pp. 894–899 (cit. on p. 21).

[101] Alexey Tikan et al. "Universality of the Peregrine soliton in the focusing dynamics of the cubic nonlinear Schrödinger equation". In: *Physical review letters* 119.3 (2017), p. 033901 (cit. on p. 21).

[102] Jianke Yang. *Nonlinear waves in integrable and nonintegrable systems*. SIAM, 2010 (cit. on pp. 21, 23, 26, 28, 29, 31, 32, 176, 177, 186).

[103] Giacomo Roberti et al. "Numerical spectral synthesis of breather gas for the focusing nonlinear Schrödinger equation". In: *Physical Review E* 103.4 (2021), p. 042205 (cit. on pp. 23, 57).

[104] T Brooke Benjamin and James E Feir. "The disintegration of wave trains on deep water Part 1. Theory". In: *Journal of Fluid Mechanics* 27.3 (1967), pp. 417–430 (cit. on p. 25).

[105] K Tai, A Hasegawa, and A Tomita. "Observation of modulational instability in optical fibers". In: *Physical review letters* 56.2 (1986), p. 135 (cit. on p. 25).

[106] LA Ostrovskii and LV Soustov. ""Selfmodulation" of electromagnetic waves in nonlinear transmission lines". In: *Radiophysics and Quantum Electronics* 15 (1972), pp. 182–187 (cit. on p. 25).

[107] Kevin E Strecker et al. "Formation and propagation of matter-wave soliton trains". In: *Nature* 417.6885 (2002), pp. 150–153 (cit. on p. 25).

[108] Thomas Brooke Benjamin. "Instability of periodic wavetrains in nonlinear dispersive systems". In: *Proceedings of the Royal Society of London. Series A. Mathematical and Physical Sciences* 299.1456 (1967), pp. 59–76 (cit. on p. 25).

[109] Bruce M Lake et al. "Nonlinear deep-water waves: theory and experiment. Part 2. Evolution of a continuous wave train". In: *Journal of Fluid Mechanics* 83.1 (1977), pp. 49–74 (cit. on p. 25).

[110] Ming-Yang Su et al. "Experiments on nonlinear instabilities and evolution of steep gravity-wave trains". In: *Journal of Fluid Mechanics* 124 (1982), pp. 45–72 (cit. on p. 25).

[111] Hwung-Hweng Hwung, Wen-Son Chiang, and Shih-Chun Hsiao. "Observations on the evolution of wave modulation". In: *Proceedings of the Royal Society A: Mathematical, Physical and Engineering Sciences* 463.2077 (2007), pp. 85–112 (cit. on p. 25).

[112] Vladimir E Zakharov and Lev A Ostrovsky. "Modulation instability: the beginning". In: *Physica D: Nonlinear Phenomena* 238.5 (2009), pp. 540–548 (cit. on pp. 25, 174).

[113] François Copie, Stéphane Randoux, and Pierre Suret. "The physics of the one-dimensional nonlinear Schrödinger equation in fiber optics: Rogue waves, modulation instability and self-focusing phenomena". In: *Reviews in Physics* 5 (2020), p. 100037 (cit. on p. 25).

[114] Vladimir E Zakharov and AA Gelash. "Nonlinear stage of modulation instability". In: *Physical review letters* 111.5 (2013), p. 054101 (cit. on p. 25).

[115] Gino Biondini and Dionyssios Mantzavinos. "Universal nature of the nonlinear stage of modulational instability". In: *Physical review letters* 116.4 (2016), p. 043902 (cit. on p. 25).

[116] Aleksei Shabat and Vladimir Zakharov. "Exact theory of two-dimensional self-focusing and one-dimensional self-modulation of waves in nonlinear media". In: *Sov. Phys. JETP* 34.1 (1972), p. 62 (cit. on pp. 26, 28, 51, 176).

[117] Peter D. Lax. "Integrals of nonlinear equations of evolution and solitary waves". In: *Communications on Pure and Applied Mathematics* 21.5 (1968), pp. 467–490 (cit. on pp. 26, 27).

[118] Alan C Newell. "The inverse scattering transform". In: *Solitons*. Springer, 1980, pp. 177–242 (cit. on p. 26).

[119] S Novikov et al. *Theory of solitons: the inverse scattering method*. Springer Science & Business Media, 1984 (cit. on pp. 26, 28, 57, 178).

[120] Chaohao Gu, Hesheng Hu, and Zixiang Zhou. *Darboux transformations in integrable systems: theory and their applications to geometry*. Springer Science & Business Media, 2004 (cit. on p. 27).

[121] Gennady El and Alexander Tovbis. "Spectral theory of soliton and breather gases for the focusing nonlinear Schrödinger equation". In: *Physical Review E* 101.5 (2020), p. 052207 (cit. on pp. 33, 37, 38, 42, 43, 48, 50, 51, 88, 136, 139, 180).

[122] Andrey Gelash et al. "Bound state soliton gas dynamics underlying the spontaneous modulational instability". In: *Physical review letters* 123.23 (2019), p. 234102 (cit. on pp. 33, 34, 58, 121, 151, 179).

[123] Andrea Costa et al. "Soliton turbulence in shallow water ocean surface waves". In: *Physical review letters* 113.10 (2014), p. 108501 (cit. on p. 33).

[124] Peter J Prins and Sander Wahls. "An accurate O (N2) floating point algorithm for the Crum transform of the KdV equation". In: *Communications in Nonlinear Science and Numerical Simulation* 102 (2021), p. 105782 (cit. on p. 34).

[125] Vladimir B Matveev and Mikhail A Salle. "Darboux transformations and solitons". In: *Springer series in nonlinear dynamics* (1991) (cit. on p. 34).

[126] AA Gelash and DS Agafontsev. "Strongly interacting soliton gas and formation of rogue waves". In: *Physical Review E* 98.4 (2018), p. 042210 (cit. on pp. 34, 57).

[127] Gou-Jun Liao and Nian-Ning Huang. "Method of Darboux Transformation Matrix for the KdV Equation1". In: *Communications in Theoretical Physics* 25.2 (1996), p. 183 (cit. on pp. 35, 121).

[128] Thibault Congy et al. "Dispersive hydrodynamics of soliton condensates for the Korteweg–de Vries equation". In: *Journal of Nonlinear Science* 33.6 (2023), p. 104 (cit. on pp. 35, 37, 48, 121, 124, 136–140, 143).

[129] Tatiana V Tarasova and Alexey V Slunyaev. "Properties of synchronous collisions of solitons in the Korteweg–de Vries equation". In: *Communications in Nonlinear Science and Numerical Simulation* 118 (2023), p. 107048 (cit. on pp. 35, 121).

[130] A El Gennady. "Soliton gas in integrable dispersive hydrodynamics". In: *Journal of Statistical Mechanics: Theory and Experiment* 2021.11 (2021), p. 114001 (cit. on pp. 38, 42, 43, 49, 131, 191).

[131] Francesco Carbone, Denys Dutykh, and GA El. "Macroscopic dynamics of incoherent soliton ensembles: Soliton gas kinetics and direct numerical modelling". In: *Europhysics Letters* 113.3 (2016), p. 30003 (cit. on pp. 41, 48).

[132] H Flaschka, M Gregory Forest, and DW McLaughlin. "Multiphase averaging and the inverse spectral solution of the Korteweg—de Vries equation". In: *Communications on Pure and Applied Mathematics* 33.6 (1980), pp. 739–784 (cit. on p. 41).

[133] Eugene D Belokolos. "Algebro-geometric approach to nonlinear integrable equations". In: *(No Title)* (1994) (cit. on p. 42).

[134] Benjamin Doyon. "Lecture notes on generalised hydrodynamics". In: *SciPost Physics Lecture Notes* (2020), p. 018 (cit. on p. 44).

[135] Alvise Bastianello et al. "Observation of a generalized Gibbs ensemble in photonics". In: *arXiv preprint arXiv:2503.16526* (2025) (cit. on pp. 44, 45).

[136] Bruno Bertini et al. “Transport in out-of-equilibrium XXZ chains: exact profiles of charges and currents”. In: *Physical review letters* 117.20 (2016), p. 207201 (cit. on p. 44).

[137] Olalla A Castro-Alvaredo, Benjamin Doyon, and Takato Yoshimura. “Emergent hydrodynamics in integrable quantum systems out of equilibrium”. In: *Physical Review X* 6.4 (2016), p. 041065 (cit. on p. 44).

[138] Max Schemmer et al. “Generalized hydrodynamics on an atom chip”. In: *Physical review letters* 122.9 (2019), p. 090601 (cit. on p. 44).

[139] Neel Malvania et al. “Generalized hydrodynamics in strongly interacting 1D Bose gases”. In: *Science* 373.6559 (2021), pp. 1129–1133 (cit. on p. 44).

[140] Isabelle Bouchoule and Jérôme Dubail. “Generalized hydrodynamics in the one-dimensional Bose gas: theory and experiments”. In: *Journal of Statistical Mechanics: Theory and Experiment* 2022.1 (2022), p. 014003 (cit. on p. 44).

[141] Benjamin Doyon, Takato Yoshimura, and Jean-Sébastien Caux. “Soliton gases and generalized hydrodynamics”. In: *Physical review letters* 120.4 (2018), p. 045301 (cit. on p. 44).

[142] Thibault Bonnemain, Benjamin Doyon, and Gennady El. “Generalized hydrodynamics of the KdV soliton gas”. In: *Journal of Physics A: Mathematical and Theoretical* 55.37 (2022), p. 374004 (cit. on pp. 44, 124, 131, 136, 139).

[143] Benjamin Doyon and Takato Yoshimura. “A note on generalized hydrodynamics: inhomogeneous fields and other concepts”. In: *SciPost Physics* 2.2 (2017), p. 014 (cit. on p. 44).

[144] Florian Lange, Zala Lenarčič, and Achim Rosch. “Time-dependent generalized Gibbs ensembles in open quantum systems”. In: *Physical Review B* 97.16 (2018), p. 165138 (cit. on p. 44).

[145] Alvise Bastianello, Andrea De Luca, and Romain Vasseur. “Hydrodynamics of weak integrability breaking”. In: *Journal of Statistical Mechanics: Theory and Experiment* 2021.11 (2021), p. 114003 (cit. on p. 44).

[146] Maciej Łebek and Miłosz Panfil. “Navier-Stokes equations for nearly integrable quantum gases”. In: *Physical Review Letters* 134.1 (2025), p. 010405 (cit. on p. 44).

[147] Elliott H Lieb and Werner Liniger. “Exact analysis of an interacting Bose gas. I. The general solution and the ground state”. In: *Physical Review* 130.4 (1963), p. 1605 (cit. on p. 44).

[148] Chen-Ning Yang, Cheng P Yang, et al. "Thermodynamics of a one-dimensional system of bosons with repulsive delta-function interaction". In: *Journal of Mathematical Physics* 10.7 (1969), p. 1115 (cit. on pp. 44, 45).

[149] Giuseppe Del Vecchio Del Vecchio et al. "Exact out-of-equilibrium steady states in the semiclassical limit of the interacting Bose gas". In: *SciPost Physics* 9.1 (2020), p. 002 (cit. on p. 45).

[150] Rebekka Koch, Jean-Sébastien Caux, and Alvise Bastianello. "Generalized hydrodynamics of the attractive non-linear Schrodinger equation". In: *Journal of Physics A: Mathematical and Theoretical* 55.13 (2022), p. 134001 (cit. on p. 45).

[151] H Ikezi, RJ Taylor, and DR Baker. "Formation and interaction of ion-acoustic solitions". In: *Physical Review Letters* 25.1 (1970), p. 11 (cit. on pp. 48, 110).

[152] R. Hirota and K. Suzuki. "Theoretical and experimental studies of lattice solitons in nonlinear lumped networks". In: *Proceedings of the IEEE* 61.10 (1973), pp. 1483–1491 (cit. on pp. 48, 93, 94, 110).

[153] Fedor M Mitschke and Linn F Mollenauer. "Experimental observation of interaction forces between solitons in optical fibers". In: *Optics letters* 12.5 (1987), pp. 355–357 (cit. on p. 48).

[154] Mohammed N Islam and CE Soccolich. "Billiard-ball soliton interaction gates". In: *Optics letters* 16.19 (1991), pp. 1490–1492 (cit. on p. 48).

[155] J Stewart Aitchison et al. "Experimental observation of spatial soliton interactions". In: *Optics letters* 16.1 (1991), pp. 15–17 (cit. on p. 48).

[156] David W Aossey et al. "Properties of soliton-soliton collisions". In: *Physical Review A* 45.4 (1992), p. 2606 (cit. on p. 48).

[157] Alexey Slunyaev, Marco Klein, and Günther F Clauss. "Laboratory and numerical study of intense envelope solitons of water waves: Generation, reflection from a wall, and collisions". In: *Physics of fluids* 29.4 (2017) (cit. on p. 48).

[158] Thibault Congy, Gennady El, and Giacomo Roberti. "Soliton gas in bidirectional dispersive hydrodynamics". In: *Physical Review E* 103.4 (2021), p. 042201 (cit. on pp. 48, 129).

[159] Thibault Bonnemain et al. "Two-dimensional stationary soliton gas". In: *Physical Review Research* 7.1 (2025), p. 013143 (cit. on p. 48).

[160] Thibault Congy et al. "Riemann problem for polychromatic soliton gases: a testbed for the spectral kinetic theory". In: *Wave Motion* (2025), p. 103480 (cit. on pp. 48, 49, 136, 138).

[161] AM Kamchatnov and DV Shaykin. "Dynamics of interaction between two soliton clouds". In: *Journal of Experimental and Theoretical Physics* 135.5 (2022), pp. 768–776 (cit. on p. 52).

[162] Félicien Bonnefoy. "Modélisation expérimentale et numérique des états de mer complexes". PhD thesis. Université de Nantes, 2005 (cit. on p. 61).

[163] J. Carvill. "7 - Engineering measurements". In: *Mechanical Engineer's Data Handbook*. Ed. by J. Carvill. Oxford: Butterworth-Heinemann, 1993, pp. 267–287 (cit. on p. 61).

[164] Vladimir E Zakharov. "Stability of periodic waves of finite amplitude on the surface of a deep fluid". In: *Journal of Applied Mechanics and Technical Physics* 9.2 (1968), pp. 190–194 (cit. on pp. 63, 64).

[165] Chiang C Mei. *The applied dynamics of ocean surface waves*. Vol. 1. World scientific, 1989 (cit. on p. 63).

[166] Amin Chabchoub et al. "The nonlinear Schrödinger equation and the propagation of weakly nonlinear waves in optical fibers and on the water surface". In: *Annals of Physics* 361 (2015), pp. 490–500 (cit. on p. 63).

[167] Annette Cazaubiel et al. "Coexistence of solitons and extreme events in deep water surface waves". In: *Physical Review Fluids* 3.11 (2018), p. 114802 (cit. on pp. 63, 64).

[168] Karsten Trulsen et al. "On weakly nonlinear modulation of waves on deep water". In: *Physics of fluids* 12.10 (2000), pp. 2432–2437 (cit. on p. 63).

[169] Ivan Redor et al. "Analysis of soliton gas with large-scale video-based wave measurements". In: *Experiments in Fluids* 61 (2020), pp. 1–14 (cit. on p. 70).

[170] Avinash C. Kak and Malcolm Slaney. *Principles of Computerized Tomographic Imaging*. Society for Industrial and Applied Mathematics, 2001 (cit. on p. 70).

[171] Ronald N Bracewell. "Strip integration in radio astronomy". In: *Australian Journal of Physics* 9.2 (1956), pp. 198–217 (cit. on p. 70).

[172] RC Hawkes et al. "Nuclear magnetic resonance (NMR) tomography of the brain: a preliminary clinical assessment with demonstration of pathology". In: *Journal of Computer Assisted Tomography* 4.5 (1980), pp. 577–586 (cit. on p. 70).

[173] Luc T. Ikelle. "Chapter 5 - Decoding of Nonlinear Mixtures". In: *Coding and Decoding: Seismic Data (Second Edition)*. Ed. by Luc T. Ikelle. Second Edition. Computational Geophysics. Elsevier, 2018, pp. 429–534 (cit. on p. 70).

[174] Weida Xia et al. "Emergence of solitons from irregular waves in deep water". In: *Journal of Marine Science and Engineering* 9.12 (2021), p. 1369 (cit. on p. 80).

[175] Alexey Tikan et al. "Nonlinear dispersion relation in integrable turbulence". In: *Scientific reports* 12.1 (2022), p. 10386 (cit. on p. 80).

[176] Alexey Tikan et al. "Prediction and manipulation of hydrodynamic rogue waves via nonlinear spectral engineering". In: *Physical Review Fluids* 7.5 (2022), p. 054401 (cit. on p. 80).

[177] Félicien Bonnefoy et al. "From modulational instability to focusing dam breaks in water waves". In: *Physical Review Fluids* 5.3 (2020), p. 034802 (cit. on pp. 80, 151).

[178] Alexey Slunyaev et al. "Super-rogue waves in simulations based on weakly nonlinear and fully nonlinear hydrodynamic equations". In: *Physical Review E—Statistical, Nonlinear, and Soft Matter Physics* 88.1 (2013), p. 012909 (cit. on p. 80).

[179] HD Zhang, C Guedes Soares, and Miguel Onorato. "Modelling of the spatial evolution of extreme laboratory wave heights with the nonlinear Schrödinger and Dysthe equations". In: *Ocean Engineering* 89 (2014), pp. 1–9 (cit. on p. 80).

[180] Kristian B Dysthe. "Note on a modification to the nonlinear Schrödinger equation for application to deep water waves". In: *Proceedings of the Royal Society of London. A. Mathematical and Physical Sciences* 369.1736 (1979), pp. 105–114 (cit. on p. 80).

[181] Karsten Trulsen and Kristian B Dysthe. "A modified nonlinear Schrödinger equation for broader bandwidth gravity waves on deep water". In: *Wave motion* 24.3 (1996), pp. 281–289 (cit. on p. 80).

[182] Frank R Kschischang. *The Hilbert Transform*. 2006 (cit. on p. 81).

[183] David Shawn Ricketts and Donhee Ham. *Electrical solitons: theory, design, and applications*. Devices, circuits, and systems. Boca Raton, FL: CRC Press, 2011 (cit. on pp. 89, 91, 95, 97, 98, 104, 105, 114, 117).

[184] S. Trillo et al. "Observation of dispersive shock waves developing from initial depressions in shallow water". In: *Physica D: Nonlinear Phenomena* 333 (2016). Dispersive Hydrodynamics, pp. 276–284 (cit. on p. 92).

[185] CC Cutler. "The regenerative pulse generator". In: *Proceedings of the IRE* 43.2 (1955), pp. 140–148 (cit. on p. 93).

[186] Ping K Tien. "Parametric amplification and frequency mixing in propagating circuits". In: *Journal of Applied Physics* 29.9 (1958), pp. 1347–1357 (cit. on p. 93).

[187] AL Cullen. "A travelling-wave parametric amplifier". In: *Nature* 181.4605 (1958), pp. 332–332 (cit. on p. 93).

[188] Rolf Landauer. "Parametric amplification along nonlinear transmission lines". In: *Journal of applied physics* 31.3 (1960), pp. 479–484 (cit. on p. 93).

[189] Morikazu Toda. "Vibration of a chain with nonlinear interaction". In: *Journal of the Physical Society of Japan* 22.2 (1967), pp. 431–436 (cit. on p. 93).

[190] Morikazu Toda. "Wave propagation in anharmonic lattices". In: *Journal of the Physical Society of Japan* 23.3 (1967), pp. 501–506 (cit. on p. 93).

[191] Hiroyuki Nagashima and Yoshimitsu Amagishi. "Experiment on the Toda Lattice Using Nonlinear Transmission Lines". en. In: *Journal of the Physical Society of Japan* 45.2 (1978), pp. 680–688 (cit. on p. 93).

[192] D Jäger and F-J Tegude. "Nonlinear wave propagation along periodic-loaded transmission line". In: *Applied physics* 15.4 (1978), pp. 393–397 (cit. on p. 93).

[193] D Jäger. "Soliton propagation along periodic-loaded transmission line". In: *Applied physics* 16.1 (1978), pp. 35–38 (cit. on p. 93).

[194] Ryogo Hirota and Kimio Suzuki. "Studies on lattice solitons by using electrical networks". In: *Journal of the Physical Society of Japan* 28.5 (1970), pp. 1366–1367 (cit. on pp. 93, 110).

[195] Dieter Jäger. "Experiments on KdV solitons". In: *Journal of the Physical Society of Japan* 51.5 (1982), pp. 1686–1693 (cit. on p. 94).

[196] Shinsuke Watanabe. "Solitons in Nonlinear Transmission Line". en. In: *Journal of the Physical Society of Japan* 51.3 (1982), pp. 1030–1036 (cit. on p. 94).

[197] Taiju Tsuboi. "Phase shift in the collision of two solitons propagating in a nonlinear transmission line". en. In: *Physical Review A* 40.5 (1989), pp. 2753–2755 (cit. on p. 94).

[198] J. I. Ramos. "Asymptotic methods for the analysis of wave propagation in nonlinear, lossless transmission lines and equivalent circuits". en. In: *Microwave and Optical Technology Letters* 8.4 (1995), pp. 186–193 (cit. on p. 94).

[199] Takao Yoshinaga and Tsunehiko Kakutani. "Asymptotic behaviour of a negative rectangular pulse on a nonlinear LC ladder line". In: *Journal of the Physical Society of Japan* 51.4 (1982), pp. 1303–1309 (cit. on p. 97).

[200] ML Lucia et al. "Capacitance measurements of pn junctions: depletion layer and diffusion capacitance contributions". In: *European journal of physics* 14.2 (1993), p. 86 (cit. on p. 97).

[201] R Lindner. "Semiconductor surface varactor". In: *Bell System Technical Journal* 41.3 (1962), pp. 803–831 (cit. on p. 97).

[202] Gerald Beresford Whitham. *Linear and nonlinear waves*. John Wiley & Sons, 2011 (cit. on p. 103).

[203] Shu Jian-Jun. "The proper analytical solution of the Korteweg-de Vries-Burgers equation". In: *Journal of Physics A: Mathematical and General* 20.2 (1987), p. L49 (cit. on p. 106).

[204] NJ Zabusky and CJ Galvin. "Shallow-water waves, the Korteweg-deVries equation and solitons". In: *Journal of Fluid Mechanics* 47.4 (1971), pp. 811–824 (cit. on p. 110).

[205] Alan C Newell. *Solitons in mathematics and physics*. SIAM, 1985 (cit. on pp. 113, 117, 118).

[206] Jon Wright. "Soliton production and solutions to perturbed Korteweg-deVries equations". In: *Physical Review A* 21.1 (1980), p. 335 (cit. on pp. 113, 116, 118).

[207] Yuri S Kivshar and Boris A Malomed. "Dynamics of solitons in nearly integrable systems". In: *Reviews of Modern Physics* 61.4 (1989), p. 763 (cit. on pp. 113, 116, 120).

[208] CJ Knickerbocker and Alan C Newell. "Propagation of solitary waves in channels of decreasing depth". In: *Journal of Statistical Physics* 39 (1985), pp. 653–674 (cit. on p. 113).

[209] Thomas Zdyrski and Falk Feddersen. "Wind-induced changes to shoaling surface gravity wave shape". In: *Physical Review Fluids* 7.7 (2022), p. 074802 (cit. on p. 113).

[210] GA El and Roger HJ Grimshaw. "Generation of undular bores in the shelves of slowly-varying solitary waves". In: *Chaos: An Interdisciplinary Journal of Nonlinear Science* 12.4 (2002), pp. 1015–1026 (cit. on p. 115).

[211] A Gudko, A Gelash, and R Mullyadzhanov. "High-order numerical method for scattering data of the Korteweg—De Vries equation". In: *Journal of Physics: Conference Series*. Vol. 1677. 1. IOP Publishing. 2020, p. 012011 (cit. on p. 115).

[212] Roger Grimshaw et al. "Generation of large-amplitude solitons in the extended Korteweg–de Vries equation". In: *Chaos: An Interdisciplinary Journal of Nonlinear Science* 12.4 (2002), pp. 1070–1076 (cit. on p. 116).

[213] David J Kaup and Alan C Newell. "Solitons as particles, oscillators, and in slowly changing media: a singular perturbation theory". In: *Proceedings of the Royal Society of London. A. Mathematical and Physical Sciences* 361.1707 (1978), pp. 413–446 (cit. on pp. 117, 118).

[214] Auro M Perego. "Optical Darboux Transformer". In: *Physical Review Letters* 132.12 (2024), p. 123801 (cit. on p. 121).

[215] GA El and MA Hoefer. "Dispersive shock waves and modulation theory". In: *Physica D: Nonlinear Phenomena* 333 (2016), pp. 11–65 (cit. on pp. 124, 140).

[216] Gennady A El, Mark A Hoefer, and Michael Shearer. "Dispersive and diffusive-dispersive shock waves for nonconvex conservation laws". In: *SIAM Review* 59.1 (2017), pp. 3–61 (cit. on p. 124).

[217] VI Karpman. "An asymptotic solution of the Korteweg-de Vries equation". In: *Physics Letters A* 25.10 (1967), pp. 708–709 (cit. on p. 124).

[218] Franck Laloë Claude Cohen-Tannoudji Bernard Diu. *Mécanique Quantique - Tome 1: Nouvelle édition*. fre. 1st ed. Les Ulis: EDP Sciences, 2018 (cit. on p. 131).

[219] Robert M Miura. "The Korteweg–deVries equation: a survey of results". In: *SIAM review* 18.3 (1976), pp. 412–459 (cit. on p. 132).

[220] Jerry Tersoff and Donald R Hamann. "Theory of the scanning tunneling microscope". In: *Physical Review B* 31.2 (1985), p. 805 (cit. on p. 132).

[221] FJ de Abajo and M Kociak. "Probing the photonic local density of states with electron energy loss spectroscopy". In: *arXiv preprint arXiv:0710.5553* (2007) (cit. on p. 132).

[222] DS Agafontsev et al. "Spontaneous modulational instability of elliptic periodic waves: the soliton condensate model". In: *arXiv preprint arXiv:2411.06922* (2024) (cit. on p. 139).

[223] Adrien Kraych. "Instabilités modulationnelles dans un anneau de recirculation fibré". PhD thesis. Université de Lille (2018-2021), 2020 (cit. on pp. 147, 149).

[224] Martin Dufour. "Interactions de solitons: effets collectifs et effets perturbatifs". PhD thesis. Université de Lille, 2023 (cit. on p. 147).

[225] Alexandre Mucci. "État lié de solitons: perturbation localisée et effet dissipatif". PhD thesis. Université de Lille, 2024 (cit. on pp. 147, 177).

[226] Bertrand Kibler et al. "The Peregrine soliton in nonlinear fibre optics". In: *Nature physics* 6.10 (2010), pp. 790–795 (cit. on p. 147).

[227] Arnaud Mussot et al. "Fermi-Pasta-Ulam recurrence in nonlinear fiber optics: the role of reversible and irreversible losses". In: *Physical Review X* 4.1 (2014), p. 011054 (cit. on p. 147).

[228] Frederic Audo et al. "Experimental observation of the emergence of Peregrine-like events in focusing dam break flows". In: *Optics Letters* 43.12 (2018), pp. 2864–2867 (cit. on p. 148).

[229] B Frisquet, B Kibler, and G Millot. "Collision of Akhmediev breathers in nonlinear fiber optics". In: *Physical Review X* 3.4 (2013), p. 041032 (cit. on p. 148).

[230] Kamal Hammani et al. "Spectral dynamics of modulation instability described using Akhmediev breather theory". In: *Optics letters* 36.11 (2011), pp. 2140–2142 (cit. on p. 148).

[231] Julien Fatome et al. "All-fiber spectral compression of picosecond pulses at telecommunication wavelength enhanced by amplitude shaping". In: *Applied optics* 51.19 (2012), pp. 4547–4553 (cit. on p. 148).

[232] Esben Ravn Andresen et al. "Spectral analog of the Gouy phase shift". In: *Physical review letters* 110.14 (2013), p. 143902 (cit. on p. 148).

[233] Luc Thévenaz. "Review and progress in distributed fiber sensing". In: *Optical fiber sensors*. Optica Publishing Group. 2006, ThC1 (cit. on p. 148).

[234] Armand Vedadi et al. "Brillouin optical time-domain analysis of fiber-optic parametric amplifiers". In: *IEEE Photonics Technology Letters* 19.3 (2007), pp. 179–181 (cit. on p. 148).

[235] Camille Sophie Brès. "Power evolution along phase-sensitive parametric amplifiers: an experimental survey". In: (2014) (cit. on p. 148).

[236] Xiaoyang Hu et al. "Distributed measurement of Fermi–Pasta–Ulam recurrence in optical fibers". In: *IEEE Photonics Technology Letters* 30.1 (2017), pp. 47–50 (cit. on p. 148).

[237] Hugo F Martins et al. "Modulation instability-induced fading in phase-sensitive optical time-domain reflectometry". In: *Optics letters* 38.6 (2013), pp. 872–874 (cit. on p. 148).

[238] Corentin Naveau et al. "Heterodyne optical time domain reflectometer combined with active loss compensation: A practical tool for investigating fermi pasta ulam recurrence process and breathers dynamics in optical fibers". In: *Frontiers in Physics* 9 (2021), p. 637812 (cit. on p. 148).

[239] E Desurvire, M Digonnet, and HJ Shaw. "Raman amplification of recirculating pulses in a reentrant fiber loop". In: *Optics letters* 10.2 (1985), pp. 83–85 (cit. on p. 148).

[240] Linn F Mollenauer et al. "Experimental study of soliton transmission over more than 10,000 km in dispersion-shifted fiber". In: *Optics letters* 15.21 (1990), pp. 1203–1205 (cit. on p. 148).

[241] G Aubin et al. "20 Gbit/s soliton transmission over transoceanic distances with a 105 km amplifier span". In: *Electronics Letters* 31.13 (1995), pp. 1079–1080 (cit. on p. 148).

[242] Neal S Bergano and CR Davidson. "Circulating loop transmission experiments for the study of long-haul transmission systems using erbium-doped fiber amplifiers". In: *Journal of Lightwave Technology* 13.5 (1995), pp. 879–888 (cit. on p. 148).

[243] K Suzuki et al. "40 Gbit/s single channel optical soliton transmission over 70000 km using in-line synchronous modulation and optical filtering". In: *Electronics Letters* 34.1 (1998), pp. 98–100 (cit. on p. 148).

[244] R-M Mu et al. "Comparison of theory and experiment for dispersion-managed solitons in a recirculating fiber loop". In: *IEEE Journal of Selected Topics in Quantum Electronics* 6.2 (2000), pp. 248–257 (cit. on p. 148).

[245] Jan-Willem Goossens, Hartmut Hafermann, and Yves Jaouën. "Experimental realization of Fermi-Pasta-Ulam-Tsingou recurrence in a long-haul optical fiber transmission system". In: *Scientific reports* 9.1 (2019), p. 18467 (cit. on p. 149).

[246] Adrien E Kraych et al. "Nonlinear evolution of the locally induced modulational instability in fiber optics". In: *Physical review letters* 122.5 (2019), p. 054101 (cit. on p. 149).

[247] Adrien E Kraych et al. "Statistical properties of the nonlinear stage of modulation instability in fiber optics". In: *Physical review letters* 123.9 (2019), p. 093902 (cit. on pp. 149, 152, 171, 174).

[248] François Copie, Pierre Suret, and Stephane Randoux. "Spatiotemporal observation of higher-order modulation instability in a recirculating fiber loop". In: *Optics Letters* 47.14 (2022), pp. 3560–3563 (cit. on p. 149).

[249] Alexandre Mucci et al. “Manipulation of strongly interacting solitons in optical fiber experiments”. In: *Physical Review Letters* 134.19 (2025), p. 193804 (cit. on p. 149).

[250] Gennady A El, Eduardo G Khamis, and Alexander Tovbis. “Dam break problem for the focusing nonlinear Schrödinger equation and the generation of rogue waves”. In: *Nonlinearity* 29.9 (2016), p. 2798 (cit. on p. 151).

[251] Giulia Marcucci et al. “Topological control of extreme waves”. In: *Nature communications* 10.1 (2019), p. 5090 (cit. on p. 151).

[252] Rustam Mullyadzhanov and Andrey Gelash. “Solitons in a box-shaped wave field with noise: Perturbation theory and statistics”. In: *Physical Review Letters* 126.23 (2021), p. 234101 (cit. on p. 151).

[253] François Copie, Pierre Suret, and Stéphane Randoux. “Controlled manipulation of solitons in a recirculating fiber loop using external potentials”. In: *arXiv preprint arXiv:2506.13544* (2025) (cit. on pp. 162–164).

[254] Jaroslaw E Prilepsky and Stanislav A Derevyanko. “Breakup of a multisoliton state of the linearly damped nonlinear Schrödinger equation”. In: *Physical Review E—Statistical, Nonlinear, and Soft Matter Physics* 75.3 (2007), p. 036616 (cit. on p. 177).

[255] Junkichi Satsuma and Nobuo Yajima. “B. Initial value problems of one-dimensional self-modulation of nonlinear waves in dispersive media”. In: *Progress of Theoretical Physics Supplement* 55 (1974), pp. 284–306 (cit. on p. 177).

[256] Alexander Tovbis, Fudong Wang, et al. “Soliton condensates for the focusing nonlinear Schrödinger equation: A non-bound state case”. In: *SIGMA. Symmetry, Integrability and Geometry: Methods and Applications* 20 (2024), p. 070 (cit. on p. 180).

[257] Dmitry S Agafontsev et al. “Bound-state soliton gas as a limit of adiabatically growing integrable turbulence”. In: *Chaos, Solitons & Fractals* 166 (2023), p. 112951 (cit. on pp. 186, 191).

[258] Daniel C Cole et al. “Soliton crystals in Kerr resonators”. In: *Nature Photonics* 11.10 (2017), pp. 671–676 (cit. on p. 186).

[259] Maxim Karpov et al. “Dynamics of soliton crystals in optical microresonators”. In: *Nature Physics* 15.10 (2019), pp. 1071–1077 (cit. on p. 186).

[260] Isabelle Bouchoule, Benjamin Doyon, and Jerome Dubail. “The effect of atom losses on the distribution of rapidities in the one-dimensional Bose gas”. In: *SciPost Physics* 9.4 (2020), p. 044 (cit. on p. 194).

[261] Andrey Gelash et al. “Bi-solitons on the surface of a deep fluid: An inverse scattering transform perspective based on perturbation theory”. In: *Physical Review Letters* 132.13 (2024), p. 133403 (cit. on p. 196).

[262] Alberto Brollo and Herbert Spohn. *The role of radiation in Toda chain hydrodynamics*. Talk presented at the Student Workshop on Integrability. Budapest, Hungary. 2025 (cit. on p. 196).

[263] Alfred R Osborne. “The Hilbert Transform”. In: *International Geophysics* 97 (2010), pp. 301–329 (cit. on p. 199).

[264] LP Silva Neto et al. “RF pulse formation in NLTLs using varactor diode”. In: *Proc. of The Symposium of Operational Applications in Areas of Defense*. 2014, pp. 1–6 (cit. on p. 205).

[265] J Pellicer-Porres and MV Andrés. “Non-linear resonance in the simplest RLC circuit”. In: *European Journal of Physics* 43.3 (2022), p. 035204 (cit. on p. 205).

[266] Jeremy Everard and Liang Zhou. “Nonlinear effects in varactor-tuned resonators”. In: *IEEE transactions on ultrasonics, ferroelectrics, and frequency control* 53.5 (2006), pp. 853–861 (cit. on p. 205).

[267] Gaofeng LI. “Primary resonance analysis of RLC series circuit with nonlinear capacitance”. In: *Chinese Journal of Computational Physics* 31.3 (2014), p. 351 (cit. on p. 205).

[268] George E Andrews et al. *Special functions*. Vol. 71. Cambridge university press Cambridge, 1999 (cit. on p. 210).

[269] Shangjian Zhang et al. “Self-calibrating measurement of high-speed electro-optic phase modulators based on two-tone modulation”. In: *Optics Letters* 39.12 (2014), pp. 3504–3507 (cit. on p. 210).

Author's bibliography

Publications in peer-reviewed journals:

- **L. Fache**; F. Bonnefoy; G. Ducrozet; F. Copie; F. Novkoski; G. Ricard; G. Roberti; E. Falcon; P. Suret; G. El; and S. Randoux. "Interaction of soliton gases in deep-water surface gravity waves." Physical Review E 109.3 (2024): 034207;

- **L. Fache**; H. Damart; F. Copie; T. Bonnemain; T. Congy; G. Roberti; P. Suret; G. El; and S. Randoux. "Dissipation-driven emergence of a soliton condensate in a nonlinear electrical transmission line." Physical Review Letters 134.14 (2025): 147201.

- **L. Fache**; F. Copie; P. Suret; and S. Randoux. "Perturbed Nonlinear Evolution of Optical Soliton Gases: Growth and Decay in Integrable Turbulence." Physical Review Letters 135.15 (2025): 157201.

Publications in preparation:

- F. Novkoski; **L. Fache**; F. Bonnefoy; G. DUcrozet; F. Copie; P. Suret; S. Randoux; and E. Falcon. "Diffraction of deep-water solitons".

Oral presentation at national and international conferences:

- **L. Fache**; H. Damart; P. Suret; F. Copie; and S. Randoux. "Génération contrôlée et propagation d'un gaz de solitons dans une chaîne électrique d'oscillateurs non-linéaires modélisée par l'équation de Korteweg-de Vries"; Turbulence intégrable, gaz de solitons, et hydrodynamique généralisée - Mini-Colloque RNL (Marc. 2023), Paris;

- **L. Fache**; F. Bonnefoy; G. Ducrozet; F. Copie; F. Novkoski; G. Ricard; G. Roberti; E. Falcon; P. Suret; G. El; and S. Randoux. "Interaction of soliton gases in deep-water surface gravity waves"; Emergent Hydrodynamics of Integrable Systems and Soliton Gases - CIRM (Nov. 2023), Marseille;

- **L. Fache**; F. Copie; P. Suret; and S. Randoux. "Evolution non-linéaire de gaz de solitons dans une boucle de recirculation fibrée"; RNL (Marc. 2025), Paris;

- **L. Fache**; F. Copie; P. Suret; and S. Randoux. "Impact of Loss and Gain on the Nonlinear Spectrum of Dense Optical Soliton Gases "; CLEO Europe (Jun. 2025), München.

Poster at national and international conferences:

- **L. Fache**; F. Bonnefoy; G. Ducrozet; F. Copie; F. Novkoski; G. Ricard; G. Roberti; E. Falcon; P. Suret; G. El; and S. Randoux. "Interacting stream flows of soliton gases in deep-water surface gravity waves"; Extreme Waves (Aug. 2023), Dresden;

- **L. Fache**; F. Bonnefoy; G. Ducrozet; F. Copie; F. Novkoski; G. Ricard; G. Roberti; E. Falcon; P. Suret; G. El; and S. Randoux. "Interaction de gaz de solitons en eau profonde"; RNL (Marc. 2024), Paris.

Contents

Nonlinear Evolution of Soliton Gases in Optical, Electrical, and Hydrodynamic Systems

Abstract

Solitons are stable, localized nonlinear wave packets that emerge in integrable systems from a balance between nonlinearity and dispersion. When large ensembles of solitons interact in random configurations, they form what is known as a *soliton gas*, a many-body nonlinear wave system whose dynamics call for a statistical treatment. While the theoretical framework for soliton gases has been extensively developed under the assumption of integrability, many physical systems exhibit weak perturbations that break this condition. The impact of such deviations on the spectral and statistical properties of soliton gases remains poorly understood. In this thesis, we experimentally investigate the dynamics of dense soliton gases in three distinct physical platforms: a large deep-water wave tank governed by the focusing nonlinear Schrödinger equation, a nonlinear electrical transmission line modeled by a dissipative KdV equation, and a recirculating optical fiber loop described by a perturbed focusing NLSE. Each system provides a setting to explore the effect of weak integrability breaking, such as damping, diffusion, or optical gain. Our results highlight the limitations of existing kinetic or hydrodynamic theories in weakly non-integrable regimes and point to the need for new frameworks capable of capturing soliton-radiation coupling, spectral reshaping, and non-isospectral evolution.

Keywords: soliton gas, integrable turbulence, integrability breaking, inverse scattering transform

---

Physique des Lasers, Atomes et Molécules (PhLAM) UMR 8523
2 Av. Jean Perrin – 59650 Villeneuve-d'Ascq Cedex – France

Évolution Non-linéaire de Gaz de Solitons dans des Systèmes Optiques, Electriques et Hydrodynamique

Résumé

Les solitons sont des paquets d'ondes non linéaires stables et localisés qui émergent dans des systèmes intégrables à partir d'un équilibre entre non-linéarité et dispersion. Lorsque de grands ensembles de solitons interagissent dans des configurations aléatoires, ils forment ce que l'on appelle un *gaz de solitons*, un système non linéaire dont la dynamique nécessite un traitement statistique. Bien que le cadre théorique des gaz de solitons ait été largement développé sous l'hypothèse d'intégrabilité, de nombreux systèmes physiques présentent de faibles perturbations qui brisent cette condition. L'impact de telles déviations sur les propriétés spectrales et statistiques des gaz de solitons reste mal compris. Dans cette thèse, nous étudions expérimentalement la dynamique de gaz de solitons denses au sein de trois plateformes physiques distinctes : un grand canal à houle en eau profonde régi par l'équation de Schrödinger non linéaire focalisante, une ligne de transmission électrique non linéaire modélisée par une équation de KdV dissipative, et une boucle de recirculation fibrée décrite par une NLSE focalisante perturbée. Chaque système constitue un cadre permettant d'explorer les effets de faibles brisures d'intégrabilité, telles que les pertes, la diffusion ou du gain optique. Nos résultats mettent en évidence les limites des théories cinétiques ou hydrodynamiques existantes dans les régimes faiblement non intégrables, et soulignent la nécessité de nouveaux cadres capables de décrire le couplage soliton-radiations, les réorganisations spectrales et les évolutions non isospectrales.

Mots clés : gaz de solitons, turbulence integrable, brisure d'integrabilité,transformée de diffusion inverse